The Electronic and Structural Properties of Semiconductor Heterostructures

Thesis submitted for the degree of

Doctor of Philosophy (Science)

in

Physics (Theoretical)

by

JOYDEEP CHATTERJEE

Department of Physics

University of Calcutta

2021

Dedicated to

The Source of All Knowledge

Acknowledgement

I wish to express my heartfelt gratitude towards my supervisor, Prof. Priya Mahadevan for her supervision and support during my Ph.D. Her gentle treatment and encouragement have helped me a lot to stay motivated over all these years of my Ph.D. Her valuable opinion and inputs have enriched my thesis. I also wish to thank my thesis committee members, Late Prof. Sugata Mukherjee and Prof. Manoranjan Kumar for their valuable suggestions during the course of my Ph.D.

I must thank the S. N. Bose Centre, for the research facilities that it provided me with, and the nice peaceful environment it has which is supportive of a focussed mindset and for the cordial people here that I came in contact with. I would also like to thank CSIR for the fellowship they provided me with to support myself during my Ph.D. period. I would like to specially thank Nibedita Madam for her constant emotional support during my times of stress. I would also thank Abhijit da and Debalina Madam of the computer cell for their frequent assistance with technical issues and the computer cell as a whole.

I would like to take this opportunity to thank all my group members, seniors as Saikat da, Hirak da, Ruma Di, Shishir Da, Sagar Da, Basudeb da, Deepika di, my contemporaries as Poonam, and juniors as Sumanti, Debayan, Prasun, Shibham, Krishnendu, for their help and support.

I also wish to thank friends and seniors in the centre, Poulomi, Subhadeep, Anita, Arpita, Karan, Hrishit, Dhani, Chandreyee, Sumonto, Sayani di, Arindam da, Ankan, Rahul, and Victor for rendering support, making up a friendly ambience, and providing a scope to share my thoughts and feelings.

Finally, I would thank my mother for her support.

Joydeep Chatterjee
S. N. Bose National Centre for Basic Sciences
Kolkata, India
2021

List Of Publications

1. Metal-chalcogen bond-length induced electronic phase transition from semiconductor to topological semimetal in ZrX_2 (X=Se and Te).
   Indrani Kar, **Joydeep Chatterjee**, Luminita Harnagea, Y. Kushnirenko, A. V. Fedorov, Deepika Shrivastava, B. Bchner, P. Mahadevan, and S. Thirupathaiah.
   Phys. Rev. B **101**, 165122 (2020).

2. Engineering spin-valley physics in bilayers of $MoSe_2$.
   Poonam Kumari, **Joydeep Chatterjee**, and Priya Mahadevan.
   Phys. Rev. B **101**, 045432 (2020).

3. The Anomalous Electronic Structure of ReS_2.
   Joydeep Chatterjee, Prasun Boyal and Priya Mahadevan.
   (manuscript submitted)

4. Strain induced changes in the electronic structure of monolayer of ReS_2.
   Joydeep Chatterjee and Priya Mahadevan.
   (manuscript under preparation)

5. Why is 1T polymorph favoured in ZrX_2?
   Joydeep Chatterjee and Priya Mahadevan.
   (manuscript under preparation)

6. Type-I to type-II electronic structure transition in GaAs/AlAs heterostructure.
   Joydeep Chatterjee and Priya Mahadevan.
   (manuscript under preparation)

Contents

List of Figures

List of Tables

Chapter 1

Introduction

Semiconductor Heterostructures

Semiconductor heterostructures have become an indispensable and central part to modern solid state physics. Initial development of heterostructures via doping a semiconductor material with impurities and injecting carriers made it possible to manipulate fundamental parameters like band gaps, effective masses of the charge carriers, mobilities and so on. In 1970, heterojunctions of III-V semiconductors were realized. The realization of p-n junction semiconductor lasers paved way for semiconductor optoelectronics [1–5]. To enhance the effect of electron confinement and optical confinement, it is preferable to sandwich a narrow bandgap semiconductor between a semiconductor having wider bandgap on both sides, thereby forming a heterojunction [7]. The narrow bandgap material serves as the active region where the electron and optical confinement happen. A rare coexistence of few favourable properties, like a small effective mass, wide bandgap, radiative recombination, sharp edge-to-edge optical absorption due to direct bandgap, high electron mobility had made GaAs a highly promising material for studying semiconductors from the very beginning. The first promising systems for realization of double heterojuncton turned out to be GaP-GaAs and AlAs-GaAs. AlAs-GaAs were preferred because they are lattice matched. Double heterostructures, quantum wells, quantum wires, and quantum dots, are being widely studied, explored and made use of in devices, like lasers, light-emitting diodes (LED's), bipolar transistors, high-mobility transistors and solar cells.

Thin films, surfaces, and heterostructure superlattices have provoked elaborate research in this area due to their importance in device fabrication and a plethora of exciting properties [8–24] they possess. In layered materials or films, the carrier motion is restricted to the direction normal to the layer or film. This imposes confinement effects similar to

that in a one-dimensional potential well. The depth of the well is taken to be infinite for films, whereas in semiconductor heterostructures the wells associated with the layers have a finite depth and they are rectangular in shape [18]. In a thin film, layered materials or semiconductor surfaces, this quantum size effect (QSE) comes into play when the thickness of the layer or the film, or surface depth becomes comparable to the De Broglie wavelength of an electron or its mean free path in the layer. Because of the confinement along the normal direction, the electrons or holes in such a film may be thought of as a two-dimensional electron gas and the particle motion in the normal direction is restricted. QSE gives rise to interesting changes in optical absorption and electron tunneling properties of the material and has been observed in semiconducting surfaces and layers [16–19], thin films and layered materials [21–24].

Quantum-confinement in heterostructures have been extensively studied since the mid-1970s [25, 26]. In type-I structures, the valence band maximum (VBM) and conduction band minimum (CBM) of the narrower-band-gap material are nested within the gap of the wider bandgap material. A staggered band alignment exists [27, 28] in type-II structures. The type-I to type-II transition can be achieved by choosing the composition and layer thickness. A crossover from type-I to type-II is obtained upon decreasing the thickness of the middle layer.

It is customary to describe the electronic structure in bulk semiconductors using the effective-mass approximation. This description is simpler than the tedious tight-binding or pseudopotential calculations. This also goes by the name of envelope function approximation. In this approach, the band dispersion at some reciprocal point is approximated with a parabola. Electronic states resulting from the quantum confinement effects [51] in layered semiconductors can be determined merely from the knowledge of bulk parameters and band offsets. The motion of charge carriers near the band extrema and charge redistribution across the interfaces in weakly varying perturbation potentials, like magnetic or electric fields or impurities, can be described using this method [52, 53]. Effective mass method (EMM) has to be used strategically to determine the electronic eigenstates in semiconductor heterostructures, superlattices, quantum wells etc. This is because for quantum wells, one important condition for the validity of this approximation, namely weak perturbation potential, is not fulfilled as the barriers at the atomically abrupt interfaces are large. One can therefore use EMM separately for each layer, where the eigenfunctions of each layer are given by envelope functions which are superpositions of periodic functions that form a complete basis set. These envelopes are then connected at the interface [57, 58]. Deriving the relevant boundary conditions has been a principal concern. Much work has been invested on setting up the boundary conditions [54–56].

A lot of efforts has been put by people in improving upon the envelope-function method to derive the effective-mass equation [59] from there. Despite the application of enevelope function theory for heterostructures being ad hoc, the 'particle in a box' model has been effectively used in heterostructures. The type-I to type-II structural transition in heterostructures can be efficiently described in terms of this model. In a type-I structure, the electrons in the conduction band and holes in the valence band can be thought of as particles confined inside one dimensional boxes made of the barriers along the growth direction. The associated changes in the energies of the carriers consequent upon increasing confinement, leading to the crossover to type-II structure, can then be described in a simpler way in terms of this picture.

Epitaxial Methods for Synthesis: MBE, Colloidal Synthesis and van der Waals Epitaxy

For the study of type-I to type-II transition and other properties of double heterostructures, superlattices, quantum wells, it is necessary to grow heterostructures where individual layers can be thinned down to few monolayers with exact control on the growth. Molecular beam epitaxy (MBE) is the most popular method adopted for the growth of thin, epitaxial films of oxides, semiconductors and semiconductor heterostructures. In MBE, beams of atoms or molecules in an ultra-high vacuum environment are incident upon a heated substrate crystal. The incident atoms or molecules move around over the surface to get into lattice sites, thus forming a crystalline layer in registry with the substrate. This is called an epitaxial film. The composition can be abruptly changed resulting in atomically sharp interfaces with precise control over the composition of each layer. Through MBE, it is possible to grow periodic repetition of alternating layers of semiconductors where individual layers can be made as thin as a few monolayers. A large variety of structures, like quantum well devices, superlattices, lasers, etc have been fabricated using MBE. By interposing one semiconducting material of narrower bandgap between a wider bandgap material on both sides, making the thickness of the narrow bandgap layer much less than the wavelength of electrons in the material, which amounts to few to tens of atom layers, a quantum well can be formed. Quantum well heterostructures are of great importance and they are studied at length. In our first project on GaAs/AlAs double heterostructures, we studied the type-I to type-II structural transition in such a quantum well structure formed by sandwicing GaAs region between AlAs regions on both sides. MBE lent high precision on thickness control and has established as the most important technique for the growth of III-V heterostructures [60]. Metal-

organic vapor-phase epitaxy (MOVPE) is also a popular approach for growth of III-V heterostructures [61, 62].

Quantum dots (QDs) find significant attention in optoelectronics [71, 72, 72–84] due to the tunablity of their optical bandgap [65–70]. In colloidal synthesis, QD nanocrystals are grown in liquid media with great control on their crystal structure, size and shape. Thus equipped with MBE and colloidal synthesis, the formation and study of heterostructures with ultrathin layers is easy to reaiize experimentally. This added to our interest to study their properties through our theoretical calculation.

In epitaxy, a crystalline material is grown on the surface of a substrate crystal, where the growth of each atomic unit requires some specific relations regarding the orientational alignment with the substrate to be fulfilled [85]. In conventional epitaxy, there happens formation of strong chemical bonds at the interface between the epitaxial material, also called the epilayer or overlayer, and the substrate. It is the presence of dangling bonds at the surface of the substrate [86, 87] that causes the atoms of the overlayer to pair with atoms in the substrate leading to epitaxial growth of the overlayer [Fig. 1.1(a)]. The atoms of the overlayer try to sit on top of the atoms of the substrate. In case of lattice-mismatch between overlayer and the substrate, this forces the cell parameters of the overlayer to change from their values in the freestanding bulk phase and match with those of the substrate. As a result, accumulation of strain energy happens in the system. The strain energy bulids up with increasing the thickness of the epilayer and the system reaches its limiting capacity in accommodating the strain energy at some critical thickness [88] of the epilayer. The system nucleates defects to relax the strain energy beyond the critical thickness.

Koma's group, in 1984, first realized what is called the van der Waals epitaxy (vDWE). They grew Se on Te and $NbSe_2$ on MoS_2 using vDWE [86]. In vDWE, the bonding between the overlayer and the substrate is via weak van der Waals interactions and not the stronger covalent bonding. Due to the weak van der Waals type binding between the overlayer and the substrate, first few layers of the overlayer don't strain much. This offers the advantage that the nucleation of defects is absent even for a large lattice mismatch. The substrate or the epilayer has smooth surfaces [86, 87, 90] with no active dangling bonds, which makes the surfaces chemically inert. The weak interionic [94] van der Waals interaction that exists between the overlayer and the substrate is due to pure Coulombic interaction between dipoles. This doesn't change the electronic structure of the interacting materials. Bulk materials have surfaces with dangling bonds. They are sometimes used as substrate only after passivating these dangling bonds [92, 93] [Fig. 1.1(c)]. Two dimensional materials are the best choice for vDWE owing to their naturally smooth sur-

faces [91] [Fig. 1.1(b)]. Using vDWE, these 2D materials can be grown on a range of substrates to fabricate heterostructure and integrated circuits.

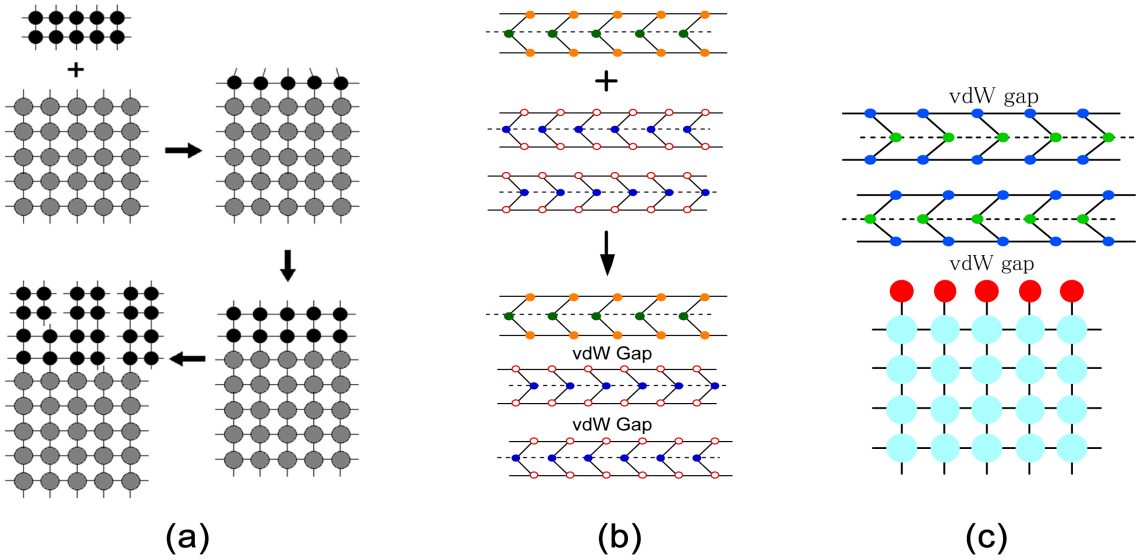

Figure 1.1: Schematic diagrams in case of lattice-mismatch of (a) conventional epitaxy resulting in strain due to covalent bond formation, (b) vDWE in layered materials with no strain accumulation, and (c) vDWE of a layered material on a passivated bulk susbtrate resulting in no strain. Figure taken from [89].

Two-Dimensional Layered Materials and Transition Metal Dichalcogenides (TMDs)

Two-dimensional layered materials (2DLMs) have received prime research interest due to the wide spectrum of physical properties they possess [95–100] and the novel applications that they find in electronics and optoelectronics. This area of research was sparked by the discovery of graphene [101–103]. Other 2DLMs have got extra advantages over graphene due to their tunability of electronic and optical properties and bandgaps suitable for optoelectronic application. There are various approaches of synthesizing two-dimensional materials, some of which are easier and inexpensive. The electronic properties of 2D layered materials range from semiconductors to metals. Atoms in each layer are chemically bonded together via covalent interactions and the surfaces are smooth and free of dangling bonds. Individual monolayers are weakly bonded via van der Waals interaction. This offers the advantage of manufacturing heterostructures by stacking one layer on top of another without incurring considerable strain even in the presence of lattice parameters

mismatch [107]. Moreover the weak van der Waals forces don't modify the electronic properties of individual layers and hence various types of materials can be combined to fabricate functional materials with diverse applications.

Electronic and optical properties of such heterostructures can be manipulated by varying the number of layers [105, 106]. There are a number of candidates belonging to the group of 2D materials with multifarious properties, namely graphene [108, 109], transition metal chalcogenides [110, 111] and transition metal dichalcogenides [112–114], hexagonal boron nitride [115], black phosphorus [116] etc. that find wide interest in experiments as well as in theoretical research. One layered material has been stacked on top of another to form 2D-2D heterostructures. There has been also growth of a layered material on a bulk substrate to fabricate 2D-3D heterojunction. 0D-2D and 1D-2D hybrids have also been formulated by growing nanostructures with 2D layered materials. These heterostructures find wide application in sensing, photovoltaics, photocatalysts etc.

Transition metal dichalcogenides (TMDs), generally represented by MX_2 (M= Transition metal ion, e.g. Mo, W etc., X= Chalcogen, e.g. S, Se or Te), are a class of 2D layered materials which come next to graphene in terms of the volume of study carried on them. They find special interest owing to their tunable electronic properties and variable bandgaps [117, 118, 123]. Their electronic properties vary from semiconductor to metal. For example, HfS_2 is insulating, MoS_2 and WS_2 are semiconducting, WTe_2 and $TiSe_2$ are found to be semi-metallic, and there are metals like NbS_2 and VSe_2. In TMDs, individual layers are stacked together via weak van der Waals forces. They are easy to be thinned down to very narrow thickness through mechanical exfoliation [119, 120]. Each monolayer consists of a hexagonal plane of metal atoms sandwiched between two hexagonal planes of chalcogens with the chalcogens coordinated around each metal ion in a trigonal prismatic arrangement. Atoms within each monolayer are strongly bonded together via covalent interaction.

In the bulk, most of the TMDs are indirect bandgap semiconductors. There occurs a crossover to a direct gap [121, 123–126] in going to the monolayer limit [Fig. 1.2], which is associated with a dramatic enhancement in photoluminescence [122]. Thus, the bandgap can be engineered by changing the number of layers [123, 127] along with a drastic change in effective masses due to changes in band curvature.

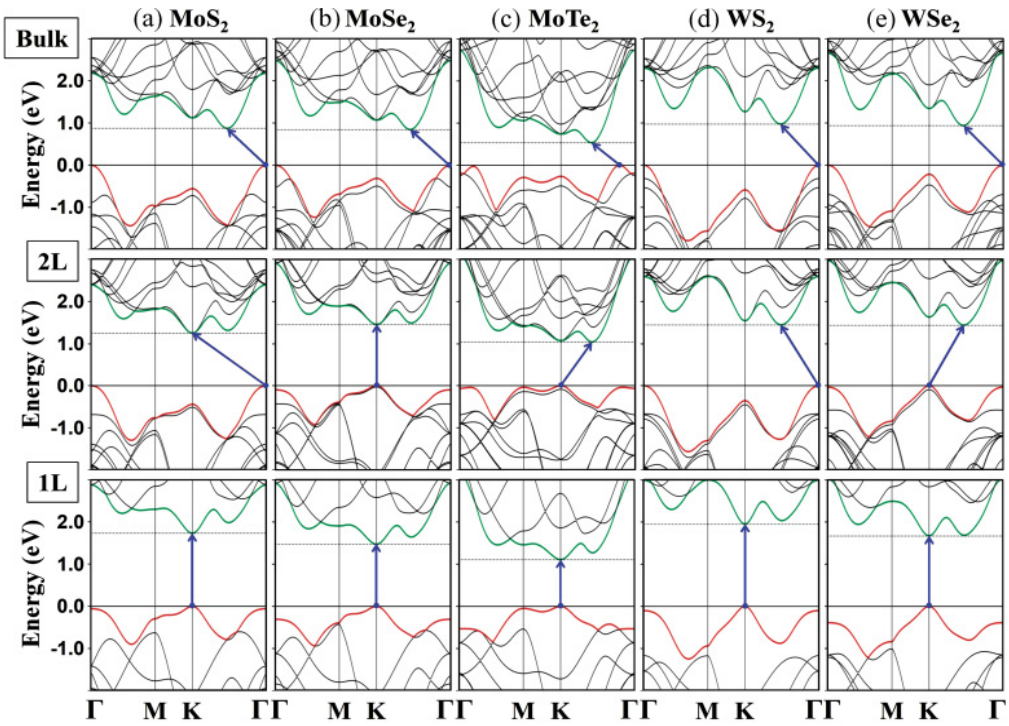

Figure 1.2: (Color online) Band structures of (a) MoS_2 , (b) $MoSe_2$, (c) $MoTe_2$, (d) WS_2 , and (e) WSe_2 from the bulk (upper panels) to double-layer (2L, middle panels) and single-layer (1L, bottom panels). The horizontal solid lines in each panel indicate the VBM and the dotted lines indicate the CBM. The solid blue arrows indicate the lowest energy transitions. Reproduced from [121]

Through application of strain also, the electronic structures can be manipulated, where a transition from a direct gap to an indirect gap can be triggered in additon to a variation in the effective masses. There is a great interest in exploring the electronic properties of low dimensional TMDs, as they are rich with exciting physics [128–130]. Monolayers of MoS_2 [123, 131] shows high on-off current ratio that makes it promising channel material in field-effect transistors (FET). The optical radiation in monolayer MX_2 makes them useful for applications in optoelectronics [133–135]. In TMDs, strong spin-orbit coupling splits the valence bands [136–139] due to broken inversion symmetry, which makes them preferable for spin-physics exploration. TMDs are also fertile for realization of valleytronics devices owing to the presence of multiple conduction and valence band valleys [140, 141]. In TMD hetero-bilayers, formed by stacking different TMD monolayers, a type-II band alignment is found that leads to bound electrons and holes being localized on different monolayers, constituting interlayer excitons. They have potential applications in 2D light-emitting diodes, lasers, and photovoltaic devices [142]. In-plane heterojunctions can be grown between the 2D monolayer TMDs by lateral hetero-epitaxy.

In-plane TMD quantum wells [143–149] with one-dimensional interfaces offer a plethora of novel physical phenomena due to quantum confinement effects in them and find applications in electronics, optoelectronics and photocatalysts. Upon introducton of strain, doping and external electric field, interesting properties may unravel [150]. A true type-II alignment is achieved in TMD quantum wells by virtue of coherent lattice and strong interface scattering. This leads to the efficient separation of excitons and ehnance the photoluminescence. Spin-orbit coupling in these materials makes it possible to achieve topological insulator state and valleytronics.

Structural Polymorphs of TMDs

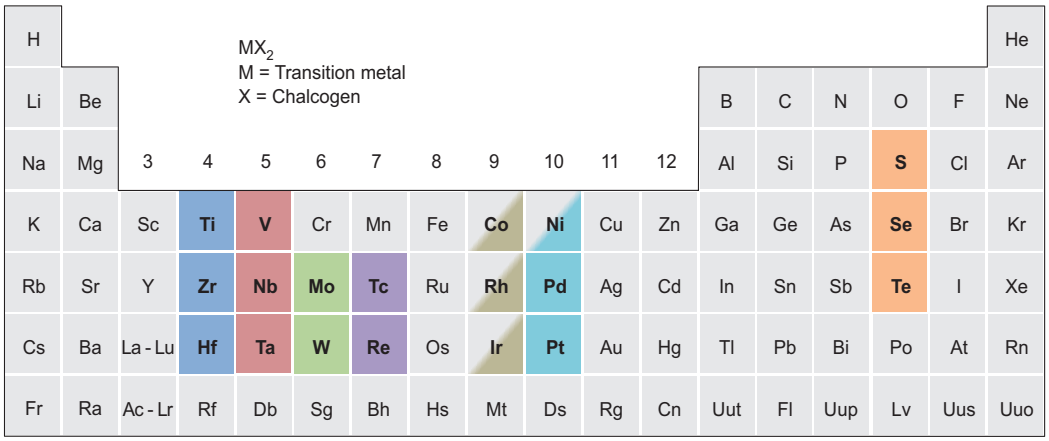

Figure 1.3: The transition metals and the three chalcogen elements that predominantly crystallize in layered structure have been highlighted in the periodic table. Reproduced from [151].

Group 4, 5, 6 and 7 TMDs mostly come in layered structures [Fig. 1.3]. Group 8 to 10 TMDs are generally found in bulk structures. For layered TMDs, the layer thickness is generally found to be $6 \sim 7$ Å. The metal atoms assume +4 valence state by giving away 4 electrons that fill the covalent bonds with the chalcogens. The chalcogens assume -2 valence states by accepting the electrons donated by metal atoms. The M-M bond length varies between 3.15 Å and 4.03 Å. The chalcogen ions coordinate themselves around each metal ion in either trigonal prismatic or octahedral structure. The octahedral structures are often distorted. Out of the two possible coordinations, which will be energetically favourable as the ground state is determined by the choice of metal and chalcogen atoms.

Bulk TMDs come in various types of polymorphs. Each polymorph exhibits a number of stacking polytypes. The most common polymorphs for layered TMDs are 1T, 2H and 3R

[Fig. 1.4]. In 1T, the letter 'T' stands for trigonal, meaning the structure has trigonal unit cell, and the number 1 implies that there is only one X-M-X unit per unit cell, or in other words in the stacking sequence. In 2H and 3R, H stands for hexagonal and R stands for rhombohedral respectively. In 2H, there are two X-M-X units in the stacking sequence. In 3R, there are three X-M-X units in the stacking sequence. MoS_2 is commonly found in 2H polymorph with trigonal prismatic coordination of metal ion. 2H polymorph comes in three different polytypes or stacking sequences. Group 4 TMDs (HfS_2, $ZrTe_2$ etc.) prefer 1T phase as their ground state structure with octahedral coordination of the metal ion.

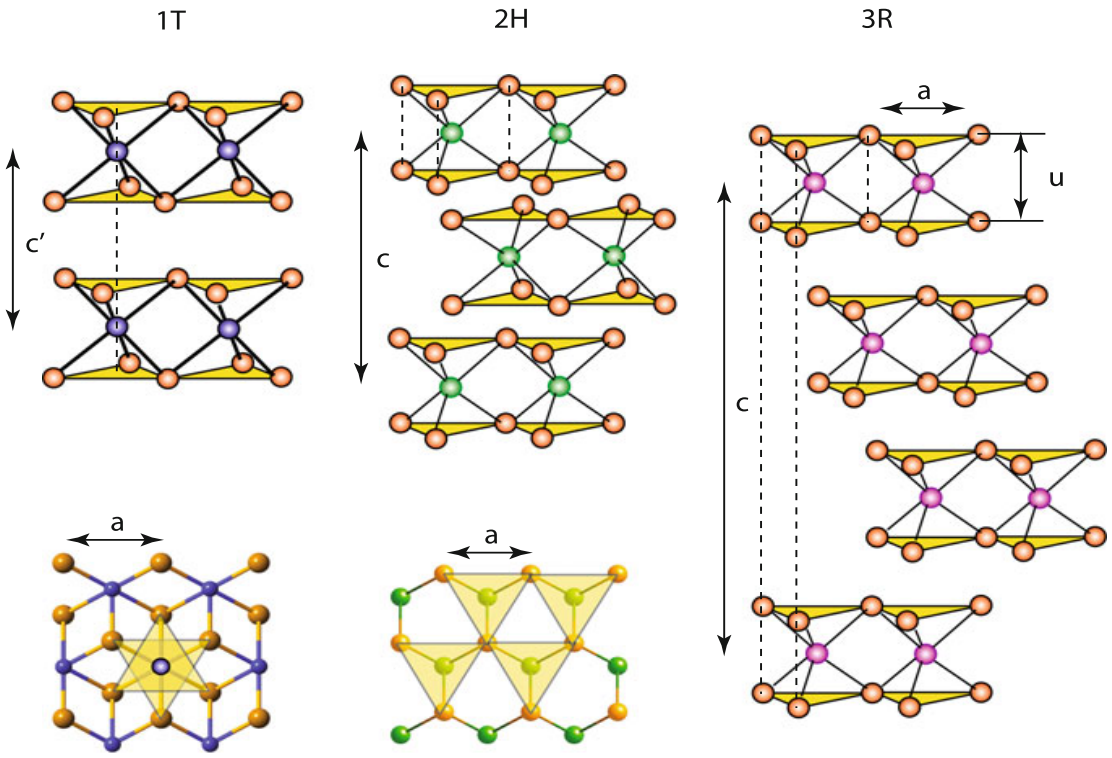

Figure 1.4: Three types of polymorphs in which bulk TMDs are found: 1T, 2H and 3R. Reproduced from [152].

Monolayer TMDs come in either of the two phases, trigonal prismatic (1H) [Fig. 1.5(a)] or octahedral (1T) [Fig. 1.5(b)]. Trigonal prismatic phase belongs to point group D_{3h} and octahedral phase belongs to point group D_{3d}. Depending on the coordination around the transition metal and its d electron count, electronic structure of TMDs show diverse properties.

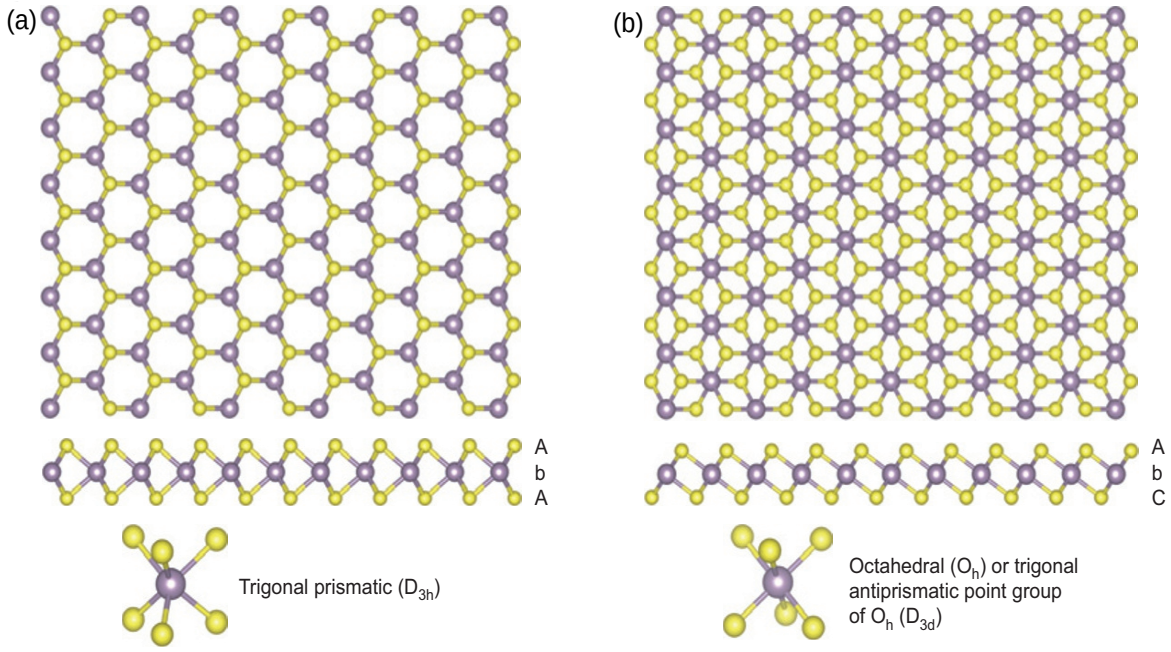

Figure 1.5: Top view and lateral view of single-layer TMD with (a) trigonal prismatic and (b) octahedral coordinations. Purple is for metal and yellow is for chalcogen. Reproduced from [151].

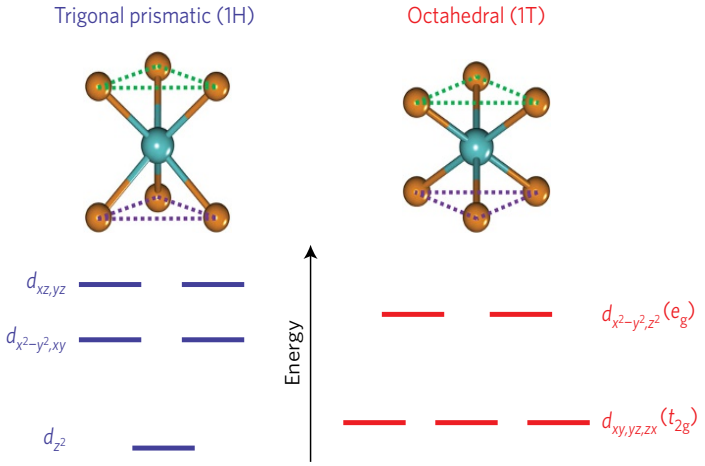

Figure 1.6: Schematic images of the splitting of d-orbital energies of transition metal in trigonal prismatic and octahedral coordination. Reproduced from [153].

The nonbonding d bands of metal ion lie between the bonding (σ) and antibonding (σ^*) bands of M-X bonds [Fig. 1.7]. Crystal field splitting in TMDs with octahedral coordination (D_{3d}) of transition metal ion divides the d orbitals of the transition metal into two sets of degenerate levels, namely e_g and t_{2g}. e_g contains d_{z^2}, $d_{x^2-y^2}$ orbitals and t_{2g} con-

tains d_{yz}, d_{xz},d_{xy} orbitals [Fig. 1.6]. The d electrons of the transition metal progressively fill up these levels. In TMDs with trigonal prismatic coordination (D_{3h}) of metal ion, the d orbitals divide into three groups, d_{z^2} (a_1), $d_{x^2-y^2}$, d_{xy} (e), and d_{xz}, d_{yz} (e') [Fig. 1.6], opening up a gap between a_1 and e.

The non-bonding d bands get progressively filled with electrons from group 4 to 10 transition metals leading to a plethora of electronic properties. A partial filling of the orbitals leads to metallic properties [Fig. 1.7], as in the case of 2H-$NbSe_2$ and 1T-ReS_2. Semiconducting properties arise when the orbitals get fully occupied [Fig. 1.7], as in the case of 1T-HfS_2, 2H-MoS_2 and 1T-PtS_2. The d bands gradually broaden with increasing atomic number of the chalcogen resulting in a reduction in the bandgap. The bandgap, for instance decreases from MoS_2 to $MoSe_2$ to $MoTe_2$.

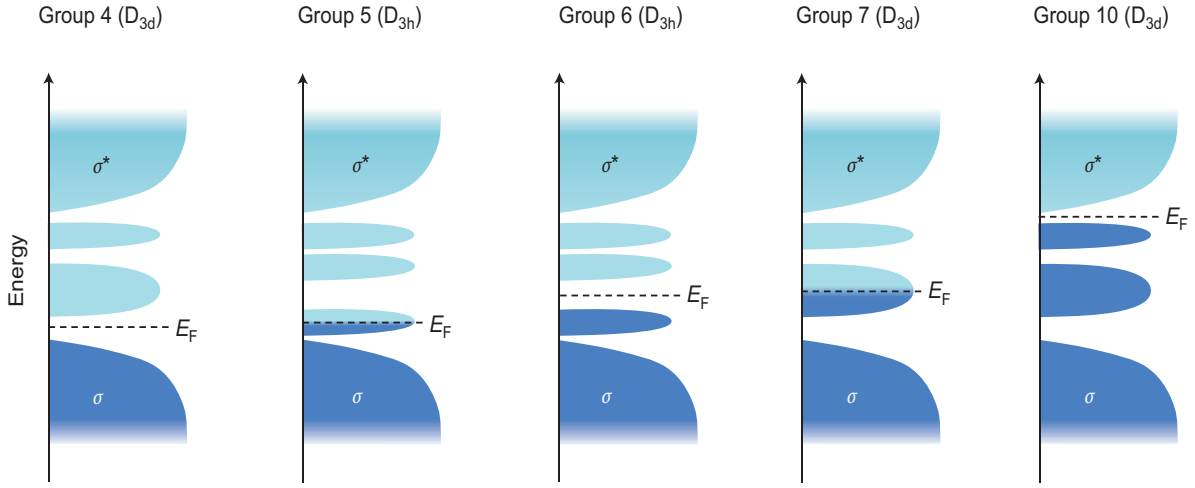

Figure 1.7: Schematic illustration showing progressive filling of d orbitals of transition metal that are located in between the bonding (σ) and anti-bonding states (σ^*) in group 4, 5, 6, 7 and 10 TMDs. D_{3d} compounds form two non-bonding d orbitals, d_{yz},d_{xz},d_{xy} (bottom) and d_{z^2}, $d_{x^2-y^2}$ (top), while D_{3h} compounds exhibit three d orbitals whose character is predomintly d_{z^2} ,$d_{x^2-y^2}$,d_{xy} (from bottom to top). Reproduced from [151].

Which phase will be preferred as the ground state configuration for a given TMD depends on the d-electron count of the transition metal. Group 4 TMDs, which have a d^0 configuration, are found in octahedral phase [Fig. 1.8(b)]. Group 5 TMDs with d^1 configuration are found in both trigonal prismatic [Fig. 1.8(a)] and octahedral [Fig. 1.8(b)] phases. Group 6 TMDS (d^2) prefer trigonal prismatic phase [Fig. 1.8(a)] and group 7 TMDs (d^3) assume a distorted octahedral coordination [Fig. 1.8(c)].

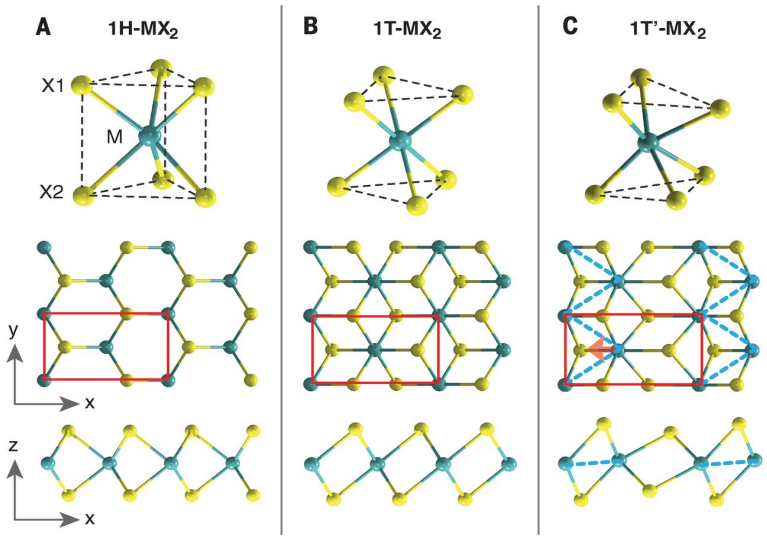

Figure 1.8: (A) Trigonal prismatic (1H), (B) octahedral (1T) and (C) distorted octahedral (1T′) phases of TMDs. Reproduced from [154].

Lattice Instabilities in TMDs, Peierls Distortion

Layered transition metal dichalcogenides (TMDs) have been observed to show a wide range of lattice instabilities [156–161]. All metallic TMDs undergo some type of lattice distortions with varying strength. In group V TMDs (M = V, Nb, Ta), the transition metal ion has the formal electronic configuration of d^1. In these TMDs, the distortions lead to charge-density-wave (CDW) phases [157] for both 1H and 1T. There has been a lot of controversies in literature as regards to the origin of distortion in group V TMDs. Initially it was attibuted to a Peierls mechanism based on the Fermi surface nesting argument [165,166], later challenged by others [167]. There have come up proposals based on real-space chemical bonding arguments [158,169]. In group VI (M = Mo, W) TMDs, the transition metal ion has the formal occupation of d^2. They are mostly found stable in 1H polymorph, but they also occur in 1T polymorph. 1T phase undergoes a distortion to end up in 1T′ phase which is metastable. Lattice distortions are much stronger [174,175] in them. This 1T′ phase has a periodicity of 2 x 1 [170,171]. A Peierls nesting mechanism was suggested for certain Mo dichalcogenides [172,173] as the possible way of distortion. This hypothesis is based on the observation of pockets in Fermi surface that are nested. Group VII TMDs with d^3 formal electron configuration are found in 1T phase which is highly unstable and transforms into a strongly distorted form, referred to as 1T′′. 1T″ structure has a periodicity of 2 x 2. In 1T″ structure, the transition metal ions tetramerize to form diamond shape clusters. These clusters are connected at the corners to form chains running parallell to each other [174,176]. Kertesz and Hoffman explained the distortion as arising from strong interactions between in-plane d_{xy} and $d_{x^2-y^2}$ orbitals [175]. Latest, a

notion has been conceived that the 1T″ phase arises consequent upon a Peierls instability of the 1T′ phase [177].

In a theorem, proposed by Rudolf Peierls in 1930s, he stated that a one-dimensional evenly-spaced metallic chain of monatomic lattice with one electron per ion in its ground state is unstable and spontaneously undergoes a transition leading to an insulating state with periodic lattice distortion. The energy gap opening associated with the distortion occurs at the zone boundaries. The proof of the theorem can be given using a simple model of a 1-D crystal with lattice spacing a [155]. Gaps appear at the edge of the Brillouin zone ka=$\pm\pi$ in the E-k diagram. This is similar to the Kronig-Penney model employed for studying the origin of band gaps in solids. Each ion contributing one electron will lead to half-filled band, i.e. upto ka=$\pm\pi/2$, in the ground state.

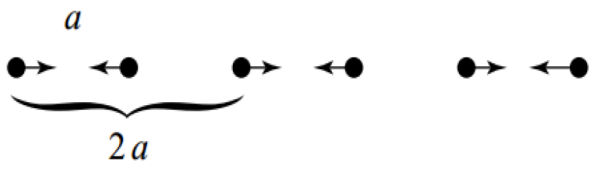

Figure 1.9: Movement of ions in Peierls Distortion for a linear chain of ions

In Peierls distortion in 1-D chain, every other ion moves closer to its neighbor on one side and further away from the neighbour on the other side [Fig. 1.9]. The energy cost in creating the longer bond between ions is outweighed by the energy gain in the formation of the shorter bond [Fig. 1.10]. As a net effect, the period of the lattice has just doubled from a to 2a along the chain. As a consequence of doubling the period, additional band gaps would appear at multiples of ka=$\pm\pi/2$ [Fig. 1.11].

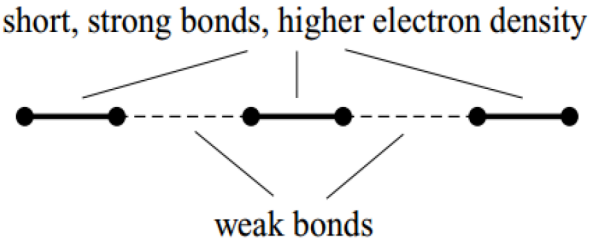

Figure 1.10: Schematic of Peierls Distortion

Introduction of the new band gaps will cause distortion of the bands in the vicinity of the these gaps resulting in the electrons having a lower energy than they would have in the

perfect crystal. Thus there is a energy gain due to the distortion of the bands. The lattice distortion becomes energetically favorable when the energy gain from the new band gaps exceeds the energy cost of reorganizing the ions.

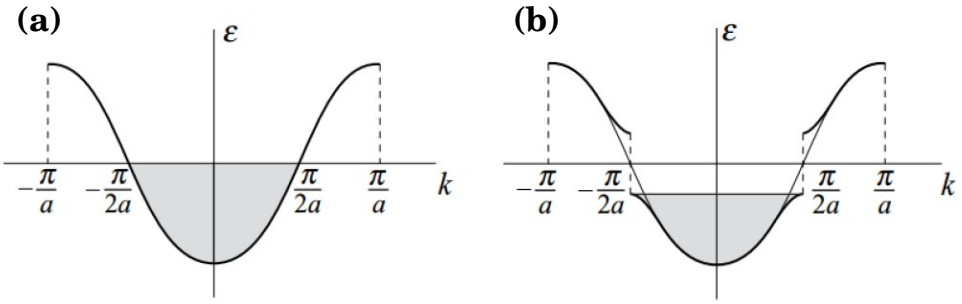

Figure 1.11: E-k dispersion curves (a) before and (b) after Peierls Distortion

It is important to mention that Peierls transition should be observed only at low temperature, when the system is close to its ground state. Because of the nature of the distortion where pair of ions come closer together on a periodic fashion, this is also called dimerization. According to Peierls, the energy gain from a distortion that we are talking about can be expressed as

$$\Delta E \propto -\tau^2 \log(\tau) \tag{1.1}$$

where τ is the relative displacement of atoms from their symmetric positions. The distortion happens to be periodic in a way that the Fermi surface intersects the edge of the Brillouin zone. For small distortions, the energy gain in Eq. 1.1 exceeds the repulsion between the atoms which varies as τ^2. Thus the one-dimensional chain is intrinsically unstable. For half-filled valence bands, it leads dimerization of the chain in which every second atom is displaced by τ. This results in the largest energy gain. One-dimensional carbon chains undergo dimerization [178, 179] that is thought to be resulting from Peierls distortion. More complex three-dimensional crystals also host Peierls-like transition [180–183]. The main concept was that lowering of energy band at the Fermi level is the reason behind the distortion. Johannes and Mazin [184] analyzed a system of Na atoms and argued that dimerization along the chain is energetically unfavorable. D. Kartoon, U. Argaman, and G. Makov reported [185] that "the distortion is not universal but conditional upon the balance between distorting and stabilizing forces". They studied the stability of quasi-one-dimensional equally spaced monatomic chains on the basis of total energy consideration. Three-dimensional calculations were employed to describe one-dimensional lattices. This is the reason they called them quasi-one-dimensional. Considering all the

energy components, they arrived at the conclusion that in the process of dimerization, it is the coulomb energy that dominates the energy gain. So the main driving forces for distortion are the electrostatic interactions between the electrons and ions. This is in contradiction to the earlier held notion that the electron band lowering at the Fermi level is responsible. This opening of the energy gap at the edges of Brillouin zone is only one of several factors contributing to the energy gain. This may cancel with other contributions. The chains are driven toward their symmetric arrangement by the action of stabilizing force derived from the electronic kinetic energy which causes an energy loss. External factors e.g., stress, affect both forces and consequently the instability of one-dimensional nanowires. So the instability of one-dimensional chains is not a universal phenomenon, rather is found to be dependent on the external stress.

Strain Engineering of Physical Properties in TMDs

Strain engineering has been largely exploited in semiconductor physics over past few decades. 2D materials has far greater capacity to withstand elastic strain than bulk materials. This makes 2D materials useful for strain engineering. Compared to bulk materials, 2D materials have more ways of inducing strain via in-plane and out of plane deformation. Even a small amount of strain can largely alter the physical propertiesa in 2D materials.

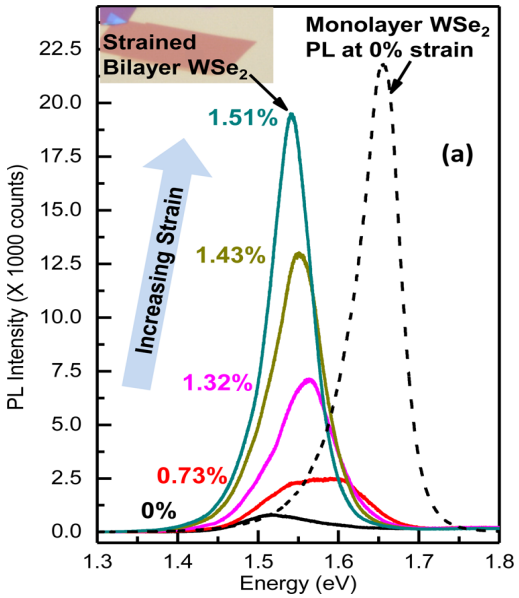

Figure 1.12: PL spectra of bilayer WSe_2 at different strain. Inset shows the optical microscope image of the bilayer WSe_2 flake. Reproduced from [194].

Electronic structure of 2D materials are altered by strain where the band gap changes significantly with strain [194, 195]. Under uniaxial homogeneous tensile strain, the PL intensity changes and the PL peak position shifts for bilayer WSe_2 [194] [Fig. 1.12]. There also takes place a transition from an indirect band gap to a direct band gap structure with uniaxial strain in MoS_2 [195], WS_2 [196] and WSe_2. For nonhomogeneous strain as in the presence of wrinkles or bubbles, PL intensity is enhanced and the PL peak position shows a red shift as a result of a 'funnel effect' [188, 191]. Upon irradiation with laser, in MoS_2 flakes with wrinkles, photogenerated excitons move to the vicinity of the wrinkles which have maximum strain [Fig. 1.13]. They recombine there. Since these regions have narrowest band gaps, it results in a red shift of PL peak position [188]. Band gap modulation via strain depends on the number of layers in 2D materials [192,193,197], like the band gap changes for monolayer and bilayer MoS_2 are found to be different under 1% uniaxial strain [193].

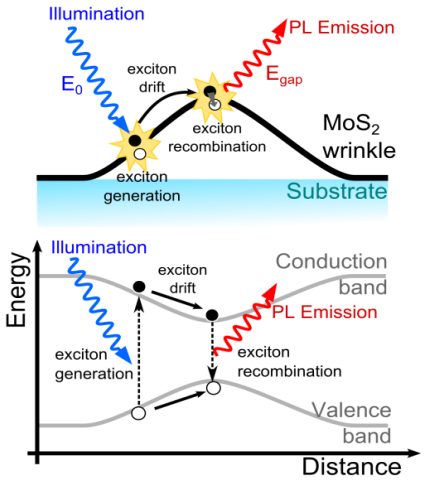

Figure 1.13: Schematic diagram explaining the funnel effect due to the non-homogeneous strain in the wrinkled MoS_2. Reproduced from [188].

Uniaxial or biaxial strain can modify the phonon structure of 2D materials which are reflected in the splitting and shifting of Raman peaks. For monolayer graphene, uniaxial tensile strain causes red shifts of G and 2D peaks and splits them [198]. For monolayer of MoS_2, uniaxial strain splits the E′ peak into E'^{+} and E'^{-} as observed by Bolotin et al. [199] [Fig. 1.14]. Red shifts of E^1_{2g} and A_{1g} peaks have been observed by Berry et al. in the wrinkled parts of MoS_2 flake [200]. In anisotropic 2D materials, uniaxial strain has dissimilar effects on Raman peaks when applied along various directions. For black phosphorus (BP) [201], this anisotropic Raman response is predicted to be originated from the changes of both bond lengths and bond angles upon applying strain in BP flakes.

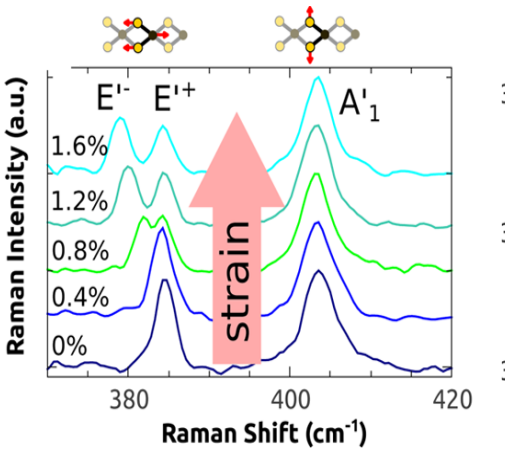

Figure 1.14: The splitting of E′ Raman peak of monolayer MoS_2 under uniaxial strain. Reproduced from [199].

To induce magnetism in 2D materials, local strain has been proven to be an efficient way. This facilitates application in spintronics. Strain can directly induce magnetism in non-magnetic 2D materials. For example, ferromagnetism can be induced via biaxial tensile strain in TaS_2 , $TaSe_2$, [202] NbS_2, $NbSe_2$, [203] $SnSe_2$, [204] and M_2C (M = Hf, Nb, Sc, Ta, V) [205] monolayers, which are nonmagnetic otherwise. In NbS_2 or $NbSe_2$, emergence of spin-polarized states happen because the strain effects the magnetic moments of S(Se) atoms and Nb atoms differently. Ferromagnetic behaviour is found as a result of a competition between through-bond and through-space interactions. For some 2D materials, like graphene and MoS_2, strain engineering can be combined with doping or defects to induce and modify magnetism. Strain induced by wrinkles or web buckles are the widespread in inducing magnetism in nonmagnetic 2D TMDs.

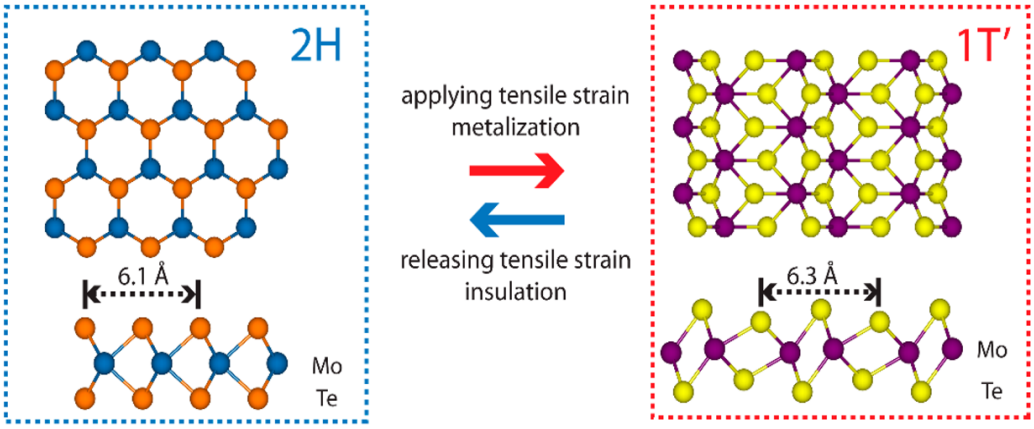

Figure 1.15: Semiconductor to metal transition in $MoTe_2$ induced by strain. Reproduced from [207].

Monolayer Mo and W based TMDs are likely to undergo a phase transition from semiconducting 2H phase with trigonal prismatic structure to metallic 1T and 1T′ phases with octahedral and distorted octahedral structures upon applying uniaxial strain, like what has been achieved in $MoTe_2$ [207] [Fig. 1.15].

The entire process occurs in steps, in which a coexistence of 2H and 1T′ phases is reached in the intermediate timeline before it completely transforms into 1T′. Upon releasing the strain, $MoTe_2$ returns to the 2H phase. In intrinsic 2D magnets, there happens coincidence of atomic and magnetic phase transitions under strain. For example, in CrI_3 [208] and Re-doped $MoTe_2$ [209], in-plane strain can cause transformation from ferromagnetic phase to Neel antiferromagnetic or ferrimagnetic phase. Such a synchronicity of structural and magnetic phase transition makes way to novel spintronic and phase-switching devices. Moreover, in 1T′ WTe_2, transition from semimetal to topological insulator phase is predicted [210] .

The enhancement in electron mobility [211, 212] upon uniaxial and biaxial strain has offered opportunities for application in transistors and improving the performance of FETs [213]. The piezoresistivity and piezoelectricity in strained 2D materials renders them suitable for applications in the sensors and photodetectors [214].

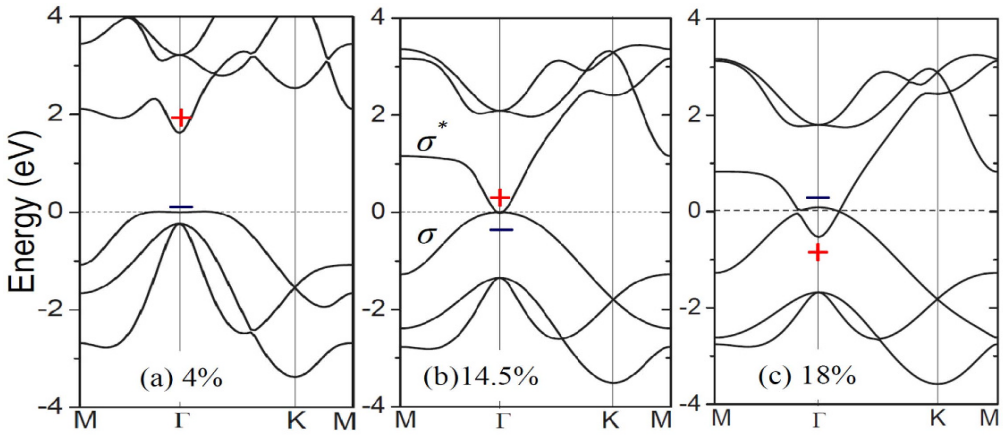

Figure 1.16: Electronic band structures of antimonene under different tensile strains obtained from DFT calculation within HSE functional. The energy at the Fermi level was set to zero. Band inversion has taken place around Γ for strain larger than 14.5%, as in (c). Reproduced from [216].

Strain can be employed to drive interesting topological transitions in 2D materials. First-principles calculations indicated that topological insulating (TI) state can be induced in antemonene by applying biaxial tensile strain larger than 14.5% which would reduce the buckling height of the lattice [216]. Hybridization of atomic orbitals get modified by

the reduction of buckling height. This leads to band inversion in the vicinity of the Γ point [Fig. 1.16] which makes the transition happen from normal semiconductor to a nontrivial topological insulator. This phase transition induced by strain is reversible and can be controlled. Dissipationless transport can be achieved in antemonene above room temperature owing to this transition which makes it befitting for future electronic devices with low power consumption.

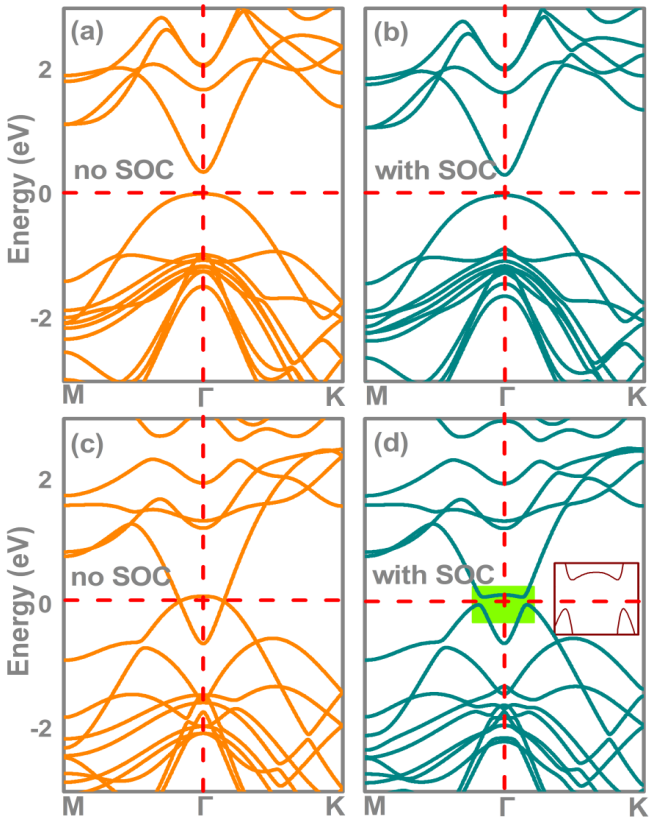

Figure 1.17: Band structures of β-InSe, with the upper row corresponding to unstrained β-InSe (a) without SOC and (b) with SOC; the lower row corresponds to band-inverted β-InSe (c) without SOC and (d) with SOC. The horizontal dashed red lines indicate the Fermi level. The inset in (d) is a magnified view near the Fermi level. (d) shows an insulating phase with a band gap of 121 meV established. Reproduced from [220].

C. Moulsdale et al. demonstrated that the topological characteristics get enhanced for the electron states in bilayer graphene by application of strain. As a result, large topological magnetic moment generates. L. Li et al. [217] have studied the effect of strain in zigzag ribbons of monolayer transition metal dichalcogenides. In the absence of strain, the system exhibits a topological phase. By inspecting the wave functions, they studied the evolution of the topological phase against application of in-plane uniaxial strain. Strain is found to shift the energy of 1D edge states leading to a topological phase transition.

Using first-principles calculations, Zhang et al. [218] have found that the electronic structure of buckled 2D monolayer tellurium can be tuned by application of strain, and leads to a topological phase transition. In 1T′ WTe_2 also, the electronic structure can be tuned via strain engineering, where uniaxial strain can open up a gap and make the material insulating. This phase transition has been confirmed by molecular beam epitaxy and in situ scanning tunneling microscopy or spectroscopy [219]. β-InSe can transform into novel three dimensional topological insulator (TI) when subjected to external strain [220], as has been predicted by ab initio calculations [Fig. 1.17]. SOC further opens a large gap of 121 meV. First-principles calculations demonstrated that with proper strain engineering, ferroelectricity and topological orders can be simultaneously established in perovskite $CsPbI_3$ [221].

Overview of the Thesis

This thesis deals with the electronic properties of semiconductor heterostructures. We use the term heterostructure loosely in the thesis and a large part of it is devoted to studying the properties of transition metal dichalcogenides (TMDs), which are 2D layered materials that are homostructures where the atoms of one layer sit on top of the atoms in the next layer with the adjacent layers interacting via weak van der Waals force.

In **Chapter 2**, the theoretical concepts behind the calculation carried out in the thesis have been discussed along with the techniques employed. The electronic structure of the materials have been calculated mostly using density functional theory and sometimes using tight binding model, both of which have been discussed in this chapter.

In **Chapter 3**, we have tried to probe the type-I to type-II electronic structure transition occurring in GaAs/AlAs heterostructures, where a GaAs region is sandwiched between two AlAs regions on both sides. We enquired whether the transition occurs abruptly or it takes place gradually over few monolayers. We followed the variation in the localization of the charge densities of carriers as a function of reducing thickness of the confinement region. We identified a sudden delocalization of electronic charge densities of the conduction band minimum occurring between 10 and 9 GaAs layers. This shows that the transition from type-I to type-II structure occurs abruplty in the system. To support our conclusion and also to understand the mechanism of the transition more clearly, we calculated the oscillator strength, which is a measure of the transition probability, for direct transition between VBM and CBM. Our result for transition probability supports our conclusion regarding the abrupt nature of the transition. We also calculated the spectral weight of various primitive cell characters present in the CBM and VBM of the supercell structures.

The spectral weights show that the Gamma characater in CBM vanishes as we move from 10 to 9 GaAs layers, which is explained by the delocalization of the electronic charges into the AlAs region. Both the oscillator strength and the spectral weights show sign of interface scattering. All these results evidently establish the abrupt nature of the transition.

In **Chapter 4**, we studied the electronic phase transition in group IVB transition metal dichalcogenides upon replacement of anions. We took ZrX_2 and HfX_2 for our studies. We found a semiconductor to metal transition upon replacing Se with Te. We first checked if charge transfer energy, which is the energy difference between the metal d and chalcogen p states, is playing the fundamental role in making the transition happen. Our results, as obtained from mapping the ab-initio band dispersions onto a tight binding model, indicated that charge transfer energy doesn't account for the phenomena. Next we looked if the metal-chalcogen bond lengths, which influence the hopping interaction strength between the metal and chalcogen ions, are important. We found that the metal-chalcogen bondlength is larger for Te coumpounds than the Se ones, which would lead to smaller hopping interaction strength for Te compounds. As a result, the gap opening becomes smaller for Te compounds. This shows that the transition from semiconductor to metal is dictated by the metal-chalcogen bondlengths.

Mo and W based TMDs are found in 2H polymorph in their ground state. But group IVB compounds prefer 1T structure as their ground state configuration. We enquired the reason behind the difference. We found that ZrX_2 in 2H structure would turn metallic with some of the notionally antibonding states, primarily contributed by d orbitals of the metal ion, coming down in energy to cross the fermi level. So the system prefers the 1T structure as it gains energy by vacating the d orbitals. We supported our results further with the comparison of the band energies computed for both 1T and 2H structures.

In **Chapter 5**, we explored our interest in the electronic properties of ReS_2, which appear to be unusual as compared to other TMDs. MoS_2 prefer 2H polymorph as its ground state and Mo has a d^2 configuration in MoS_2. Crystal field splitting in 2H structure leads to the degeneracy lifting of d states of Mo, and the lowest lying level gets occupied by the 2 electrons in the d shell of Mo. This makes MoS_2 semiconducting. But Re has a d^3 cofiguration in ReS_2 and is still semiconducting, which is strange. Upon looking at the structure of ReS_2, we found that the Re planes consist of diamond chains, which are one-dimensional chains of interconnected clusters of Re ions. Each cluster is comprised of 4 Re ions in the shape of a parallellogram. We conjectured that it is the formation of such Re clusters that may have played the fundamental role in making the material semiconducting. Using tight-binding model, we switched off various components of the

interactions within the Re plane and we arrived at the conclusion that it is the mutual interactions of Re ions within each cluster that is responsible for opening up a band gap and making the material semiconducting. There is another aspect of ReS_2 that is unusual. This is the negligible thickness dependence of the bandgap with the number of layers. This is in contrast to what have been observed for other TMDs. We found that it is the strong localization of the wavefunctions associated with the valence band maximum (VBM) and conduction band minimum (CBM) in the Re plane that leads to weak interlayer interaction and consequently the weak layer dependence of the bandgap.

Chapter 6 is devoted to investigating the evolution of the electronic structure of monolayer ReS_2 upon application of strain. We found the emergence of a double hump like feature in the valence band upon compression along in plane lattice vector b. This offers a fertile ground to induce a topological phase transition of the Fermi surface by doping the system with carriers. We also observed a band inversion taking place upon compression which we verified by analysing the charge densities and orbital projected band structures.

Bibliography

[1] N. G. Basov, O. N. Krokhin, and Yu. M. Popov, J. Exptl. Theoret. Phys. (U.S.S.R.) **40**, 1879-1880 (1961)

[2] D. N. Nasledov, , A. A. Rogachev, S. M. Ryvkin, and B. V. Tsarenkov, Sov. Phys. Solid State **4**, 782 (1962)

[3] R. N. Hall, G. E. Fenner, J. D. Kingsley, T. J. Soltys, and R. O. Carlson, Phys. Rev. Lett. **9**, 366 (1962)

[4] N. Holonyak Jr. And S. F. Bevacqua, Appl. Phys. Lett. **1**, 82 (1962)

[5] M. I. Nathan, W. P. Dumke, G. Burns, F. H. Dill Jr., and G. Lasher Appl. Phys. Lett. **1**, 62 (1962)

[6] H. Kroemer, Proc. IRE 45, 1535 (1957); RCA Rev. **28**, 332 (1957)

[7] Alferov and Kazarinov, 1963; Kroemer, 1963

[8] G. Dorda, "Surface Quantization in Semiconductors" in: Festkörper-Probleme XIII (Advances in Solid State Physics), p. 215, Pergamon-Vieweg (1973).

[9] C. C. Grimes, and T. R. Brown, Phys. Rev. Lett. 32, 280 (1974), ibid **29**, 1233 (1972).

[10] M. W. Cole, Rev. Mod. Phys. 46, 451 (1974).

[11] R. C. Jaklevic, , J. Lambe, M. Mikkar, , and W. C. Vassell, Phys. Rev. Lett. **26**, 88 (1971).

[12] R. C. Jaklevic, J. Lambe, M. Mikkar, and W. C. Vassel, Sohd State Commun. **10**, 199 (1972).

[13] R. C. Jaklevic, and J. Lambe, Surface Sci. **37**, 922 (1973).

[14] J. M. Rowell, Phys. Rev. Lett. **30**, 167 (1973).

[15] J. M. Rowell, , J. Vac. Sci. Technol. **10**, 702 (1973).

[16] Reviewed by Dorda, [Ref. 1].

[17] L. L. Chang, L. Esaki, and R. Tsu, Appl. Phys. Lett. **24**, 593 (1974).

[18] R. Dingle, W. Wiegmann, and C. H. Henry, Phys. Rev. Lett. **33**, 827 (1974).

[19] O. N. Filatov, and I. A. Karpovitch, Fiz. Tverd. Tela. **10**, 2886 (1968).

[20] Reviewed by M. I. Elinson, V. A. Volkov, V. N. Lutskij, , and T. N. Pinsker, , Thin Solid Films **12**, 383 (1972).

[21] L. A. Ageev, V. K. Miloslavskii, and I. N. Shklyarevskii, Fiz. Tverd. Tela. **15**, 2794 (1973), Soy. Phys. Solid State **15**, 1861 (1974).

[22] F. Consadori and R. F. Frindt, Phys. Rev. B **2**, 4893 (1970).

[23] K. Heidrich, W. Staude, and J. Treusch, Phys. Rev. Lett. **33**, 1220 (1974).

[24] A. D. Yoffe, , Festkörper-Probleme XIII (Advances in Solid State Physics), p. 1

[25] R. Dingle, A. C. Gossard, and W. Wiegmann, Phys. Rev. Lett. **34**, 1327 (1975).

[26] B. A. Wilson, IEEE Journal of Quantum Electronics, **24**(8), 1763-1777 (1988)

[27] T. J. Drummond and I. 1. Fritz, Appl. Phys. Lett. **47**, 284 (1985).

[28] P. Dawson, B. A. Wilson, C. W. Tu, and R. C. Miller, Appl. Phys. Lett. **48**, 541 (1986).

[29] H. Kroemer and G. Griffiths, IEEE Trans. Electron Devices EDL- **4**, 20 (1983)

[30] A. N. Baranov, B. E. Dzhurtanov, A. N. Imenkov, A. A. Rogachev, Yu. M. Shernyakov, and Yu. P. Yakovlev, Fiz. Tekh. Poluprovodn. **20**, 2217 (1986) [Sov. Phys. Semicond. **20**, 1385 (1986)]

[31] T. J. Drummond, E. D. Jones, H. P. Hjalmerson, and B. L. Doyle, lnst. Phys. Conf. Ser. **83**, 331 (1986).

[32] E. Finkman, M. D. Sturge, and M. C. Tamargo, Appl. Phys. Lett. **49**, 1229 (1986).

[33] E. Finkman, M. D. Sturge, M.-H. Meynadier, R. E. Nahory, M. C. Tamargo, D. M. Hwang, and C. C. Chang, J. of Lumin. **39**, 57 (1987)

[34] P. Dawson, K. 1. Moore, and C. T. Foxon, Proc. SPIE Symp. Quantum Well Superlattice Phys. **792**, 208 (1987).

[35] K, 1. Moore, P. Dawson, and C. T. Foxon, J. Phys. (Paris) C **5**, 525 (1987).

[36] J. Nagle, M. Garriga, W. Stolz, T. Isu, and K. Ploog, 1. Phys. (Paris) C **5**, 495 (1987).

[37] G. Danan, F. R. Ladan, F. Mollat, R. Planel, J. Phys. Colloques, C5 **48** , 499-502 (1987)

[38] G. Danan, B. Etienne, F. Mollot, R. Planel, A. M. Jean-Louis, F. Alexandre, B. Jusserand, G. Le Roux, J. Y. Marzin, H. Savary, and B. Sermage, Phys. Rev. B **35**, 6207 (1987).

[39] I. Minami, K. Hirata, K. Era, T. Yao,and Y. Masumoto. Phys. Rev. B **36**, 2875 (1987).

[40] M. H. Meynadier, M. D. Sturge, M. C. Tamargo, D. M. Hwang, and C. C. Chang, Phys. Rev. Lett. **60**, 1338 (1988).

[41] B. A. Wilson, IEEE J. Quantum Electron. **QE24**, 1763 (1988)

[42] G. Danan, B. Etienne, F. Mollot, R. Planel, A. M. Jean-Louis, F. Alexandre, B. Jusserand, G. Le. Roux, J. Y. Marzin, H. Savary, and B. Sermage, Phys. Rev. B **35**, 6207 (1987)

[43] E. Finkman, M. D. Sturge, M. H. Meynadier, R. E. Nahory, M. C. Tamargo, D. M. Hwang, and C. C. Chang, J. Lumin. **39**, 57 (1987)

[44] D. S. Jiang, K. Kelting, T. Isu, H. J. Queisser, and K. Ploog, J. Appl. Phys. **63**, 845 (1988)

[45] K. J. Moore, G. Duggan, P. Dawson, and C. T. Foxon, Phys. Rev. B **38**, 5535 (1988)

[46] R. Cingolani, L. Baldassarre, M. Ferrara, M. Lugara, Phys Rev B, **40**, 9 (1989)

[47] T. Nakayama and H. Kamimura, J. Phys. Soc. Jpn. **54**, 4726 (1985).

[48] M. A. Gell, D. Ninno, M. Jaros, and D. C. Herbert, Phys. Rev. B **34**, 2416 (1986

[49] J. B. Xia, Phys. Rev. B **38**, 8357 (1988)

[50] G. Li, D. Jiang, H. Han, and Z. Wang, Phys Rev B, **40**, 15 (1989)

[51] C. Cornet, A. Schliwa, J. Even, F. Dore, C. Celebi, A. Letoublon, E. Mace, C. Paranthoen, A. Simon, P. M. Koenraad, N. Bertru, D. Bimberg, S. Loualiche, Phys. Rev. B **74**, 035312 (2006)

[52] J. M. Luttinger, W. Kohn, Pys. Rev. **97**, 869-883 (1955)

[53] W. Kohn, Solid State Phys. **5**, 257 (1957)

[54] M. Altarelli, Phys. Rev. B **28**, 842 (1983)

[55] D. L. Smith, C. Mailhiot, Phys. Rev. B **33**, 8345 (1986)

[56] G. A. Baraff, D. Gershoni, Phys. Rev. B **43**, 4011-4022 (1991)

[57] G. Bastard, J. A. Brum, R. Ferreira, Solid State Phys. **44**, 229 (1991)

[58] M. G. Burt, J. Phys. Condens. Matter **4**, 6651 (1992)

[59] M. G. Burt, Semicond. Sci. Technol **3**, 739 (1988)

[60] A. Y. Cho, J. Vac. Sci. Technol. **8**, 31 (1971); A. Y. Cho, Appl. Phys. Lett. **19**, 467 (1971)

[61] H. M. Manasevit, Appl. Phys. Lett. **12**, 156 (1968)

[62] R. D. Dupuis and P. D. Dapkus, Appl. Phys. Lett. **31**, 466 (1977)

[63] S. Baskoutas, A. F. Terzis, J. Appl. Phys. **99**, 013708 (2006)

[64] J. R. Petta, A. C. Johnson, J. M. Taylor, E. A. Laird, A. Yacoby, M. D. Lukin, C. M. Marcus, M. P. Hanson, A. C. Gossard, Science **309**, 2180-2184 (2005)

[65] X. Dai, Y. Deng, X. Peng, Y. Jin, Adv. Mater. **29**, 1607022 (2017)

[66] H. Mattoussi, M. J. Mauro, E. R. Goldman, G. P. Anderson, V. C. Sundar, V. F. Mikulec, M. G. Bawendi, J. Am. Chem. Soc. **122**, 12142-12150 (2000)

[67] T. Jamieson, R.Bakhshi, D.Petrova, R.Pocock, M.Imani, A. M.Seifalian, Biomaterials **28**, 4717-4732 (2007)

[68] J. Park, C. Dvoracek, K. H.Lee, J. F.Galloway, H. C.; Bhang, M. G.Pomper, P. C. Searson, Small **7**, 3148-3152 (2011)

[69] Q. Ma, X. Su, Analyst **135**, 1867-1877 (2010)

[70] P. Jiang, C.-N. Zhu, Z.-L. Zhang, Z.-Q. Tian, D.-W. Pang, Biomaterials **33**, 5130-5135 (2012)

[71] D.C. Lee, F.V. Mikulec, J.M. Pelaez, B. Koo, B.A. Korgel, J. Phys. Chem. B **110**, 11160 (2006)

[72] D. Yang, J. Hu, S. Fu, J. Phys. Chem. C **113**, 7646 (2009)

[73] H. Chen, C. Deng, X. Zhang, Angew. Chem. Int. Ed. **49**, 607 (2010)

[74] C. Cannas, A. Musinu, A. Ardu, F. Orrù, D. Peddis, M. Casu, et al., Chem. Mater. **22**, 3353 (2010)

[75] V. Salgueirino-Maceira, F. Caruso, L.M. Liz-Marzàn, J. Phys. Chem. B **107**, 10990 (2003)

[76] J. Tang, X. Wang, L. Brzozowski, D. A. R. Barkhouse, R. Debnath, L. Levina, E. H. Sargent, Adv. Mater. **22**, 1398 (2010)

[77] J.C. Park, J.U. Bang, J. Lee, C.H. Ko, H. Song, J. Mater. Chem. **20**, 1239 (2010)

[78] V. Salgueirino-Maceira, M.A. Correa-Duarte, M. Spasova, L.M. Liz-Marzàn, M. Farle, Adv. Funct. Mater. **16**, 509 (2006)

[79] Y. Song, X. Cao, Y. Guo, P. Chen, Q. Zhao, G. Shen, Chem. Mater. **21**, 68 (2009)

[80] F. Zhang, G.B. Braun, Y. Shi, Y. Zhang, X. Sun, N.O. Reich, et al., J. Am. Chem. Soc. **132**, 2850 (2010)

[81] T. Ung, L.M. Liz-Marzàn, P. Mulvaney, J. Phys. Chem. B **103**, 6770 (1999)

[82] J.I. Park, J. Cheon, J. Am. Chem. Soc. **123**, 5743 (2001)

[83] W.R. Lee, M.G. Kim, J.R. Choi, J.I. Park, S.J. Ko, S.J. Oh, et al., J. Am. Chem. Soc. **127**, 16090 (2005)

[84] S.-J. Cho, J.-C. Idrobo, J. Olamit, K. Liu, N.D. Browning, S.M. Kauzlarich, Chem. Mater. **17**, 3181 (2005)

[85] J. E. Ayers, Heteroepitaxy of Semiconductors: Theory, Growth, and Characterization, CRC Press, Boca Raton, FL, 2007.

[86] A. Koma, K. Sunouchi and T. Miyajima, Microelectron. Eng., **2**, 129-136 (1984)

[87] A. Koma, K. Sunouchi and T. Miyajima, J. Vac. Sci. Technol., B, **3**, 724 (1985)

[88] F. C. Frank and J. H. van der Merwe, Proc. R. Soc. London, Ser. A, **198**, 216 (1949)

[89] Van der Waals epitaxy, http://van-der-waals-epitaxy.info/wp-content/uploads/vDWE.jpg.

[90] A. Koma and K. Yoshimura, Surf. Sci., 174, 556-560 (1986)

[91] Handbook of layered materials, ed. S. M. Auerbach, K. A. Carrado and P. K. Dutta, Marcel Dekker, Inc., New York, 2004.

[92] A. Koma, K. Saiki and Y. Sato, Appl. Surf. Sci., **41-42**, 451-456 (1989)

[93] C. Hammond, A. Back, M. Lawrence, K. Nebesny, P. Lee, R. Schlaf and N. R. Armstrong, J. Vac. Sci. Technol., A, **13**, 1768-1775 (1995)

[94] B. S. Mitchell, An Introduction to Materials Engineering and Science: For Chemical and Materials Engineers, Wiley, New York, 2008.

[95] Q. H. Wang, K. Kalantar-Zadeh, A. Kis, , J. N. Coleman and M. S. Strano, Nat. Nanotechnol. **7**, 699-712 (2012).

[96] A. K. Geim, I. V. Grigorieva, Nature. **499**, 419-425 (2013).

[97] M. Chhowalla, H. S. Shin, G. Eda, L.-J. Li, K. P. Loh, H. Zhang, Nat. Chem.**5**, 263-275 (2013)

[98] G. Fiori et al. Nat. Nanotechnol. **9**, 768-779 (2013)

[99] D. Jariwala, V. K. Sangwan, L. J. Lauhon, T. J. Marks, M. C. Hersam, ACS Nano **8**, 1102-1120 (2014)

[100] H. Zhang, ACS Nano **9**, 9451-9469 (2015)

[101] K.S. Novoselov, Science. **306**, 666-669 (2004)

[102] A.K. Geim, K.S. Novoselov, Nat. Mater. **6**, 183-191 (2007)

[103] A.D. Bartolomeo, F. Giubileo, S. Santandrea, F. Romeo, R. Citro, T. Schroeder, G. Lupina, Nanotechnology. **22**, 275702 (2011)

[104] K.S. Novoselov, D. Jiang, F. Schedin, T.J. Booth, V.V Khotkevich, S.V . Morozov, A.K. Geim, Proc. Natl. Acad. Sci. USA. **102**, 10451-10453 (2005)

[105] X.-L. Li, W.-P. Han, J.-B. Wu, X.-F. Qiao, J. Zhang, P.-H. Tan, Adv. Funct. Mater. **27**, 1604468 (2017)

[106] A. Di Bartolomeo, A. Pelella, X. Liu, F. Miao, M. Passacantando, F. Giubileo, A. Grillo, L. Iemmo, F. Urban, S. Liang, Adv. Funct. Mater. **29**, 1902483 (2019)

[107] A.K. Geim, I.V. Grigorieva, Nature. **499**, 419-425 (2013)

[108] E.P. Randviir, D.A.C. Brownson, C.E. Banks, Mater. Today. **17**, 426-432 (2014)

[109] F. Giubileo, A. Di Bartolomeo, Prog. Surf. Sci. **92**, 143-175 (2017)

[110] S. Shanmugaratnam, S. Rasalingam, In Nanocatalysts, I. Sinha, M. Shukla, Eds.; IntechOpen: London, UK, 2019; ISBN 978-1-78984-159-6.

[111] X. Zhou, E.E. Rodriguez, Chem. Mater. **29**, 5737-5752 (2017)

[112] R. Lv, J. A. Robinson, R. E. Schaak, D. Sun, Y. Sun, T. E. Mallouk, M.Terrones, Acc. Chem. Res. **48**, 56-64 (2015)

[113] F. Urban, F. Giubileo, A. Grillo, L. Iemmo, G. Luongo, M. Passacantando, T. Foller, L. Madaub, E. Pollmann, M.P. Geller et al. 2D Materials. **6**, 045049 (2019)

[114] T. Heine, Acc. Chem. Res. Textbf48, 65-72 (2015)

[115] G.R. Bhimanapati, N.R. Glavin, J.A. Robinson, Semiconductors and Semimetals. **95**, 101-147 (2016)

[116] Y. Xu, Z. Shi, X. Shi, K. Zhang, H. Zhang, Nanoscale. **11**, 14491-14527 (2019)

[117] Q. H. Wang, K. Kalantar-Zadeh, A. Kis, J. N. Coleman, M. S. Strano, Nat. Nanotechnol. **7**, 699-712 (2012).

[118] X. Duan, C. Wang, A. Pan, R. Yu, X. Duan, Chem. Soc. Rev. **44**, 8859-8876 (2015)

[119] K. S. Novoselov, A. K. Geim, S. V. Morozov, D. Jiang, Y. Zhang, S. V. Dubonos, I. V. Grigorieva, and A. A. Firsov, Science **306**, 666 (2004).

[120] K. S. Novoselov, D. Jiang, F. Schedin, T. J. Booth, V. V. Khotkevich, S. V. Morozov, and A. K. Geim, P. Natl. Acad. Sci. USA **102**, 10451 (2005).

[121] W. S. Yun, S. W. Han, S. C. Hong, I. G. Kim, and J. D. Lee, Phys. Rev. B **85**, 033305 (2012)

[122] A. Splendiani, L. Sun, Y. Zhang, T. Li, J. Kim, C. Chim, G. Galli, and F. Wang, Nano Lett. **10**, 1271 (2010)

[123] K. F. Mak, C. Lee, J. Hone, J. Shan, T. F. Heinz, Phys. Rev. Lett. **105**, 136805 (2010)

[124] Y. Zhang, T. Chang, B. Zhou, Y. Cui, H. Yan, Z. Liu, F. Schmitt, J. Lee, R. Moore, Y. Chen, H. Lin, H. Jeng, S. Mo, Z. Hussain, A. Bansil and Z. Shen, Nature Nanotechnol. 9, 111-115 (2014).

[125] J. K. Ellis, M. J. Lucero, G. E. Scuseria, Appl. Phys. Lett. 99, 261908 (2011).

[126] A. Kumar, P. K.Ahluwalia, Eur. Phys. J. B 85, 186 (2012).

[127] H. Liu, A. T. Neal, Z. Zhu, Z. Luo, X. Xu, D. Tománek, P. D. Ye, ACS Nano **8**, 4033-4041 (2014)

[128] B. Radisavljevic, A. Radenovic, J. Brivio, V. Giacometti, A. Kis, Nat. Nanotechnology **6**, 147 (2011)

[129] T. Korn, S. Heydrich, M. Hirmer, J. Schmutzler, C. Schuller, Appl. Phys. Lett. **99**, 102109 (2011)

[130] Y. Yoon, K. Ganapathi, S. Salahuddin, Nano Lett. **11**, 3768 (2011)

[131] B. Radisavljevic , A. Radenovic, J. Brivio, V. Giacometti, A. Kis, Nature Nanotech **6**, 147-150 (2011)

[132] K. F. Mak, C. Lee, J. Hone , J. Shan, T. F. Heinz, Phys. Rev. Lett. **105**, 136805 (2010)

[133] W. M. R. Divigalpitiya, R. F. Frindt, S. R. Morrison, Science. **246**, 369-371 (1989)

[134] B. K. Miremadi, S. R. Morrison, J. Catalysis. **103**, 334-345 (1987)

[135] R. F. Frindt, A. S. Arrott, A. E. Curzon, B. Heinrich, S. R. Morrison, J. Appl. Phys. **70**, 6224 (1991)

[136] Z. Y. Zhu, Y. C. Cheng, and U. Schwingenschlögl, Phys. Rev. B **84**, 153402 (2011).

[137] D. Xiao, G. B. Liu, W. Feng, X. Xu, and W. Yao, Phys. Rev. Lett. **108**, 196802 (2012).

[138] Z. Y. Zhu, Y. C. Cheng, U. Scwingenshlögl, Phys. Rev. B **84**, 153402 (2011).

[139] T. Cheiwchanchamnangij, W. R. L. Lambrecht, Phys. Rev. B **85**, 205302 (2012).

[140] A. Rycerz, J. Tworzydlo, and C. W. J. Beenakker, Nature Phys. **3**, 172 (2007)

[141] K. F. Mak, K. He, J. Shan, and T. F. Heinz, Nature Nano **7**, 494 (2012)

[142] P. Rivera, J. R. Schaibley, A. M. Jones, J. S. Ross, S. Wu, G. Aivazian, P. Klement, N. J. Ghimire, J. Yan, D. G. Mandrus, W. Yao, X. Xu, Nature Comm. **6**, 6242 (2015)

[143] X. Q. Zhang, C. H. Lin, Y. W. Tseng, K. H. Huang, and Y. H. Lee, Nano Lett. **15**, 410-415 (2015)

[144] X. Duan, C. Wang, J. C. Shaw, R. Cheng, Y. Chen, H. Li, X. Wu, Y. Tang, Q. Zhang, A. Pan, J. Jiang, R. Yu, Y. Huang and X. Duan, Nature Nanotechnol. **9**, 1024-1030 (2014).

[145] C. Huang, S. Wu, A. M. Sanchez, J. J. P. Peters, R. Beanland, J. S. Ross, P. Rivera, W. Yao, D. H. Cobden and X. Xu, Nature Mater. **13**, 1096-1011 (2014).

[146] Y. Gong, J. Lin, X. Wang, G. Shi, S. Lei, Z. Lin, X. Zou, G. Ye, R. Vajtai, B. I. Yakobson, H. Terrones, M. Terrones, B. K. Tay, J. Lou, S. T. Pantelides, Z. Liu, W. Zhou and P. M. Ajayan, Nature Mater. **13**, 1135-1142 (2014).

[147] G. S. Duesberg, Nature Mater. **13**, 1075-1076 (2014).

[148] L. A. Ponomarenko, R. V. Gorbachev, G. L. Yu, D. C. Elias, R. Jalil, A. A. Patel, A. Mishchenko, A. S. Mayorov, C. R. Woods, J. R. Wallbank, M. Mucha-Kruczynski, B. A. Piot, M. Potemski, I. V. Grigorieva, K. S. Novoselov, F. Guinea, V. I. Falko and A. K. Geim, Nature **497**, 594-597 (2013).

[149] C. R. Dean, L. Wang, P. Maher, C. Forsythe, F. Ghahari, Y. Gao, J. Katoch, M. Ishigami, P. Moon, M. Koshino, T. Taniguchi, K. Watanabe, K. L. Shepard, J. Hone and P. Kim, Nature **497**, 598-602 (2013).

[150] W. Wei, Y. Dai, C. Niu and B. Huang, Sci. Rep. **5**, 17578 (2015)

[151] M. Chhowalla, H. S. Shin, G. Eda, L. J. Li, K. P. Loh, H. Zhang, Nat Chem. **5**, 263-275 (2013)

[152] A. V. Kolobov and J. Tominaga, Two-Dimensional Transition-Metal Dichalcogenides, (Springer Nature, Switzerland 2016)

[153] H. Yang, S. W. Kim, M. Chhowalla and Y. H. Lee, Nature Physics. **13**, 931-937, (2017)

[154] X. Qian, J. Liu, L. Fu, J. Li, Science. **346**, 1344-1347, (2014)

[155] R. E. Peierls, Clarendon Press. (1996)

[156] J. A. Wilson, F. J. Di Salvo, and S. Mahajan, Phys. Rev. Lett. **32**, 882 (1974).

[157] J. A. Wilson, F. J. Di Salvo, and S. Mahajan, Adv. Phys. **24**, 117 (1975).

[158] M. H. Whangbo and E. Canadell, J. Am. Chem. Soc. **114**, 9587 (1992).

[159] A. H. Castro Neto, Phys. Rev. Lett. **86**, 4382 (2001).

[160] K. Rossnagel, J. Phys.: Condens. Matter **23**, 213001 (2011).

[161] S. Manzeli, D. Ovchinnikov, D. Pasquier, O. V. Yazyev, and A. Kis, Nat. Rev. Mater. **2**, 17033 (2017).

[162] Q. H. Wang, K. Kalantar-Zadeh, A. Kis, J. N. Coleman, and M. S. Strano, Nat. Nanotechnol. 7, 699 (2012).

[163] M. Chhowalla, H. S. Shin, G. Eda, L.-J. Li, K. P. Loh, and H. Zhang, Nat. Chem. **5**, 263 (2013).

[164] L. F. Mattheiss, Phys. Rev. B **8**, 3719 (1973).

[165] R. E. Peierls, Quantum Theory of Solids (Oxford University Press, New York, 1955).

[166] S.-K. Chan and V. Heine, J. Phys. F: Met. Phys. 3, 795 (1973).

[167] M. D. Johannes and I. I. Mazin, Phys. Rev. B 77, 165135 (2008).

[168] X. Zhu, Y. Cao, J. Zhang, E. W. Plummer, and J. Guo, Proc. Natl. Acad. Sci. USA 112, 2367 (2015).

[169] S. Yi, Z. Zhang, and J.-H. Cho, Phys. Rev. B 97, 041413(R) (2018).

[170] J.-H. Choi and S.-H. Jhi, J. Phys.: Condens. Matter **30**, 105403 (2018).

[171] K.-A. N. Duerloo, Y. Li, and E. J. Reed, Nat. Commun. **5**, 4214 (2014).

[172] D. H. Keum, S. Cho, J. H. Kim, D.-H. Choe, H.-J. Sung, M. Kan, H. Kang, J.-Y. Hwang, S. W. Kim, H. Yang, K. J. Chang, and Y. H. Lee, Nat. Phys. **11**, 482 (2015).

[173] S. N. Shirodkar and U. V. Waghmare, Phys. Rev. Lett. **112**, 157601 (2014).

[174] J. C. Wildervanck and F. Jellinek, J. Less-Common Met. **24**, 73 (1971).

[175] M. Kertesz and R. Hoffmann, J. Am. Chem. Soc. **106**, 3453 (1984).

[176] S. Tongay, H. Sahin, C. Ko, A. Luce, W. Fan, K. Liu, J. Zhou, Y.-S. Huang, C.-H. Ho, J. Yan et al., Nat. Commun. **5**, 3252 (2014).

[177] R. E. Peierls, Quantum Theory of Solids (Oxford University Press, New York, 1955).

[178] G. Casillas, A. Mayoral, M. Liu, A. Ponce, V. I. Artyukhov, B. I. Yakobson, and M. Jose-Yacaman, Carbon **66**, 436 (2014).

[179] A. La Torre, A. Botello-Mendez, W. Baaziz, J. Charlier, and F. Banhart, Nat. Commun. **6**, 6636 (2015).

[180] H. Jones, Proc. Royal Soc. A **147**, 396 (1934).

[181] A. B. Shick, J. B. Ketterson, D. L. Novikov, and A. J. Freeman, Phys. Rev. B **60**, 15484 (1999).

[182] S. Shang, Y. Wang, H. Zhang, and Z.-K. Liu, Phys. Rev. B **76**, 052301 (2007).

[183] J. P. Gaspard, C. R. Physique **17**, 389 (2016).

[184] M. D. Johannes and I. I. Mazine, Phys. Rev. B **77**, 165135 (2008).

[185] D. Kartoon, U. Argaman, and G. Makov, Phy. Rev. B **98**, 165429 (2018)

[186] S. E. Thompson, M. Armstrong, C. Auth et al. IEEE Trans Electron Dev. **51**, :1790-1797 (2004)

[187] C. R. Zhu, G. Wang, B. L. Liu et al. Phys Rev B. **88**, 121301 (2013)

[188] A. Castellanos-Gomez, R. Roldan, E. Cappelluti et al. Nano Lett. **13**, 5361-5366 (2013)

[189] Y. D. Ma, Y. Dai, M. Guo, C. W. Niu, Y. T. Zhu, B. B. Huang, ACS Nano. **6**, 1695-1701 (2012)

[190] J. Hu, J. Gou, M. Yang et al. Adv Mater. **32**, 2002201 (2020)

[191] S. X. Yang, C. Wang, H. Sahin et al. Nano Lett. **15**, 1660-1666 (2015)

[192] A. M. Creary, R. Ghosh, M. Amani et al. ACS Nano. **10**,3186-3197 (2016)

[193] H. J. Conley, B. Wang, J. I. Ziegler, R. F. Haglund, S. T. Pantelides, K. I. Bolotin, Nano Lett. **13**, 3626-3630 (2013)

[194] S. B. Desai, G. Seol, J. S. Kang et al. Nano Lett. **14**, 4592-4597 (2014)

[195] K. L. He, C. Poole, K. F. Mak, J. Shan, Nano Lett. **13**, 2931-2936 (2013)

[196] Y. L. Wang, C. X. Cong, W. H. Yang et al. Nano Res. **8**, 2562-2572 (2015)

[197] S. Y. Huang, G. W. Zhang, F. R. Fan et al. Nat Commun. **10**, 2447 (2019)

[198] T. M. G. Mohiuddin, A. Lombardo, R. R. Nair et al. Phys Rev B. **79**, 205433 (2009)

[199] H. J. Conley, B. Wang, J. I. Ziegler, R. F. Haglund, S. T. Pantelides, K. I. Bolotin, Nano Lett. 2013;**13**, 3626-3630 (2013)

[200] S. K. Deng, S. W. Che, R. Debbarma, V. Berry, Nanoscale. 2019;**11**, 504-511 (2019)

[201] Y. Y. Li, Z. X. Hu, S. H. Lin, S. K. Lai, W. Ji W, S. P. Lau, Adv Funct Mater. **27**, 1600986 (2017)

[202] P. Manchanda, V. Sharma, H. B. Yu, D. J. Sellmyer, R. Skomsk, Appl Phys Lett. 6bf107, 032402 (2015)

[203] Y. G. Zhou, Z. G. Wang, P. Yang et al. ACS Nano. **6**, 9727-9736 (2012)

[204] Y. C. Huang, C. Y. Ling, H. Liu, S. F. Wang, B. Y. Geng, J Phys Chem C. **118**, 9251-9260 (2014)

[205] S. J. Zhao, W. Kang, J. M. Xue, Appl Phys Lett. **104**, 133106 (2014)

[206] K. A. N. Duerlool KAN, Y. Li Y, E. J. Reed EJ, Nat Commun. **5**, 4214 (2014)

[207] S. Song, D. H. Keum, S. Cho, D. Perello, Y. Kim, Y. H. Lee, Nano Lett. **16**, 188-193 (2016)

[208] M. Pizzochero, O. V. Yazyev, J Phys Chem C. **124**, 7585-7590 (2020)

[209] Y. W. Zhao, Y. Li, M. X. Liu, K. W. Wu, F. Ma, J Phys Chem C. **124**, 4299-4307 (2020)

[210] C. X. Zhao, M. L. Hu, J. Qin et al. Phys Rev L. **125**, 046801 (2020)

[211] J. Liang, J. H. Wang, Z. H. Zhang et al. Nanoscale. **10**,11441-11451 (2018)

[212] H. L. Shi, H. Pan, Y.-W. Zhang, B. I. Yakobson et al. Phys Rev B. **87**, 155304 (2013)

[213] Y. Wu, K. Xu, C. C. Ma et al. Nano Energy. **63**, 103870 (2019)

[214] F. Li, T. Shen, C. Wang, Y. P. Zhang, J. J. Qi, H. Zhang, Nano-Micro Lett. **12**,1-44 (2020)

[215] W. Z. Wu, L. Wang, Y. L. Li et al. Nature. **514**, 470-474 (2014)

[216] M. Zhao, M. X. Zhang, L. Li, Sci. Rep. **5**, 16108 (2015)

[217] L. Li, E. V. Castro, and P. D. Sacramento, Phys. Rev. B. **94**, 195419 (2016)

[218] W. Zhang, Q. S. Wu, O. V. Yazyev, H. Weng, Z. Guo, W.-D. Cheng, and G.-L. Cha, Phys. Rev. B **98**, 115411 (2018)

[219] C. Zhao, M. Hu, J. Qin, B. Xia, C. Liu , S. Wang, D. Guan, Y. Li , H. Zheng, J. Liu , and J. Jia, Phys. Rev. Lett. **125**, 046801 (2020)

[220] Y. Ma, Y. Dai, L. Yu, C. Niu, B. Huang, New Journal of Physics **15**, 073008 (2013)

[221] S. Liu, Y. Kim, L. Z. Tan, A. M. Rappe, Nano Lett. **16**, 1663-1668 (2016)

Chapter 2

Theoretical Concepts

2.1 Introduction

In quantum mechanics, all the material properties are derivable from a knowledge of the wavefuncion which is a function of many variables. By solving the Schrödinger equation we can find the wavefunction which completely describes the state of a system and from it we can work out all the measurable quantities. Materials are collections of mutually interacting nuclei and electrons which interact among themselves through electrostatic Coulomb interaction. Nuclei, being almost ∼1800 times heavier than electrons can be treated as classical particles fixed at lattice sites, whereas the electrons are treated quantum mechanically.

Presence of more than one mutually interacting electrons which repel each other electrostatically, makes it a many-body problem and the solution of it requires a many-body Schrödinger equation to be solved which is a difficult task. Various computational methods have come into existence in an attempt to get an approximate solution to this many-body problem. But all these methods fall quite insufficient while dealing with large systems. They can handle at most up to 1000 electrons and they are computationally costly.

So, exact many body wavefunction remains impossible to determine for most systems. As an approximation, the many-particle Schrödinger equation is reduced to some effective single particle equations which are easier to solve. In 1960's, Hohenberg, Kohn and Sham formulated Density Functional Theory which reduces this many-particle problem into an effective single particle problem. In DFT, the total energy of a system is expressed as a functional of its electron density E [n($\mathbf{r}$)]. From a knowledge of the ground state electron density one can uniquely determine the ground state energy of the system as well as the

ground state electronic structure. It greatly facilitates the problem as it effectively reduces to working with a quantity which is a function of only three variables, rather than finding out the complex wavefunction of 3N variables, where N is the number of electrons.

We use Vienna ab initio Simulation Package (VASP) [2, 3] which implements DFT to calculate the electronic structure and structural properties of the systems. DFT has become a standard tool for studying material properties and understanding them at the atomic level. It also turns out to be very useful in predicting material properties which are challenging to probe experimentally as in extreme conditions, as shown in the work of Umemoto, Wentzcovitch, and Allen [4].

In this chapter, we give a brief introduction to the density functional theory and its implementation as a density functional based approach. We also represent some technical details used in DFT based computations. For a periodic solid, the electronic states are described in terms of Bloch states [5] which are delocalized/extended electronic states, each assigned a quantum number k for the crystal momentum, together with a band index n. An expansion of these states in terms of plane waves as basis states are preferred. Apart from this, alternative representations are in use too.

In Wannier representation, a real-space picture in terms of localized orbitals is provided [6–8]. Each wannier function is assigned the lattice vector **R** of the unitcell where the orbital is localized, together with a band-like index **n**. These two quantities serve as quantum numbers in this scheme. Wannier functions can be a potent tool in the study of the electronic and dielectric properties of materials. It has got an extra advantage of lending insight into the nature of chemical bonding, which is absent in the band picture of extended orbitals [9]. The VASP to WANNIER90 [10–12] interface allows us to map the Bloch states onto Wannier functions, localized on the respective atoms via a unitary transformation. This provides us a tight binding representation of the Hamiltonian in the basis of the maximally localized Wannier functions. It allows us to calculate bonding energies of specific inter-atomic bonds. So, we also give a brief introduction to Wannier functions and its properties.

2.2 Formulation of Density Functional Theory

2.2.1 Many body Hamiltonian

The electrostatic interaction between the nuclei and the electrons determine the electronic property of a solid. The properties of such a collective system of interacting charge carriers

are governed by the time independent Schrödinger equation which has a simple form of an eigenvalue equation $H\psi$=Eψ. Here H is the many-body Hamiltonian and ψ is a set of eigenstates of H.

H can be expressed as summation of the kinetic energies of the charge carriers and their mutual electrostatic interaction potential energies.

$$H = -\frac{\hbar^2}{2m_e}\sum_i \nabla_i^2 - \frac{\hbar^2}{2M_I}\sum_I \nabla_I^2 + \frac{1}{2}\sum_{i\neq j}\frac{e^2}{|\mathbf{r}_i - \mathbf{r}_j|} + \frac{1}{2}\sum_{I\neq J}\frac{Z_I Z_J e^2}{|\mathbf{R}_I - \mathbf{R}_J|} - \sum_{i,I}\frac{Z_I e^2}{|\mathbf{R}_I - \mathbf{r}_i|} \quad (2.1)$$

In the above equation, the variables i and j refer to the electrons whereas the indices I and J correspond to the nuclei. $\mathbf{r_i}$ and $\mathbf{R_I}$ are the positions of the electrons and the nuclei respectively. Similarly m_e and M_I represent the masses of the electrons and nuclei respectively. $Z_I e$ is the charge of the nucleus and $\hbar$ is the Plank's constant.

The first term in 2.1 is the kinetic energies of all the electrons collectivel, the second term is that of the nuclei. The Laplacians involve second derivative with respect to the electronic and ionic coordinates. The third term is the electron-electron repulsion. The fourth term is the repulsion among the nuclei. The fifth term represents the attractive Coulomb interaction between the electrons and the nuclei.

Equation 2.1 can also be written as

$$H = T_e(\mathbf{r}) + T_N(\mathbf{R}) + V_{ee}(\mathbf{r}) + V_{NN}(\mathbf{R}) + V_{eN}(\mathbf{r}, \mathbf{R}) \quad (2.2)$$

In 2.2, $\mathbf{R}$ represents a set of nuclear coordinates, and $\mathbf{r}$ represents electronic coor dinates. $T_e(\mathbf{r})$ represents the kinetic energy of the electrons and and $V_{ee}(\mathbf{r})$ the electron-electron Coulomb repulsion. $T_N(\mathbf{R})$ and $V_{NN}(\mathbf{R})$ represent the kinetic energy of the nuclei and repulsive interaction between them respectively. The last term $V_{eN}(\mathbf{r, R})$ represents the interaction between electrons and nuclei and couples the electronic and nuclear degrees of freedom.

By solving this many-body Hamiltonian using Schrödinger equation we can get the wave-function that contains all the relevant information regarding the system. But presence of a large number of coordinates and their mutual coupling make it a difficult task. So we resort to various approximations to make it easy. One such approximations is Born-Oppenheimer Approximation which will be discussed in the next subsection.

2.2.2 Born-Oppenheimer Approximation

The last term in 2.2 couples the nuclear coordinates with the electronic coordinates and makes the problem difficult. In the absence of the term, the total wavefunction could have been written as a product of electronic and nuclear parts $\psi(\mathbf{r};\mathbf{R}) = \psi(\mathbf{r})\eta(\mathbf{R})$. Since the nuclei are ∼1800 times heavier than the electrons, we can assume that the nuclei are relatively fixed in position as compared to the electrons. So the $\mathbf{R}$ dependence becomes parametric. The electrons move much rapidly in response to a small change in nuclear configuration and hence for a given nuclear configuration, the electrons are always at their ground state. This allows us to separate the nuclear and electronic degrees of freedom. This is an Adiabatic Approximation called Born-Oppenheimer Approximation, named after Max Born, and J. Robert Oppenheimer [12].

As the nuclei are considered fixed, their kinetic energy can be ignored and the nuclear-nuclear interaction term can be considered a constant and is called Madelung energy [13]. Thus the Hamiltonian after applying Born-Oppenheimer Approximation becomes

$$H_{BOA}^{ele} = T_e(\mathbf{r}) + V_{ee}(\mathbf{r}) + V_{eN}(\mathbf{r},\mathbf{R}) \tag{2.3}$$

For any system, the first step would be to get the solution for the hamiltonian, which would give the ground state energy of the electrons . This ground state energy of electrons can be expressed as a function of nuclear positions $\mathbf{R}$, $E_0^{ele}(\{\mathbf{R}\})$. This is called adiabatic potential energy surface of the electrons. Once we know the adiabatic surface, we can trace the evolution of the ground state energy with change in nuclear configuration.

The adiabatic approximation facilitates the solution of the problem by simplifying the form of the hamiltonian to a great extent. But even after BOA, the simplest form of electronic hamiltonian 2.3 is difficult to solve. This is because of the presence of the term $V_{ee}(\mathbf{r})$ which represents the electron-electron repulsion. It prevents us from separately writing out the wavefunction for each electron without requiring to have a knowledge of the other electrons. If this term was absent, the system under study would turn into a non-interacting many-electron problem. Then the many-body schrödinger equation would reduce to a set of single-particle equations of the form

$$h_i\phi(\mathbf{r_i}) = \epsilon\phi(\mathbf{r_i}) \; with \; i = 1, 2, 3.....N \tag{2.4}$$

where N is the total number of electrons and h_i is the summation of the kinetic as well as the potential energies of the i^{th} electron. Each of these single-particle equations yields the same set of eigenfunctions ϕ_n with eigenenergies ϵ_n. Thus the ground state wavefunction

of the many-electron system is given by some simple or complex product of the lowest energy eigenstates $\phi_1(\mathbf{r_1})$, $\phi_2(\mathbf{r_2})$, $\phi_3(\mathbf{r_3})$, ...$\phi_N(\mathbf{r_N})$ associated with the 1^{st} , 2^{nd} , ... ,N^{th} electron respectively. In band theory of periodic solids, the same approach has been adopted and these single-particle states are called Bloch states [5]. But due to the presence of the electron-electron repulsion term, the wavefuction for an individual electron can't be found without knowing the wavefuctions for all the other electrons. This makes it a many-body problem and we have to make additional approximations to reduce it to single-particle problem. Various methods have been formulated to this end. Hartee-Fock and DFT are the two successful theories satisfying the need. A short discussion has been given in the following chapters on Density Functional Theory (DFT) which underlies the analysis used in the work presented in this thesis.

2.2.3 Density Functional Theory (DFT)

Hohenberg and Kohn, in 1964, developed Desity Functional Theory (DFT) [15] to solve the many-body problem and explore its ground state properties, whose aim was to reduce the number of variables involved. We used DFT as implemented in Vienna Ab-initio Simulation Package (VASP) [16–19], to study the electronic structure of materials. What was fundamental in DFT was based onn the proposition that all the properties we ca ask about a system in its ground state are derivable from a knowldge of its ground state electro density which is a function of only three variables. The physical interpretation of this electron density is the probabilty of finding an electronn in a specific location around an atom or molecule. Density for an N-electron system is derived from normalized N-electron wavefunction.

Mathematically, density for an N-electron system can be given as

$$n(\mathbf{r}_i) = N \int \Psi^*(\mathbf{r}_1, \cdots, \mathbf{r}_i, \cdots, \mathbf{r}_N)\Psi(\mathbf{r}_1, \cdots, \mathbf{r}_i, \cdots, \mathbf{r}_N) d\mathbf{r}_1 d\mathbf{r}_2 d\mathbf{r}_3 .. d\mathbf{r}_{(i+1)} .. d\mathbf{r}_N \qquad (2.5)$$

Integrating the electron density over all space gives the number of electrons. This electron density is a measurable quanity and can be measured by X-ray diffraction experiment [20]. The greatest advantage of using the electron-density instead of the N-electron wave function is that it allows us to work with ony three varaibles instread of 3N number of coordinate where N is the number of electrons. If we are able to express the total energy of the electronic system as a functional of the electron-density $n(\mathbf{r})$, i.e. $E[n(\mathbf{r})]$, then applying variational principle we can get the ground state electron density $n_0(\mathbf{r})$ that

gives the ground state energy $E_0[n(\mathbf{r})]$, and from it all the relevant information regarding the ground state of the electronic system including the ground state wavefunction Ψ_0.

Similar to the single-particle density in 2.5, a two-particle can be defined as follows

$$n(\mathbf{r}_i, \mathbf{r}_j) = N \int \Psi^*(\mathbf{r}_1, \cdot\cdot, \mathbf{r}_i, \cdot\cdot, \mathbf{r}_j \cdot\cdot, \mathbf{r}_N)\Psi(\mathbf{r}_1, \cdot\cdot, \mathbf{r}_i, \cdot\cdot, \mathbf{r}_j \cdot\cdot, \mathbf{r}_N) \\ d\mathbf{r}_1 d\mathbf{r}_2 \cdot\cdot d\mathbf{r}_{(i-1)} d\mathbf{r}_{(i+1)} \cdot\cdot d\mathbf{r}_{(j-1)} d\mathbf{r}_{(j+1)} \cdot\cdot d\mathbf{r}_N \tag{2.6}$$

which is the probability of finding an electron at $\mathbf{r}_i$ in the presence of another electron at $\mathbf{r}_j$.

For a system of two completely uncorrelated electrons, this two-particle density can be written as a product of the single-particle densities for the individual electrons as

$$n(\mathbf{r}_i, \mathbf{r}_j) = n(\mathbf{r}_i)n(\mathbf{r}_j) \tag{2.7}$$

But for real systems, there are interactions between two electrons, an in that case the two-electron density is written as

$$n(\mathbf{r}_i, \mathbf{r}_j) = n(\mathbf{r}_i)n(\mathbf{r}_j)\Delta n(\mathbf{r}_i, \mathbf{r}_j) \tag{2.8}$$

where $\Delta n(\mathbf{r}_i, \mathbf{r}_j)$ is the correlation term.

It was the hypothesis, that a knowledge of the ground-state density, $n(\mathbf{r})$, for any electronic system uniquely determines the system, that became the starting point of modern density functional theory(DFT) as formulated by Kohn, Hohenberg, and Sham. The validity of density functional theory rests on two fundamental mathematical theorems proposed by Hohenberg and Kohn [21] and the derivation of a set of equations by Kohn and Sham [22] in 1960's.

2.2.4 The Hohenberg-Kohn Theorems

Theorem 1 : The external potential $V_{ext}(\mathbf{r})$ of a system of electrons is uniquely determined by the ground state electron density $n(\mathbf{r})$. Since $V_{ext}(\mathbf{r})$ in turn fixes H, the full many particle ground state is a unique functional of $n(\mathbf{r})$.

Proof: Let V_1 be an external potential yielding ground state density $n(\mathbf{r})$. The hamiltonian is H_1 whose ground state wavefunction is Ψ_1 and ground state energy E_1. Hence

$$H_1\Psi_1 = E_1\Psi_1. \tag{2.9}$$

Let there be another external potential V_2 that yields the same ground state electron density $n(\mathbf{r})$. The hamiltonian is H_2 whose ground state wavefunction is Ψ_2 and ground state energy E_2.

$$H_2\Psi_2 = E_2\Psi_2. \tag{2.10}$$

v_1 and V_2 differ atleast by a contant. $H_1 = T_e + V_{ee} + V_1$ and $H_2 = T_e + V_{ee} + V_2$, where T_e is the kinetic energy of the electrons and V_{ee} is the electron-electron repulsion term.

From 2.9,

$$E_1 = \langle\Psi_1|H_1|\Psi_1\rangle \tag{2.11}$$

$$= \langle\Psi_1|T_e + V_{ee}|\Psi_1\rangle + \langle\Psi_1|V_1|\Psi_1\rangle \tag{2.12}$$

$$= \langle\Psi_1|T_e + V_{ee}|\Psi_1\rangle + \int n(\mathbf{r})V_1(\mathbf{r})d^3r \tag{2.13}$$

From 2.10,

$$E_2 = \langle\Psi_2|H_2|\Psi_2\rangle \tag{2.14}$$

$$= \langle\Psi_2|T_e + V_{ee}|\Psi_2\rangle + \langle\Psi_2|V_2|\Psi_2\rangle \tag{2.15}$$

$$= \langle\Psi_2|T_e + V_{ee}|\Psi_2\rangle + \int n(\mathbf{r})V_2(\mathbf{r})d^3r \tag{2.16}$$

Now since Ψ_2 does not corresponds to the ground state wave-function of H_1, we can write the following inequality

$$E_1 \;<\; \langle\Psi_2|H_1|\Psi_2\rangle \tag{2.17}$$

$$E_1 \;<\; \langle\Psi_2|H_2|\Psi_2\rangle + \langle\Psi_1|[H_1 - H_2]|\Psi_1\rangle \tag{2.18}$$

$$E_1 \;<\; \langle\Psi_2|H_2|\Psi_2\rangle + \langle\Psi_1|[V_1 - V_2]|\Psi_1\rangle \tag{2.19}$$

In terms of density,

$$E_1 \;<\; E_2 + \int n(\mathbf{r})[V_1(\mathbf{r}) - V_2(\mathbf{r})]d^3r \tag{2.20}$$

Similarly we can obtain an expression for E_2

$$E_2 \;<\; E_1 + \int n(\mathbf{r})[V_2(\mathbf{r}) - V_1(\mathbf{r})]d^3r \tag{2.21}$$

Adding the above two equations we have

$$E_1 + E_2 < E_2 + E_1 + \int n(\mathbf{r})[V_1(\mathbf{r}) - V_2(\mathbf{r})]d^3r + \int n(\mathbf{r})[V_2(\mathbf{r}) - V_1(\mathbf{r})]d^3r \tag{2.22}$$

or

$$E_1 + E_2 < E_2 + E_1 + \int n(\mathbf{r})[V_1(\mathbf{r}) - V_2(\mathbf{r})]d^3r - \int n(\mathbf{r})[V_1(\mathbf{r}) - V_2(\mathbf{r})]d^3r \tag{2.23}$$

which finally gives

$$E_1 + E_2 \;<\; E_2 + E_1 \tag{2.24}$$

This is a contradiction and hence proves that there cannot be two different $V_{ext}(\mathbf{r})$ that yield the same ground state electron density, or, in other words, that the ground state density uniquely specifies the external potential $V_{ext}(\mathbf{r})$.

Theorem 2 : The statement of the second theorem is that the energy of a system can be written as a functional of the electron density, $E[n(\mathbf{r})]$. This functional delivers the lowest energy if and only if the input density is the true ground state electron density of the system $n_0(\mathbf{r})$.

$$E[n'(\mathbf{r})] \geq E[n_0(\mathbf{r})] \tag{2.25}$$

2.2.5 Kohn-Sham Formulation

For a system of N interacting electrons, the Hamiltonian can be written as $H = T_e + V_{ee} + V_{ext}$. The toal energy can be written as a functional of the electron-denstiy as

$$E[n(\mathbf{r})] = T[n(\mathbf{r})] + E_{ee}[n(\mathbf{r})] + \int n(\mathbf{r}) V_{ext}(\mathbf{r}) d^3r \tag{2.26}$$

$T[n(\mathbf{r})]$ is the kinetic energy and $V_{ee}(\mathbf{r})]$ is the electron-electronn repulsion term. THe first two terms together can be written as

$$F[n(\mathbf{r})] = T[n(\mathbf{r})] + E_{ee}[n(\mathbf{r})] \tag{2.27}$$

$F[n(\mathbf{r})]$ is called Hohenberg-Kohn functional.

The ground state energy can be obtained by minimizing the energy functional variationally subject to constraint that the total number of electrons N $[\int n(\mathbf{r}) d^3r = N]$ remains constant. This leads to

$$\frac{\delta}{\delta n(\mathbf{r})} \left[F[n(\mathbf{r})] + \int n(\mathbf{r}) V_{ext}(\mathbf{r}) d^3r - \mu_L \left(\int n(r) d^3r - N \right) \right] = 0 \tag{2.28}$$

with the Euler equation

$$\mu_L = \frac{\delta F[n(\mathbf{r})]}{\delta n(\mathbf{r})} + V_{ext}(\mathbf{r}) \tag{2.29}$$

where μ_L is a Lagrange multiplier.

The actual form of the energy functional in terms of density for a system of interacting electrons is unknown. In practice some approximation is used. A way round the problem is to replace the system of interacting electrons with a hypothetical non-interacting one with the same ground state electron-density as the interacting system.

Then the density of this system of non-interacting electrons can be written in terms of single-eletron wavefunctions as

$$n(\mathbf{r}) = 2 \sum_{i=1}^{N} \phi_i^*(\mathbf{r}) \phi_i(\mathbf{r}) \tag{2.30}$$

the factor 2 is here to take into account the spin-degeneracy.

Now the Hohenberg-Kohn funcational can be written as a sum of three tarms,

$$F[n(\mathbf{r})] = T_0[n(\mathbf{r})] + E_H[n(\mathbf{r})] + E_{XC}[n(\mathbf{r})] \tag{2.31}$$

$T_0[n(\mathbf{r})]$ is the kinetic energy of the non-interacting electron gas with density $n(\mathbf{r})$ and can be written in terms of the single electron wavefunctions as

$$T_0[n(\mathbf{r})] = \sum_{i=1}^{N} \langle \phi_i | -\frac{\hbar^2}{2m_e} \bigtriangledown^2 | \phi_i \rangle \tag{2.32}$$

$E_H[n(\mathbf{r})]$ is the classical electron-electron replusion energy called the Hartree energy.

$$E_H[n(\mathbf{r})] = \frac{e^2}{2} \int \int \frac{n(\mathbf{r})n(\mathbf{r}')}{|\mathbf{r}_i - \mathbf{r}_j|} d^3r d^3r' \tag{2.33}$$

E_{XC} is the exchange-correlation energy which contains the correction terms to compensate for the difference between the actual interacting system and the hypothetical non-interacting system of electrons. It is the summation of the difference in kinetic energies between the two systems and the non-classical contribution to the electron-electron interaction.

$$E_{XC}[n(\mathbf{r})] = T[n(\mathbf{r})] - T_0[n(\mathbf{r})] + E_{ee}[n(\mathbf{r})] - E_H[n(\mathbf{r})] \tag{2.34}$$

From 2.28,

$$\frac{\delta}{\delta n(\mathbf{r})} \Bigg[T_0[n(\mathbf{r})] + E_H[n(\mathbf{r})] + E_{XC}[n(\mathbf{r})] + \int n(\mathbf{r}) V_{ext}(\mathbf{r}) d^3r - \mu_L \left(\int n(\mathbf{r}) d^3r - N \right) \Bigg] = 0 \tag{2.35}$$

which ultimately leads to the Kohn-Sham equations

$$[-\frac{\hbar^2}{2m} \nabla^2 + V_{ext}(\mathbf{r}) + V_H(\mathbf{r}) + V_{XC}(\mathbf{r})]\phi_i(\mathbf{r}) = \epsilon_i \phi_i(\mathbf{r}) \tag{2.36}$$

where ϕ_i's are Kohn-Sham orbitals.

$V_H(\mathbf{r})$ is the classical part of the Hartree potential which describes the Coulomb repulsion felt by a single electron in any of the Kohn-Sham orbitals due the electron-density defined

by all the other electrons in the system. This also includes the self-interaction energy, that is the interaction of an electron with itself and the correction for it can be incorporated in $V_{XC}(\mathbf{r})$, for example in calculations using hybrid functionals, like HSE06. But in all the work presented in this thesis, we have not done any calculation that included any such corrections. The expression for $V_H(\mathbf{r})$ would be

$$V_H(\mathbf{r}) = \frac{E_H[n(\mathbf{r})]}{\delta n(\mathbf{r})} \tag{2.37}$$

$V_{XC}(\mathbf{r})$ is the exchange-correlation potential given by

$$V_{XC}(\mathbf{r}) = \frac{E_{XC}[n(\mathbf{r})]}{\delta n(\mathbf{r})} \tag{2.38}$$

All the terms in 2.36 are known except V_{XC}. 2.36 can also be written as

$$[-\frac{\hbar^2}{2m}\nabla^2 + V_{KS}(\mathbf{r})]\phi_i(\mathbf{r}) = \epsilon_i\phi_i(\mathbf{r}) \tag{2.39}$$

We solve the Kohn-Sham equations for the alternative non-interacting system. The solutions to the Kohn-Sham equations are the Kohn-Sham orbitals. The ground state electron-density is calculated from the ground state Kohn-Sham orbitals. This ground state electron-density equals exactly to the ground state electron-density of the interacting system of electrons. Now ,to solve the Kohn-Sham equations, we need to know the Hartree potential $V_H(\mathbf{r})$. A knowledge of the Hartree potential $V_H(\mathbf{r})$ requires a knowledge of the density. Hence we solve 2.39 iteratively in the following steps:

Step 1 : The electron density is initially guessed by a trial function $n(r)$.

Step 2 : Kohn-Sham equations are solved using the trial electron-density. The solutions are the single particle wave functions ϕ_i's.

Step 3 : From the single particle wave functions, we calculate the free energy E of the system. We also calculate the electron density $n_{KS}(\mathbf{r}) = 2\sum_i \phi_i^\star(\mathbf{r})\phi_i(\mathbf{r})$ and therefrom, the charge density. This calculated charge density is then mixed with the older one to generate a new charge density.

Step 4 : We tally the new free energy E with the initial free energy. If they converge to some defined precision, we accept this as the ground state energy and the associated charge density as the ground state charge density. If the two values of free energy are different, we begin again from step 2 with updated density.

This has been pictorially shown in Figure 2.1

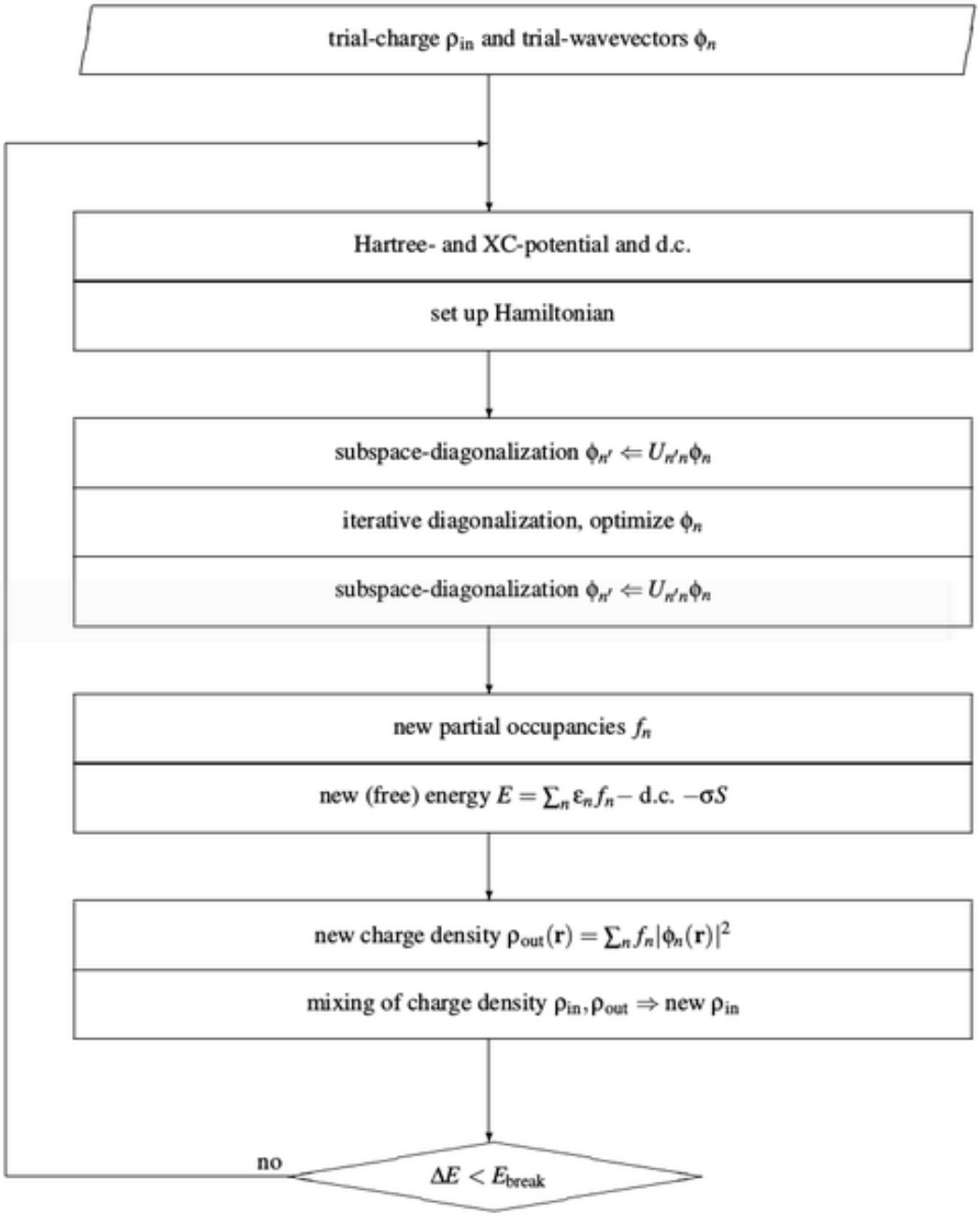

Figure 2.1: Flowchart of DFT (Taken from Vaspwiki)

2.2.6 Approximations for Exchange-Correlation Functional

Here a general discussion is going to be provided on how the approximations are made for the exchange-correlation functionals. If Ψ be the ground state wavefunction for the electronic hamiltonian for the system of N electrons, the expectation value for the electron-

electron repulsion V_{ee} is given by,

$$\langle \Psi | V_{ee} | \Psi \rangle = \frac{e^2}{2} \int \frac{P(\mathbf{r}, \mathbf{r}^{'})}{|\mathbf{r} - \mathbf{r}^{'}|} d^3 r d^3 r^{'} \tag{2.40}$$

where $P(\mathbf{r}, \mathbf{r}^{'})$ is the pair density, means the probability of simultaneously finding an electron at $\mathbf{r}$ where another electron at $\mathbf{r}^{'}$. For a non-interacting system, where there is no correlation , the pair density is the simple product of the two individual electron densities,

$$P^{classical}(\mathbf{r}, \mathbf{r}^{'}) = n(\mathbf{r}) n(\mathbf{r}^{'}) \tag{2.41}$$

which gives the classical Hartree energy 2.33.

But quantum mechanically, due to exchange and correlation effects, the density of electron at $\mathbf{r}$ gets reduced due to the presence of another electron at $\mathbf{r}^{'}$. As aresult, around each electron, there is a depletion of electron-density, or hole. Taking into account the hole, the pair density can be written as

$$P^{QM}(\mathbf{r}, \mathbf{r}^{'}) = n(\mathbf{r}) n(\mathbf{r}^{'}) + n(\mathbf{r}) n_{XC}(\mathbf{r}, \mathbf{r}^{'}) \tag{2.42}$$

$n_{XC}(\mathbf{r}, \mathbf{r}^{'})$ is the exchange-correlation hole density. The exchange-correlaation functional can be defined as [23],

$$E_{XC}[n(\mathbf{r})] = \int n(\mathbf{r}) \epsilon_{xc}(\mathbf{r}) d^3 r \tag{2.43}$$

where

$$\epsilon_{xc}(\mathbf{r}) = \frac{e^2}{2} \int \frac{n_{xc}(\mathbf{r}, \mathbf{r}^{'})}{|\mathbf{r} - \mathbf{r}^{'}|} d^3 r^{'} \tag{2.44}$$

is the exchange-correlation energy per particle. There are various approaches inn which the functional $\epsilon_{xc}(\mathbf{r})$ has been constructed, and it depends on how the density has been sampled around each electron.

Local Density Approximation(LDA):

Local density approximation(LDA) was proposed by Hohenberg and Kohn in their original DFT paper [21]. LDA approximates the exchange-correlation energy of a system at some point in space by the exchange-correlation energy of a homogeneous electron gas (HEG) of the same density at that point. Homogeneous electron gas is the only system for which the electron density is explicitly known. The exchange-correlation functional is written

in terms of the local density as

$$E_{XC}^{LDA}[n(\mathbf{r})] = \int n(\mathbf{r})\varepsilon_{XC}^{HEG}(\mathbf{r})d^3r) \tag{2.45}$$

here $\varepsilon_{XC}^{HEG}(\mathbf{r})$, is the exchange-correlation energy density of a homogeneous electron gas of density $n(\mathbf{r})$. $\varepsilon_{XC}^{HEG}(\mathbf{r})$ can be separated into exchange and correlation parts as,

$$\varepsilon_{XC}^{HEG}(\mathbf{r}) = \varepsilon_{X}^{HEG}(\mathbf{r}) + \varepsilon_{C}^{HEG}(\mathbf{r}). \tag{2.46}$$

Dirac derived this exchange part $\varepsilon_{X}^{HEG}(\mathbf{r})$ analytically [23]. But the analytic expression for the other term ε_{C}^{HEG} is known only in the limits of high [24, 25] and low densities [26].

Generalized Gradient Approximation (GGA) :

For real systems, the density is not uniform. non-uniformity in density arises due to spatially directed bonds. Generalized gradient approximation (GGA) takes care of this non-uniformity by expressing the exchange-correlation energy in terms of density as well as gradient of electron density. The exchange-correlation functional under GGA approximation can be expressed as,

$$E_{XC}^{GGA}[n(\mathbf{r})] = \int n(\mathbf{r})\varepsilon_{XC}^{HEG}[n(\mathbf{r}), |\nabla n(\mathbf{r})|]d^3r \tag{2.47}$$

Perdew and co-workers had done the most important work towards development of GGA functional [27]. A number of variants have been devepoled depending on the ways the grandient of density has been used, some popular forms of them are Perdew and Wang [28], Becke-Lee-Yang-Par (B-LYP) [29–31] and Burke and Enzerhof (PBE) [32] functionals.

Meta Generalized Gradient Approximation (MGGA) :

The next type of correction is incorporated in Meta Generalized Gradient Approximation (MGGA) which also includes information of $\bigtriangledown^2 n(\mathbf{r})$. The kinetic energy density corresponding to the Kohn-Sham orbitals,

$$\tau(\mathbf{r}) = \frac{1}{2}\sum_{i=1}^{N} |\bigtriangledown \phi_i(\mathbf{r})|^2 \tag{2.48}$$

is equivalent to the Laplacian of density, and hence is used in MGGA instead of $\bigtriangledown^2 n(\mathbf{r})$. The Modified Perdew-Burke-Johnson potential (MBJLDA) [34, 35] is an example of MGGA and has been used in the work of the thesis. THis gives better accurcy for the bandgap value.

Hybrid Functionals :

Another approximation for exchange-correlation energy are hybrid functionals. It has contributions from the exact (Hartree-Fock) energy with a GGA functional. Its general form is

$$E_{XC}^{Hybrid} = \alpha(E_X^{HF} - E_X^{GGA}) + E_{XC}^{GGA} \tag{2.49}$$

E_X^{HF} is the exact hartree -fock exchange energy calculated using Kohn-Sham orbitals. This funcaiotnal is non-local in the sense that to evaluate it at a particular point, the Kohn-Sham orbitals ϕ_i's at all the other points need to be known. α is determines the amountof mixing with exact exchange energy. One of the various hybrid functionals is HSE, named after J. Heyd, G. E. Scuseria, and M. Ernzerhof [35]. These functional guve accurate results for strongly correated systems due to their large self-interaction correction but are computationally expensive due to their non-local nature.

2.3 Numerical Approximations for DFT Calculations

In DFT, a collection of atoms is defined by a set of equations (Kohn-Sham equations) with an approximate form for the exchange-correlation functional. The solutions give us the electronic structure of the system. These equations can't be solved analytically. So numerical methods are employed to solve them where they are solved iteratively to give the ground state electron density. Some approximations are made to solve the numerical problem. For example, integrations are done over a finite grid to reduce the infinite sum into a finite one, which adds errors. So, an well-converged solution of the DFT problem is very close to the exact solution. The numercal approximations are discusssed in the following chapters.

2.3.1 Plane Wave Basis and Cut-off Energy

To numerically solve the Kohn-Sham equations, we need a basis set to expand the Kohn-Sham orbitals. Since we are working with periodic crystal, the single-electron wavefunctions, called the Bloch states, can be expressed as

$$\phi_{\mathbf{k}}(\mathbf{r}) = e^{i\mathbf{k}\cdot\mathbf{r}} u_{\mathbf{k}}(\mathbf{r}) \tag{2.50}$$

$u_{\mathbf{k}}(\mathbf{r})$ is a periodic function with the periodicity of the crystal, i.e. $u_{\mathbf{k}}(\mathbf{r} + n_1\mathbf{a}_1 + n_2\mathbf{a}_2 + n_3\mathbf{a}_3) = u_{\mathbf{k}}(\mathbf{r})$ where $\mathbf{a}_1$, $\mathbf{a}_2$, $\mathbf{a}_3$ are the lattice vectors of the crystal and n_1, n_2, n_3 are a set

of integers. So, Bloch states are basically plane waves modulated by a periodic function $u_{\mathbf{k}}(\mathbf{r})$.

Since $u_{\mathbf{k}}(\mathbf{r})$ is periodic, it can be expanded in terms of plane waves,

$$u_{\mathbf{k}}(\mathbf{r}) = \sum_{\mathbf{G}} C_{\mathbf{G}} e^{i\mathbf{G}\cdot\mathbf{r}} \tag{2.51}$$

$\mathbf{G}$ here is the reciprocal lattice vector and is defined in terms of reciprocal unit lattice vectors $\mathbf{b}_1$,$\mathbf{b}_2$,$\mathbf{b}_3$ as $\mathbf{G} = m_1\mathbf{b}_1 + m_2\mathbf{b}_2 + m_3\mathbf{b}_3$ for a set of integers m_1, m_2 ,m_3. Now using the definition of $u_{\mathbf{k}}(\mathbf{r})$ from Equation 2.51 into the Equation 2.50 we get

$$\phi_{\mathbf{k}}(\mathbf{r}) = \sum_{\mathbf{G}} C_{\mathbf{G}+\mathbf{k}} e^{i(\mathbf{G}+\mathbf{k})\cdot\mathbf{r}} \tag{2.52}$$

Equation 2.52 involves a sum over infinite number of plane waves for infinite number of possibe values of $\mathbf{G}$. These plane waves have kinetic energies given by $E = \frac{\hbar^2}{2m}|\mathbf{k}+\mathbf{G}|^2$. For practical purpose, we need to truncate this infinite sum to a finite one. This is done by defining a cut off energy as

$$E_{cut} = \frac{\hbar^2}{2m} G_{cut}^2 \tag{2.53}$$

So, only those plane wave whose kinetic energies are lower than the defined cut off energy are included in the basis set. The error incurred in this approximation can be lowered by increasing the cutoff energy until the energy of the system converges and no significant variation in the energy is observed with further change in E_{cut}.

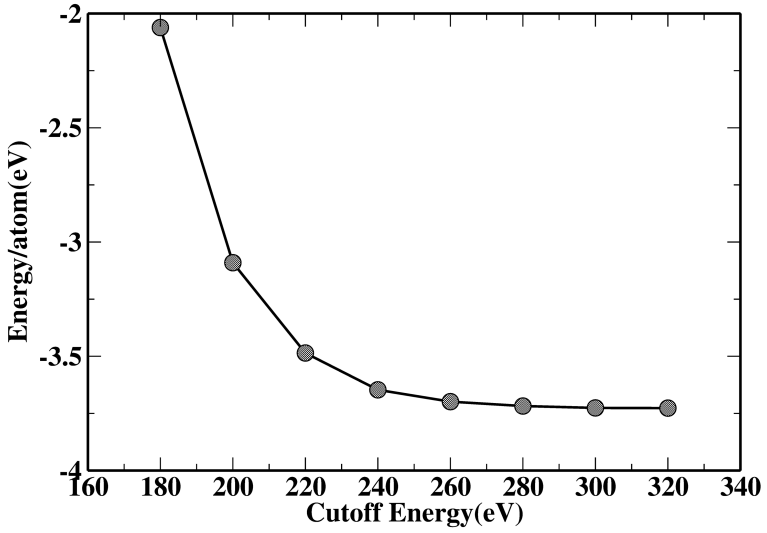

Figure 2.2: Total energy per atom of fcc Cu using a 10x10x10 k-points grid as a function of the cutoff

Figure gives the convergence of total energy per atom of fcc Cu as a function of E_{cut}. GGA was considered for the exchange-correlation functional. A $10X10X10$ Monkhorst-Pack k-mesh was used for performing the k-space integrations. We can see from that, changing value of E_{cut} from 300 to 320 eV, the total energy change per atom is less than 1 meV. Hence we can use E_{cut} = 300 eV for the above calculation for a well converged result.

2.3.2 K-Space Integrations

In all DFT calculations, a large amount of time is spent in performing integrals over Brilloin zone in k-space. These integrals have the general form [19],

$$g = \frac{V_{cell}}{(2\pi)^3} \int_{BZ} g(\mathbf{k}) d\mathbf{k} \tag{2.54}$$

Here V_{cell} is the volume of the unit cell. In order to evaluate the intergral in 2.54 numerically, we evaluate the value of $g(\mathbf{k})$ at some finite k-points in the Brillouin zone with proper weights. Such methods give more and more accurate results with increase in the number of k-points, and the numerical result may converge to the exact result. There are various methods in use to choose the k-points properly. The most widely used one has been introduced by Monkhorst and Pack [39]. In this scheme, equally spaced k-points are taken along various unit vectors of the reciprocal space. For a cubic cell, for example, the reciprocal cell is also cubic. If N_k equally spaced points are taken along each reciprocal cell unit vectors, then it will be labelled as N_{k_x} x N_{k_y} x N_{k_z} k-mesh calculation. A calculation is considered to have converged, if upon increasing the number of k-points, there is no significant change in the energy value.

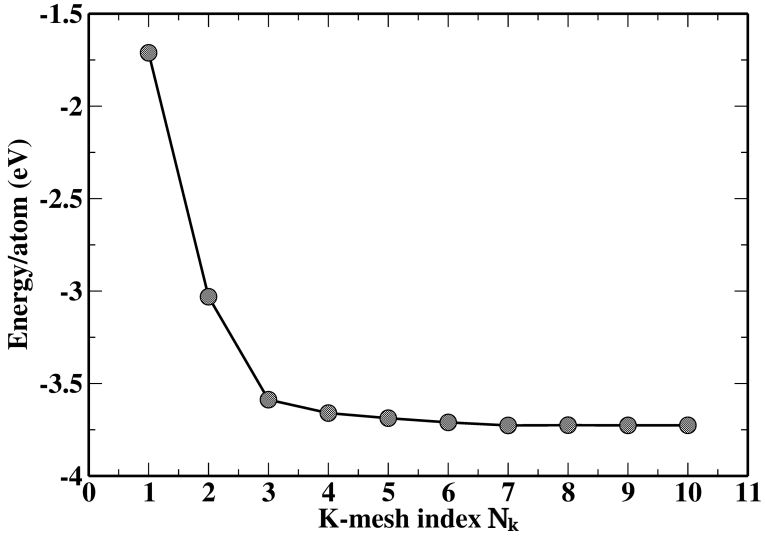

Figure 2.3: Total energy per atom for fcc Cu as a function of N_k implying a N_{k_x} x N_{k_y} x N_{k_z} k-points calculation

Figure 2.3 shows the convergence of the total energy calculated using DFT, of fcc Cu as a function of N_k. GGA was considered for exchange-correlation functional with a converged E_{cut} value of 300 eV. Changing the value of N_k from 7 to 8, the total energy change per atom is less than 1 meV. Hence convergence is reached for 7 x 7 x 7 or 8 x 8 x 8 k-points grid.

2.3.3 Pseudopotential and Frozen core approximation

The valence electrons in an atom are those which are chemically active as they take part in forming bonds. Core electrons remain tightly bound to the nucleus. The wavefunctions for the valenceelectrons show rapid oscillations near the core region, and for this a large cutoff energy value is needed to represent the associated states in terms of plane wave basis. This makes it computationally costly. A way to bypass the problem is to make approximations that will replace the effects of core electrons in a way that will reduce the computational cost by lowering the number of plane waves in the basis set.

A popular approach is to use pseudopotentials to replace the effect of the core electrons. A pseudopitential replaces the charge density of core electrons with a smoothened charge density that will lead to the same physical and mathematical properties. This is called frozen core approximation. If $|\psi^c\rangle$ and $|\psi^v\rangle$ represent the wavefunctions for the core and valence electrons respectively, then we can construct a smoother valence wavefunction

$|\phi^v\rangle$ that is orthogonal to $|\psi^c\rangle$ as [40]

$$|\phi^v\rangle = |\psi^v\rangle + \sum_c \alpha_c \psi^c(\mathbf{r}) \tag{2.55}$$

The values of α_c's are determined from the orthogonality condition $\langle\phi^v|\psi^c\rangle = 0$ here the orthogonality condition $\alpha_c = \langle\psi^c|\phi^v\rangle$ can be used to determine α_c. These pseudo-wavefunction satisfies the modified Schrödinger equation

$$\left[H + \sum_c (\epsilon^v - \epsilon^c)|\psi^c\rangle\langle\psi^c|\right]|\phi^v\rangle \;\; = \;\; \epsilon^v|\phi^v\rangle \tag{2.56}$$

hence a pseudo Hamiltonian is given as

$$H^{PH} = \left[H + \sum_c (\epsilon^v - \epsilon^c)|\psi^c\rangle\langle\psi^c|\right] \tag{2.57}$$

This pseudo Hamiltonian has the same eigenvalues with smoother eigenfunctions. The corresponding potential

$$V^{PP} = V + \sum_c (\epsilon^v - \epsilon^c)|\psi^c\rangle\langle\psi^c| \tag{2.58}$$

is called pseudo-potantial. In 2.58, V is the nuclear potential. The second term is the coorection term which is repulsive in nature, as $(\epsilon^v > \epsilon^c)$ indicating the electrons feel a net repulsion due to the core electrons. A schematic illustration of pseudo potential approach is given in Figure 2.4

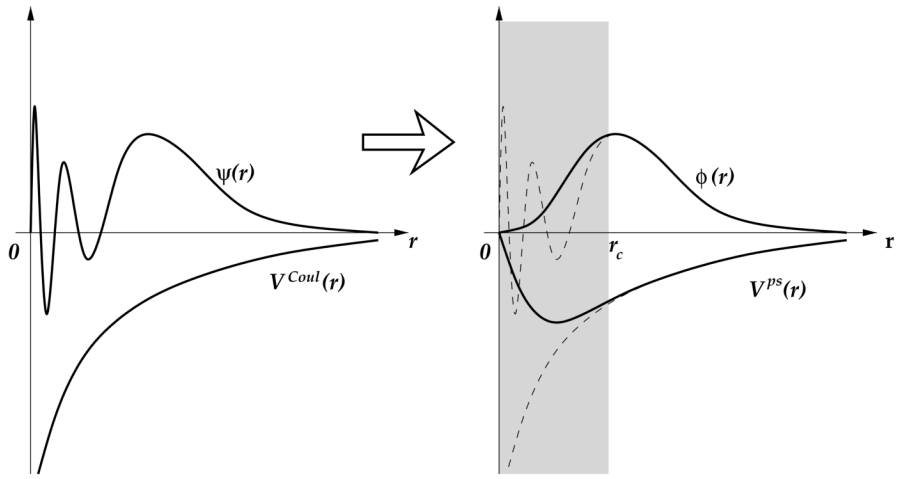

Figure 2.4: Schematic diagram of the Pseudopotential $V^{PS}(r)$ and pseudo-wavefunction $\phi(r)$. The left figure shows valence wave function $\psi(r)$ and Coulomb potential $V^{Coul}(r)$. In the right figure, r_c represents the cutoff radius beyond which the wave function and the potential are not affected.(Taken from, Atomic and Electronic Structure of Solids, E. Kaxiras, Cambridge University Press [38])

Beyond a cutoff radius r_c the pseudo wavefunction and the pseudo potential coincide with all electron wavefunction and the all electron potential respectively. Within r_c a smoother potential is experienced by the new set of valence states.

Constant efforts are there to generate pseudo-potentials which are accurate as well as efficient. In norm-conserving pseudo-potential method, the all-electron and pseudo-wave function agree beyond some chosen radius (r_c). Sometimes the pseudo-potentials generated using this method not quite smoother. This problem was overcome in ultrasoft pseudo potentials (USPP) introduced by Vanderbilt in 1990 [42]. The norm-conservation criteria was relaxed in this case. The energy cutoff is very small and hence the number of planewaves. Another popular approach better than USPP is projector augmented-wave(PAW) method.

2.3.4 Projector Augmented-Wave(PAW) Method

One major disadvantage of using USPP's is that the construction of the potential for each atom requires the specification of a number of empirical parameters. The DFT codes currently use ony those USPP's which have been carefully developed and tested. But, some of the codes use more than one USPP's with various degrees of softness for some elements [19]. The other frozen core approach that overcomes the difficulties in

USPP is Projector Augmented Wave (PAW) method originally introduced by Blochl [49] and later adopted for plane-wave calculations by Kresse and Joubert [50].

In this approximation, an all-electron wavefunction is constructed to calculate all the integrals which is a combination of the smooth function over space and contributions from localized muffin-tin orbitals [51, 53]. As a result, we have the total wavefunction which is a combination of wavefunction of the valence states $\tilde{\psi_i^v}(\mathbf{r})$ as well as a linear transformation function which relates an all electron valence function $\psi_j^v(\mathbf{r})$ to $\tilde{\psi_i^v}(\mathbf{r})$. This is given as

$$\psi_j^v(\mathbf{r}) = \tilde{\psi_j^v}(\mathbf{r}) + \sum_i (|\phi_i\rangle - |\tilde{\phi_i}\rangle)\langle\tilde{p_i}|\tilde{\phi_i}\rangle \tag{2.59}$$

In this equation, the atomic site $\mathbf{R}$ is represented by the index i. $|\tilde{p_i}\rangle$ represents the projector functions for localized pseudo partial wave. They satisfy the orthogonality condition, $\langle\tilde{p_i}|\tilde{\phi_j}\rangle = \delta_{i,j}$. In this formalism, the all electron charge density can be derived from Equation 2.59 as

$$n(\mathbf{r}) = \tilde{n}(\mathbf{r}) + n^1(\mathbf{r}) - \tilde{n}^1(\mathbf{r}), \tag{2.60}$$

here,

$$\tilde{n}(\mathbf{r}) = \sum_i f_i |\tilde{\psi}_i(\mathbf{r})|^2 \tag{2.61}$$

$$n^1(\mathbf{r}) = \sum_i f_i \sum_{j,k} \langle\tilde{\psi}_i|\tilde{p_j}\rangle \phi_j(\mathbf{r})\phi_k(\mathbf{r})\langle\tilde{p_k}|\tilde{\psi}_i\rangle \tag{2.62}$$

$$\tilde{n}^1(\mathbf{r}) = \sum_i f_i \sum_{j,k} \langle\tilde{\psi}_i|\tilde{p}_j\rangle \tilde{\phi}_j(\mathbf{r})\tilde{\phi}_k(\mathbf{r})\langle\tilde{p}_k|\tilde{\psi}_i\rangle \tag{2.63}$$

In this expressions, f_i's are the occupancies of the eigenstates $\tilde{\psi}_i$. $\tilde{n}(\mathbf{r})$ is the pseudo-charge density which is calculated from the pseudo-wavefunctions with plane wave basis. $n^1(\mathbf{r})$ and $\tilde{n}^1(\mathbf{r})$ are the onsite charge densities localized within the augmented sphere around each atom. The total energy of the system when calculated from these charge densities can also be divided into three parts.

2.4 Van der Waals Correction: DFT-D2 Method

Long range non-local forces, such as van der Waals (vdW) are not incorporated in the exchange-correlation functionals used in DFT. So additional estimations need to made to

take into account these forces. DFT-D2 is one such approach, which was proposed by Grimme [55]. A semi-empirical term which is attractive in nature is added to the total energy calculated by DFT. This term takes into consideration the long range dispersive forces and hence we call it E_{disp}. The total energy thus becomes

$$E_{DFT-D2} = E_{DFT} + E_{disp} \tag{2.64}$$

E_{disp} is given as

$$E_{disp} = -s_6 \sum_{i=1}^{N_{at}-1} \sum_{j=i+1}^{N_{at}} \frac{C_6^{ij}}{R_{ij}^6} f_{damp}(R_{ij}) \tag{2.65}$$

The number of atoms in the system here is given here by N_{at}. s_6 is a scaling factor and it depends on the exchange correlation functional used. R_{ij} is the distance between the atoms i and j. C_6^{ij} are the dispersion coefficients between the $i-th$ and the $j-th$ atom. The singularity at R_{ij} can be avoided by the damping factor $f_{damp}(R_{ij})$ and is given as

$$f_{damp}(R_{ij}) = \frac{1}{1 + e^{-d(R_{i,j}/R_0^{i,j}-1)}} \tag{2.66}$$

For a pair of atoms, $R_0^{i,j}$ is the cut off radius. It is given as the average of their van der Waal radii [56]. d is a damping constant and it determines the steepness of the function [55].

2.5 Introduction to Wannier Functions

The electronic structure of a periodic solid is described in terms of extended/delocalized electronic states, called Bloch states [5]. Each of the Bloch states is assigned a reciprocal lattice vector **k** for the crystal momentum and a band index n. This is widely used in electronic structure calculations but alternate representations are also available. The Wannier representation [6–8] is a real-space picture in terms of localized orbitals. It assigns to each state, as quantum numbers, the lattice vector **R** of the unit cell in which the orbital is localized and a band-like index n. Wannier functions can be a powerful tool in the study of the electronic and dielectric properties of materials and can provide an insightful picture of the nature of chemical bonding, otherwise missing from the band picture of extended orbitals [9].

In a periodic solid, the single-electron states for the system of non-interating electrons are called Bloch states which have the general form

$$\phi_{n\mathbf{k}}(\mathbf{r}) = u_{n\mathbf{k}}(\mathbf{r})e^{i\mathbf{k}\cdot\mathbf{r}} \tag{2.67}$$

where n is the band-index. $u_{n\mathbf{k}}(\mathbf{r})$ is periodic in space with the periodicity of the lattice i.e. $u_{n\mathbf{k}}(\mathbf{r}+\mathbf{R}) = u_{n\mathbf{k}}(\mathbf{r})$, where $\mathbf{R}$ is any lattice vector, $\mathbf{R} = n_1\mathbf{a_1} + n_2\mathbf{a_2} + n_3\mathbf{a_3}$. In tight-binding approximation, a crystal is described in terms of a collection of localized atomic orbitals where there is negilgilble overlap between the valence electrons. Then we can express $\Phi_{n\mathbf{k}}(\mathbf{r})$ as linear combination of atomic orbitals $\psi_n(\mathbf{r})$ located at the lattice points $\mathbf{R}$:

$$\Phi_{n\mathbf{k}}(\mathbf{r}) = \sum_{\mathbf{R}} e^{i\mathbf{k}\cdot\mathbf{R}}\psi_n(\mathbf{r}-\mathbf{R}) \tag{2.68}$$

$\psi_n(\mathbf{r}-\mathbf{R})$ is the n^{th} atomic orbital at lattice point $\mathbf{R}$. The wavefunction in 2.68 satisfies Bloch condition,

$$\Phi_{n\mathbf{k}}(\mathbf{r}+\mathbf{R}) = \sum_{\mathbf{R}'} e^{i\mathbf{k}\cdot\mathbf{R}'}\psi_n(\mathbf{r}+\mathbf{R}-\mathbf{R}') \tag{2.69}$$

$$= e^{i\mathbf{k}\cdot\mathbf{R}}\sum_{\mathbf{R}'} e^{i\mathbf{k}\cdot(\mathbf{R}'-\mathbf{R})}\psi_n(\mathbf{r}-(\mathbf{R}'-\mathbf{R})) \tag{2.70}$$

$$= e^{i\mathbf{k}\cdot\mathbf{R}}\Phi_{n\mathbf{k}}(\mathbf{r}) \tag{2.71}$$

The resulting energy bands show no dispersion with $\mathbf{k}$. A way round te problem is to define functions $\phi_n(\mathbf{r})$ that are some linear combinations of atomic orbitals as,

$$\phi_n(\mathbf{r}) = \sum_m b_{mn}\psi_m(\mathbf{r}) \tag{2.72}$$

In terms of these functions the Bloch states are represented as,

$$\Phi_{n\mathbf{k}}(\mathbf{r}) = \sum_{\mathbf{R}} e^{i\mathbf{k}\cdot\mathbf{R}}\phi_n(\mathbf{r}-\mathbf{R}) \tag{2.73}$$

These functions $\phi_n(\mathbf{r}-\mathbf{R})$ are called Wannier functions, which are the Fourier coefficients of the inversion formula and are expressed in terms of the Bloch states $\Phi_{m\mathbf{k}}$ as,

$$\phi_n(\mathbf{r}-\mathbf{R}) = \frac{V}{(2\pi)^3}\int_{BZ}\left[\sum_m U^{\mathbf{k}}_{mn}\Phi_{m\mathbf{k}}(\mathbf{r})\right]e^{-i\mathbf{k}\cdot\mathbf{r}}d\mathbf{k} \tag{2.74}$$

The Wannier functions $\phi_n(\mathbf{r}-\mathbf{R})$ for all n and $\mathbf{R}$ form a complete orthogonal set to describe the Bloch states.

In the Equation 2.74, V is volume of the unit cell and integration is over the whole Brillouin zone. $U_{\mathbf{k}}$ is the unitary matrix which is used to mix the Bloch states at each $\mathbf{k}$ point in the Brillouin zone of the crystal and is not a unique one. Depending upon the choice of $U_{\mathbf{k}}$, the spatial extensions of Wannier functions vary. This non-uniqueness of $U_{\mathbf{k}}$ arise from the fact that orbitals represented by Bloch states belong to a set of bands that are separated by energy gaps from each other but have degeneracies within themselves and thus at each $\mathbf{k}$ point there will be many unitary transformations possible within themselves. This makes uses of Wannier functions unsuitable for real problems. A way to eliminate this arbitrariness was proposed by Marzari and Vanderbilt [11]. In this method, iteratively redefined transformations would lead to uniquely defined set of maximally-localized Wannier functions (MLWFs). This approach can be applied to a variety of problems starting from an isolated system to a periodic solid. For the entanglement band problem, this approach was extended by Souza et al. [12].

Bibliography

[1] G. Kresse and J. Hafner, Phys. Rev. B **47**, 558 (1993) ; G. Kresse and J. Hafner, Phys. Rev. B **49**, 14251 (1994); G. Kresse and J. Furthmüller, Phys. Rev. B **54**, 11169 (1996).

[2] G. Kresse and J. Furthmüller, Comput. Mater. Sci., **6**, 15 (1996).

[3] K. Umemoto, R. M. Wentzcovitch, and P. B. Allen, Science **311**, 983 (2006).

[4] F. Bloch, Z. Physik **52**, 555 (1928)

[5] G. H. Wannier, Physical Review **52**, 191 (1937).

[6] W. Kohn, Physical Review **115**, 809 (1959).

[7] J. des Cloizeaux, Physical Review **129**, 554 (1963).

[8] N. Marzari, A. A. Mostofi, J. R. Yates, I. Souza, and D. Vanderbilt, Rev. Mod. Phys. **84**, 1419 (2012).

[9] A. A. Mostofi, J. R. Yates, Y.-S. Lee, I. Souza, D. Vanderbilt, and N. Marzari, Comput. Phys. Comm **178**, 685 (2008).

[10] N. Marzari and D. Vanderbilt, Phys. Rev. B **56**, 12847 (1997).

[11] I. Souza, N. Marzari and D. Vanderbilt, Phys. Rev. B **65**, 035109 (2001).

[12] M. Born and J. R. Oppenheimer, Zur Quantentheorie der Molekeln, Ann. Physik **84**, 457(1927).

[13] C. Kittel, Introduction to Solid State Physics, Wiley, New York, (1996).

[14] P. Hohenberg and W. Kohn, Phys. Rev. **136** 3B (1964).

[15] G. Kresse and J. Furthmüller, Phys. Rev. B **54**, 11169 (1996).

[16] G. Kresse and J. Furthmüller, Comput. Mater. Sci., **6**, 15 (1996).

[17] F. Bloch, Z. Physik **52**, 555 (1928).

[18] D. S. Sholl and J. A. Steckel, Density Functional Theory : A Practical Introduction (Wiley-Interscience) (2009).

[19] W. Koch and M. C. Holthausen. A Chemist's Guide to Density Functional Theory. Wiley-VCH, (2001).

[20] P. Hohenberg and W. Kohn, Phys. Rev. **136** 3B (1964).

[21] W. Kohn and L. J. Sham, Phys. Rev. **140**, A1133 (1965).

[22] J. P. Perdew, K. Burke, and Y. Wang, Phys. Rev. B **54**, 16533 (1996)

[23] P. A. M. Dirac, Proc. Cambridge Phil. Roy. Soc. **26**, 376 (1930).

[24] M. Gell-Mann and K. A. Brueckner, Phys. Rev. **106**, 364 (1957).

[25] W. J. Carr and A. A. Maradudin, Phys. Rev. **133**, A371 (1964).

[26] E. Wigner, Phys. Rev. **46**, 1002 (1934).

[27] J. P. Perdew, Phys. Rev. Lett. **55**, 2370 (1985).

[28] J. P. Perdew and Y. Wang, Phys. Rev. B **45**, 13244 (1992).

[29] A. D. Becke, Phys. Rev. A **38**, 3098 (1988).

[30] C. Lee, W. Yang, R. G. Parr, Phys. Rev. B **37**, 785 (1988)

[31] A. D. Becke, J. Chem. Phys. **96** 2155 (1992).

[32] J. P. Perdew, K. Burke, and M. Ernzerhof, Phys. Rev. Lett. **77**, 3865 (1996).

[33] A. D Becke, E. R. Johnson, J. Chem Phys. **124**,221101(2006)

[34] F. Tran, P. Blaha, Phys. Rev.Lett **102**, 226401 (2009)

[35] J. Heyd, G. E. Scuseria, and M. Ernzerhof, J. Chem. Phys. **118**, 8207 (2003).

[36] Hendrik J. Monkhorst and James D. Pack, Phys. Rev. B **13**, 5188 (1976).

[37] James C. Phillips and Leonard Kleinman, Phys. Rev. **116**, 287 (1959).

[38] E. Kaxiras, Atomic and Electronic Structure of Solids, Cambridge University Press, UK,(2003).

[39] D. Vanderbilt, Phys. Rev. B. **41**, 8412 (1990).

[40] P.E. Blochl, Phys. Rev. B **50**, 17953 (1994).

[41] G. Kresse, and J. Joubert, Phys. Rev. B **59**, 1758 (1999).

[42] O. K. Andersen and R. V. Kasowski, Phys. Rev. B **4**, 1064 (1971).

[43] O. K. Andersen, 1971, Computational Methods in Band Theory, p. 178, edited by P. M. Marcus, J. F. Janak and A. R. Williams (Plenum Press)

[44] S. Grimme, Journal of Computational Chemistry, **27** 15 1787-1799, (2006).

[45] S. Grimme, Journal of Computational Chemistry **25** 12, 1463-1473, (2004).

Chapter 3

Type-I to Type-II Electronic Structure Transition in GaAs/AlAs Heterostructure

3.0.1 Introduction

The formation of heterojunctions between two semiconductors paved the way for modern day electronics [1,3]. Depending on the material, modifications in the layer thickness is a route by which one can modify the location of the valence band maximum and conduction band minimum in each layer, thereby modifying the band alignment between them [6]. One could therefore move from a regime where one had a confinement potential for both electrons and holes, to one where one had a confinement potential for only one type of charge carrier or sometimes for neither. Depending on the type of device envisaged, one would like different types of band alignments. For instance, in cases where the material is a part of a solar cell, separation of the photo-generated electron and hole is essential. In these materials one would like a band offset in which the hole and electron are localized in different layers, and so can get harvested easily [4,6]. The thickness dependence allows one to modify the band alignments keeping the pair of materials the same [7]. The presence of two different materials across the interface, brings in strain as an additional parameter to tune relative positions of band edges [6].

The topic of semiconductor heterostructures is more than half a century old. With the advent of molecular beam epitaxy which allowed a control of the thickness of each layer, one had unprecedented control on the level of quantum confinement. This proved to be

important from a basic science point of view as well as technological point of view and the topic has been investigated extensively. Recent advances in colloidal synthesis [8] routes have brought forth tremendous control on growth by soft chemistry methods. This allows the growth of various II-VI semiconductor heterostructures with both layers containing just a few monolayers. We therefore reinvestigate the evolution of the electronic structure of the classic heterostructure containing GaAs and AlAs. As these semiconductors are lattice-matched, strain does not play a major role in the modifications of the band offsets that one finds. Using functionals that give us the band gaps of both GaAs and AlAs quite accurately, we examine the localization of the electron and the hole wavefunction as we explore the change in the nature of the confinement with decreasing layer thickness. The issue of the abruptness of the change is an aspect that hasn't been addressed before. This is monitored by examining the charge density across the transition as well as the oscillator strength for the band edge optical transition, suggesting how the nature of the transition can be monitored experimentally. Looking at the nature of the envelopes of the charge density distributions, assuming the carrier motions to be described by the outer envelopes, we find that the standing waves generated by the presence of the interface behave differently for the conduction band minimum and the valence band maximum. This reflects the potential barrier at the interface.

At this point let us get introduced to some concepts that will prove useful in further understanding and analysis of the problem.

What are the various types of heterojunctions that can be realized ?

A heterojunction is the interface between two layers of regions of semiconductors with dissimilar crystalline structures. These semiconductors have unequal bandgaps in contrast to homojunctions that have equal bandgaps on both sides. The band alignment of a typical heterojunction has been shown in Figure 3.1.

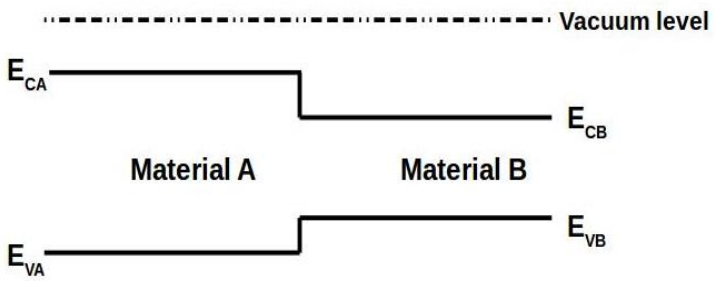

Figure 3.1: The band alignments of a typical heterojunction

Semiconductor interfaces may come in three types of heterojunctions. Each of these three types of heterojuntions has been shown with the respective band alignements in Figure 3.2.

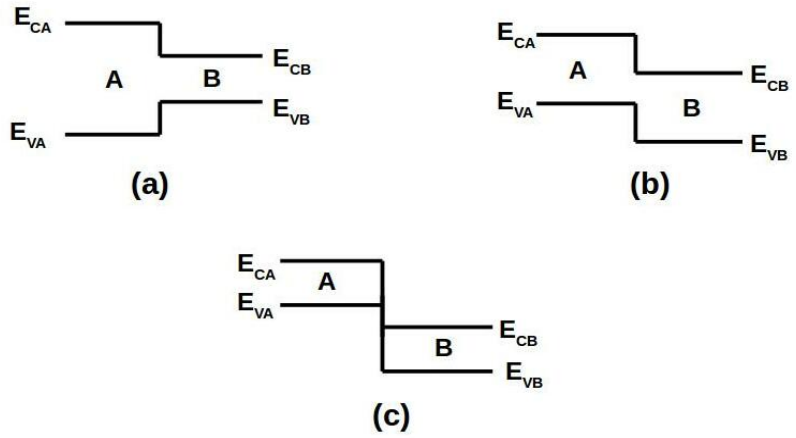

Figure 3.2: Three types of heterojunctions with the associated band alignents (a) type-I (b) type-II and (c) type-III

In type-I heterojuntion, also called straddling gap heterojunction, the band alignment is such that the bandgap of one material is completely contained in the bandgap of the other. Both electrons and holes have their wells inside the same component [Fig. 3.2(a)] leading to the confinement of electrons and holes in the same material. Both electrons and holes need energy to travel from the material with smaller bandgap to that with larger gap.

In type-II heterojuntion, also called staggered gap heterojunction, the band alignment is such that the bandgaps of the two materials overlap. Electrons and holes have their wells in alternate componenets of the heterostructure [Fig. 3.2(b)]. Confinement of electrons and holes occur in the different materials. Here for the charge carriers to move from one material to the other, one type of carriers need energy while the other type of carriers gain energy.

In type-III heterojuntion, also called broken gap heterojunction, the bandgaps of the two materials don't overlap [Fig. 3.2(c)]. The well for electrons in the conduction band and the well for holes in the valence band lie in alternate materials. The bottom of the well for electrons lies below the bottom of the well for the holes along the energy axis. Here again, like type-II, for the charge carriers to move from one material to the other, one type of carriers need energy while the other type of carriers gain energy.

For practical purposes, various types of band alignment of the heterojunction are realized upon taking various combinations of materials. Via doping in one or both the components,

changes in the band alignement can be induced. We can mention, for example, InAs/AlSb double quantum wells. They belong to the class of two-dimensional topological insulators (2DTIs) that have an insulating bulk and gapless helical edges [9–12]. InAs/AlSb DQWs have a type-II broken gap band alignment with electrons and holes spatially separated. The top of the valence band in GaSb lies above the bottom of the conduction band in InAs. The two bands cross and the coupling of the electrons and holes opens up a bulk gap [13–20] and there are gapless edge states. With doping, this DQWs can be transformed into type-I structure that results in strong interband transitions [21]. Upon proper doping, the InAs layer changes from a barrier to a well for holes. The associated band bending converts the structure to type-I.

Semiconductior heterostructure quantum wells also provide opportunities for realizing band inversion and topological insulators. Mercury telluride/cadmium telluride (HgTe/CdTe) semiconductor quantum wells come first in this category. These QWs exhibits quantum spin Hall (QSH) effect, a state in which the topological properties are different from band insulators. Upon varying the thickness, the material switches between normal to inverted band alignment at some critical thickness, associated with a phase transition between a band insulator and a topological insulator showing QSH effect [22]. The rich topological properties in HgTe quantum wells can also be explored with by application of strain [23] and temperature [24].

How a change in the band alignment can be triggered by increasing the confinement : transition from type-I to type-II structure

the various primitive characters present in the CBM and VBM of the supercell In a semiconductor heterostructure, an increase in the degree of confinement of charge carriers by way of reducing the confinement length can shift the positions of the band extrema between alternate components, thereby leading to a transition from one band alignment to another. In the present project we are focussing on the prospect and nature of such a transition in (AlAs)/(GaAs) heterostructures. We are now going to analyse the detailed mechanism of a transition from type-I to type-II electronic structure known to occur in (AlAs)/(GaAs) heterostructures. Such a transition can be triggered by reducing the thickness of the confinement region of electrons and holes in the GaAs layers in the type-I structure that will cause the conducton band bottom to shift from the GaAs layers to the AlAs layers, resulting in a type-II band alignment.

The (AlAs)/(GaAs) heterostructure is composed by sandwiching a GaAs region in between two AlAs regions of both sides. When the thickness of the GaAs region is large, the

conduction band minimum (CBM) lies inside the GaAs region. It provides a confinement potential inside the GaAs region along the growth direction for the electrons occupying the CBM. The barriers lie inside the AlAs regions on both sides. Similarly, the valence band maximum (VBM) lies inside the GaAs region. This creates a confinement potential inside the GaAs region for the holes occupying the VBM with barriers inside the AlAs regions on both sides. As a result, both the electrons and holes get trapped inside the GaAs layers which has a shorter bandgap of ~ 1.424 eV as compared to AlAs, which has a bandgap of ~ 2.12 eV. Thus the lineup of the band extrema form a type-I electronic structure for the system.

In parabolic band approximation [Fig. 3.3], the band structure E($\mathbf{k}$) near the valleys at the conduction band minimum and the valence band maximum inside the GaAs region can be locally approximated as

$$E(\mathbf{k}) = E_0 + \frac{\hbar^2 \mathbf{k}^2}{2m^*} \tag{3.1}$$

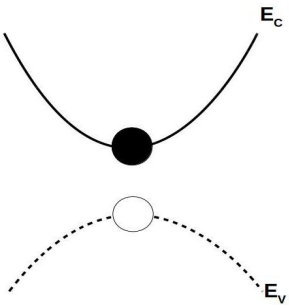

Figure 3.3: Effective masses of the electrons occupying CBM and holes occupying VBM can be approximated by parabolas

where E($\mathbf{k}$) is the energy of an electron at wavevector k in that band, E_0 is a constant giving the edge of energy of that band, and m^* is a constant (the effective mass). Hence, the band structure is approximated as parabolas. It can be shown that the electrons or holes in these band extrema behave as free particles with an effective mass.

We can therefore approximate the situation in type-I (AlAs)/(GaAs) heterostrcuture with a particle in a box picture, where both the electrons occupying the CBM and the holes occupying the VBM can be thought of as particles confined in a one-dimensional box inside the GaAs region along the growth axis with barriers inside the AlAs regions on

both sides [Fig.3.4]. The ground state energies of these fictitious particles inside their respective potential wells will correspond to the band extrema.

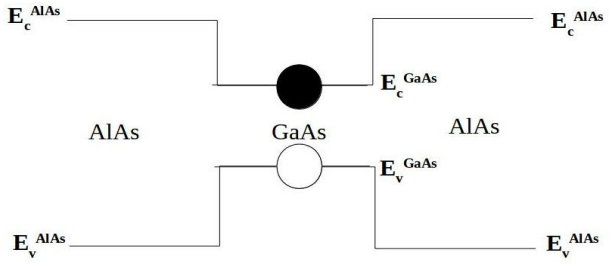

Figure 3.4: Electrons and holes confined inside the GaAs region in the type-I structure of (AlAs)/(GaAs) heterostructure can be approximated with particles confined inside a one-dimensional box along the growth axis.

The effective masses of the electrons and the holes can be computed from the curvatures of the parabolas corresponding to CBM and VBM respectively using the following formula,

$$m^* = \frac{\hbar^2}{\frac{d^2E(\mathbf{k})}{dk^2}} \tag{3.2}$$

where $\frac{d^2E(\mathbf{k})}{dk^2}$ is the curvature of the parabola.

In our particle in a box picture, the charge carriers, considered as confined particles, are supposed to be moving with these effective masses. Depending on the respective effective masses, the pace with which the ground state energies of the electrons and the holes will shift in response to a change in the thickness of the wells will vary. This will directly correspond to the shift in energies of CBM and VBM with change in confinement inside the GaAs region.

This seems obvious because the energy of the particle is inversely proportional to its effective mass.

$$E \propto \frac{\hbar^2 k^2}{2m^*} \tag{3.3}$$

where m^* is the effective mass of the particle. Here $\hbar k$ represents the crystal momentum. k depends on the de Broglie wavelength which keeps changing with change in confinement length.

Between the two types of charge carries involved, the ground state energy of the representing particle will rise faster for the one with a smaller effective mass as is implied by [Eqn. 3.3]. This will decide whether the CBM or the VBM will move faster. It turns out

that the holes have heavier effective mass than the electrons [46]. So it is expected that the VBM will move slower than the CBM upon confinement.

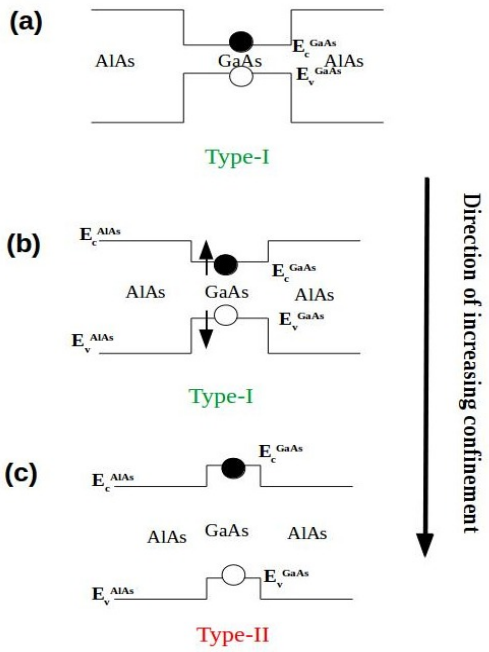

Figure 3.5: Schematic depiction of the gradual transition from type-I to type-II band alignment upon confinement in (AlAs)/(GaAs) heterostructure within particle in a box approximation for the charge carriers : (a) Initial state of type-I alignment (b) Intermediate state with the CBM moving up and VBM moving down (c) Final state of type-II band alignment.

Now, as we gradually start reducing the thickness of the GaAs region, the confinement for the electrons and the holes increase. As a result, the ground state energies of the particles in our model start rising inside their respective wells. This is equivalent to CBM rising up and VBM moving down in energy inside the GaAs region [Fig. 3.5(b)]. This causes a reduction in the barriers at the interfaces for both the electrons and the holes and an increase in the bandgap inside the GaAs region. At some critical thickness, the barrier for the electrons shifts inside the GaAs region which is equivalent to the CBM shifting inside the AlAs region. At this point, the electrons get delocalized inside the AlAs region. But the VBM is still lying inside the GaAs region and the holes are trapped in there because of the confinenemt potential. Thus the structure changes to a type-II alignment of band extrema [Fig. 3.5(c)]. The fact that the change occurs in conduction band and not in the valence band is contributed by two factors. First one is that the band offset is larger for VBM than for CBM. Secondly, the holes are heavier with a larger effective mass than the electrons. This causes the VBM to shift slower than the CBM with confinement. The mechanism of gradual transition from type-I to type-II structure is shown in Figure

3.5. Our obejective is to investigate whether this transition from the type-I to type-II structure takes place abruptly or it happens gradually over few monolayers.

3.0.2 Methodology

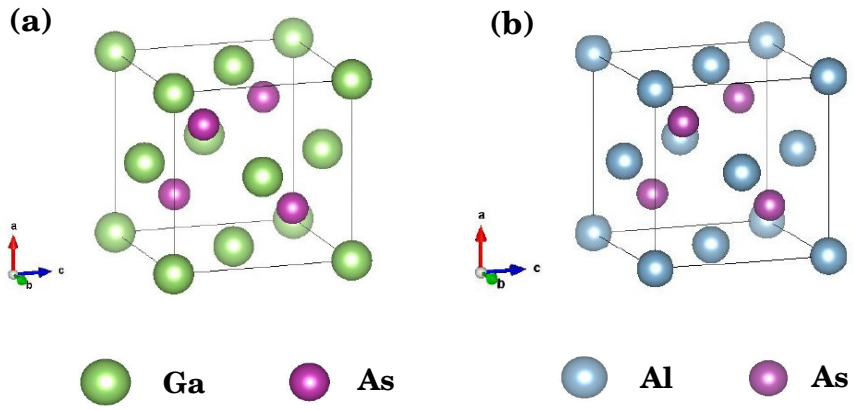

Figure 3.6: Convention cubic cell of (a) bulk GaAs and (b) bulk AlAs.

Both bulk GaAs and bulk AlAs are III-V semiconductors with fcc zinc blende crystal structure. The conventional cells are cubic and are shown in Figure 4.1. The lattice parameters are a = b = c = 4.00 Å. The anions coordinate themselves around each of the cations in a tetrahedral structure.

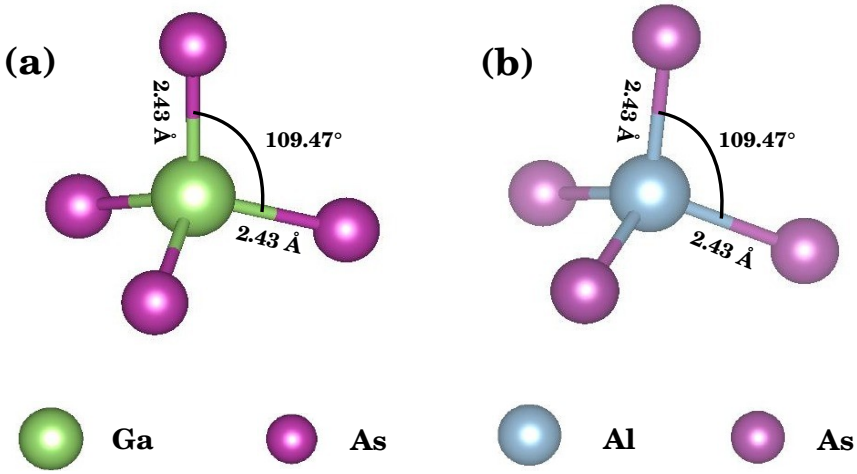

Figure 3.7: Tetrahedral coordination of anions around each cation in (a) bulk GaAs and (b) bulk AlAs

One such tetrahedron for each of the materials is shown in Figure 3.7 with the bondlengths and bond angles indicated. We can see from Figure 3.7 that the bondlengths and the bond angles are the same for both the materials. Hence the heterostructure comprised of these two compounds is lattice matched.

To construct the heterostructure supercells, we grow the conventional cell along any of the lattice vectors, and then sandwich the GaAs layers between AlAs layers on both sides. The conventional cubic cell for an fcc structure of GaAs or that of AlAs contains 4 cations and 4 anions. To reduce the cost for the calculations, we constructed new unit cells with dimension $\frac{a}{\sqrt{2}} \times \frac{a}{\sqrt{2}}$ in the ab-plane. a is the lattice constant of the conventional cubic cell in the ab-plane. The lattice vectors of this new unit cell are given as

$$\vec{a'} = \frac{a}{2}\hat{x} + \frac{a}{2}\hat{y} \tag{3.4}$$

$$\vec{b'} = -\frac{a}{2}\hat{x} + \frac{a}{2}\hat{y} \tag{3.5}$$

This new unit cell contains 2 cations and 2 anions. Hence along $\vec{c}$, one monolayer contains 1 cation and 1 anion. That would mean if we grow the unit cell along $\vec{c}$ to build a supercell, the number of monolyers along $\vec{c}$ is the same as the number of cations or the number of anions in the supercell. This would greatly lessen the computational burden and associated cost, at the same time maintaining the freedom to enlarge the supercell along $\vec{c}$.

Heterostructure supercells $(AlAs)_m/(GaAs)_n$

Number of AlAs layers m	Number of GaAs layers n	(m+n)
48	48	96
54	42	96
64	32	96
73	23	96
81	15	96
85	11	96
86	10	96
87	9	96
88	8	96
89	7	96

Table 3.1: Different heterostructure supercells constructed for the purpose of calculation by varying the number of GaAs layers

To form a heterostructure, we sandwiched GaAs layers between AlAs regions on both sides. We kept changing the number of GaAs layers in steps towards smaller values to increase the degree of confinement of electrons and holes inside the GaAs region. This gave us a numbe of supercells. But the total number of monolayers was kept constant

at 96 by ensuring that m+n=96, where m is the number of AlAs layers and n is the number of GaAs layers. All the supercells for the heterostructure, that we constructed by varying the number of GaAs layers, have been listed in [Table 3.1]. We could have kept the number of AlAs layers fixed and vary the number of GaAs layers. That would lead to the total number of layers to change. We kept the total number of layers fixed because it would facilitate our calculation of spectral weights, where we would need to employ the relations between the reciprocal lattice vectors of the supercell and the reciprocal lattice vectors of the primitive cell. Keeping the size of the supercell the same by keeping the number of layers fixed offered us the advantage of running the same code for each of the structures without requiring to change the parameters. If we allowed the total number of layers in SC to change, we would have to adjust the parameters accordingly each time. This is because the varying length of the SC reciprocal vector along $\vec{c}$ would cause the relations between the SC and PC reciprocal vectors change from one supercell structure to another. Moreover, in pursuit of tracing the effect of confinement on the localization of electrons and holes, we plotted the planar averaged charge densities along the direction of growth with changing confinement. With the length of the supercell kept fixed along the direction of confinement, the charge density plots would look better and easy to compare among various structures.

The ground state energies were calculated within a plane-wave implementation of density functional theory in Vienna Ab-initio Simulation Package (VASP) [53] using projector augmented wave (PAW) [55, 56] potentials. The lattice parameters were kept fixed while the internal positions were optimized till an energy convergence of 10^{-5} eV and force convergence of 5 meV/A have been achieved. For all relaxation calculations of the bulks as well as the heterostructures, we have used the local density approximation (LDA) for the exchange correlation functional. A Γ centred mesh of 4x4x1 k-points has been used for relaxing all the heterostructure supercells. A cutoff energy of 241.0 eV has been chosen for the plane wave basis. Since LDA underestimates the bandgap, we used MBJLDA (Modified Becke Johnson potential) for calculating the bandstructures of bulk materials. MBJLDA gives bandgaps with accuracies equivalent to the bandgaps generated using hybrid functionals or GW methods, but with less computational cost. This was particularly important for more accurate determination of valence band offset. With MBJLDA, however, we don't relax the structures.

In our study, where we are working with heterostructure supercells (SC) involving two different species of cations, it is impossible to construct the primitive cell (PC). As a consequence, electronic structure for the primitive cell is not available and we have to

work with the supercells. The E versus k picture corresponding to the PC can be restored from the SC bandstructure using band unfolding techniques [5–9].

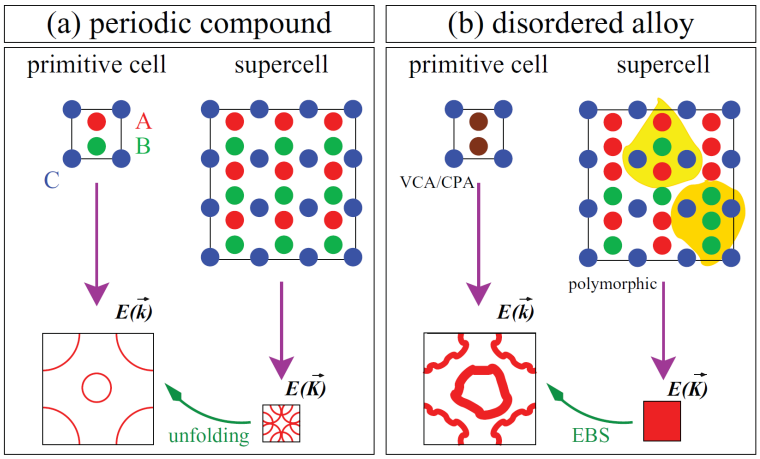

Figure 3.8: Two-dimensional representation of (a) a simple unfolding of bands for a periodic fictitious system ABC and (b) the analogy with periodic systems when treating an alloy $A_{1-x}B_xC$ by effective medium and polymorphic model approaches. Reproduced from [30]

For a fictitious 2D system ABC, the concept has been presented in Figure 3.8(a) and Figure 3.8(b). The reciprocal space can be defined either in terms of PC wave vectors ($\vec{k}$) or the SC wave vectors ($\vec{K}$). The primitive cell energy dispersion $E(\vec{k})$ can be recovered from a supercell energy dispersion $E(\vec{K})$ calculation, to gain meaningful insight into the primitive cell bandstructre and to find a one-to-one mapping between the SC and PC bandstructures, using the unfolding technique.

Determination of the effective band structure (EBS) of the primitive cell requires the evaluation of spectral weights of a large number [16] of SC eigenstates. A spectral function needs to be defined out of the data. The popular choice of basis for this purpose are localized [12, 14, 15] or plane-waves [13, 17]. Aided by a k-unfolding algorithm [14], the spectral decomposition would generate the EBS for the PC.

A primitive wave vector $\vec{k}$ folds onto a supercell wave vector $\vec{K}$ [Fig.3.9(b)] by translation through a reciprocal lattice vector $\vec{G}_0$ as

$$\vec{K} = \vec{k} - \vec{G}_0 \tag{3.6}$$

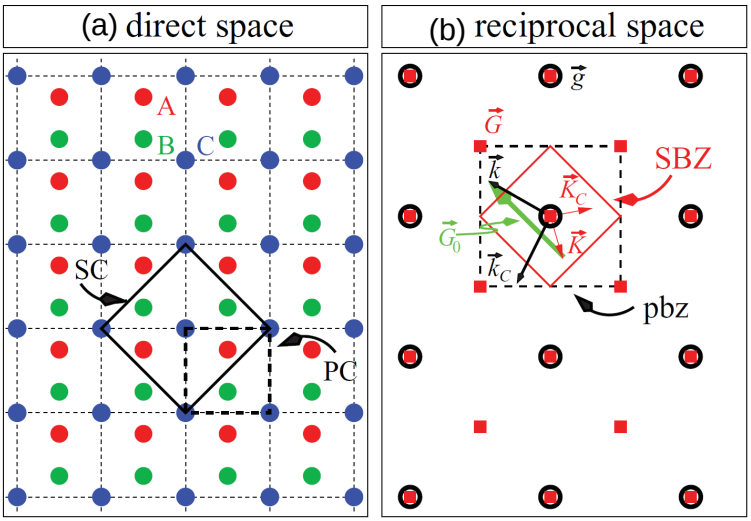

Figure 3.9: The connection between the two representations of a primitive cell (PC) and a supercell (SC) in (c) direct space and (d) reciprocal space. The PC and SC are related by a transformation similar to Eq. (1). The corresponding primitive (pbz) and supercell (SBZ) Brillouin zones, their associated wave vectors $\vec{k}(\vec{K})$ and translation vectors $\vec{g}(\vec{G})$ as well as folding (unfolding) relations are also illustrated. In panel (d), $\vec{k}_C$ and $\vec{K}_C$ are wave vectors equivalent to $\vec{k}$ and $\vec{K}$ by a symmetry operation C of both pbz and SBZ. Reproduced from [30]

On the other hand, a supercell wave vector $\vec{K}$ unfolds into primitive wave vectors $\vec{k}_i$ as

$$\vec{k}_i = \vec{K} + \vec{G}_i, i = 1, 2, ...N_{\vec{K}} \tag{3.7}$$

For a given $\vec{k}$, the pair ($\vec{K}$,$\vec{G}_0$) is unique in Eqn. 3.6. This means that a given wave vector $\vec{k} \in pbz$ folds onto a definite wave vector $\vec{K} \in SBZ$, where pbz stands for primitive cell Brillouin zone and SBZ stands for supercell Brillouin zone. In Eqn. 3.7, however, for a given wave vector $\vec{K}$, a number $N_{\vec{K}}$ of different $(\vec{k}_i, \vec{G}_i)$ pairs can exist. This implies that the wave vector $\vec{K}$ can unfold into a number $N_{\vec{K}}$ of different wave vectors $\vec{k}_i \in pbz$.

$$N_{\vec{K}} = det\underline{M} \tag{3.8}$$

In Figure3.9(b), the latter case has been illustrated for the 2D model system. In this case $\vec{K}$ unfolds into $\vec{k}_1 = \vec{K}(\vec{G}_1 \equiv \vec{0})$ and $\vec{k}_2 = \vec{k}(\vec{G}_2 \equiv \vec{G}_0)$ $[N_{\vec{K}} = 2]$.

As consequence of the above, any SC eigenvector $|\vec{K}m\rangle$ (m is the band index) can be expressed as a linear combination of PC eigenvectors $|\vec{k}_i n\rangle$ $(i = 1, 2, ...N_{\vec{K}}$ and n is the

band index) [13, 18].

$$|\vec{K}m\rangle = \sum_{i=1}^{N_{\vec{K}}} \sum_{n} F(\vec{k_i}, n; \vec{K}, m)|\vec{k_i}n\rangle \tag{3.9}$$

Using the unfolding procedure, we recover from the calculation of SC banstructure, either (i) the PC eigenvectors $|\vec{k_i}n\rangle$ and their weight in the SC eigenstates $|\vec{K}m\rangle$, or (ii) the $E(\vec{k})$ picture of the PC from the $E(\vec{K})$ dispersion of the SC.

A quantity spectral weight [12, 13] can be defined as

$$P_{\vec{K}m}(\vec{k_i}) = \sum_{n} |\langle \vec{K}m|\vec{k_i}n\rangle|^2 \tag{3.10}$$

The interpretation of **spectral weight** is the probability for a set of PC states $|\vec{k_i}n\rangle$ folding onto the SC state $|\vec{K}m\rangle$. In other words, it is the degree in which $|\vec{k_i}n\rangle$ is present in $|\vec{K}m\rangle$ at the same energy $E_n = E_m$ [12, 13]. A spectral function (SF) of continuous variable E can be defined as

$$A(\vec{k_i}, E) = \sum_{m} P_{\vec{K}m}(\vec{k_i})\delta(E_m - E) \tag{3.11}$$

The study of quantum wells and/or a superlattice systems A_n/B_m, where A and B are zinc-blende III-V materials [19, 20], are performed using supercell structures. The corresponding electronic bandstructure $E(\vec{K})$ can be directly calculated. In our present discussion we have $(AlAs)_m/(GaAs)_n$ $[m + n = 96]$. It is indeed difficult to construct the PC of such a heterostructure and to get the corresponding band dispersion $E(\vec{k})$. The symmetry of the SC is different from that of the PC causing the bulk states $|\vec{k_i}n\rangle$ to have different representations in the SC. They also couple between themselves. So more than one bulk states may fold onto a given SC state.

Though both GaAs and AlAs contituting the heterostructure supercells are ordered compounds, the spectral weights in [Eqn. 3.10] may not be integer values. Instead, $P_{\vec{K}m}(\vec{k_i})$ may have nonzero values for different $\vec{k_i}$ wave vectors at the same energy E_m, implying that a given SC state $|\vec{K}m\rangle$ has contributions from several PC wave vectors $\vec{k_i}$ at the same energy. An SF analysis will determine which of the PC eigenstates $|\vec{k_i}n\rangle$ contribute to a given SC state and also calculate the amount of each such PC states present in the SC state under discussion. This way the SF decomposition facilitates the analysis of the SC bandstructure in the Brillouin zone of the underlying PC.

As a part of this project, we developed a Fortran code which is based on the concept of folding-unfolding of states as discussed above for our heterostructure supercells of $(AlAs)_m/(GaAs)_n$ $[m + n = 96]$. It aptly calculates the contributions of all the bulk states that fold onto the conduction band minimum and the valence band maximum at high-symmetry point Γ of the heterostructure SC. The aim is to get an estimate of how the probability for the direct transition at Γ of the supercell BZ is affected by change in the confinement of electrons and holes in the GaAs well region.

In [20], it has been explicitly derived that in a plane wave basis that we have used for our calculations, the spectral weight [Eqn. 3.10], which quantitatively measures the amount of PC character $|\vec{k_0}\rangle$ present in the SC eigenvector $|\vec{K}m\rangle$, can be expressed as

$$P_{\vec{K}m}(\vec{k_0}) = \sum_{\vec{g}} |C_{\vec{K}m}(\vec{g} + \vec{k_0} - \vec{K})|^2 \tag{3.12}$$

The sum in [Eqn. 3.12] is over all PC reciprocal lattice vectors $\vec{g}$. $C_{\vec{K}m}$'s are expansion coeffiecients of the SC state $|\vec{K}m\rangle$ in plane wave expansion,

$$|\vec{K}m\rangle = \left[\sum_{\vec{G}} C_{\vec{K}m}(\vec{G}) e^{i\vec{G}\cdot\vec{r}}\right] e^{i\vec{K}\cdot\vec{r}}, \vec{K} \in SBZ \tag{3.13}$$

where $\vec{G}$'s are the reciprocal lattice vectors of the SC.

From [Eqn. 3.12], it is clear that only those expansion coefficients in [Eqn. 3.13] will contribute to the spectral weight that are associated with the SC reciprocal lattice vectors $\vec{G}$'s satisfying the relation

$$\vec{G} = \vec{g} + \vec{k_0} - \vec{K} \tag{3.14}$$

Since we are using VASP for all our calculations, all the information regarding each of the eigenfunctions and their expansion coefficents are available in the output file WAVECAR. But WAVECAR is written in machine level language. Using the open source software WaveTrans to convert WAVECAR into a human readable format [21], we could extract the expansion coefficients of all the SC eigenstates. The human readable file lists all the expansion coefficients and the associated reciprocal lattice vectors for each of the SC eigenstates. Our code reads the coeffiencts and the associated reciprocal lattice vectors $\vec{G}$ and runs a checking for the fulfillment of the condition [Eqn. 3.14]. Only those coefficients that satisfy the test are added up to get the spectral weight in [Eqn. 3.12].

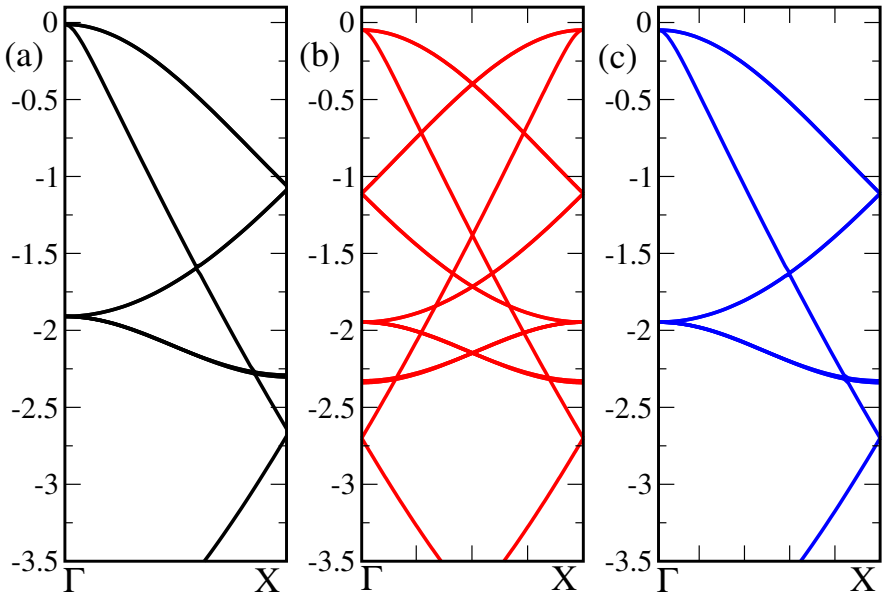

Figure 3.10: a)Ab-initio bandstructure along the Γ to X direction for the conventional cubic cell of CdSe with zinc blende structure. b) The supercell bandstructure along Γ to X direction c) The unfolded bandstructure of the 1x2x1 supercell of CdSe along Γ to X direction with the spectral weights proportional to band thickness

To verify the accuracy and efficiency of the code, we first tested it on a purely periodic system. We took conventional cubic cell of zinc blende CdSe structure as my primitive cell. Bandstructure was calculated for this PC along Γ to X direction. This is shown in Figure 3.10(a). We then generated a supercell out of this PC by doubling it along $\hat{y}$. We calculated the bandstructure of this SC along the primitive cell Γ to X direction, which has been shown in Figure 3.10(b). The bandstructure of the PC recovered from the SC bandstructure using the method described above is shown in Figure 3.10(c).

3.0.3 Results and Discussion

The bandstructures for the bulk materials constituting the heterostructure have been calculated using the MBJLDA potential. MBJLDA gives better estimate for the bandgaps and at the same time is less expensive than the hybrid functionals or the GW method. The resulting bandstructures have been plotted in Figure 3.11. From Figure 3.11(a), we see that bulk GaAs has a direct bandgap of 1.5 eV. The bandgap is close to the experimentally found bandgap of 1.42 eV. The CBM and VBM both lie at Γ for GaAs. On the other hand, bulk AlAs is found to have an indirect bandgap in its electronic structure and the bandgap is 2 eV. The experimentally found bandgap for AlAs is 2.12 eV. The VBM for

AlAs lies at Γ while the CBM lies at X-point. VBM of both the materials are seen to have a threefold degeneracy.

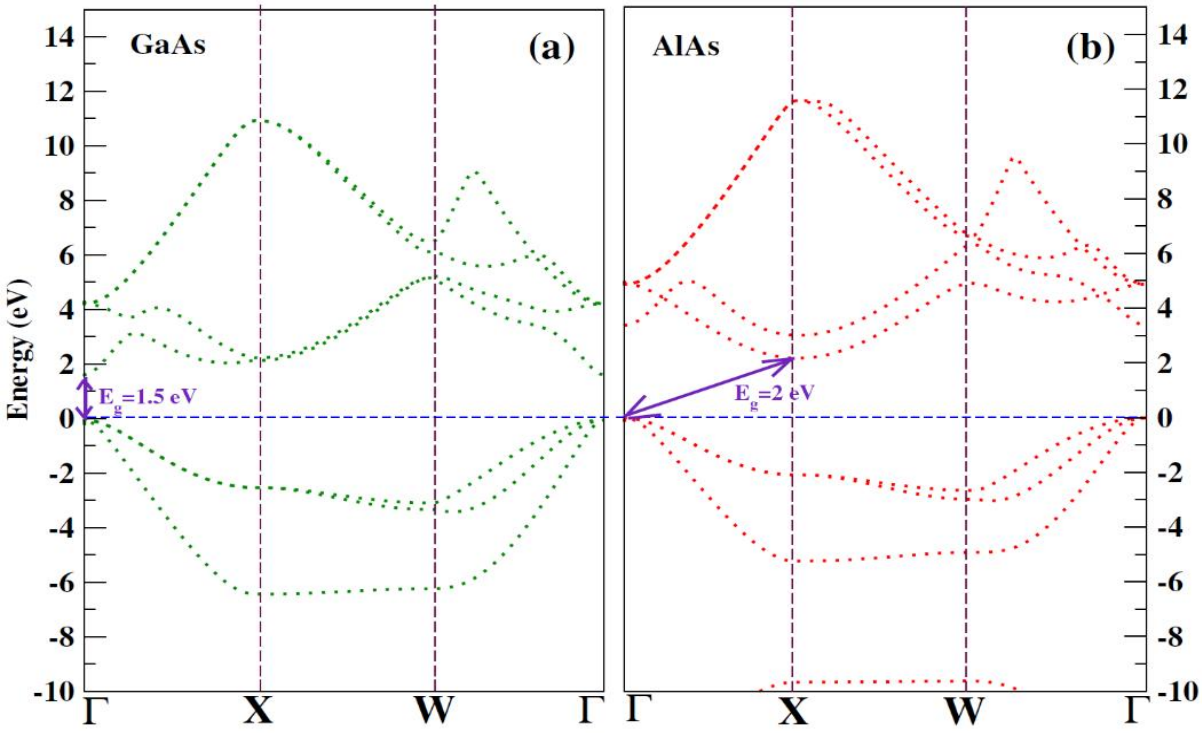

Figure 3.11: Bandstructures of (a) bulk GaAs and (b) bulk AlAs. Both have been calculated with MBJLDA potentials for better estimate of the bandgaps.

When two constituent materials are brought together to form a heterostructure, they interact between themselves causing the bandstructures of the two materials align themselves at the interface. This alignment is done to ensure that the Fermi level remains continuous throughout the material. This relative alignment of the energy bands of the two materials at the heterojunction is called band offset. A good estimate of the band offsets will help us determine whether the heterostructure has a type-I or type-II band alignment to start with. Correct estimation of the conduction band offset requires the accurate determination of the bandgaps which is achieved in our calculation by the use of MBJLDA potentials. There have been a lot of efforts, both in experiments and theory, to measure the valence band offset for GaAs/AlAs heterojunctions. The range of values suggest the valence band offset to be centred around 0.45 eV.

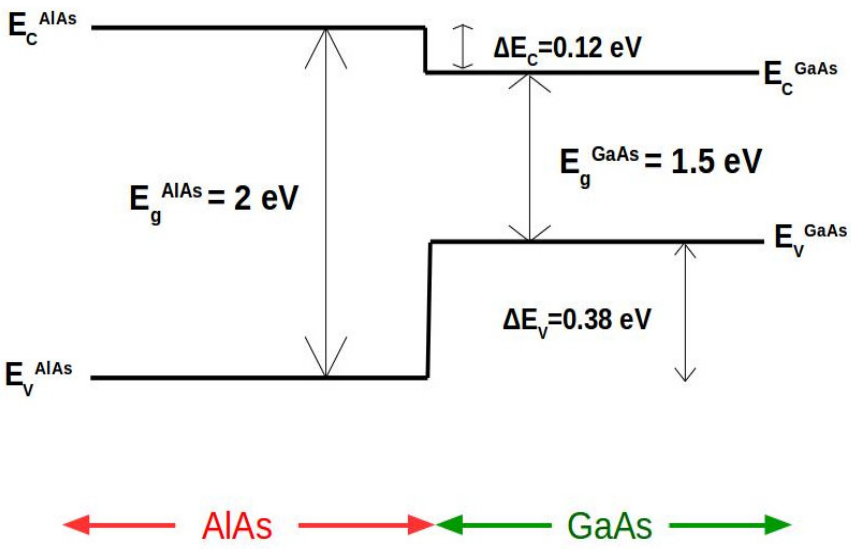

Figure 3.12: Valence band offset and conduction band offset values for GaAs/AlAs heterostructure as calculated using MBJLDA potentials

Figure 3.12 shows the band offsets for GaAs/AlAs heterojunction as have been found from our own calculations. We used the method laid down in [51] to calculate the valence band offset. The relevant formula is given as

$$\Delta E_v(GaAs/AlAs) = \Delta E_{v,C'}^{AlAs} - \Delta E_{v,C}^{GaAs} + \Delta E_{C,C'}^{GaAs/AlAs} \tag{3.15}$$

where

$$\Delta E_{v,C}^{GaAs} = E_v^{GaAs} - E_C^{GaAs} \tag{3.16}$$

is the energy separation from a core level (C) to valence band maximum for bulk GaAs. and

$$\Delta E_{v,C'}^{AlAs} = E_v^{AlAs} - E_{C'}^{AlAs} \tag{3.17}$$

is the energy separation from a core level (C') to valence band maximum for bulk AlAs.

$$\Delta E_{C,C'}^{GaAs/AlAs} = E_{C'}^{AlAs} - E_C^{GaAs} \tag{3.18}$$

gives the difference in the core level energies between GaAs and AlAs at the GaAs/AlAs heterojunction.

We took the electrostatic potential on the As atoms in the bulk as our reference core level energy for both GaAs and AlAs. Our calculation gave $\Delta E_v = 0.38$ and $\Delta E_c = 0.12$ eV [Fig. 3.12].

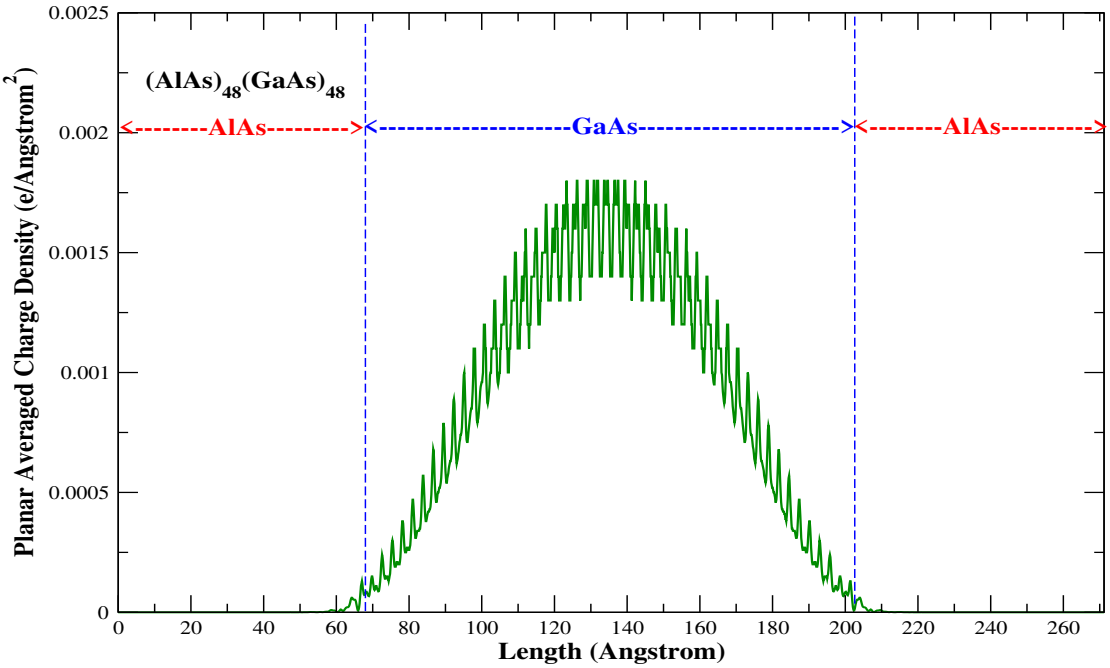

Figure 3.13: Charge densities of electrons occupying the CBM along the growth direction of the heterostructure supercell $(AlAs)_{48}/(GaAs)_{48}$

To examine the variation in the localization of the electron and the hole wavefunctions with increasing confinement, we plotted the planar averaged charge density distributions of the electrons occupying the conduction band minimum and the holes occupying the valence band maximum along the growth direction $\vec{c}$ for all the supercell structures that we considered. From the charge density distribution of CBM electrons for $(AlAs)_{48}$ /$(GaAs)_{48}$ [Fig. 3.13], we see that it is well localized inside the GaAs region. The envelope function is mostly smooth but has a flat shape in the middle region. It almost resembles the ground state wave function of a particle confined inside a one-dimensional box.

Upon looking at the charge densities of the holes occupying the VBM for the same supercell structure [Fig. 3.14], we find similar feature of the envelope function, i.e. the hole wavefunction is also localized inside the GaAs region and the enevelope function of the hole charge density distribution resembles the ground state wavefunction of a particle confined inside a one-dimensional box. This justifies our particle in a box picture to interprete the changes in energy quantization of electrons and holes with confinement.

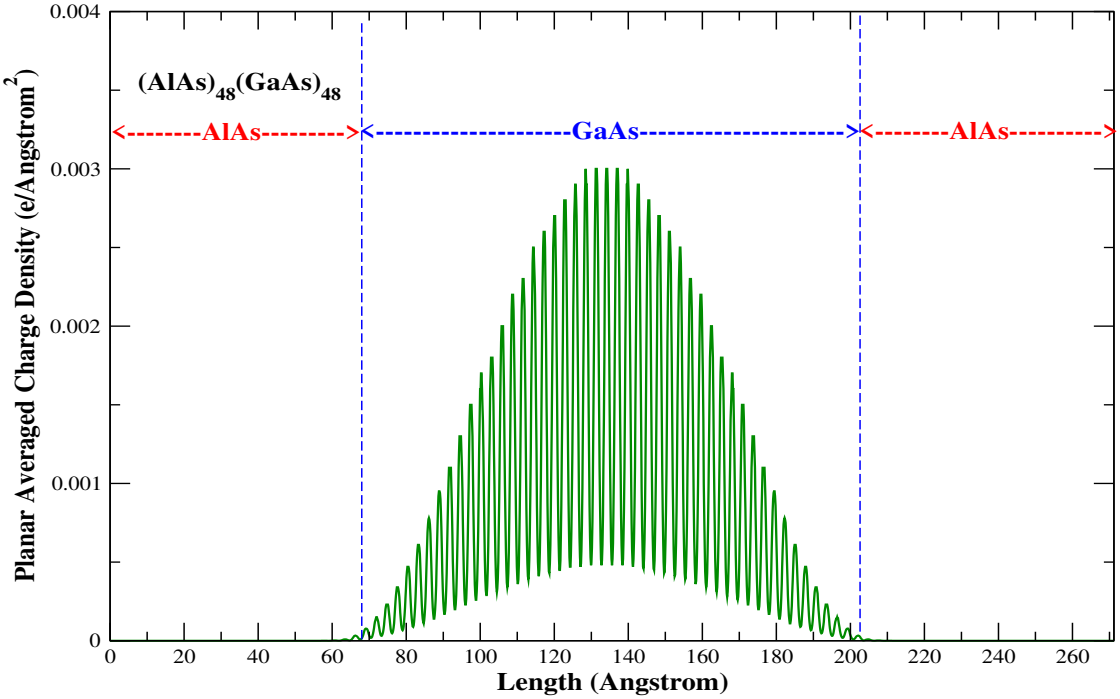

Figure 3.14: Charge densities of electrons occupying the VBM along the growth direction of the heterostructure supercell $(AlAs)_{48}/(GaAs)_{48}$

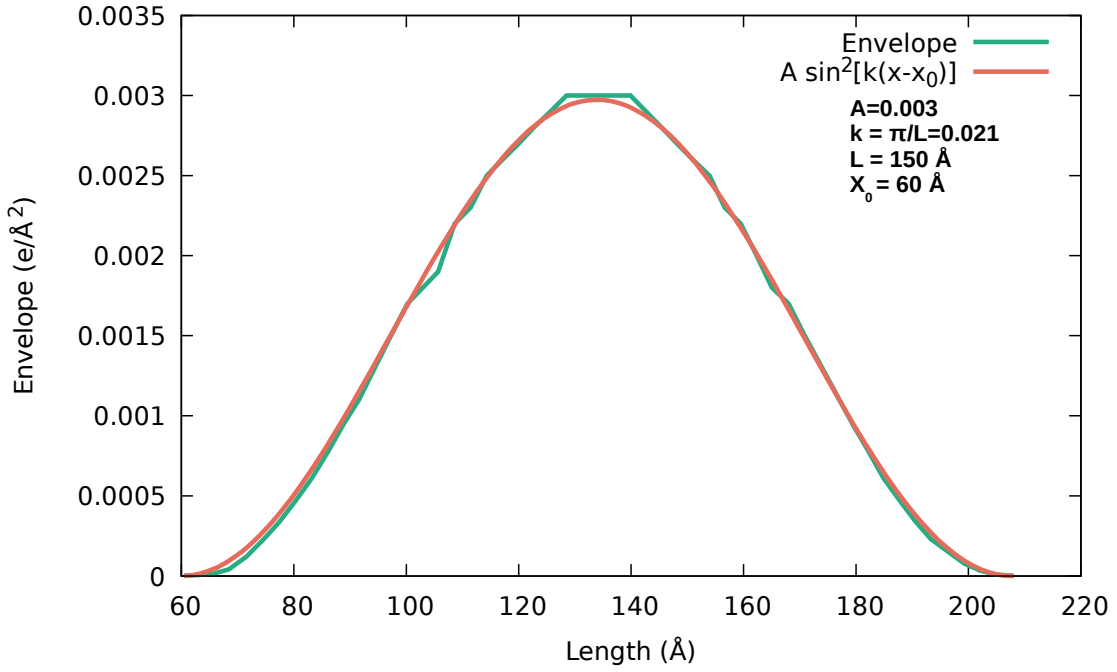

Figure 3.15: Fitting of the envelope of the VBM charge density for the $(AlAs)_{48}/(GaAs)_{48}$ supercell with a $sin^2(x)$ function

We could fit the envelope of the charge density distribution with a $sin^2(kx)$ function [Fig. 3.15]. This shows our particle in a box approximation to be valid. Combining the facts that both the electron and hole wavefunctions are localized inside the GaAs region for $(AlAs)_{48}$ /$(GaAs)_{48}$ structure, we can say that the GaAs region provides a confinement potential for both the electrons and holes. This establishes the type-I nature of the band alignment of the heterostructure for this confinement regime.

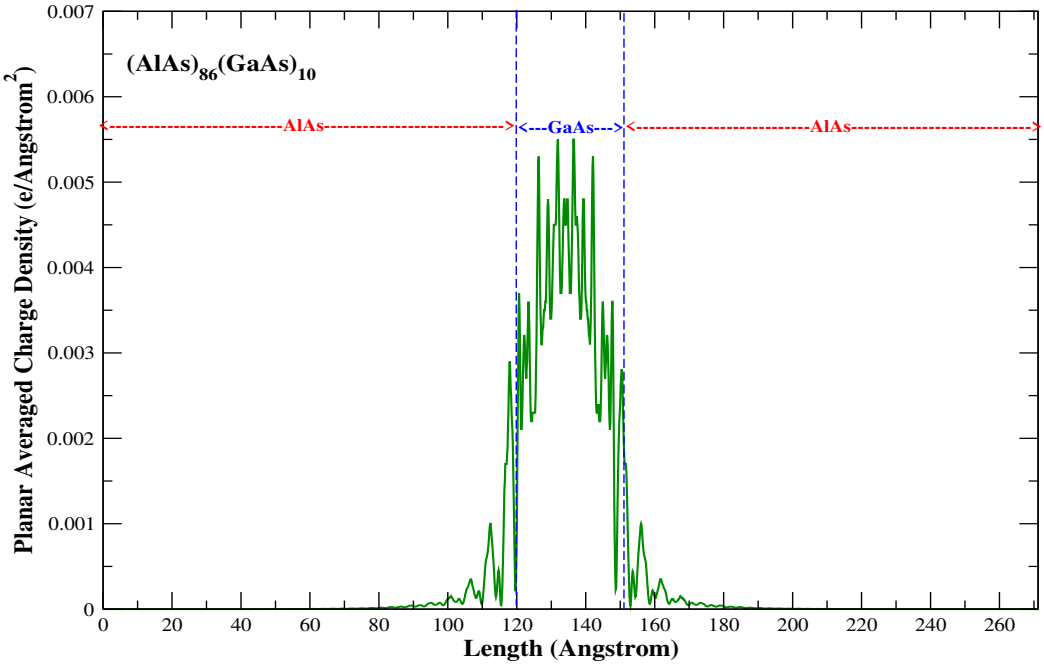

Figure 3.16: Charge densities of electrons occupying the CBM along the growth direction of the heterostructure supercell $(AlAs)_{86}/(GaAs)_{10}$

As we gradually move towards smaller thickness of the GaAs region, we find that the envelope function of the CBM charge distribution starts deviating gradually from the shape of the ground state wave function of a particle in a box. The envelope function starts becoming jagged more and more with increase in the degree confinement inside the GaAs region. If we consider the case of $(AlAs)_{86}$ /$(GaAs)_{10}$ [Fig. 3.16], we find this feature to have manifested quite prominently. The electronic charge density also starts spreading into the AlAs region upon increasing the confinement due to tunnelling through barrier at the interfaces. This can be explained by the fact that with increasing confinement, the depth of the well for the electrons keeps reducing which leads to enhanced tunnelling of electronic wavefunctions through the interfaces and also the deviation of the envelope function from the shape of the ground state wave function of a particle in a box.

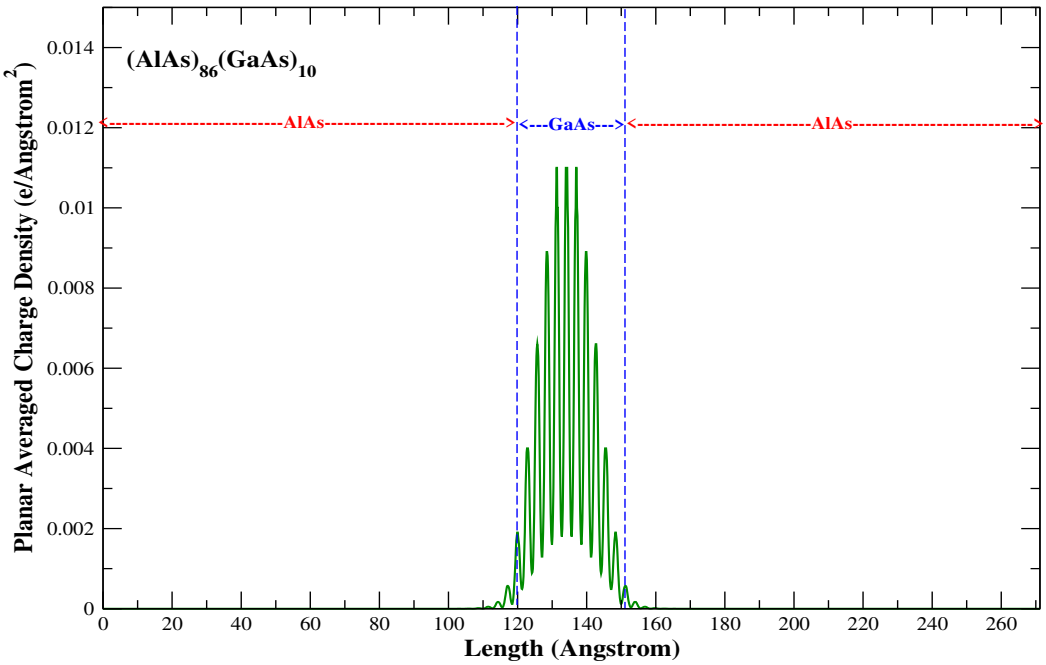

Figure 3.17: Charge densities of electrons occupying the VBM along the growth direction of the heterostructure supercell $(AlAs)_{86}/(GaAs)_{10}$

But if we look at the charge densities of the holes occupying the VBM for the $(AlAs)_{86}$ $/(GaAs)_{10}$ structure [Fig. 3.17], we find the tunnelling of the hole wavefunctions into the AlAs region to be small. The envelope function of the hole charge distribution remains smooth and its resemblance with the ground state wave function of a particle inside a one-dimensional box remains intact. The jaggedness which appears in the electron charge distribution does not appear in the hole charge distribution. These phenomena can be explained by taking into account the fact that the barriers at the interfaces are larger for holes because of the larger band offset for VBM. This tries to prevent the tunnelling of the holes from GaAs into the AlAs region through the interfaces. The hole charge densities remain well localized inside the GaAs part and it retains its semblance with the smooth ground state wavefunction of a particle in a box.

Until 10 GaAs layers, the charge density distribution for the electrons occupying the CBM remain localized inside GaAs region with considerable tunnelling into the AlAs layers. There takes place a sudden transfer of the electronic charge density into the AlAs layers at 9 GaAs layers [Fig. 3.18], i.e. the $(AlAs)_{87}$ $/(GaAs)_9$ structure, which marks a complete delocalization of the electronic wavefunction into the AlAs region. This indicates that between 10 and 9 GaAs layers, there takes place a transition in the alignment of the CBM throughout the heterostructure along the growth direction.

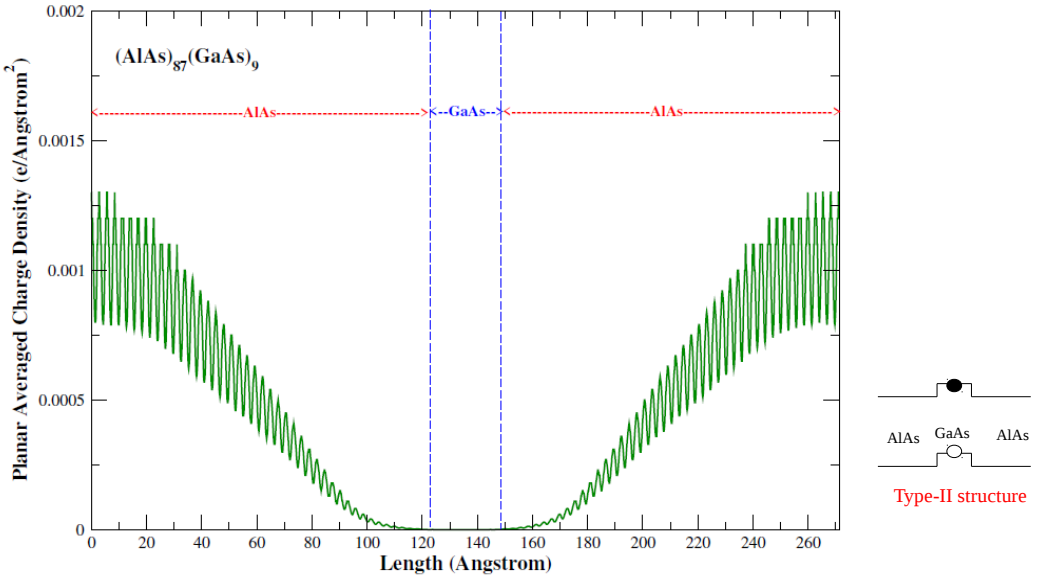

Figure 3.18: Charge densities of electrons occupying the CBM along the growth direction of the heterostructure supercell $(AlAs)_{87}/(GaAs)_9$

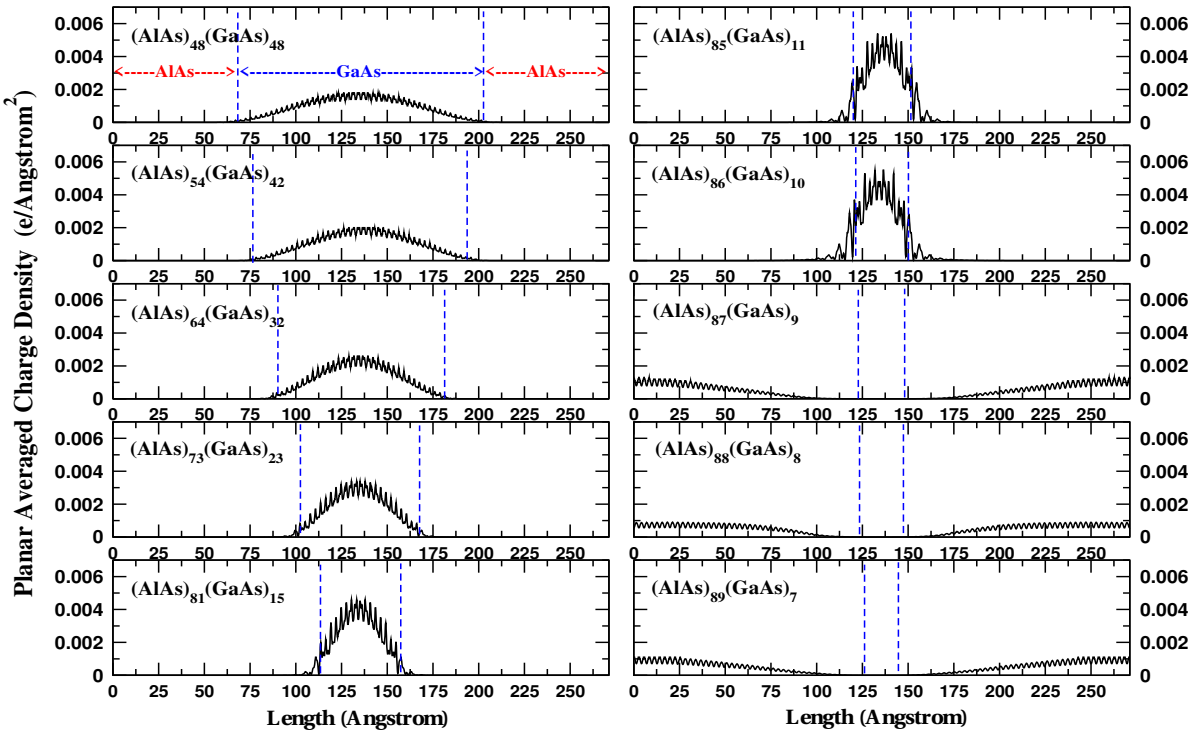

Figure 3.19: Charge densities of electrons occupying the CBM along the growth direction of the heterostructure supercells for various degrees of confinement in the GaAs region

This becomes evident upon looking at the electronic charge densities for all the various supercell structures that we considered [Fig. 3.19]. Upon gradual reduction in the thickness

of the confinement region inside the GaAs part, the depth of the confinement potential for the electrons keeps reducing. This phenomenon can be better understood in terms of our particle in a box model. In this scheme, the confinement potential for the electrons inside the GaAs region has been approximated by a one-dimensional well. A reduction in thickness in the GaAs layers in equivalent to the reduction in the thickness of the well. As a consequence, the ground state energy of the electrons inside the well keeps gradually moving up along the energy axis, leading to the reduction in the depth of the well. At some point, the well gets shifted inside the AlAs region. This occurs when the ground state energy of the electrons inside the GaAs region becomes higher than that indside the AlAs region. The electrons prefer to get trapped inside the AlAs region and this should be marked by a transfer of the electronic charge densities from GaAs to AlAs region. This is what we observe from our results on the electronic charge densities.

Till 10 GaAs layers, the CBM would lie inside the GaAs region, providing the confinement potential for the electrons inside the GaAs region. Equivalently, in our particle in a box model, the well for the electrons is located inside the GaAs region. The electrons are trapped inside the GaAs region and the electronic wavefunction remains localized inside GaAs part till this point. At 9 GaAs layers, the CBM shifts inside the AlAs region. The confinement potential or the well for the electrons is now inside the AlAs layers. As a result, the electrons are now trapped inside the AlAs part and this is reflected in the sudden delocalization of the electronic charge densities from GaAs region into AlAs region.

But if we look at the charge densities of the holes occupying the VBM, we find that there takes place no such transfer of hole charge densities [Fig. 3.20] until 7 GaAs layers. So the alignment of the VBM retains its profile till this point. This striking difference in the case of VBM alignement in contrast to the CBM alignment can be accounted for by noting that the offset for VBM is larger than the offset for CBM. From the electronic and hole charge density profiles, we figure out that until 10 GaAs layers, the confinement potential for the electrons as well as that for the holes remain located inside the GaAs layers. This shows that the heterostructure remains type-I. At 9 GaAs layers, the confinement potential for the electrons is located inside the AlAs region, but the confinement potential for the holes is located inside the GaAs region. As a result, the band alignement is rendered type-II. Hence we can say that a transition from type-I to type-II band alignment is taking place between 10 and 9 GaAs layers and it turns out to be abrupt in nature.

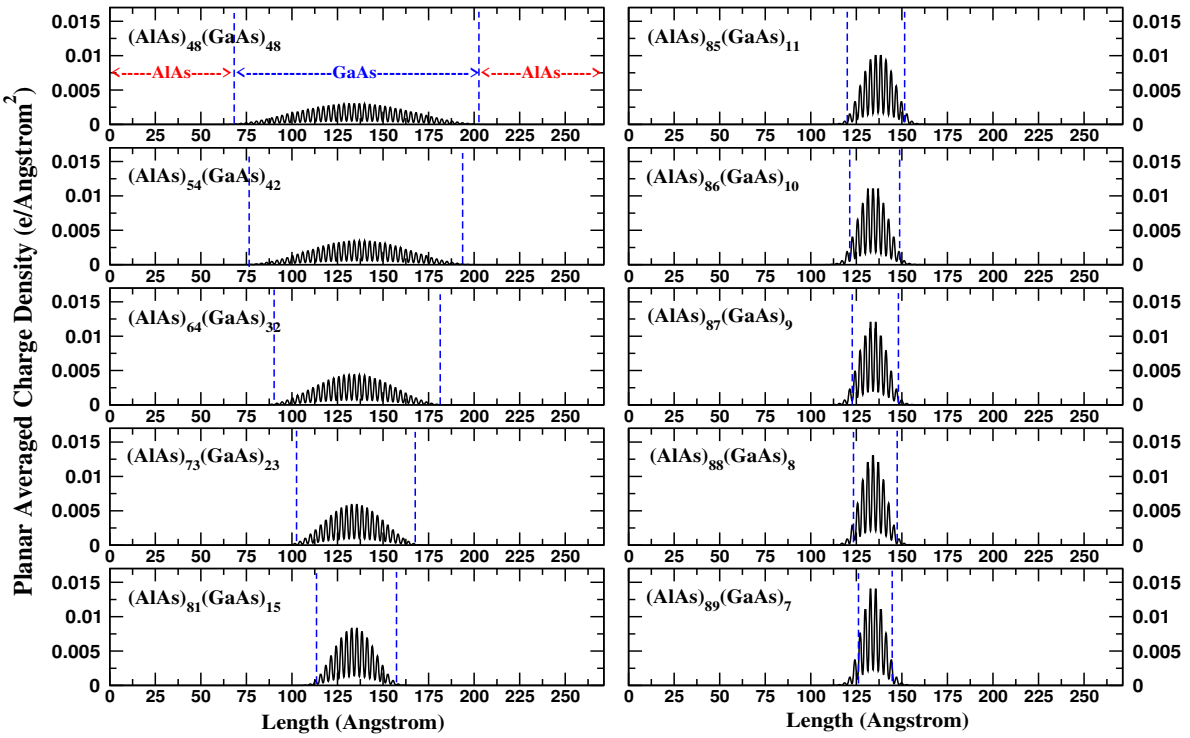

Figure 3.20: Charge density distribution of holes occupying the VBM along the growth direction of the heterostructure supercells for various degrees of confinement in the GaAs region

There is another point worth mentioning here. The fact that upon increasing the degree of confinement, the change in the band alignment occurs in CBM and not in the VBM is not only contributed by the fact that the offset is larger for VBM than CBM. There is another factor at play. It is the effective masses of the respective charge carriers. For GaAs, we see from Figure 3.11, the curvature of the CBM is greater than the curvature of VBM. As a result, from Eqn. 3.2, the effective mass of a CBM electron is smaller than the effective mass of a VBM hole. From literature, we see that the experimentally found values for the effective masses to be 0.067 for the electrons and 0.57 for the heavy holes [46]. Consequently, the electrons in the CBM respond quicker to the change in confinement than the holes in the VBM. From 3.3, we can therefore infer that the ground state energy of the CBM electrons would rise much faster inside the well as compared to the the ground state energy of the holes. This adds to the phenomenon of the change of band alignement, in which the confinement potential shifts from GaAs to AlAs region, occurring in CBM and not in VBM.

Associated with the transition from type-I to type-II band alignment, there should take place a transition from direct to indirect bandgap electronic structure. As long as the electrons remain confined inside the GaAs region in the type-I structure, the heterostruc-

ture should follow the nature of bulk GaAs and remain a direct bandgap material. Upon transition to type-II structure, as the electrons get shifted inside the AlAs region, the bandgap should follow the nature of bulk AlAs and change into indirect. This change from direct to indirect bandgap accompanied with the type-I to type-II transition should get reflected in the transition probability. The transition probability for direct transition should fall to zero upon transition to type-II structure. So we have the opportunity to harness this phenomenon to further confirm the nature of the transition, as to whether it happens abruptly or gradually over few monolayers. Interface scattering causes the electrons to scatter to other states. As a result, an electron with momentum k gets scattered into other states with different momenta. So, CBM and VBM gains contribution from primitive cell k-points other than Γ. This may cause gradual reduction in the optical transition probability in lower thickness regime. Loss due to tunnelling should add to this effect. We should be able to characterize all these phenomena from the variation of the transition probability with confinement. To this end, we plotted the band edge optical transition probability for direct transition between CBM and VBM at Γ of the supercell for varying degrees of confinement [Fig. 3.21].

In spectroscopy, optical transition probability is given by the oscillator strength of the associated transition. Oscillator strength is a dimensionless quantity and it presents the probability of absorption or emission of radiation while making a transition between two energy levels of an atom or molecule [22, 23]. The physical significance of oscillator strength can be cast in terms of a single electron oscillator. When the oscillator has the same frequency as the transition [24], the oscillator strength gives the ratio between the quantum mechanical transition rate and the classical rate of absorption or emission. Let us assume an atom or molecule undergoing a transition from a lower quantum state $|1\rangle$ to an upper quantum state $|2\rangle$ as a result of absorbing a photon.

The associated oscillator strength f_{12} is given by

$$f_{12} = \frac{2}{3}\frac{m_e}{\hbar^2}(E_2 - E_1) \sum_{\alpha=x,y,z} |\langle 1m_1|R_\alpha|2m_2\rangle|^2 \tag{3.19}$$

where m_e is the electronic mass and $\hbar$ is reduced Planck constant. Is has been assumed that the quantum states $|n\rangle, n = 1, 2$ have multiple degenerate sub-states denoted by m_n.

The operator R_x represents the sum of the x-coordinates $r_{i,x}$ of all the electrons in the system.

$$R_\alpha = \sum_{i=1}^{N} r_{i,\alpha} \tag{3.20}$$

We calculated the probability of direct transition between CBM and VBM at Γ of the Brillouin zones of the heterostructure supercells by enumerating the oscillator strengths of the associated transitions using an facility implemented within VASP. We computed the transition probabilities for optical transitions between CBM and VBM at Γ for all the different heterostructure supercells that we considered. We plotted the values against the number of GaAs layers in Figure 3.21.

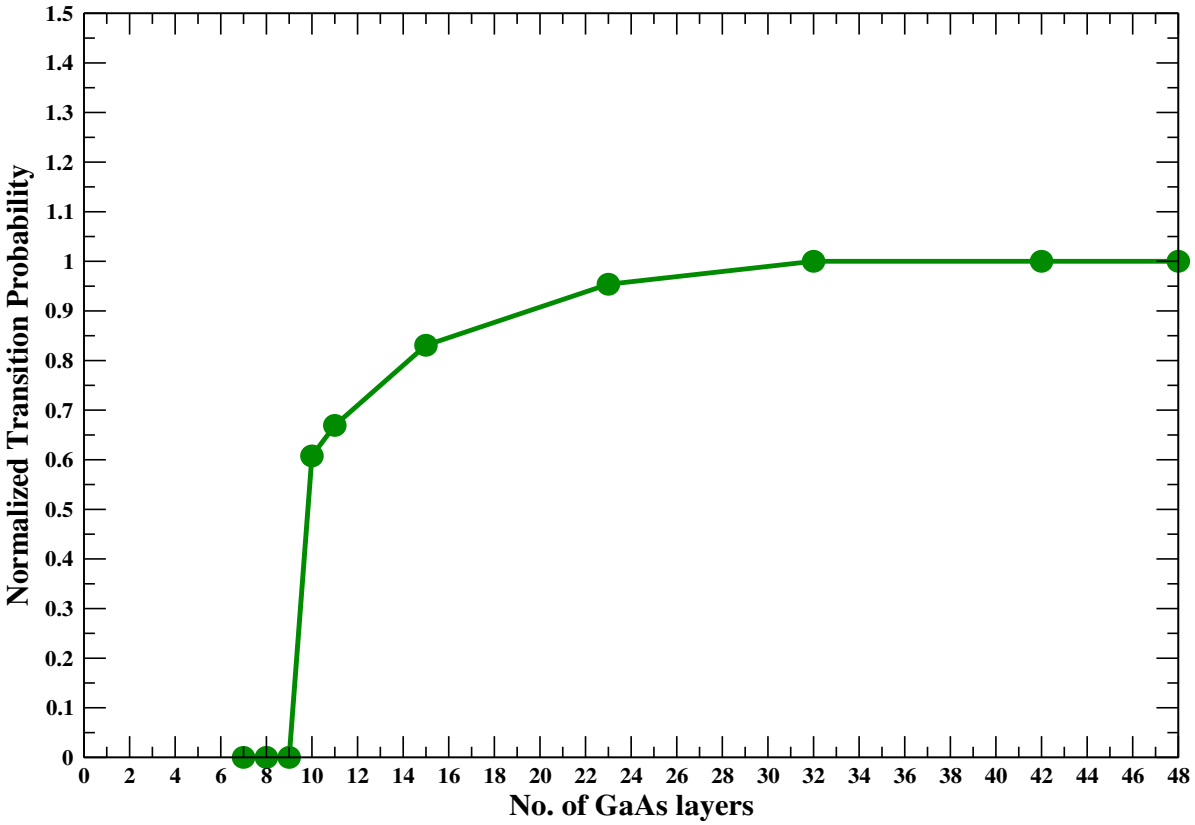

Figure 3.21: Variation of the Normalized Transition Probability for optical transition between CBM and VBM of the heterostructure supercells as a function of the number of GaAs layers

In Figure 3.21, all the values of the transition probabilities have been normalized with respect to its value at $(AlAs)_{48}/(GaAs)_{48}$. We see that the probability for direct transition at Γ for $(AlAs)_{48}/(GaAs)_{48}$ structure almost sustains its value until $(AlAs)_{64}/(GaAs)_{32}$ supercell. Starting from $(AlAs)_{64}/(GaAs)_{32}$ onwards, the value of the transition probability starts falling gradually. This gradual fall continues to happen untill $(AlAs)_{86}/(GaAs)_{10}$. The gradual fall in the transition probability can be accounted for by the interface scattering and tunnelling of the charge carriers into the AlAs region, both of which increase upon narrowing down the confinement potential.

We see that the normalized transition probability falls sharply from some finite value at 10 GaAs layers to zero at 9 GaAs layers. We can interprete the result by contemplating upon our charge density results. Our charge density results showed that till 10 GaAs layers, the heterostructure has a type-I band alignment. Until this point, the electrons remain localized inside the GaAs region. As bulk GaAs is direct bandgap, the transition probability for direct transition is appreciable. At 9 GaAs layers, the electrons get delocalized inside the AlAs region. The structure changes to type-II. As bulk AlAs has an indirect bandgap, the bandstructure changes sharply from direct to indirect. Consequently, the transition probability for direct transition drops sharply to zero. Hence the sudden fall in the transition probability reflects the abrupt nature of the transition from type-I to type-II structure. This is in conformity with our charge density results and hence further strengthens our conclusion.

When we build a supercell out of a primitive cell, several points of the Brillouin zone of the primitive cell get folded onto the Brillouin zone of the supercell, because the BZ of the supercell is smaller in size. Here we build up the heterostructure supercell, starting from the fcc primitive cell of GaAs. If the supercell was pure bulk GaAs, the CBM and VBM would be purely derived from the CBM and VBM characters of bulk GaAs and hence they would possess Γ character alone. But we made heterostructures out of bulk GaAs and bulk AlAs. The CBM and VBM of the supercell will no longer be contributed solely by the bulk GaAs characters. Hence the CBM and VBM of the supercell won't be purely Γ derived. Due to mixing of species and scattering at the interfaces, the CBM and VBM of the supercell will have contributions from a number of other primitive characters. Upon transition to type-II structure, the bandgap becomes indirect. This should lead to total loss of Γ character in the CBM. If we could trace all these changes in the CBM and VBM characters, we should be able to combine them to accurately interprete the variation in the optical transition probabilities. An estimation of the spectral weights for the various primitive characters present in the CBM and VBM of the supercell would help us. It would further elucidate the underlying physical mechanism of the transition and the associated changes in the characters of the eigenstates.

We wrote a code of our own to accomplish this job. The process of buliding up the heterostructure supercells out of the fcc primitive cell has been described in detail in the methodology section. In the beginning, we took the conventional cubic cell and made the $\frac{a}{\sqrt{2}} \times \frac{a}{\sqrt{2}}$ cell out of it. A folding of the BZ has happened associated with this transformation. Let us label the reciprocal lattice vectors of the $\frac{a}{\sqrt{2}} \times \frac{a}{\sqrt{2}}$ cell by $\vec{G_1'}, \vec{G_2'}, \vec{G_3'}$. Further we built the heterostructure supercell by growing the $\frac{a}{\sqrt{2}} \times \frac{a}{\sqrt{2}}$ cell along lattice vector $\vec{c}$. Let us label the reciprocal lattice vectors of the supercell by $\vec{G_1}, \vec{G_2}, \vec{G_3}$. As a

result, multiple states along reciprocal lattice vector $\vec{G_3'}$, which corresponds to $\vec{c}$, will fold onto the Γ of the SC. The number of such states will depend on the relative lengths of $\vec{G_3'}$ and $\vec{G_3}$ which are along the direction corresponding to $\vec{c}$. Our heterostructure supercells have a length along $\vec{c}$ that is 48 times as large as the length of the $\frac{a}{\sqrt{2}} \times \frac{a}{\sqrt{2}}$ cell in the same direction. Hence, in the reciprocal space, SC reciprocal lattice vector $\vec{G_3}$ should be $\frac{1}{48}$ times the length of $\vec{G_3'}$. It becomes evident that there are 48 wave vectors along $\vec{G_3'}$ that will fold onto Γ-point of the BZ of SC, and there are similar wave vectors along $-\vec{G_3'}$ that will fold onto Γ-point of the BZ of SC. We went on to calculate the spectral weights of the PC characters corresponding to these points that fold onto the CBM and VBM of SC at Γ. Our code for calculating the spectral weights carried out this job accurately. The underlying principle has been discussed in the methodology section. The spectral weights calculated in this way have been tabulated in Table 3.2 and Table 3.3 for various choices of supercells that we considered in the our calculation.

Reciprocal points $(n_1, n_2, n_3) \equiv n_1\vec{g_1} + n_2\vec{g_2} + n_3\vec{g_3}$	**Heterostructure Supercells**								
	$(AlAs)_{48}$ $(GaAs)_{48}$	$(AlAs)_{64}$ $(GaAs)_{32}$	$(AlAs)_{73}$ $(GaAs)_{23}$	$(AlAs)_{81}$ $(GaAs)_{15}$	$(AlAs)_{85}$ $(GaAs)_{11}$	$(AlAs)_{86}$ $(GaAs)_{10}$	$(AlAs)_{87}$ $(GaAs)_{9}$	$(AlAs)_{88}$ $(GaAs)_{8}$	$(AlAs)_{89}$ $(GaAs)_{7}$
$(\frac{1}{2}, \frac{1}{2}, 0)$							0.71	0.79	0.77
$(\frac{47}{96}, \frac{47}{96}, 0)$							0.14		0.11
$(\frac{2}{96}, \frac{2}{96}, 0)$			0.12	0.12	0.10				
$(\frac{1}{96}, \frac{1}{96}, 0)$	0.25	0.24	0.20	0.16	0.13	0.11			
Γ(0, 0, 0)	0.45	0.32	0.24	0.17	0.13	0.12			
$(-\frac{1}{96}, -\frac{1}{96}, 0)$	0.25	0.24	0.20	0.16	0.13	0.11			
$(-\frac{2}{96}, -\frac{2}{96}, 0)$			0.12	0.12	0.10				
$(-\frac{47}{96}, -\frac{47}{96}, 0)$							0.14		0.11

Table 3.2: Spectral decomposition of CBM of SC at Γ in the BZ of PC. $\vec{g_1}, \vec{g_2}, \vec{g_3}$ are reciprocal vectors of the fcc primitive cell

Table 3.2 contains the spectral decomposition of CBM of SC at the Γ-point of the SC BZ in the BZ of the PC. From Table 3.2, we see that the CBM electrons get scattered into various PC states other than Γ. This is supposed to have caused by mixing of species and impurity scattering at the GaAs/AlAs interfaces.

Reciprocal points (n_1, n_2, n_3) $\equiv n_1\vec{g_1} + n_2\vec{g_2} + n_3\vec{g_3}$	**Heterostructure Supercells**								
	$(AlAs)_{48}$ $(GaAs)_{48}$	$(AlAs)_{64}$ $(GaAs)_{32}$	$(AlAs)_{73}$ $(GaAs)_{23}$	$(AlAs)_{81}$ $(GaAs)_{15}$	$(AlAs)_{85}$ $(GaAs)_{11}$	$(AlAs)_{86}$ $(GaAs)_{10}$	$(AlAs)_{87}$ $(GaAs)_{9}$	$(AlAs)_{88}$ $(GaAs)_{8}$	$(AlAs)_{89}$ $(GaAs)_{7}$
$(\frac{1}{2}, \frac{1}{2}, 0)$									
$(\frac{47}{96}, \frac{47}{96}, 0)$									
$(\frac{2}{96}, \frac{2}{96}, 0)$			0.12	0.12	0.11	0.10			
$(\frac{1}{96}, \frac{1}{96}, 0)$	0.25	0.23	0.20	0.15	0.13	0.12	0.11	0.11	0.10
$\Gamma(0, 0, 0)$	0.43	0.30	0.23	0.16	0.14	0.13	0.12	0.11	0.11
$(-\frac{1}{96}, -\frac{1}{96}, 0)$	0.25	0.23	0.20	0.15	0.13	0.12	0.11	0.11	0.10
$(-\frac{2}{96}, -\frac{2}{96}, 0)$			0.12	0.12	0.11	0.10			
$(-\frac{47}{96}, -\frac{47}{96}, 0)$									

Table 3.3: Spectral decomposition of VBM of SC at Γ in the BZ of PC. $\vec{g_1}, \vec{g_2}, \vec{g_3}$ are reciprocal vectors of the fcc primitive cell

We note that the the Γ contribution gradually keeps reducing towards the narrower thickness of the the GaAs region. Its value goes from 0.45 for $(AlAs)_{48}/(GaAs)_{48}$ to 0.32 for $(AlAs)_{64}/(GaAs)_{32}$ to 0.13 for $(AlAs)_{85}/(GaAs)_{11}$. As we narrow down the GaAs region, the interfaces come closer and the effect of impurity scattering increases. As a result, the Γ character in CBM gets smaller. The picture is similar for the VBM [Table 3.3]. The value of the Γ character of PC in the VBM of SC changes from 0.43 for $(AlAs)_{48}/(GaAs)_{48}$ to 0.30 for $(AlAs)_{64}/(GaAs)_{32}$ to 0.14 for for $(AlAs)_{85}/(GaAs)_{11}$. This gradual reduction in the Γ character in the CBM as well as in the VBM leads to the gradual fall in the optical transition probability for direct transition at Γ, as has been observed in Figure 3.21.

The Γ character in the CBM remains finite till 10 GaAs layers, but vanishes completely at 9 GaAs layers. But VBM continues to have finite Γ character till 7 GaAs layers. For the SC, this marks a transition from a direct to indirect bandgap material happening between 10 and 9 GaAs layers. This is consistent with the charge density results. In Figure 3.19, we saw that the CBM charge density remains localized inside the GaAs region until 10 GaAs layers and suddenly gets delocalized into the AlAs region at 9 GaAs layers. Bulk AlAs, having its CBM at X, makes the Γ character vanish. Thus a transition from type-I to type-II should be associated with a transition from direct to indirect bandgap. Due to this sudden transition from direct to indirect gap, the optical transition probability for direct transition at Γ drops drastically to zero at 9 GaAs layers [Fig. 3.21]. So, our spectral decomposition results are consistent with the charge density results and it

explains well the variation of transition probability and thereby establishes the type-I to type-II transition in $(GaAs)_m/(AlAs)_n$ heterostructure as an abrupt occurrence.

3.0.4 Conclusion

In our study on GaAs/AlAs heterostructure, we probed the type-I to type-II transition in this heterostructure in a quest to figure out whether this transition is abrupt or gradual. Our plots on the planar averaged charge densities of CBM electrons and VBM holes clearly pointed out the transition to be an abrupt one occurring between 10 and 9 GaAs layers. The CBM electrons are found to get delocalized from GaAs region into the AlAs region at 9 GaAs layers. Band edge optical transition probability showed sharp fall between 10 and 9 GaAs layers due to the transition from direct to indirect bandgap which accompanies the delocalization of electrons into AlAs region. This further strengthens our conclusion regarding the abrupt nature of the transition. Finally, the spectral decomposition of CBM and VBM of supercells bring forth the detailed physical mechanism of the transition by depicting in elaboration the changes in the CBM and VBM characters. Our results from sprectral decomposition could aptly explain the variation in optical transition probability and are in complete consistency with the charge density results. So, we could conclusively establish that the transition is an abrupt one.

Bibliography

[1] H. Morkoc, S. N. Mohammad. Science **267**, 51-55, 1995

[2] P. S. Zory, (Academic, 1993).

[3] T. Minura, S. Hiyamizu, T. Fujii, K. Nanbu, J. Appl. Phys. **19**, 225-227, 1980

[4] C. Huang, S. Wu, A. M. Sanchez, J. J. P. Peters, R. Beanland, J. S. Ross, P. Rivera;, W. Yao, D. H. Cobden, X. Xu. Nature Mater. **13**, 1096-1011, 2014

[5] Y. Gong, J. Lin, X. Wang, G. Shi, S. Lei, Z. Lin, X. Zou, G. Ye, R. Vajtai, B. I. Yakobson, H. Terrones, M. Terrones, B. K. Tay, J. Lou, S. T. Pantelides, Z. Liu, W. Zhou, P. M. Ajayan, Nature Mater. **13**, 1135-1142, 2014

[6] W. Wei, Y. Dai, C. Niu and B. Huang, Sci. Rep. **5**, 17578, 2015

[7] P. T. K. Chin, C. D. M. Donega, S. S. Bavel, S. C. J. Meskers, N. Sommerdijk, R. A. J. Janssen, J. Am. Chem. Soc. , **129** , 14880, 2007

[8] J. J. Li, J. M. Tsay, X. Michalet, S. Weiss, Chem. Phys. **318**, 82, 2005

[9] C. L. Kane and E. J. Mele, Phys. Rev. Lett. **95**, 226801 (2005).

[10] B. A. Bernevig and S.-C. Zhang, Phys. Rev. Lett. **96**, 106802 (2006).

[11] B. A. Bernevig, T. L. Hughes, and S.-C. Zhang, Science **314**, 1757 (2006).

[12] M. König, S. Wiedmann, C. Brüne, A. Roth, H. Buhmann, L. W. Molenkamp, X.-L. Qi, and S.-C. Zhang, Science **318**, 766 (2007).

[13] S. de-Leon, L. D. Shvartsman, and B. Laikhtman, Phys. Rev. B **60**, 1861 (1999).

[14] M. Yang, C. H. Yang, B. R. Bennett, and B. V. Shanabrook, Phys. Rev. Lett. **78**, 4613 (1997).

[15] M. Altarelli, Phys. Rev. B **28**, 842 (1983).

[16] M. Lakrimi, S. Khym, R. J. Nicholas, D. M. Symons, F. M. Peeters, N. J. Mason, and P. J. Walker, Phys. Rev. Lett. **79**, 3034 (1997).

[17] I. Knez, R. R. Du, and G. Sullivan, Phys. Rev. B **81**, 201301 (2010).

[18] F. Nichele, A. N. Pal, P. Pietsch, T. Ihn, K. Ensslin, C. Charpentier, and W. Wegscheider, Phys. Rev. Lett. **112**, 036802 (2014).

[19] K. Suzuki, Y. Harada, K. Onomitsu, and K. Muraki, Phys. Rev. B **87**, 235311 (2013).

[20] W. Pan, J. F. Klem, J. K. Kim, M. Thalakulam, M. J. Cich, and S. K. Lyo, Appl. Phys. Lett. **102**, 033504 (2013).

[21] K. I. Kolokolov and C. Z. Ning, Appl. Phys. Lett. **83**, 8 (2003)

[22] B. A. Bernevig, T. L. Hughes and S.-C. Zhang, Science **314** , 1757-1761 (2006)

[23] C. Brüne, C. X. Liu, E. G. Novik, E. M. Hankiewicz, H. Buhmann, Y. L. Chen, X. L. Qi, Z. X. Shen, S. C. Zhang, and L. W. Molenkamp, Phys. Rev. Lett. **106**, 126803 (2011)

[24] A. M. Kadykov, S. S. Krishtopenko, B. Jouault, W. Desrat, W. Knap, S. Ruffenach, C. Consejo, J. Torres, S. V. Morozov, N. N. Mikhailov, S. A. Dvoretskii, and F. Teppe, Phys. Rev. Lett. **120**, 086401 (2018)

[25] T. G. Dargam, R. B. Capaz, and B. Koiller, Phys. Rev. B **56**, 9625 (1997).

[26] L.-W. Wang, L. Bellaiche, S.-H. Wei, and A. Zunger, Phys. Rev. Lett. **80**, 4725 (1998).

[27] T. B. Boykin, N. Kharche, G. Klimeck, and M. Korkusinski, J. Phys.: Condens. Matter **19**, 036203 (2007).

[28] W. Ku, T. Berlijn, and C.-C. Lee, Phys. Rev. Lett. **104**, 216401 (2010).

[29] Y. Zhang and L.-W. Wang, Phys. Rev. B **83**, 165208 (2011).

[30] V. Popescu and A. Zunger, Phys. Rev. B **85**, 085201 (2012)

[31] W. Ku, T. Berlijn, and C.-C. Lee, Phys. Rev. Lett. **104**, 216401 (2010).

[32] T. G. Dargam, R. B. Capaz, and B. Koiller, Phys. Rev. B **56**, 9625 (1997).

[33] L.-W. Wang, L. Bellaiche, S.-H. Wei, and A. Zunger, Phys. Rev. Lett. **80**, 4725 (1998).

[34] T. B. Boykin, N. Kharche, G. Klimeck, and M. Korkusinski, J. Phys.: Condens. Matter **19**, 036203 (2007).

[35] W. Ku, T. Berlijn, and C.-C. Lee, Phys. Rev. Lett. **104**, 216401 (2010).

[36] Y. Zhang and L.-W. Wang, Phys. Rev. B **83**, 165208 (2011).

[37] Y. Zhang, A. Mascarenhas, and L.-W. Wang, Phys. Rev. Lett. **101**, 036403 (2008).

[38] L. Bellaiche, S.-H. Wei, and A. Zunger, Phys. Rev. B **56**, 10233 (1997).

[39] R. G. Dandrea and A. Zunger, Phys. Rev. B **43**, 8962 (1991).

[40] V. Popescu and A. Zunger, Phys. Rev. B **84**, 125315 (2011).

[41] R. M. Feenstra, N. Srivastava, Q. Gao, B. D. M. Widom, T. Ohta, G. L. Kellogg, J. T. Robinsonand, and I. V. Vlassiouk, Phys. Rev. B **87**, 041406 (2013).

[42] W. Demtröder, Laser Spectroscopy: Basic Concepts and Instrumentation, Springer (2003)

[43] James W. Robinson, Atomic Spectroscopy (1996)

[44] R. C. Hilborn, Am. J. Phys. **50** , 982 (1982)

[45] E. A. Kraut, R. W. Grant, J. R. Waldrop, and S. P. Eowalczyk, Phys. Rev. Lett. **44**, 24 (1980)

[46] N. Bouarissa, H. Aourag, Infrared Physics & Technology **40** 343-349 (1999)

[47] G. Kresse and J. Furthmüller, Phys. Rev. B **54**, 11169 (1996).

[48] G. Kresse and D. Joubert, Phys. Rev. B **59**, 1758 (1999).

[49] P. E. Blöchl, Phys. Rev. **50**, 17953 (1994)

Chapter 4

Electronic Structure of $ZrSe_2$ and $ZrTe_2$

4.1 What determines the electronic structure in ZrX_2

[1]

4.1.1 Introduction

Transition metal dichalcogenides (TMDCs) [2–4] are recently gaining enhanced interest in research, especially, over the past few decades owing to their potential applications in spintronics [5–9] and in optoelectronics [10–14]. The interest and utility of this class of materials come from their wide range of electronic properties, like transition from the metallic [15–17], to the semimetallic [18–21], to the semiconducting [22–25], and to the Mott-insulators [26–28]. Such transitions are obtained mainly by the band engineering [29–31]. In addition, the plethora of electronic properties of TMDCs include the charge density wave (CDW) [32, 33], the magnetism [34–36], the superconductivity [37–39], and the tunable band gap [40–43].

In this project, we studied the ground-state electronic structure of bulk $ZrTe_2$ and $ZrSe_2$ using density functional theory. Earlier experimental studies with ARPES report the electronic structure of $Zr(Se_{1-x}\ S_x)_2$ to be semiconducting [44–48]. Several theoretical reports on $ZrTe_2$ predicted it to be a metal [49–51]. A recent ARPES study on monolayer $ZrTe_2$ hints at its being another topological system [57]. So we went on to study the electronic

[1] A large part of this chapter is based on a publication in Physical Review B in the year 2020 [1]

structure of $ZrTe_2$ to find any evidence of a topological property. Our calculations show, in agreement with existing reports, that $ZrSe_2$ is a semiconductor with an indirect band gap. On the other hand, $ZrTe_2$ is found to be metallic in nature.

In $ZrTe_2$, we realize three holelike non-degenerate band dispersions near the Γ point and an electron like band dispersion at the M. Our DFT calculations show that all hole pockets are composed by the Te p orbital characters and the electron pocket is composed by the Zr d_{z^2} orbital character. In addition, our DFT calculations on $ZrTe_2$ in presence of spin-orbit coupling (SOC) predict a level inversion involving Te p and Zr d orbitals near Γ point, indicating the likelihood of $ZrTe_2$ to be a topological system.

In order to understand the origin of metallic state in $ZrTe_2$ and semiconducting state in $ZeSe_2$, we quantified the electronic structure by mapping it onto a tight-binding model. This allows us to trace the dependence of the electronic structure on metal-chalcogen bondlengths and demonstrate how the change in the Zr-X bondlength in going from $ZrSe_2$ to $ZrTe_2$ leads to the transition from semiconductor to metal.

Further, by studying other compounds belonging to the same column of periodic table, namely HfX_2, we arrived at the conclusion that a similar mechanism governs the electronic structure of Hf based compounds too. Here also, the metal-chalcogen bond length dictates the nature of the underlying ground state, rendering $HfSe_2$ semiconducting while $HfTe_2$ is metallic.

4.1.2 Methodology

The electronic structure of $ZrSe_2$ and $ZrTe_2$ have been calculated within a projected augmented plane wave (PAW) method of density functional theory as implemented in the Vienna Ab-initio Simulation Package (VASP) [57, 58]. A k-mesh of 16 x 16 x 16 was considered for the k-point integration while plane-wave cutoff 700 eV was used for the basis sets. The GGA-PBE approximation to the exchange correlation functional was used [59]. The experimental crystal structures were taken for the starting structural information. A full optimization of the lattice parameters as well as the internal positions was carried out. The optimized in-plane lattice parameter for $ZrSe_2$ was found to be a = b = 3.735 Å and that along the stacking direction c = 6.206 Å. Similarly for $ZrTe_2$, the optimized lattice parameters along the in-plane direction a = b = 3.909 Å and that along the stacking direction c = 6.749 Åwere obtained. They represent about 1-2 % deviations from the experimental values. In order to quantify the electronic structure changes between $ZrTe_2$ and $ZrSe_2$, we carried out a DFT band mapping onto a tight-binding model using the VASP to Wannier90 interface [60,61] which had maximally localized Wannier function for

the radial parts of the wave function. Zr d and Se/Te s and p states were included for the band mapping. Similar calculations are performed on $HfSe_2$ and $HfTe_2$. The structural parameters used for the calculations are shown in [4.3].

4.1.3 Results and Discussions

The crystal structures of both $ZrTe_2$ and $ZrSe_2$ are trigonal [Fig. 4.1]. But, interestingly, the ground state electronic structures of $ZrTe_2$ and $ZrSe_2$ widely differ from each other.

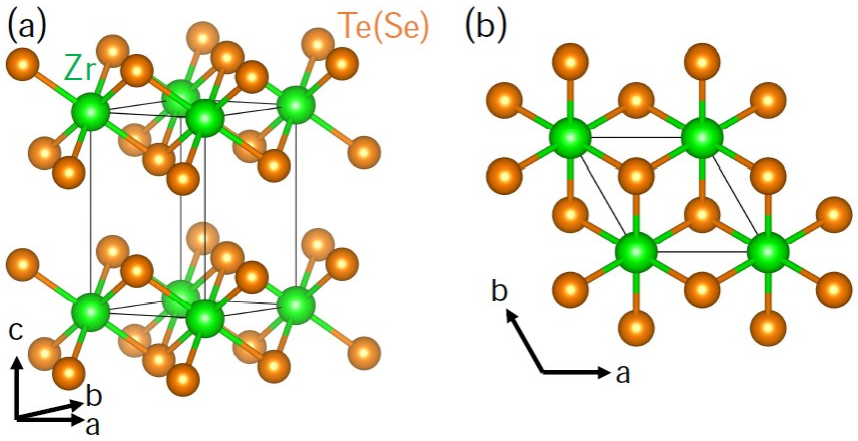

Figure 4.1: (a) Trigonal crystal structure of $ZrTe_2$ and $ZrSe_2$. (b) ZrX_2 layer projected on the ab-plane, showing the metal-chalcogen hexagonal pattern.

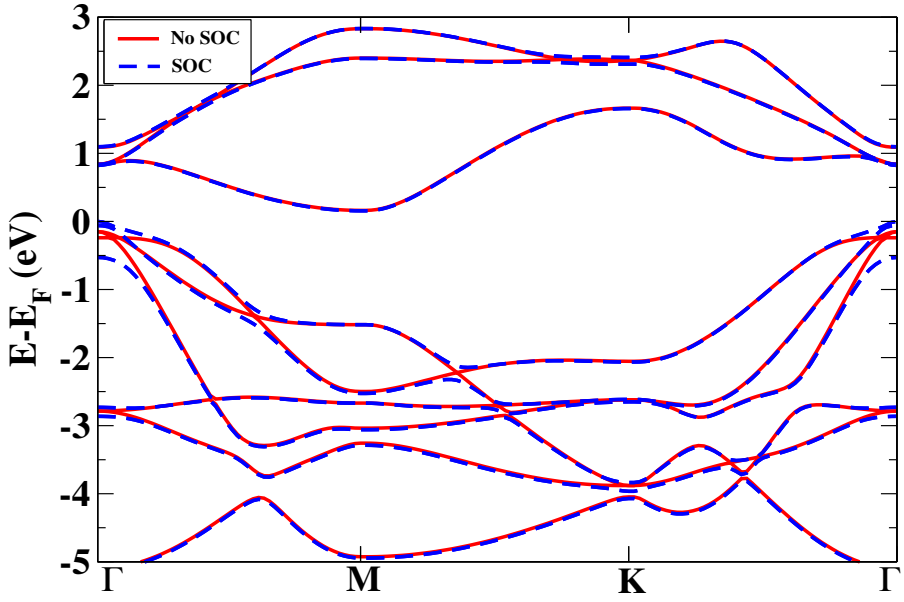

Figure 4.2: Calculated bandstructures of $ZrSe_2$ with and without SOC

The electronic structure of $ZrSe_2$ shows characteristic of semiconductors [Fig. 4.2]. It has an indirect bandgap with the conduction band minimum lying at high-symmetry point M and the valence band maximum lying at high-symmetry point Γ. The conduction states are primarily contributed by the Zr d orbitals [Fig. 4.3] whereas the valence states are primarily contributed by the Se p orbitals [Fig. 4.4].

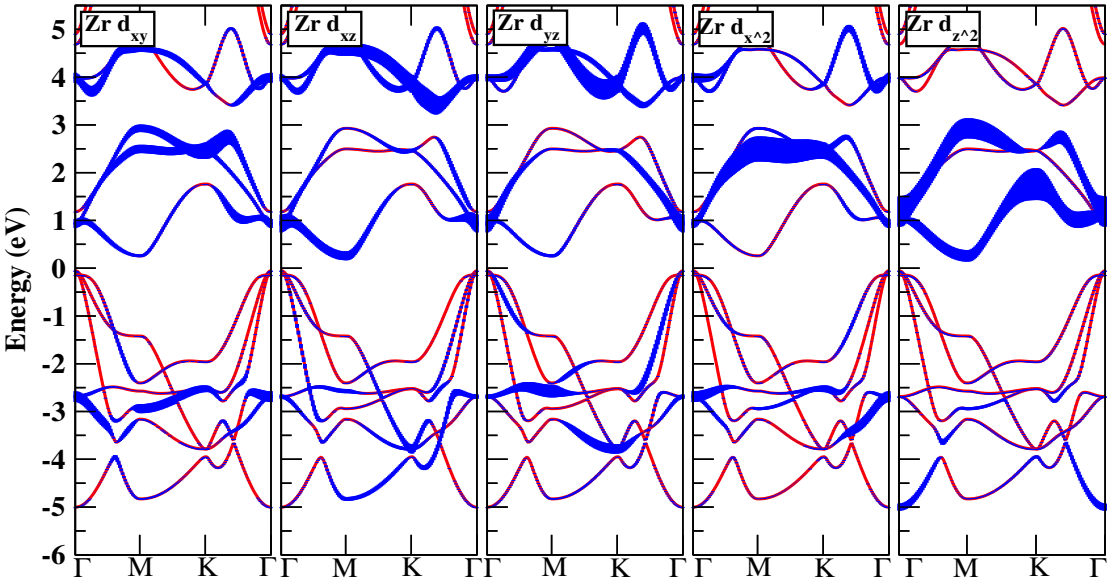

Figure 4.3: Orbital resolved calculated band structure of $ZrSe_2$ without SOC for Zr d states

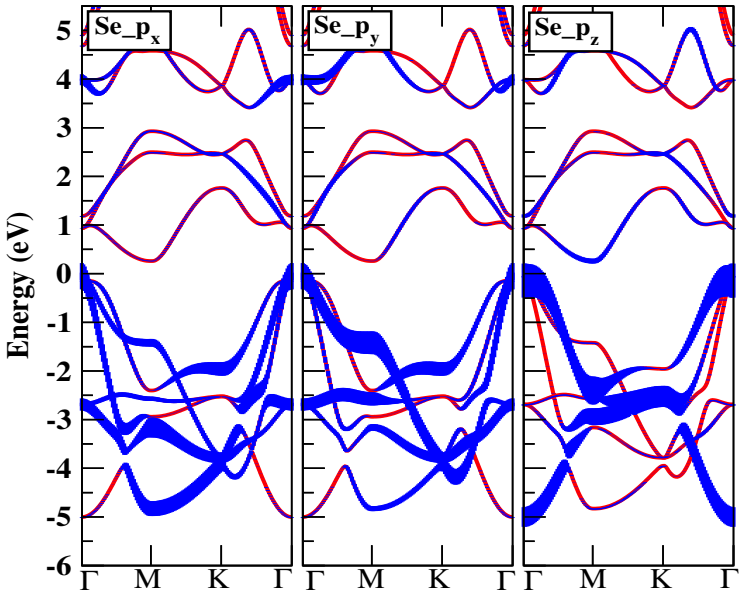

Figure 4.4: Orbital resolved calculated band structure of $ZrSe_2$ without SOC for Se p states

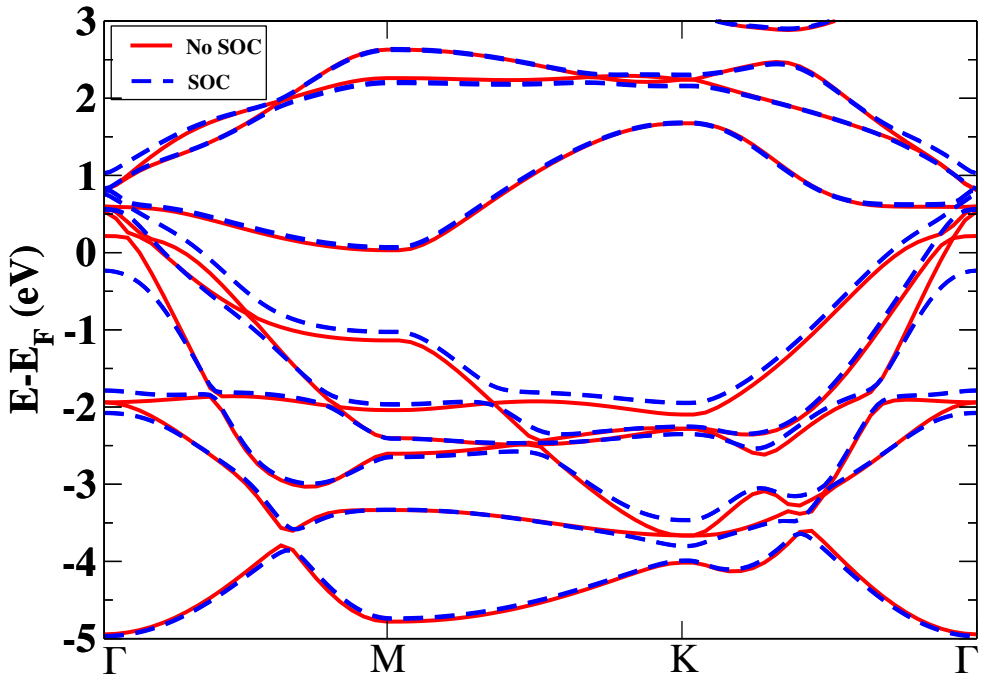

Figure 4.5: Calculated bandstructures of $ZrTe_2$ with and without SOC

In contrast, $ZrTe_2$ shows metallic character [Fig. 4.5] where the valence band and the conduction band overlap above Fermi level at Γ point. Here also, the bands lying above the Fermi level are primarily contributed by the Zr d orbitals [Fig.4.6], and the bands lying below the Fermi level are primarily contributed by Te p orbitals [Fig. 4.7].

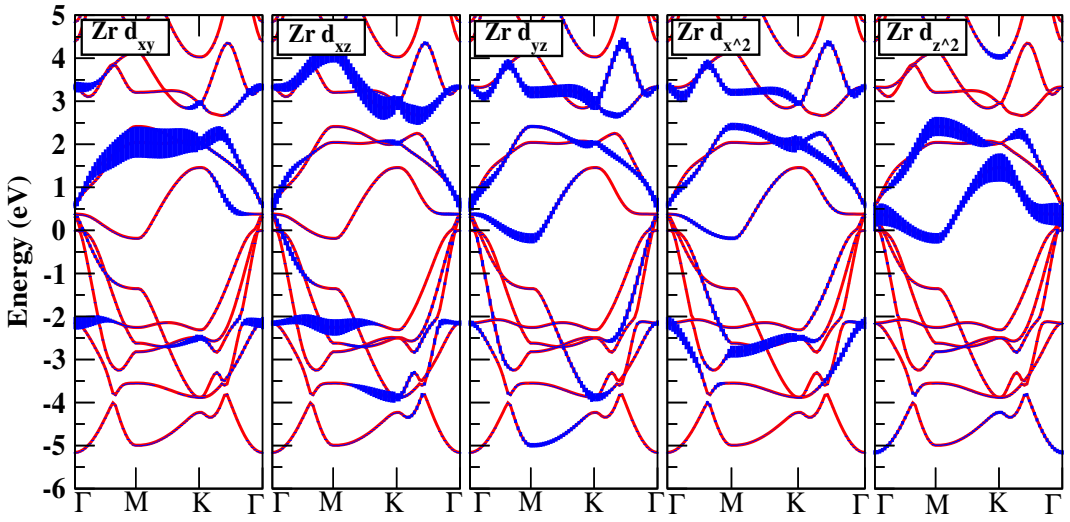

Figure 4.6: Orbital resolved calculated band structure of $ZrTe_2$ without SOC for Zr d states

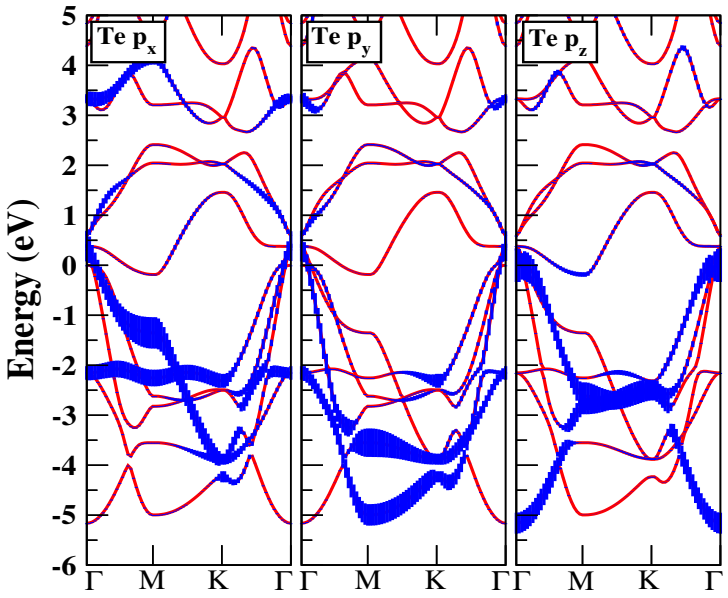

Figure 4.7: Orbital resolved calculated band structure of $ZrTe_2$ without SOC for Te p states

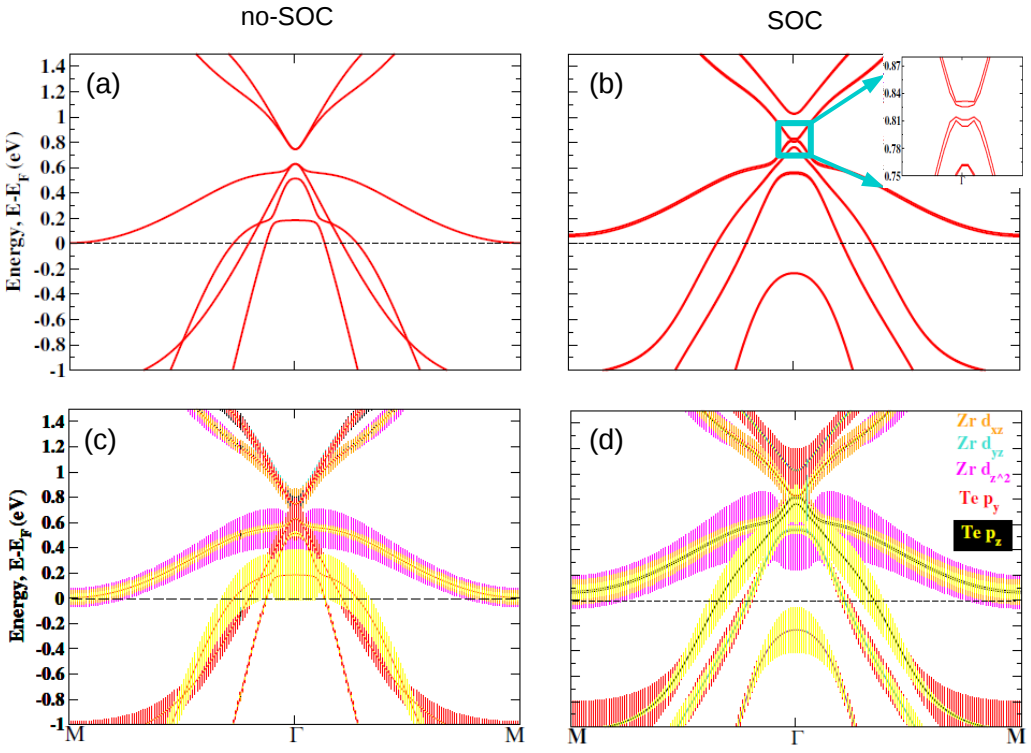

Figure 4.8: Calculated band structure of $ZrTe_2$ (a) without SOC and (b) with SOC. (c) and (d) are same as (a) and (b) but with orbital information. Inset in (b) shows a gap of 10 meV opening at the Γ point due to the band inversion under the SOC.

A band inversion is observed to happen at Γ, occurring between the non spin-orbit and spin-orbit bandstructures of $ZrTe_2$ [Fig. 4.8]. This can be clearly identified from the orbital-projected bandstructures of $ZrTe_2$ for non spin-orbit and spin-orbit calculations. The conduction band at Γ is composed of Zr d-orbitals. But in $ZrTe_2$, the Zr d_{z^2} state comes quite below so as to almost touch the valence band at Γ. In the presence of spin-orbit coupling, Zr d_{z^2} state moves even lower into the valence band at Γ. On the other hand, the Te p_y state at Γ moves upward into the conduction band. Hence there is clearly a band inversion happening at Γ and a bandgap of 10 meV has been observed to happen [inset of Fig. 4.8(b)]. This shows that $ZrTe_2$ is topologically interesting.

In order to better understand the mechanism underlying the transition from semiconductor to metal in going form $ZrSe_2$ to $ZrTe_2$, we map the ab-initio bandstructures of these two materials onto a tight-binding model. The hamiltonian in a tight-binding model is given as

$$\hat{H} = \sum_i \epsilon_i c_i^\dagger c_i - \sum_{i,j} t_{i,j} c_i^\dagger c_j + h.c. \tag{4.1}$$

Here $t_{i,j}$ is the hopping interaction parameter between the i^{th} and j^{th} orbitals. and ϵ_i is the on-site energy of orbital i. From the tight-binding parameters, the charge transfer energy Δ is measured between cation d and anion p orbitals, $\Delta = \epsilon_d(Zr) - \epsilon_p(X)$.

The tight-binding bandstructures of the bulk materials have been calculated using WANNIER90 to VASP interface. In WANNIER90, the radial parts of the wavefunctions are given by maximally localized wannier functions. This successfully reproduced the ab-initio bandstructures of both $ZrSe_2$ [Fig. 4.9] and $ZrTe_2$ [Fig. 4.10]. This allowewd us to use this tight-binding model and the associated parameters to study further changes in the electronic structure.

Se lies above Te in the periodic table. It implies that Se is more electronegative than Te. Hence the p-states of Se should lie deeper below the Fermi level compared to Te p states. This is reflected in the values of the charge transfer energy, $\Delta = \epsilon_d(Zr) - \epsilon_p(X)$, when compared between the two compounds. Δ is smaller by 0.141 eV for $ZrTe_2$ than $ZrSe_2$ [Table 4.1]. Since Zr is in a +4 valence state in $ZrTe_2$ and $ZrSe_2$, Zr has a d^0 electron configuration. The interactions between Zr d and X p states give rise to bonding-antibonding splitting and opens up a gap. The splitting should depend on the p-d interaction strength in the compound as well as the value of Δ. For the same p-d hopping interaction strength (t) between Zr d and X p orbitals, Δ decreases in going from $ZrSe_2$ to $ZrTe_2$. This should lead to larger bonding-antibonding splitting in $ZrTe_2$. This is

because for a smaller Δ, the Zr d and X p orbitals come closer in energy and consequently they interact more to cause larger splitting.

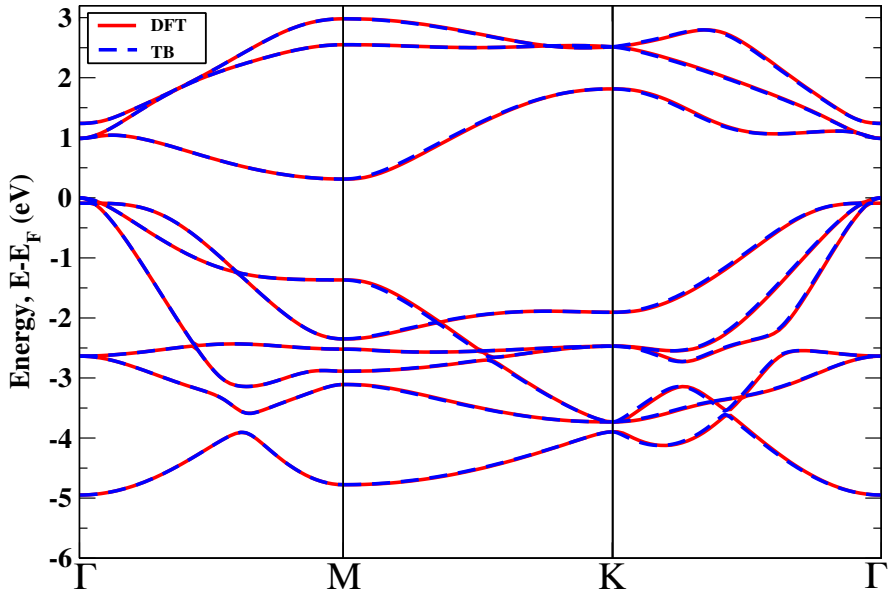

Figure 4.9: Energy-momentum plots of $ZrSe_2$ obtained from the DFT calculations and with overlapped bands derived from the tight-binding (TB) fittings

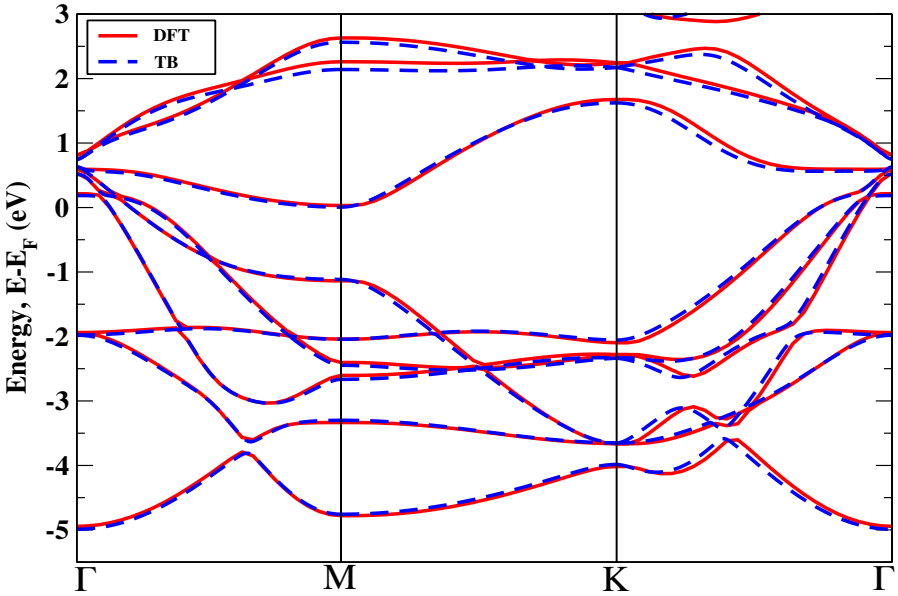

Figure 4.10: Energy-momentum plots of $ZrTe_2$ obtained from the DFT calculations and with overlapped bands derived from the tight-binding (TB) fittings

This is, of course, in contrary to what has been found from the electronic structure calculation for $ZrTe_2$, as we saw that $ZrTe_2$ is metallic. So, the charge transfer energy, Δ,

does not account for the transition from semiconducting to metallic eletronic character in going from $ZrSe_2$ to $ZrTe_2$.

$ZrSe_2$

Element	On-site energies (eV)	Charge transfer energy Δ (eV)	Lattice parameters before optimization (Å)	Lattice parameters after optimization (Å)
Zr (d)	4.140	2.282	3.771	3.735
	4.175		3.771	3.735
	4.209		6.184	6.206
	5.281			
	5.323		Zr-Zr bondlength= 3.735 Å	Zr-Se bondlength= 2.690 Å
Se1 (p)	1.784			
	1.830			
	1.858			
Se2 (p)	1.783			
	1.830			
	1.858			

$ZrTe_2$

Element	On-site energies (eV)	Charge trasfer energy Δ (eV)	Lattice parameters before optimization (Å)	Lattice parameters after optimization (Å)
Zr (d)	6.201	2.141	3.950	3.908
	6.202		3.950	3.908
	6.236		6.630	6.749
	7.345			
	7.346		Zr-Zr bondlength= 3.909 Å	Zr-Te bondlength= 2.894 Å
Te1 (p)	3.951			
	4.060			
	4.060			
Te2 (p)	3.951			
	4.060			
	4.060			

Table 4.1: Lattice parameters, Bond lengths, On-site energies and Charge transfer energies of $ZrSe_2$ and $ZrTe_2$.

The assumption of the similar values of t for both systems is what was wrong in our analysis that led to the discrepancy. Here, it is not Δ that determines the bonding-antibonding splitting and the semiconductor to metal transition, but it is the hopping interaction strength t that does it. Moreover, the hopping interaction strength is expected to scale as $\frac{1}{r^4}$ for p-d interaction, according to the Harrison's empirical law [62]. Here,

Composition	Δ (eV)	M-M bondlength (Å)	M-X bondlength (Å)
$ZrSe_2$	2.282	3.735	2.690
$ZrTe_2$	2.141	3.908	2.894
$HfSe_2$	3.015	2.710	2.660
$HfTe_2$	2.332	3.846	2.856

Table 4.2: Tight binding parameters of MX_2 (M= Zr and Hf; X=Se and Te). Here (Δ) is the charge transfer energy between transition-metal (M) and chalcogen ion (X).

r is the distance between the Zr and X ions. If we look at the crystal structures of $ZrSe_2$ and $ZrTe_2$, we see that the Zr-Te bondlength is 2.894 Å which is larger than the Zr-Se bondlength in $ZrSe_2$, which is 2.690 Å. Hence the value of t should be smaller for $ZrTe_2$ compared to $ZrSe_2$. This smaller value of t in $ZrTe_2$ dominates the electronic structure changes. Hence, though Δ decreses as we go from $ZrSe_2$ to $ZrTe_2$, the bonding-antibonding splitting may be smaller for $ZrTe_2$. Hence the metallicity of $ZrTe_2$ is induced by the metal-chalcogen bondlength. For the same reasons, the larger value of t in $ZrSe_2$ makes it semiconducting.

It is worth noting that the Zr-Zr distances [Table 4.2] are larger than the Zr-X distances in $ZrSe_2$ and $ZrTe_2$. This is reason why the effect of Zr-Zr bondlength has weaker effect on the electronic structure changes. This property is opposite to what is observed in WTe_2 and $MoTe_2$, both having the same ctrystal structure of $1T'$. W-W distance in WTe_2 is 2.857 Å which is comaparble to the W-Te distance which is 2.706 Å. Mo-Mo distance in $MoTe_2$ is 2.899 Å which is comaparble to the Mo-Te distance which is 2.699 Å.

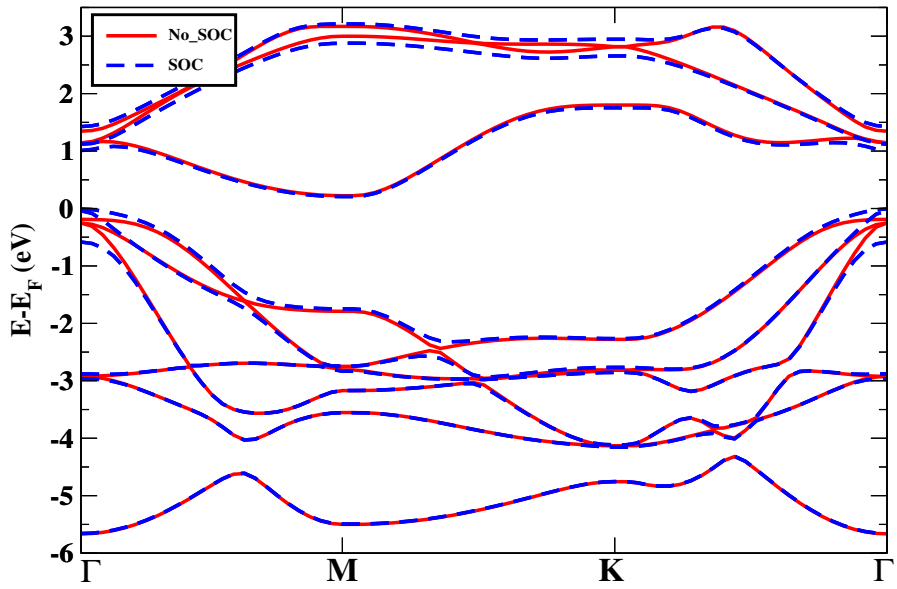

Figure 4.11: Calculated bandstructures of $HfSe_2$ with and without SOC

We went on to examine further whether this is the generic feature of Group-IV compounds in the periodic table. We replaced Zr by Hf and performed similar calculations as done for $ZrSe_2$ and $ZrTe_2$. One extra advantage of working with HfX_2 is that both ZrX_2 and HfX_2 share same crystal structure that is 1T. Similar to ZrX_2, our ab-initio electronic structure calculations showed $HfSe_2$ to be semiconducting [Fig. 4.11] and $HfTe_2$ to be metallic [Fig. 4.12]. The calculated electronic properties are in accordance with existing literature [53, 54].

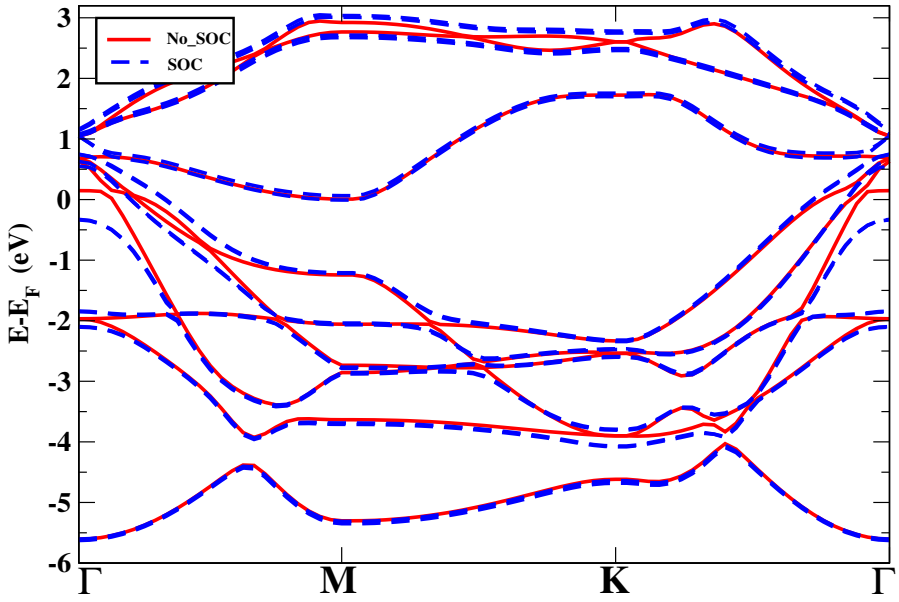

Figure 4.12: Calculated bandstructures of $HfTe_2$ with and without SOC

We fitted the ab-initio bandstructures of $HfSe_2$ and $HfTe_2$ with tight-binding model and obtained reasonably good description [Fig. 4.13 and Fig. 4.14].

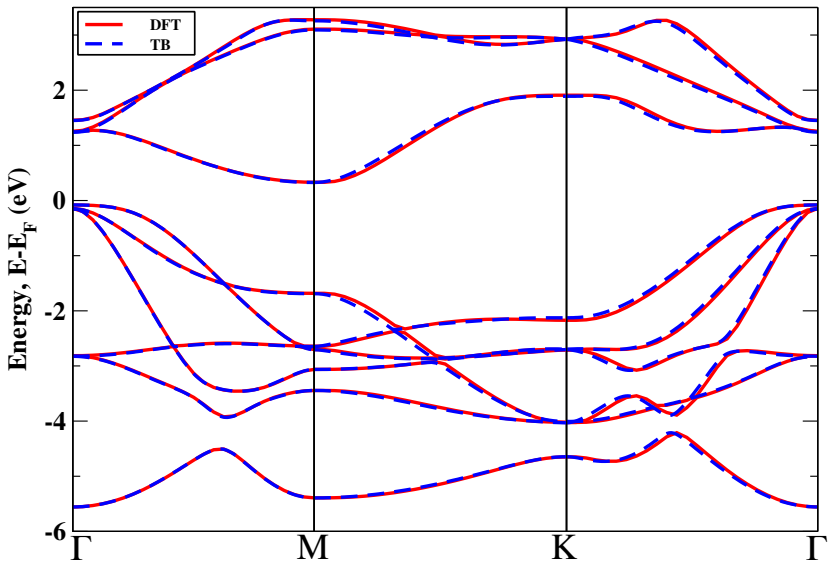

Figure 4.13: Energy-momentum plots of $HfSe_2$ obtained from the DFT calculations and with overlapped bands derived from the tight-binding (TB) fittings

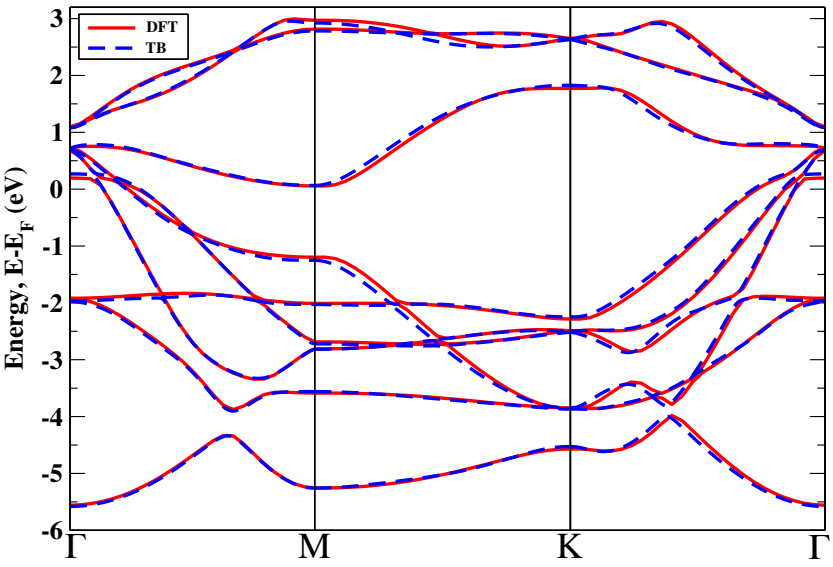

Figure 4.14: Energy-momentum plots of $HfTe_2$ obtained from the DFT calculations and with overlapped bands derived from the tight-binding (TB) fittings

From our tight-binding calculations, we extracted out the onsite-energies of metal as well as chalcogen ions and calculated the charge transfer energies Δ for both the materials. Here again, we found that Δ is smaller for $HfTe_2$ as copmpared to $HfSe_2$ [Table 4.3]. We found similar trends in the bondlengths for ZrX_2 and HfX_2. Hf - Te bond length is larger than that of Hf - Se [Table 4.2]. Consequently, $HfTe_2$ has smaller bonding-antibonding splitting compared to $HfSe_2$ which explains the metallic character of $HfTe_2$. Thus, similar

to ZrX_2, the electronic properties of the HfX_2 compounds also are being dictated by the Hf d - X p interactions.

$HfSe_2$

Element	On-site energies (eV)	Charge trasfer energy Δ (eV)	Lattice parameters before optimization (Å)	Lattice parameters after optimization (Å)
Hf (d)	5.161	3.017	3.733	3.710
	5.165		3.733	3.710
	5.215		6.146	6.043
	6.672			
	6.697		Hf-Hf bond length= 3.710 Å	Hf-Se bond length= 2.660 Å
Se1 (p)	1.870			
	1.906			
	2.140			
Se2 (p)	1.949			
	1.981			
	2.144			

$HfTe_2$

Element	On-site energies (eV)	Charge trasfer energy Δ (eV)	Lattice parameters before optimization (Å)	Lattice parameters after optimization (Å)
Hf (d)	6.986	2.332	3.910	3.846
	7.028		3.910	3.846
	7.067		6.658	6.673
	8.155			
	8.189		Hf-Hf bond length= 3.846 Å	Hf-Te bondlength= 2.856 Å
Te1 (p)	4.441			
	4.628			
	4.653			
Te2 (p)	4.373			
	4.607			
	4.631			

Table 4.3: Lattice parameters, Bond lengths, On-site energies and Charge transfer energies of $HfSe_2$ and $HfTe_2$.

4.2 What determines the ground state crystal structure in $ZrSe_2$

There is another issue that evoked our curiosity study this material further. We know that MoX_2 stabilizes in 2H polymorph in its ground state. But for ZrX_2, in contrast, the ground state configuration is 1T. 2H phase of MX_2 has hexagonal structure where 1T phase has a tetragonal unit cell [Fig. 4.15].

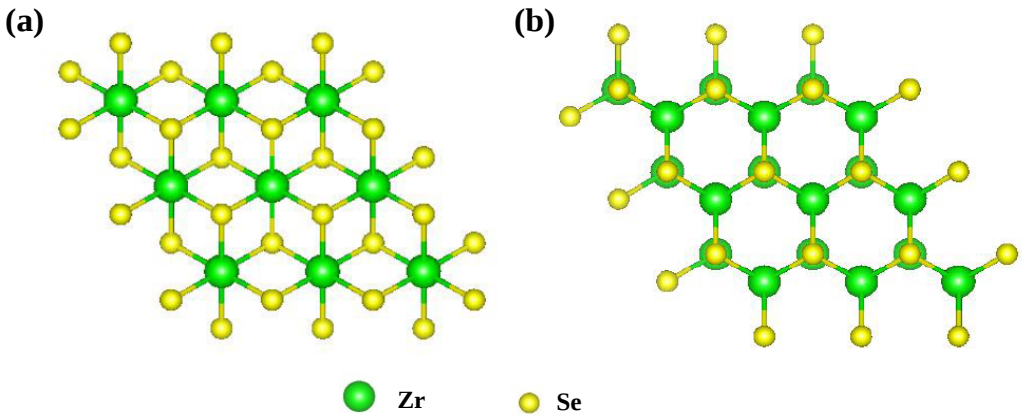

Figure 4.15: Arrangement of atoms in the two possible polymorphs of $ZrSe_2$. Top views of (a) 1T structure, (b) 2H structure

In 2H $ZrSe_2$, the coordination of six chalcogen atoms about each cation would form a trigonal prismatic structure [Fig. 4.16(b)]. In 1T structure, on the other hand, the chalcogens atoms have an octahedral coordination about each cation. [Fig.4.16(a)]

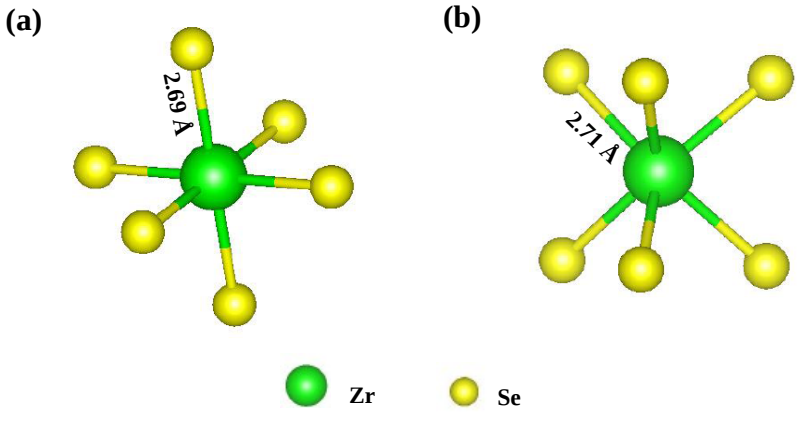

Figure 4.16: Coordination of chalcogens around a cation for $ZrSe_2$ in (a) 1T structure, (b) 2H structure

The interlayer separations of the two possible polymorphs after optimization of the ionic positions differ little [Fig. 4.17]

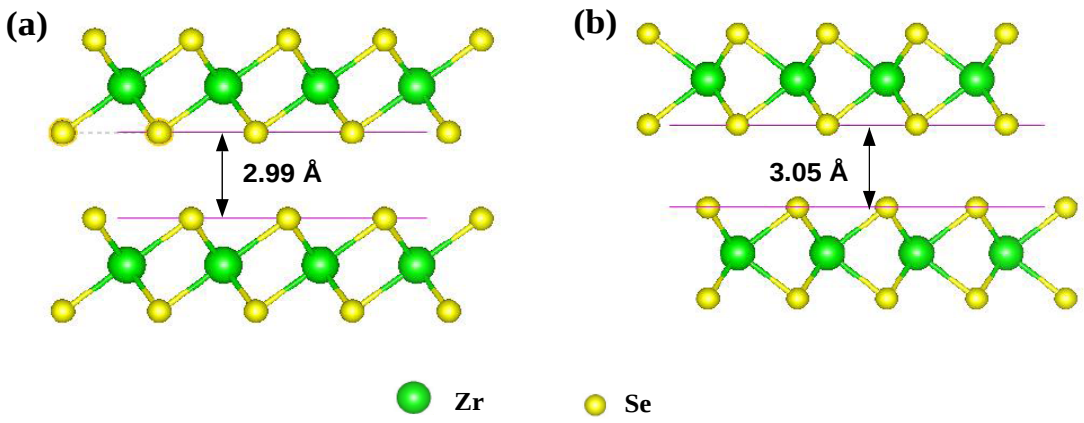

Figure 4.17: Distance between two consecutive layers of $ZrSe_2$ in (a) 1T structure, (b) 2H structure

We enquire the reason behind this unusual behaviour in ZrX_2. We took first $ZrSe_2$ for our study. We went on to calculate the bandstructure of 2H $ZrSe_2$ and compare its various features with those of the banstructure of 1T $ZrSe_2$.

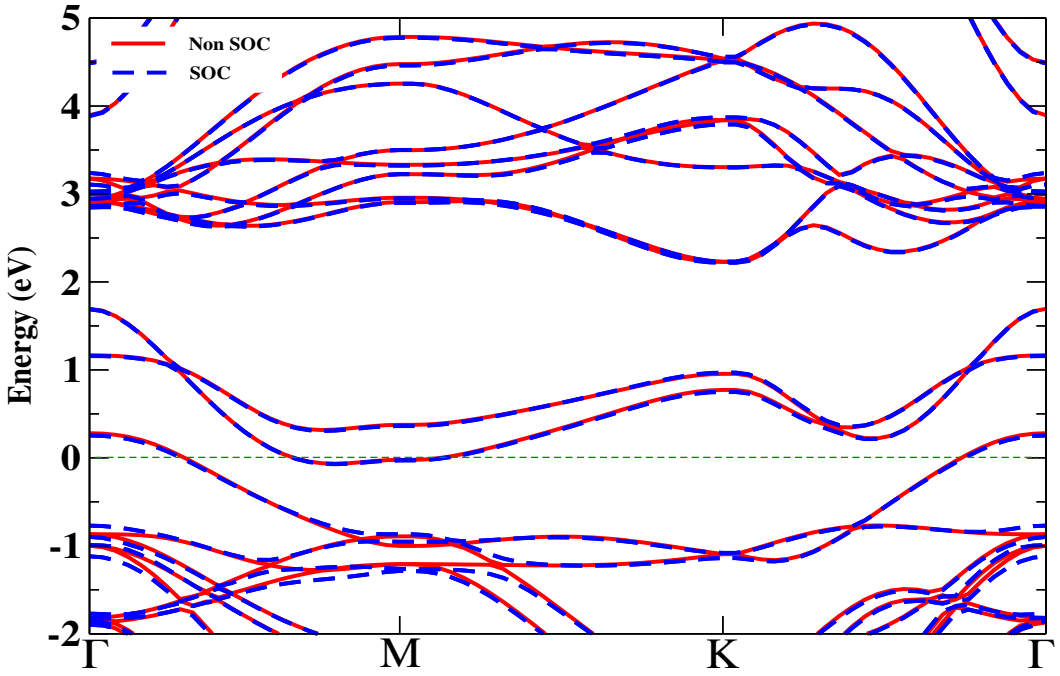

Figure 4.18: Energy-momentum plots of 2H bulk $ZrSe_2$ with spin-orbit interaction and without spin-orbit interaction,as obtained from the DFT calculations, superposed over each other

Where bulk 1T structure of $ZrSe_2$ is semiconducting [Fig. 4.2], the 2H polymorph is found to be metallic in its bulk structure [Fig. 4.18]. We found little difference between bandstructures for spin-orbit and non spin-orbit calculations for 2H [Fig. 4.18]. Monolayer structure of 2H $ZrSe_2$ is found to be semiconducting in nature [Fig. 4.19]. In each of the figures, 0 represents the Fermi energy.

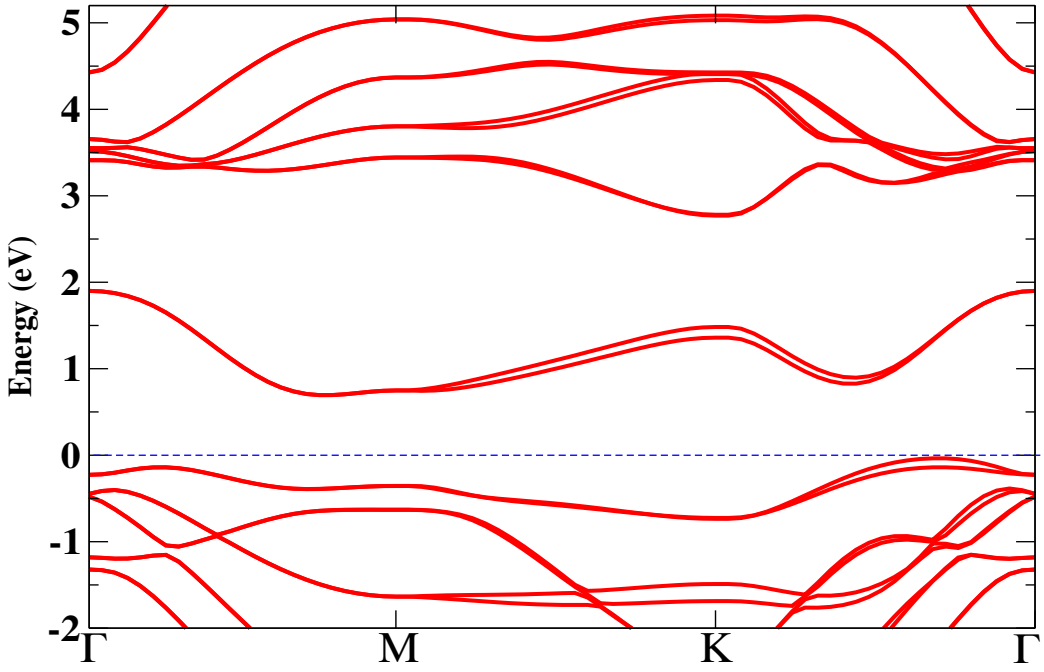

Figure 4.19: Energy-momentum plots of monolayer of 2H $ZrSe_2$ with spin-orbit interaction incorporated

Se has an electron configuration of $4s^2$ $4p^4$ in its outermost shell. Zr has the electron arrangement as $4d^2$ $5s^2$ in its outer shell. In $ZrSe_2$, Zr is in 4^+ valence state with its d shell empty. Se has its p shell completely filled rendering itself in 2^- valence state. In order of energy, the Se p states being completely filled should lie below the empty Zr d states in $ZrSe_2$. In transition metal dichalcogenides, the conduction states are generally contributed by the transition metal d orbitals and the valence states are contributed by the chalcogen p orbitals. Since it is a d^0 system, we can think of it as a two level system where an interaction between the transition metal d level and the chalcogen p level gives rise to bonding-antibonding like splitting of energy levels opening up a gap in between. The bonding states are the valence states lying below the fermi level and have primarily the chalcogen p characters. The antibonding states are the conduction states lying above the fermi level and are primarily contributed by the metal d characters.

From the orbital projected bandstructures, we find that for 1T structure in bulk [Fig. 4.3], the conduction states are contributed chiefly by Zr d orbitals and they can be identified

as the antibonding states here. The bonding states [Fig. 4.4] are the valence states lying below the Fermi level and are principally contributed by Se p orbitals.

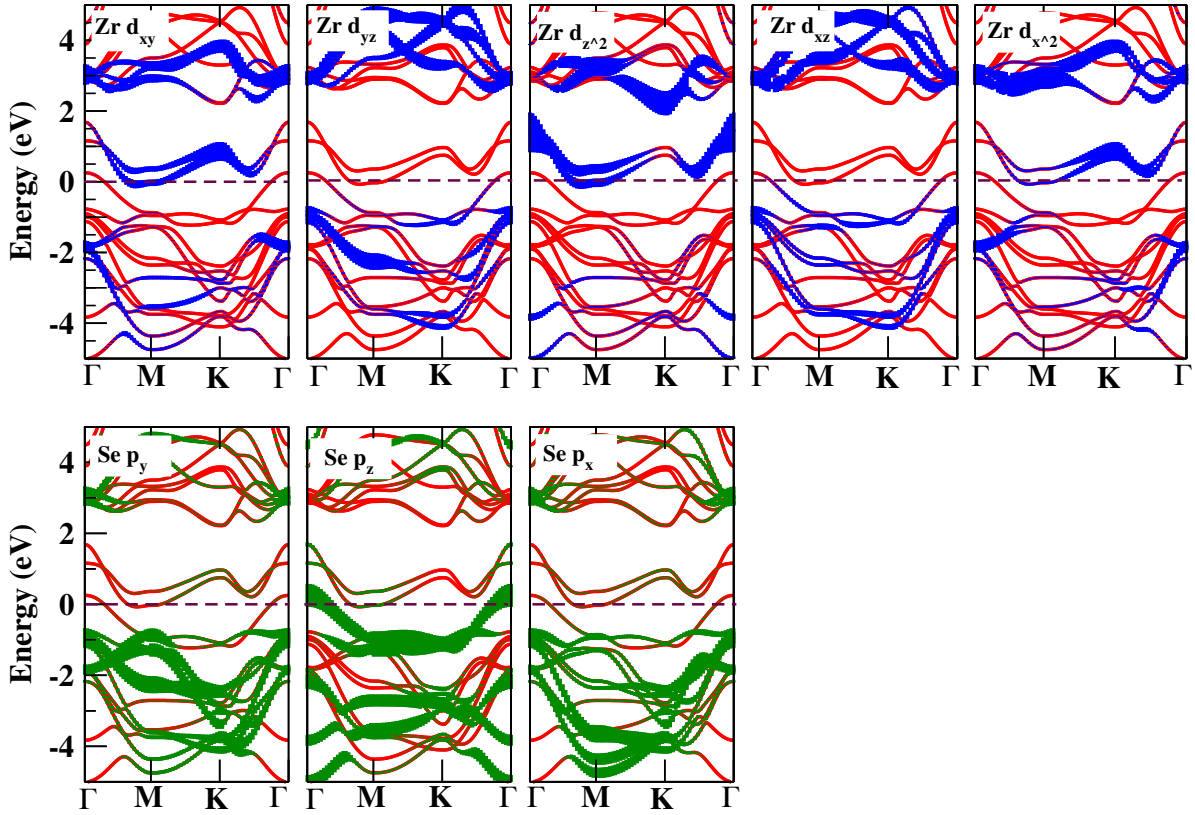

Figure 4.20: Orbital resolved calculated band structure of 2H $ZrSe_2$ with SOC for Zr d and Se p states

For 2H structure, however, the Fermi energy passes through one of the antibonding states [Fig. 4.20] as two of the antibonding states come down in energy. Hence some of the antibonding states get partially occupied in 2H structure. But in 1T, all the antibonding states were completely empty. Since $ZrSe_2$ is a d^0 system, this partial occupation of its antibonding states contributed by Zr d orbitals, which would otherwise be left empty, leads to rise in the total energy of the system. Hence the 2H structure of $ZrSe_2$ is higher in energy as compared to 1T. We found confirmation to our conclusion by looking at the band energies, which are summation of the eigenenergies, as obtained from our DFT calculations. We see that the gain from band energies for 1T is -28.66 eV per formula unit which is higher than that in the 2H structure. For 2H structure, the value is -28.11 eV per formula unit. This justifies why the 2H polymorph is unstable for $ZrSe_2$ and 1T polymorph is preferred as the ground state for this material.

The next question that comes is why there happens a transition from semiconductor to metal as we go from 1T to 2H structure in $ZrSe_2$?

We first suspected the charge transfer energy, $\Delta = \epsilon_d(Zr) - \epsilon_p(X)$ to be responsible. So we mapped the ab-initio bandstructure of 2H bulk $ZrSe_2$ onto a tight binding model and obtained a good description [Fig. 4.21]. We took Zr d and Se p into our basis.

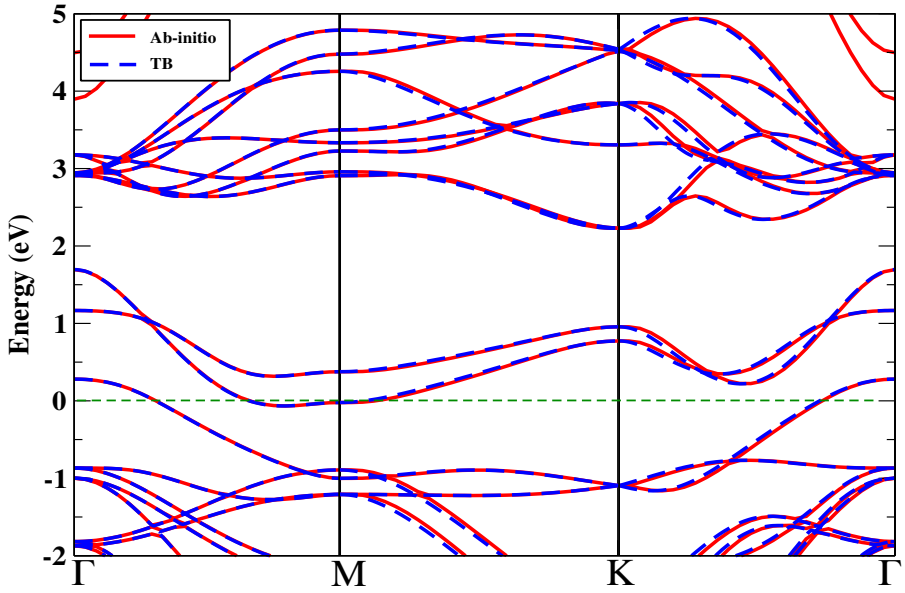

Figure 4.21: Energy-momentum plots of 2H $ZrSe_2$ obtained from the DFT calculations overlapped with bands derived from the tight-binding (TB) fittings

1T bulk $ZrSe_2$				
Element	On-site energies (eV)	Charge trasfer energy Δ (eV)	Lattice parameters before optimization (Å)	Lattice parameters after optimization (Å)
Zr (d)	4.140	2.282	3.771	3.735
	4.175		3.771	3.735
	4.209		6.184	6.206
	5.281			
	5.323		Zr-Zr bondlength= 3.735 Å	Zr-Se bondlength= 2.690 Å
Se1 (p)	1.784			
	1.830			
	1.858			
Se2 (p)	1.783			
	1.830			
	1.858			

Table 4.4: Lattice parameters, Bond lengths, On-site energies and Charge transfer energies of 1T and 2H bulk $ZrSe_2$.

2H bulk $ZrSe_2$				
Element	On-site energies (eV)	Charge trasfer energy Δ (eV)	Lattice parameters before optimization (Å)	Lattice parameters after optimization (Å)
Zr (d)	4.38	2.61	3.771	3.679
	4.38		3.771	3.679
	4.43		12.927	12.838
	5.20			
	5.20		Zr-Zr bond length= 3.679 Å	Zr-Se bondlength= 2.711 Å
Se (p)	1.68			
	1.77			
	1.77			

Table 4.5: Lattice parameters, Bond lengths, On-site energies and Charge transfer energies of 1T and 2H bulk $ZrSe_2$.

From the onsite energies derived from the tight-binding hamiltonian, we calculated Δ for 1T as well as for 2H structure. We found Δ to be 2.61 eV for 2H structure which is larger than the value of Δ for 1T $ZrSe_2$ which is 2.282 eV [Table 4.5]. A larger Δ would imply a smaller bonding-antibonding splitting in 2H $ZrSe_2$. That would explain the metallic behaviour in 2H structure of this compound.

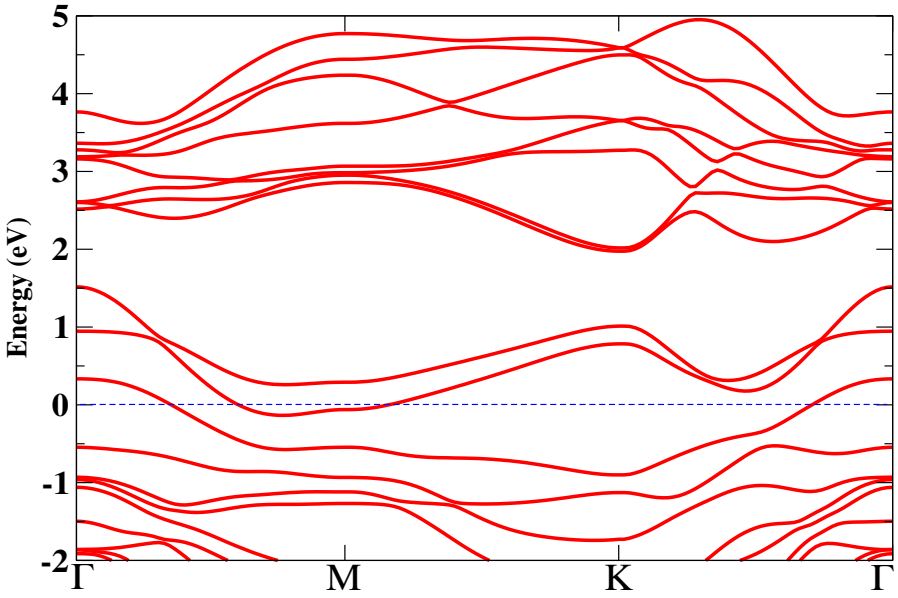

Figure 4.22: Energy-momentum plot of 2H $ZrSe_2$ derived from tight-binding fittings using the on-site energies of 1T $ZrSe_2$.

To confirm our conclusion, we replaced the onsite energies in the tight binding model for 2H structure with the onsite energies from the tight binding model for 1T. We found that the resulting bandstructure continues to be metallic [Fig. 4.22]. This establishes that Δ is not playing the fundamental role here in dictating the transition from semiconductor to metal in going from 1T to 2H structure.

Composition	Δ (eV)	Zr-Zr bondlength (Å)	Zr-Se bondlength (Å)
1T $ZrSe_2$	2.282	3.735	2.690
2H $ZrSe_2$	2.61	3.679	2.711

Table 4.6: Charge transfer energy (Δ) and bondlengths of 1T and 2H structures of $ZrSe_2$. Here (Δ) is calculated between transition-metal Zr and chalcogen ion Se

The next possibility is that the bondlengths are at play. We see that the Zr-Zr bondlengths change only by 0.05 Å between 1T and 2H. The Zr-X bondlengths also change very little [Table 4.6]. To be more precise about the effect of bondlengths on the transtion, we adjusted the Zr-Zr bondlength and Zr-Se bondlength in 2H structure to make them equal to their values in 1T $ZrSe_2$. We replaced the in-plane lattice parameters in 2H structure with those of the 1T structure such that the value of Zr-Zr bondlength becomes exactly equal to that in 1T $ZrSe_2$.

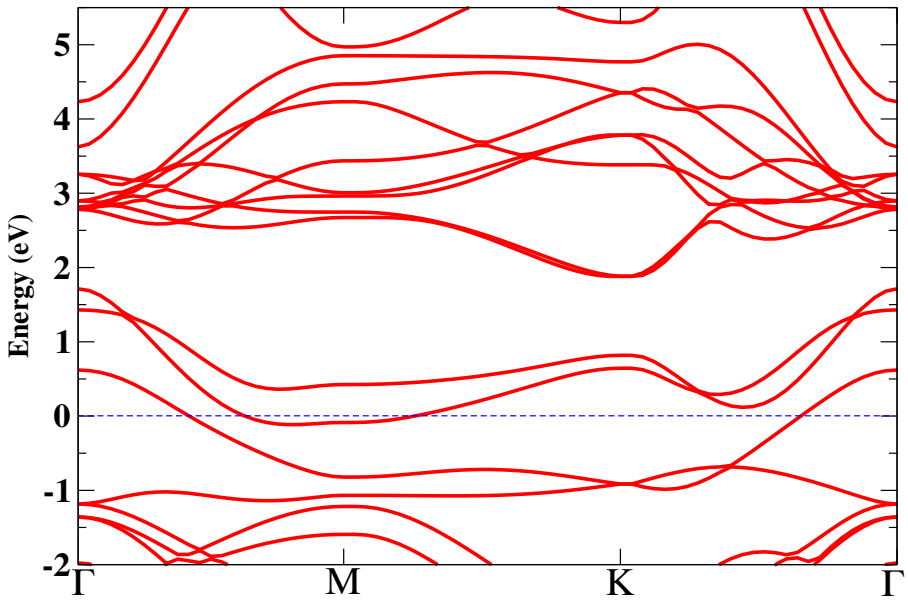

Figure 4.23: Energy-momentum plot of 2H $ZrSe_2$ with Zr-Zr bondlength and Zr-Se bondlength set equal to those in 1T $ZrSe_2$

Further we adjusted the metal-chalcogen bondlength in 2H structure by manualy shifting the positions of the chalcogen atoms. This way we set the Zr-X bondlength in 2H $ZrSe_2$ exactly equal to that in 1T $ZrSe_2$. The resultng band structure again turns out to be metallic [Fig. 4.23]. Hence we can safely conclude that the metal-metal or the metal-chalcogen bondlengths are not dictating the trasition.

The metallic character can be understood by examining the Se network around each transition metal atom. One finds that the $TMSe_6$ polyhedra lead to wider bands in the 2H polymorph than in the 1T structure, emerging from the phases of the associated hopping integrals. This therefore leads to the notionally anti-bonding states arising from transition metal d and anion p interactions being partially occupied in 2H. That makes the 2H structure metallic.

4.3 Conclusion

In conclusion, we systematically studied the low energy electronic structure of $ZrTe_2$ and $ZrSe_2$ using density functional theory calculations. The DFT calculations of $ZrTe_2$ in the presence of spin-orbit coupling shows metallic character and suggests a band inversion involving Te p and Zr d orbitals near Γ point. This suggests that $ZrTe_2$ is a topological metal. Our studies on $ZrSe_2$ further suggest it to be a semiconductor with an indirect band gap between Γ and M high-symmetry points. Our calculations further establishes that it is the metal-chalcogen bondlengths that is vital in causing the electronic phase transition from semiconductor to topological metal in going from $ZrSe_2$ to $ZrTe_2$. This trend is observed to be true for other Group-IV compounds as well. This is supported by our systematic calculations performed on another composition HfX_2.

In $ZrSe_2$, 1T polymorph is favoured as the ground state cnfiguration unlike other TMDs in which the ground state is 2H. This turns out to be resulting from the chalcogen network around each cation that leads to wider bands, phase factors in the hopping integrals playing the major role. This larger bandwidth leads to some of the antibonding states to be occupied which enhances the total energy in 2H structure, causing 1T polymorph to be the favoured ground state configuration in $ZrSe_2$ and $HfSe_2$.

Bibliography

[1] I. Kar, J. Chatterjee, L. Harnagea, Y. Kushnirenko, A. V. Fedorov, D. Shrivastava, B. Büchner, P. Mahadevan, S. Thirupathaiah, Phys. Rev. B **101**, 165122 (2020)

[2] R. G. Dickinson and L. Pauling, J. Am. Chem. Soc. **45**, 1466 (1923).

[3] J. Wilson and A. Yoffe, Adv. Phys. **18**, 193 (1969).

[4] L. F. Mattheiss, Phys. Rev. B **8**, 3719 (1973).

[5] R. Sph, U. Elrod, M. Lux-Steiner, E. Bucher, and S. Wagner, Appl. Phys. Lett. **43**, 79 (1983).

[6] D. Jim enez, Appl. Phys. Lett. **101**, 243501 (2012).

[7] Q. H. Wang, K. Kalantar-Zadeh, A. Kis, J. N. Coleman, and M. S. Strano, Nature Nanotechnology **7**, 699 (2012).

[8] H. Zeng, J. Dai, W. Yao, D. Xiao, and X. Cui, Nature Nanotechnology **7**, 490 (2012).

[9] R. Cheng, S. Jiang, Y. Chen, Y. Liu, N. Weiss, H.-C. Cheng, H. Wu, Y. Huang, and X. Duan, Nat. Commun. **5** (2014), 10.1038/ncomms6143.

[10] S. J. Li, J. C. Bernede, J. Pouzet, and M. Jamali, Journal of Physics: Condensed Matter **8**, 2291 (1996).

[11] M. S. Fuhrer and J. Hone, Nat. Nanotechnol. **8**, 146 (2013).

[12] W. Wu, L. Wang, Y. Li, F. Zhang, L. Lin, S. Niu, D. Chenet, X. Zhang, Y. Hao, T. F. Heinz, J. Hone, and Z. L. Wang, Nature **514**, 470 (2014).

[13] C. Gong, Y. Zhang, W. Chen, J. Chu, T. Lei, J. Pu, L. Dai, C. Wu, Y. Cheng, T. Zhai, L. Li, and J. Xiong, Adv. Sci. **4**, 1700231 (2017).

[14] M. Khan and M. N. Leuenberger, Nanophotonics **7**, 1589 (2018).

[15] A. T. Neal, Y. Du, H. Liu, and P. D. Ye, ACS Nano **8**, 9137 (2014).

[16] Z. Zhang, J. Niu, P. Yang, Y. Gong, Q. Ji, J. Shi, Q. Fang, S. Jiang, H. Li, X. Zhou, L. Gu, X. Wu, and Y. Zhang, Adv. Mater. **29**, 1702359 (2017).

[17] J. Zhang, B. Yang, H. Zheng, X. Han, and Y. Yan, Phys. Chem. Chem. Phys. **19**, 24341 (2017).

[18] M. N. Ali, J. Xiong, S. Flynn, J. Tao, Q. D. Gibson, L. M. Schoop, T. Liang, N. Haldolaarachchige, M. Hirschberger, N. P. Ong, and R. J. Cava, Nature **514**, 205 (2014).

[19] J. Jiang, Z. Liu, Y. Sun, H. Yang, C. Rajamathi, Y. Qi, L. Yang, C. Chen, H. Peng, C.-C. Hwang, S. Sun, S.-K. Mo, I. Vobornik, J. Fujii, S. Parkin, C. Felser, B. Yan, and Y. Chen, Nat. Commun. **8**, 13973 (2017).

[20] S. Thirupathaiah, R. Jha, B. Pal, J. S. Matias, P. K. Das, P. K. Sivakumar, I. Vobornik, N. C. Plumb, M. Shi,R. A. Ribeiro, and D. D. Sarma, Phys. Rev. B (R) **95**, 241105 (2017).

[21] H. Ma, P. Chen, B. Li, J. Li, R. Ai, Z. Zhang, G. Sun, K. Yao, Z. Lin, B. Zhao, R. Wu, X. Tang, X. Duan, and X. Duan, Nano Letters **18**, 3523 (2018).

[22] X. guaug Zheng, H. Kuriyaki, and K. Hirakawa, Journal of the Physical Society of Japan **58**, 622 (1989).

[23] Y.-C. Lin, D. O. Dumcenco, Y.-S. Huang, and K. Suenaga, Nat. Nanotechnol. **9**, 391 (2014).

[24] H. M. Hill, A. F. Rigosi, K. T. Rim, G. W. Flynn, and T. F. Heinz, Nano Lett. **16**, 4831 (2016).

[25] M. Salavati, Frontiers of Structural and Civil Engineering **13**, 486 (2018).

[26] T. Pillo, J. Hayoz, H. Berger, R. Fasel, L. Schlapbach, and P. Aebi, Phys. Rev. B **62**, 4277 (2000).

[27] L. Perfetti, P. A. Loukakos, M. Lisowski, U. Bovensiepen, H. Berger, S. Biermann, P. S. Cornaglia, A. Georges, and M. Wolf, Phys. Rev. Lett. **97**, 067402 (2006).

[28] C. Zhang, S. KC, Y. Nie, C. Liang, W. G. Vandenberghe, R. C. Longo, Y. Zheng, F. Kong, S. Hong, R. M.Wallace, and K. Cho, ACS Nano **10**, 7370 (2016).

[29] K. F. Mak, C. Lee, J. Hone, J. Shan, and T. F. Heinz, Phys. Rev. Lett. **105**, 136805 (2010).

[30] A. Kumar and P. K. Ahluwalia, The European Physical Journal B **85** (2012), 10.1140/epjb/e2012-30070-x.

[31] W. Choi, N. Choudhary, G. H. Han, J. Park, D. Akinwande, and Y. H. Lee, Mater. Today **20**, 116 (2017).

[32] M. Porer, U. Leierseder, J.-M. Menard, H. Dachraoui, L. Mouchliadis, I. E. Perakis, U. Heinzmann, J. Demsar, K. Rossnagel, and R. Huber, Nat. Mater. **13**, 857 (2014).

[33] L. J. Li, W. J. Zhao, B. Liu, T. H. Ren, G. Eda, and K. P. Loh, Applied Physics Letters **109**, 141902 (2016).

[34] Y. Ma, Y. Dai, M. Guo, C. Niu, Y. Zhu, and B. Huang, ACS Nano **6**, 1695 (2012).

[35] X. Zhu, Y. Guo, H. Cheng, J. Dai, X. An, J. Zhao, K. Tian, S. Wei, X. C. Zeng, C. Wu, and Y. Xie, Nat. Commun. **7** (2016), 10.1038/ncomms11210.

[36] H. Xiang, B. Xu, Y. Xia, J. Yin, and Z. Liu, Sci. Rep. **6** (2016), 10.1038/srep39218.

[37] Y. I. Joe, X. M. Chen, P. Ghaemi, K. D. Finkelstein, G. A. de la Pe na, Y. Gan, J. C. T. Lee, S. Yuan, J. Geck, G. J. MacDougall, T. C. Chiang, S. L. Cooper, E. Fradkin, and P. Abbamonte, Nat. Phys. **10**, 421 (2014).

[38] C.-X. Liu, Phys. Rev. Lett. **118**, 087001 (2017).

[39] S. C. de la Barrera, M. R. Sinko, D. P. Gopalan, N. Sivadas, K. L. Seyler, K. Watanabe, T. Taniguchi, A. W. Tsen, X. Xu, D. Xiao, and B. M. Hunt, Nat. Commun. **9** (2018), 10.1038/s41467-018-03888-4.

[40] A. Ramasubramaniam, D. Naveh, and E. Towe, Phys. Rev. B **84**, 205325 (2011).

[41] R. Das, B. Rakshit, S. Debnath, and P. Mahadevan, Phys. Rev. B **89**, 115201 (2014).

[42] H. C. P. Movva, T. Lovorn, B. Fallahazad, S. Larentis, K. Kim, T. Taniguchi, K. Watanabe, S. K. Banerjee, A. H. MacDonald, and E. Tutuc, Phys. Rev. Lett. **120**, 107703 (2018).

[43] M. Aghajanian, A. A. Mosto, and J. Lischner, Sci. Rep. **8** (2018), 10.1038/s41598-018-31941-1.

[44] H. E. Brauer, H. I. Starnberg, L. J. Holleboom, and H. P. Hughes, J. Phys.: Condens. Matter **7**, 7741 (1995).

[45] M. Moustafa, T. Zandt, C. Janowitz, and R. Manzke, Phys. Rev. B **80**, 035206 (2009).

[46] M. Moustafa, A. Ghafari, A. Paulheim, C. Janowitz, and R. Manzke, J. Electron Spectrosc. Relat. Phenom. **189**, 35 (2013).

[47] M. J. Mleczko, C. Zhang, H. R. Lee, H.-H. Kuo, B. Magyari-Kpe, R. G. Moore, Z.-X. Shen, I. R. Fisher, Y. Nishi, and E. Pop, Science Advances **3**, e1700481 (2017).

[48] A. Ghafari, M. Moustafa, G. D. Santo, L. Petaccia, and C. Janowitz, Appl. Phys. Lett. **112**, 182105 (2018).

[49] A. H. Reshak and S. Auluck, Physica B **353**, 230 (2004).

[50] A. Kumar, H. He, R. Pandey, P. K. Ahluwalia, and K. Tankeshwar, Phys. Chem. Chem. Phys. **17**, 19215 (2015).

[51] A. J. S. Machado, N. P. Baptista, B. S. de Lima, N. Chaia, T. W. Grant, L. E. Correa, S. T. Renosto, A. C. Scaramussa, R. F. Jardim, M. S. Torikachvili, J. A. Aguiar, O. C. Cigarroa, L. T. F. Eleno, and Z. Fisk, Phys. Rev. B **95** (2017), 10.1103/physrevb.95.144505.

[52] P. Tsipas, D. Tsoutsou, S. Fragkos, R. Sant, C. Alvarez, H. Okuno, G. Renaud, R. Alcotte, T. Baron, and A. Dimoulas, ACS Nano **12**, 1696 (2018).

[53] M. J. Mleczko, C. Zhang, H. R. Lee, H.-H. Kuo, B. Magyari-Kpe, R. G. Moore, Z.-X. Shen, I. R. Fisher, Y. Nishi, and E. Pop, Science Advances **3**, e1700481 (2017).

[54] S. Mangelsen, P. G. Naumov, O. I. Barkalov, S. A. Medvedev, W. Schnelle, M. Bobnar, S. Mankovsky, S. Polesya, C. Näther, H. Ebert, and W. Bensch, Phys. Rev. B **96**, 205148 (2017).

[55] A. Ghafari, M. Moustafa, G. D. Santo, L. Petaccia, and C. Janowitz, Appl. Phys. Lett. **112**, 182105 (2018).

[56] K. Nikonov, N. Ehlen, B. Senkovskiy, N. Saigal, A. Fedorov, A. Nefedov, C. Wll, G. D. Santo, L. Petaccia, and A. Grneis, Dalton Trans. **47**, 2986 (2018).

[57] G. Kresse and J. Furthmüller, Phys. Rev. B **54**, 11169 (1996).

[58] G. Kresse and D. Joubert, Phys. Rev. B **59**, 1758 (1999).

[59] J. P. Perdew, K. Burke, and M. Ernzerhof, Phys. Rev. Lett. **77**, 3865 (1996).

[60] A. A. Mostofi, J. R. Yates, Y.-S. Lee, I. Souza, D. Vanderbilt, and N. Marzari, Comput. Phys. Commun **178**, 685 (2008).

[61] C. Franchini, R. Kovacik, M. Marsman, S. S. Murthy, J. He, C. Ederer, and G. Kresse, J. Phys. : Condens. Matter **24**, 235602 (2012).

[62] W. A. Harrison, Electronic structure and the properties of solids: The physics of the chemical bond (Dover, New York, USA, 1967).

Chapter 5

Anomalous Electronic Properties of Rhenium Based Dichalcogenides, ReX_2 (X=S, Se)

5.1 Introduction

The transition metal dichalcogenides [1–4] have been studied closely among the two-dimensional materials, a story which began with the isolation of a single layer of graphene [5, 6]. The presence of a band gap in most of these members has led to exploring their use in electronics based on two-dimensional materials. The Mo and W based members in their most stable ground state, referred to as the 2H polymorph, are found to be semiconducting [7–10]. This happens because they have a formal d electron count of two on the transition metal site which is located in a trigonal prismatic crystal field arising from its anion neighbours. This leads to a level ordering in which the lowest set of crystal field levels with transition metal d character are doubly degenerate, thereby explaining the semiconducting ground state. However the same arguments should have us expect the Re based compounds which have three d electrons at each transition metal site to be metallic. For an odd number of electrons at each transitions metal site, one could have strong electron-electron interaction effects being responsible for the insulating ground state as in various transition metal monoxides. However electron-electron interactions are not expected to be strong among these materials. Further, an effective single particle calculation as carried out in the present work for ReS_2 has an insulating ground state. An alternative explanation for this could be the presence of magnetic order, however, we do not see any

evidence of magnetic ordering. MoS_2 in another polymorph, referred to as 1T, is found to be metallic by crystal field arguments. However, the system is unstable and dimerises, with pairs of Mo atoms coming closer by 0.43 Å, leading to a small bandgap of 0.045-0.09 eV opening up with the structural transition [11,12]. ReS_2 also has a 4 Re atom cluster in each unit cell which is suggestive of a Peierl's transition [13] in this system also. However, usually the band gap scales with the distortion in such instances, while here the bandgap is 1.08 eV which is significantly larger than what is expected. Alternate explanations that have been suggested are of a charge density wave that drives the tetramerisation [14], as well as the half-filling of the t_{2g} band that drives the distortions [15].

An aspect of these systems that has received a lot of attention in recent times has been the nature of the band gap as well as its variation as a function of the number of layers [16–20]. The close proximity of the direct and indirect band gap has contributed to this confusion. The Mo and W based TMDCs show a change in both the nature as well as the magnitude of the band gap. Taking the example of MoS_2, one finds that it has a direct band gap of 1.71 eV at the monolayer limit. This changes to an indirect band gap of 1.16 eV for a bilayer [18]. Additionally, there is a decrease in the bandgap with layers, reaching a value of 0.82 eV for the bulk. In contrast, ReS_2 has been unusual in the layer dependence of the band gap. It has been found to change by less than 0.1 eV in going from monolayer to bilayer, after which it remains almost constant. As the electronic structure changes with the number of layers have been found to be determined by interlayer hopping interactions [21], the small changes found here indicate that the interlayer hopping interactions are small.

In this work we have examined the unusual aspects of the electronic and structural properties of ReS_2. In order to probe the role of the presence of the four Re atom clusters, we have calculated the *ab-initio* electronic structure and mapped it onto a tight binding model. These calculations find an insulating state as the ground state. However, when hopping between the Re atoms of the cluster are switched off, the system is found to become metallic. This indicates that the formation of the Re clusters is responsible for the insulating state, with the cluster eigenfunctions determining the character of the band extrema. As a result, one has weakly dispersing bands contributing to the valence band maximum and conduction band minimum, in addition to being strongly localized on the Re atoms. This leads to the weak layer dependence of the band gap. Inspite of there being a large contribution to the bonding from Re-Re interactions, the shortest bondlengths are still those between Re and S atoms, implying that one would still find significant Re-S

interactions. This, we show, leads to a double hump feature in the vicinity of the Γ point for the highest occupied band of the monolayer. This is exemplified by artificially tuning the relative contributions arising from p-d and d-d interactions. This also leads to the close proximity of the direct and the indirect band gaps in these systems at the monolayer limit.

5.2 Methodology

The electronic structure of ReS_2 has been calculated using a plane wave implementation of density functional theory within the Vienna ab-initio simulation package (VASP) [25–28] which uses projected augmented wave (PAW) [29, 30] potentials. The generalized gradient approximation [31] was used for the exchange-correlation functional, and dispersional corrections were included within the DFT-D2 approach [32]. The experimental crystal structure [33] has been taken in the case of bulk ReS_2. A monolayer was constructed out of the bulk unit cell and a vacuum of 12 Å was included along the stacking direction which was along $\vec{a}$ in this case. While the lattice parameters were kept fixed at the experimental values, the internal positions were optimized in each case. To calculate the electronic structure self-consistently we used a k-points mesh of 8 x 8 x 8 for bulk and 1 x 8 x 8 for monolayer. A cutoff energy of 258.7 eV was used for the plane waves included in the basis. As Re is a 5d transition metal atom, spin-orbit interactions may be large. Hence spin-orbit interactions were included in the calculation of the electronic structure. In order to understand features of the electronic structure, the ab-initio bandstructure calculated without spin-orbit interactions was mapped onto a tight-binding model which had maximally localized wannier functions for its radial part. We used the VASP to Wannier90 interface for this analysis [34, 35]. Re d as well as S p states were included in the basis for the mapping.

5.3 Results and Discussions

The calculated band structure for bulk ReS_2 incorporating spin-orbit coupling is shown in Figure 5.1 along various symmetry directions. A direct band gap of 1.08 eV is found in this case with both the valence band maximum and conduction band minimum at the X point. This is similar to the values reported in the literature from experiment which

ranges from 1.3 eV [36,37] to 1.6 eV [22]. The calculated band structure for the monolayer is shown in Figure 5.2. Here, the band gap is found to increase to 1.32 eV.

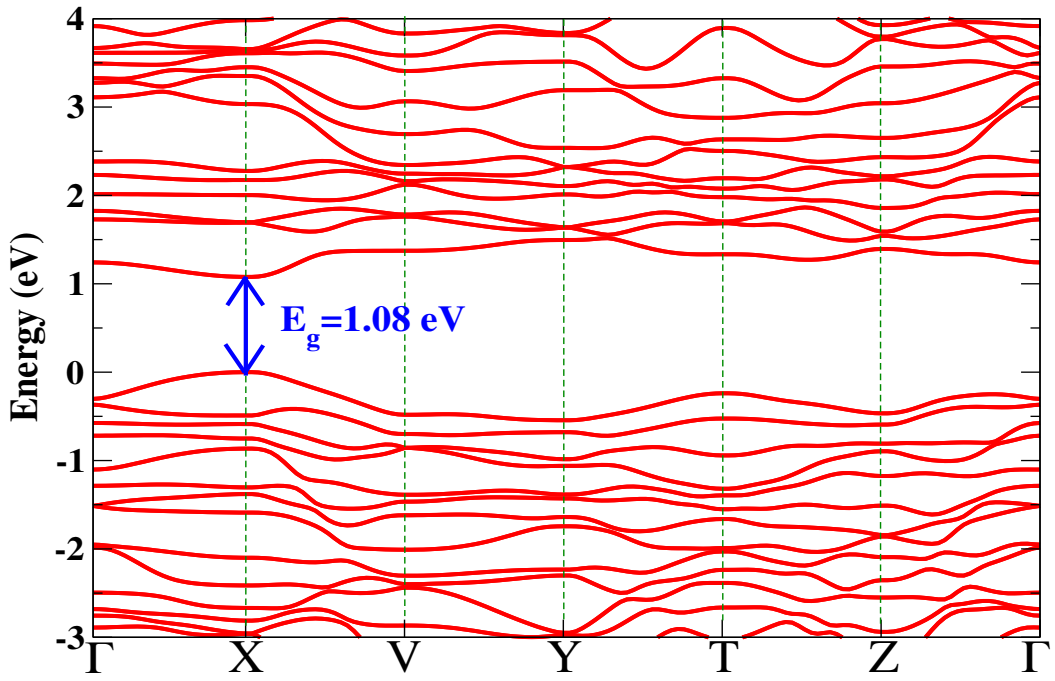

Figure 5.1: Band structure of bulk ReS_2, incorporating spin-orbit coupling

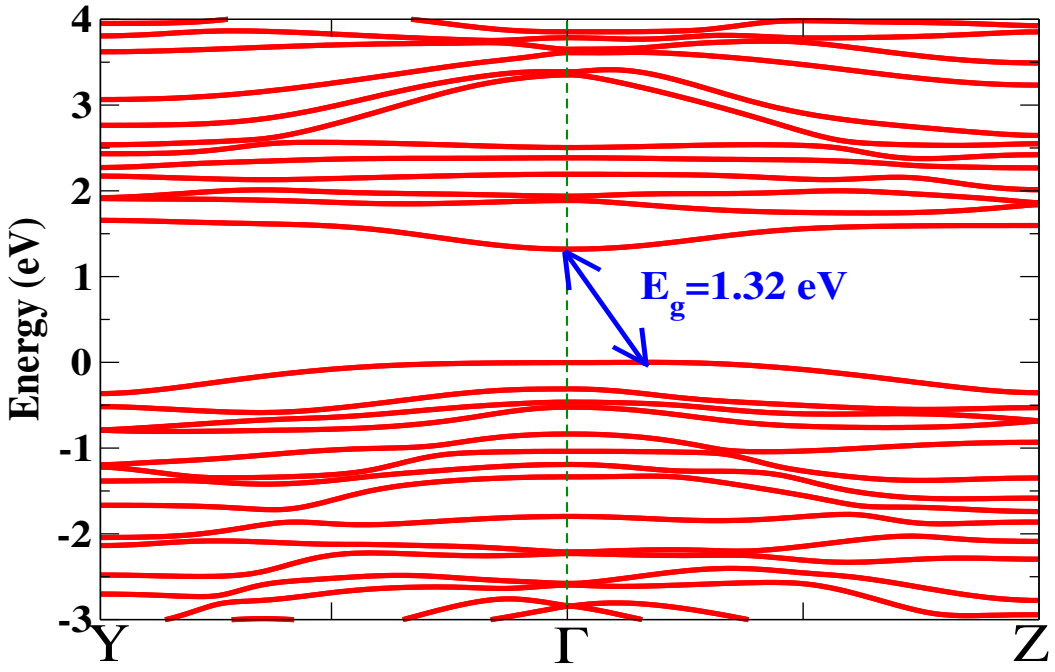

Figure 5.2: Band structure of monolayer ReS_2, incorporating spin-orbit coupling

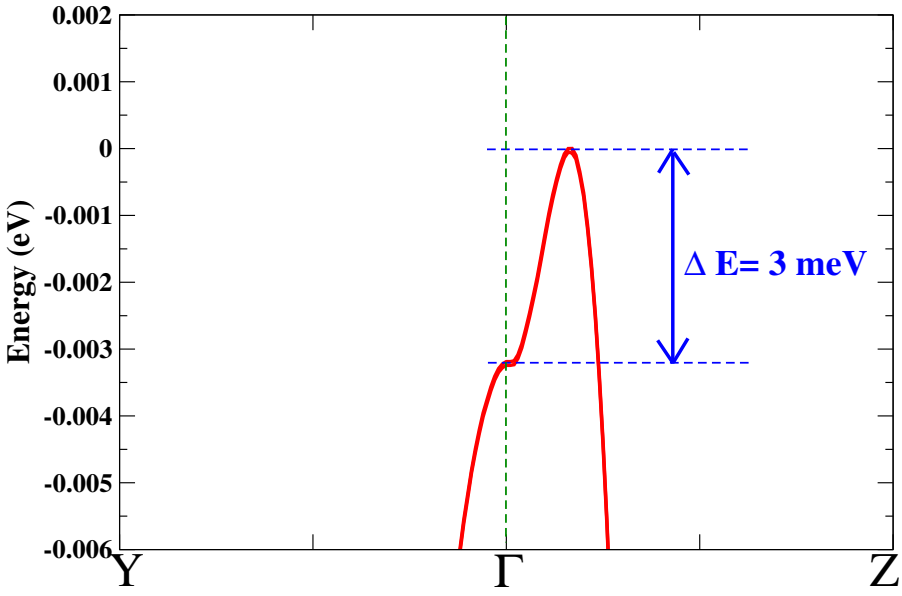

Figure 5.3: The difference in energy between highest occupied band at Γ and the VBM in the band structure of monolayer ReS_2

As the X point which had the band extrema for the bulk case is along the stacking direction of the van der Waals layers, we find that at the monolayer limit, the X point folds to Γ. The CBM is therefore found at Γ, however, the VBM is now at a k-point along the Γ-Z direction. This makes monolayer ReS_2 an indirect bandgap material. The highest occupied band at Γ is just 3 meV below the valence band maximum and this is shown in Figure 5.3. It is not often that we find two band extrema for the valence band maximum so close in energy, and we will examine this aspect later in the chapter. These values for the bandgap are similar to the values found in the literature using GGA for the exchange correlation functional [38], though approaches using GW have found a bandgap of 1.85 eV at the monolayer limit and a value of 1.57 eV for the bulk [39]. When we do not include spin-orbit interactions, the band gap for the bulk limit is found to be 1.23 eV [Fig. 5.4].

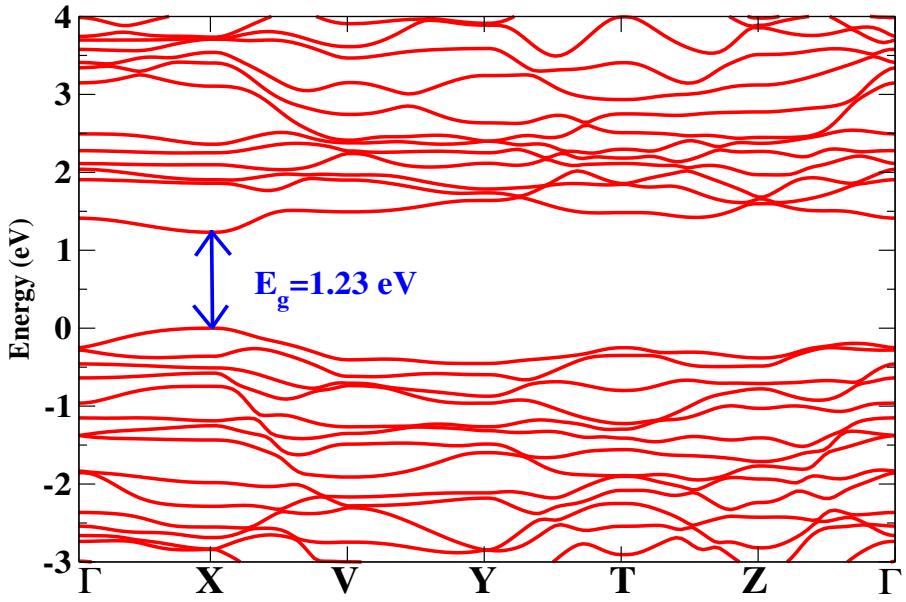

Figure 5.4: Ab-initio band dispersion of bulk ReS_2, without incorporating spin-orbit coupling

A dependence of both the nature of the band gap as well as the magnitude on the number of layers has been seen in other transition metal dichalcogenides. Contrasting the present results to the Mo based transition metal dichalcogenides, one finds that the decrease in the band gap in going from the monolayer to the bulk is just 0.24 eV. In contrast it is much larger for the Mo based transition metal dichalcogenides. This has been pointed out earlier from experiments by Tongay *et al.* [22]. Additionally the Mo based counterparts are direct band gap at the monolayer limit and become indirect beyond, in contrast to what is found here.

Re has a formal d^3 configuration in ReS_2, associated with the +4 oxidation state. The first question that follows is the origin of the insulating state. As the GGA based *ab-initio* electronic structure calculations are able to capture the insulating nature, we can infer that electron-electron interaction effects at the Re site do not play such an important role in opening up a bandgap in ReS_2. This is to be expected as ReS_2 involves a $5d$ transition metal atom for which the electron-electron interaction effects are expected to be weaker due to wider bands being formed. There is also no magnetic order found here, which could provide a possible explanation for the insulating state.

A closer examination of the structure, reveals some possible clues. The Re network that one finds in each layer consists of parallely running chains of interconnected Re clusters [Fig. 5.5(a)]. The Re plane is normal to the lattice vector $\vec{a}$. Each cluster is composed

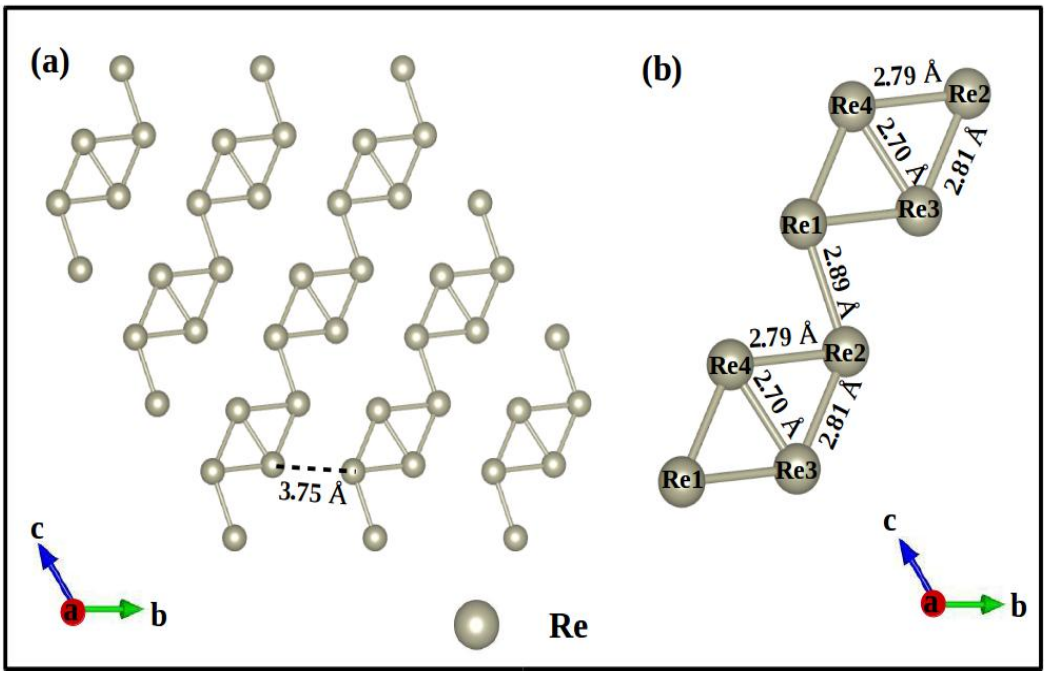

Figure 5.5: (a) Network of Re atoms in a plane. (b) Bondlengths between Re atoms belonging to adjacent Re clusters connected at their corners.

of four Re atoms located at the corners of a parallelogram, with two consecutive clusters along the chain connected through a bond of length 2.89 $\mathring{A}$. All the bonds within a given cluster are smaller than the bond connecting two clusters along the chain by atleast 0.08 $\mathring{A}$, and their bondlengths are shown in Figure 5.5(b). A quick scan of the literature of Re compounds with Re-Re bondlengths less than 2.81 $\mathring{A}$ finds that the nature of the bonding at these separations is discussed in terms of Re-Re bonding [40]. This then prompted us to examine the role of various structural components on the electronic structure. This was done by mapping the *ab-initio* band structure calculated without spin-orbit interactions onto a tight-binding model. We incorporated Re d states and S p states in the basis of our tight-binding model as they are the states that chiefly contribute around the Fermi energy [Fig. 5.6]. These states had maximally localized wannier functions as their radial parts, with the process of mapping involving optimization of the localization of the wannier functions. The spatial extent as measured by $<r^2>$ is found to be less than 2.3 $\mathring{A}^2$. Additionally we have a good description of the *ab-initio* band structure within the tight-binding model [Fig. 5.7], which allows us to selectively switch off certain interactions and examine its effect on the electronic structure.

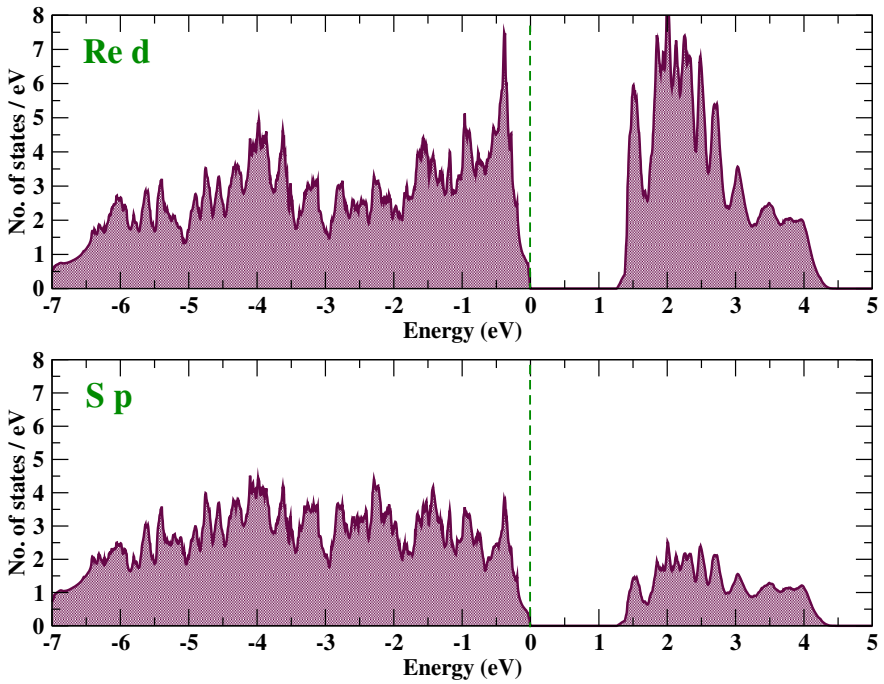

Figure 5.6: Orbital projected density of states for Re d and S p states of ReS_2. Fermi energy is set to zero.

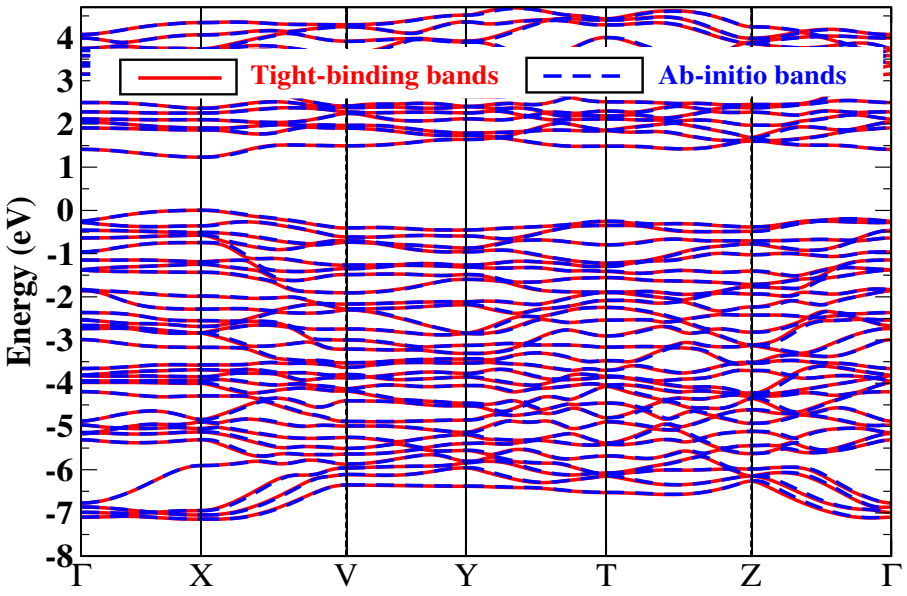

Figure 5.7: Ab-initio band structure of bulk ReS_2, without incorporating spin-orbit coupling, superposed with the band dispersions from the tight-binding model

[Fig. 5.9] shows the Brillouin zone of ReS_2. It appears that Γ-X direction in the reciprocal space corresponds to the out of plane direction in the direct lattice.

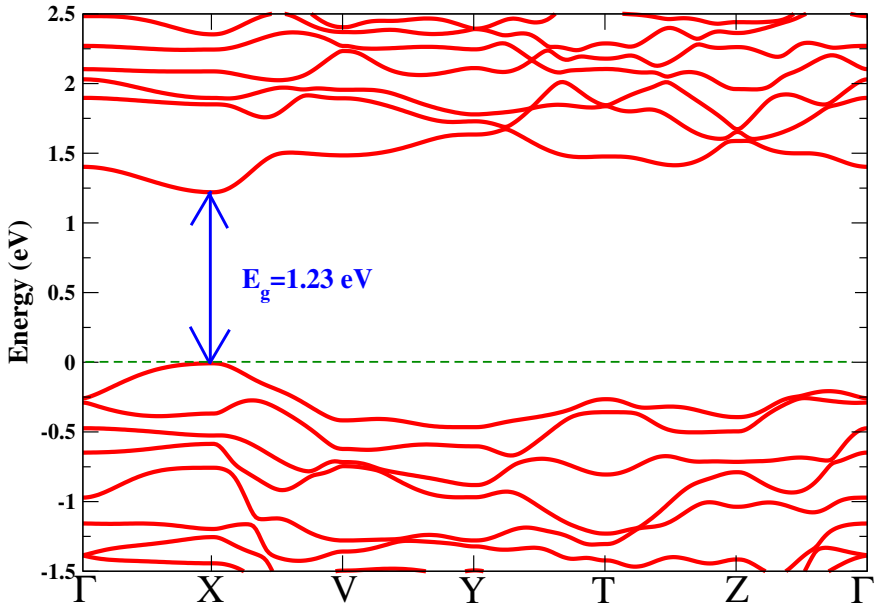

Figure 5.8: Tight-binding band dispersion of bulk ReS_2 without incorporating spin-orbit coupling

In order to probe the role of the Re-Re interactions, we first switch off the interactions betwen Re atoms belonging to different chains. The system remains insulating, however, we find a reduction in the band gap from 1.23 eV [Fig. 5.8] to 1.06 eV [Fig. 5.10]. The small change of 14% is consistent with the fact that the interchain Re-Re separation is 3.75 $\AA$, suggesting a weak coupling between the chains.

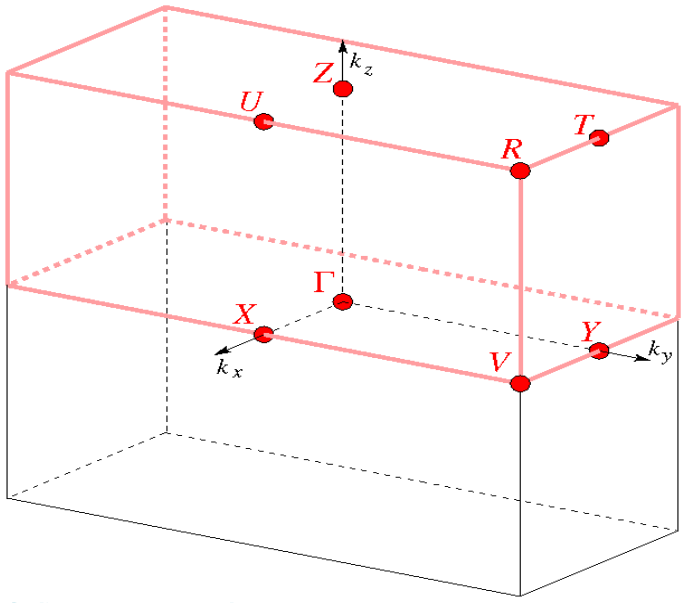

Figure 5.9: Brillouin zone of structure of ReS_2 in triclininc crystal structure with space group P-1 (Taken from 'Bilbao Crystallographic Server')

[Fig. 5.9] shows the Brillouin zone of ReS_2. It appears that Γ-X direction in reciprocal space corresponds to the out of plane direction in direct lattice.

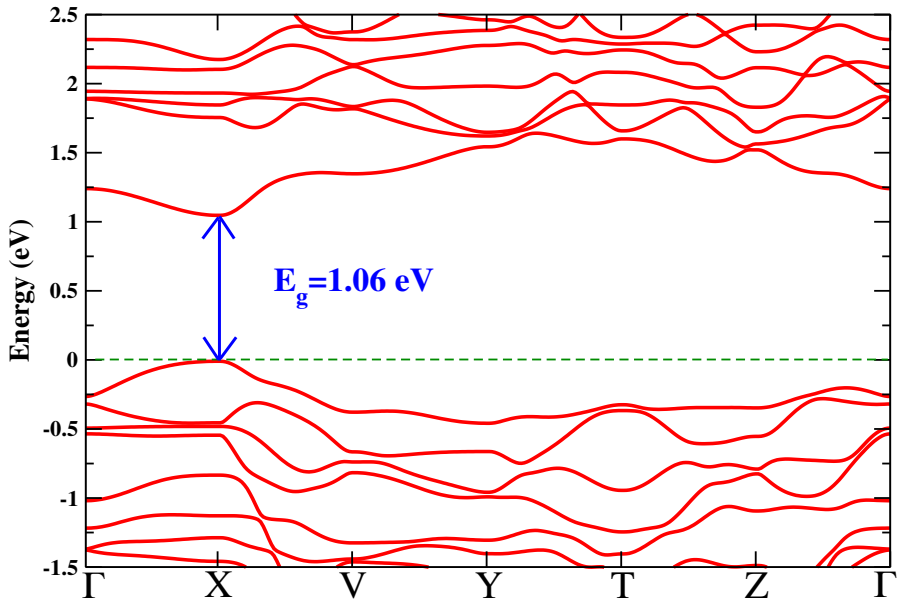

Figure 5.10: Band structure of bulk ReS_2, with the coulping between adjacent Re-chains switched off in the tight-binding model

We then proceeded to switch off the intercluster Re-Re interactions. The resulting band structure we find is still insulating, though the band gap is now reduced to 0.5 eV [Fig. 5.11]. As a final step we switched off the Re-Re interactions present in the 4 atom clusters. This led to a collapse of the band gap as shown in Figure 5.12, verifying that the formation of the clusters was responsible for the insulating state.

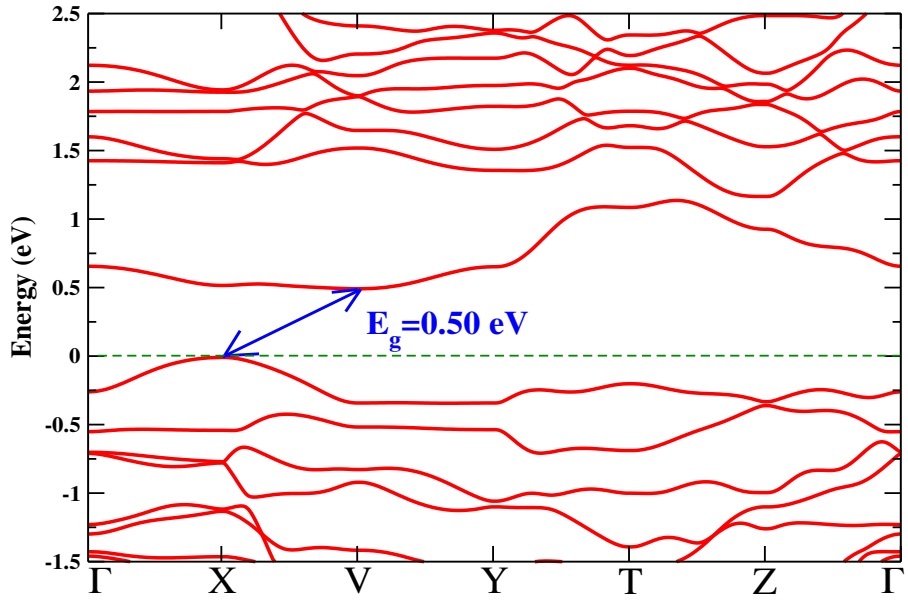

Figure 5.11: Band structure of bulk ReS_2, with the coupling between any two adjacent Re-clusters switched off in addition to switching off the coupling between Re-chains, as obtained from the tight-binding model

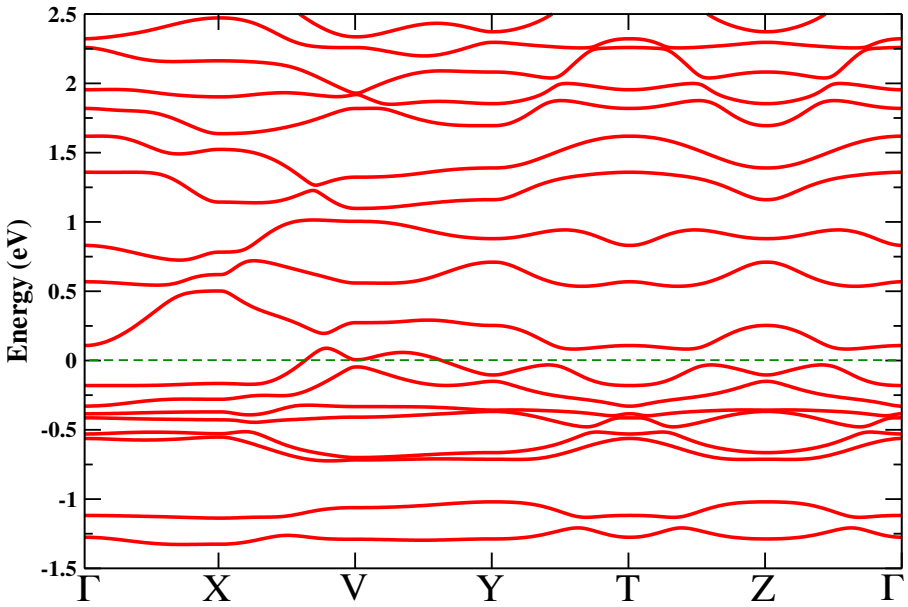

Figure 5.12: Band structure of bulk ReS_2, with all Re-Re hopping interactions switched off in the tight-binding model

We then go on to quantify the role of the Re-Re bonding. This is done by calculating the band energy within our tight-binding Hamiltonian, which is calculated as the sum over the occupied eigenvalues. The difference in the band energy for the full Hamiltonian and that calculated with the d-d interactions switched off gives us the contribution emerging

from Re-Re interactions alone. This turns out to contribute 13.37 eV, indicating the presence of significant Re-Re interactions, which is what drives the cluster formation.

Having understood the origin of the insulating state, we went on to examine the weak thickness dependence of the band gap that is found experimentally and reproduced within our calculations. In an earlier study [41], it was observed that in MX_2 (M=Mo,W and X=S,Se and Te), it is the interlayer interactions which are responsible for the change in the electronic structure with thickness. So for ReS_2, the weak dependence of the bandgap on thickness indicates negligible interlayer interactions. The most obvious factor governing the interlayer interactions could be the interlayer separation. Harrison's law [42], which provides a power law relationship between the hopping parameters and the interatomic distance, suggests that the interactions between two adjacent layers should be larger for a smaller interlayer separation. So we examined the experimental structure to determine the interlayer separation and compared it with that for 2H-MoS_2.The interlayer separation in ReS_2 is found to be 2.72 Å [Fig. 5.13(a)] and that in MoS_2 to be 2.98 Å [Fig. 5.13(b)]. So it appears puzzling that despite the interlayer separation being smaller, the interlayer interactions are weak. This also indicates that the interlayer separation is not a good parameter as a measure of the interlayer interaction in a material. Here, as the coupling is weak between the layers, it could be that the layers come closer to maximize the energy gain from interlayer interactions leading to a smaller separation compared to MoS_2.

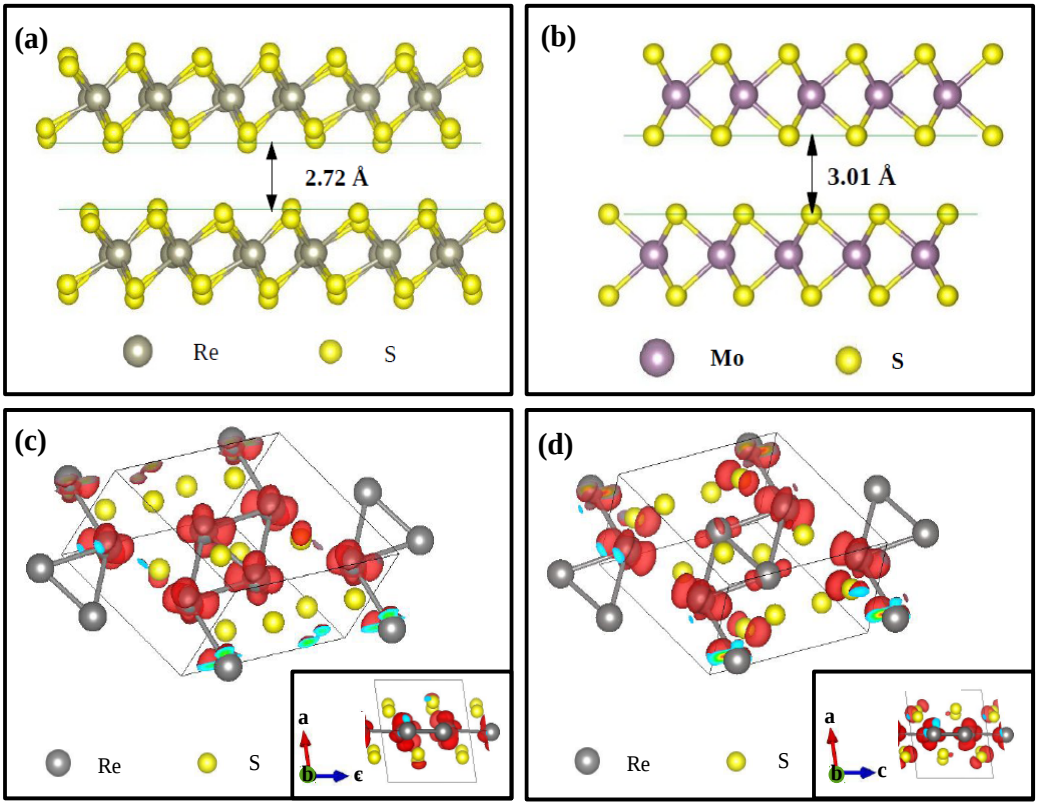

Figure 5.13: Interlayer spacing in (a) ReS_2 and (b) MoS_2. Charge density of (c) valence band maximum and (d) conduction band minimum in ReS_2

The next possibility that can influence the interlayer interaction is the nature of the orbitals associated with the conduction band minimum and the valence band maximum. Earlier work had shown that for MoS_2, the highest occupied band at Γ is contributed by d_{z^2} of Mo and p_z of S, both of which are directed out-of-plane. On the other hand, the highest occupied band at K is contributed by in-plane $d_{x^2-y^2}$ and d_{xy} orbitals of Mo. Adding the next layer for the bilayer allows for interactions between the orbitals of the two layers. This shifts the valence band maximum of the monolayer from K to Γ. Similarly, the conduction band minimum of monolayer MoS_2 at K is contributed by in-plane d-orbitals of Mo whereas at T it is contributed by out-of-plane orbitals. Hence for the bilayer, the CBM shifts to T due to interactions between the out-of-plane orbitals of two adjacent layers. This also explains the large changes that we see in the electronic structure with thickness in MoS_2. As we have discussed earlier, in ReS_2 a band gap opens up as a result of the interactions between the Re atoms within each cluster that we find in the structure. The interactions between neighbouring clusters along the one-dimensional chains formed enhance the band gap, with the coupling between the chains enhancing it further. This analysis clearly indicates that the wavefunctions corresponding to the VBM

and the CBM are found to be dominantly localized on the Re atoms. This is consistent with earlier reports in the literature [38]. Plotting the corresponding charge densities [Fig. 5.13(c) and 5.13(d)], we find that they remain confined principally in the plane containing the transition metal atoms and don't spread into the van der Waals gap. Consequently, the interlayer hopping interaction is quite weak here.

One finds another aspect about the electronic structure of ReS_2 that is unusual. At the monolayer limit, one finds that it is indirect gap, with the direct gap transition energy just 3 meV higher in energy. For the bulk case, however, we find that it is direct. These results are in contrast with the Mo based TMDs where one finds a direct band gap at the monolayer limit and an indirect band gap beyond. Also the presence of two closely lying band gap transitions at the monolayer limit is puzzling. Examining the band dispersions, one finds that for the bulk case, the band extrema lie at the X point, where ΓX is parallel to the stacking direction. In the monolayer case, we have the VBM along ΓZ direction. Examining the structure, the intercluster coupling could have a larger value along this direction in contrast to the ΓY direction where the electronic structure is dictated by interchain interactions. A part of the intercluster interaction emerges from *p-d* interactions and so has a different dependence compared to the part originating from *d-d* interactions. This results in the small rise as we move away from Γ along this direction, and hence the VBM lies along this direction. This effect would have been there for the bulk case also, except that the stronger inter-layer hopping interactions leads to the valence band maximum at the X point. To examine the hypothesis of competing p-d and d-d interactions giving rise to the hump of the highest occupied band along the ΓZ direction, we work with the tight-binding Hamiltonian which allows us to vary one set of interactions, keeping the other fixed. The results of the calculations varying the strength of the p-d interactions keeping the d-d interactions fixed for three cases are shown in Figure 5.14 along ΓY and ΓZ directions. The first is the result in the the absence of any scaling. The second is for the case where the p-d interaction strengths are scaled to 80 % of their values. The third is for the case where the p-d interaction strengths are scaled to 120 % of their values. The hump that we find becomes more prominent for the case where the p-d interaction strengths are scaled down. This indicates that while the d-d interactions would like the band to disperse downwards, the p-d interactions would like the band to disperse upwards. Increasing the component of the p-d interactions to 120 % removes the observed hump. In the context of MX semiconductors, the hump has been discussed in terms of a level repulsion picture of higher and lower energy levels [43]. We present an alternate explanation in the present case.

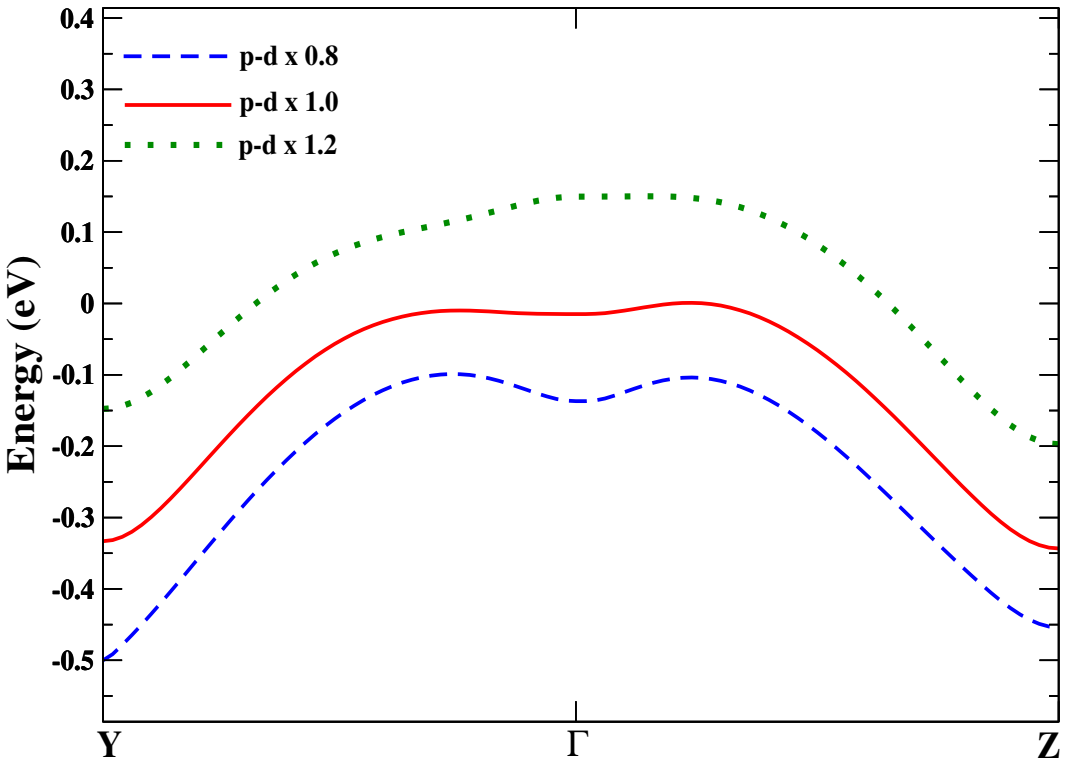

Figure 5.14: Dispersion of the highest occupied band along ΓY and ΓZ directions calculated for monolayer ReS_2 within the mapped tight-binding model with the p-d interactions at 80% (blue dashed), 100% (red solid) and 120% (green dotted) of their mapped values.

There has been a lot of discussion in the literature of the nature of the bandgap at the monolayer as well as the bulk limit. Gehlman at al. [39] use GW calculations to address this question and find an indirect bandgap at both the monolayer as well as the bulk limit. On the other hand Zhong et al. [38] find a direct gap for the monolayer. Our work finds the monolayer to have an indirect gap, though the direct one is just 3 meV larger. The small energetics therefore make it difficult to conclusively settle the issue. The cluster formation leads to small intercluster interactions. Additionally we find that the simultaneous presence of p-d interactions as well as d-d interactions leads to the small rise in the dispersion of the highest occupied band along ΓZ direction before it decreases again. An additional problem is that the interlayer separation from experiment is found to be 2.72 Å while an optimization using dispersion corrections gives us 2.50 Å. This modifies the dispersional width of the highest occupied band in the ΓX direction by 0.05 eV. So a competition of the dispersional width in the ΓX and ΓZ directions determines the nature of the bandgap. While calculations have played an important role in addressing the nature of the bandgap, uncertainties between different approaches exist because of the need for accurate values of the interlayer separations.

We went further on to investigate another Rhenium based dichalcogenide, namely $ReSe_2$. We enquire whether $ReSe_2$ has similar issues as we witnessed in ReS_2. Figure 5.15 shows the ab-initio band structure of bulk $ReSe_2$ as calculated by us incorporating spin-orbit coupling. Earlier experimental studies using optical absorption spectroscopy had found bulk $ReSe_2$ to have an indirect bandgap of 1.17 to 1.19 eV [44, 45]. From our calculated band structure, we found bulk $ReSe_2$ to have a direct bandgap of 1.01 eV with both the conduction band minimum and the valence band maximum lying at the high-symmetry k-point X. We remind ourselves that for bulk ReS_2 also, the VBM and CBM were at X-point. Our calculated value of the bandgap of $ReSe_2$ is similar to the values found in earlier density functional theory based calculations that range from 0.86 to 1.06 eV [46, 48]. But these calculations found the bandgap to be indirect. However, use of GdW approximation has found the bandgap to turn direct with a value of 1.49 eV [48].

So, same as ReS_2, our band structure calculations establishes bulk $ReSe_2$ to be semiconducting. In $ReSe_2$ also, the Re ion is in 4+ valence state, leading to d^3 configuration. So, going by the same logic as we put forth in the case of ReS_2, the origin of the semiconducting property of $ReSe_2$ is worth probing into.

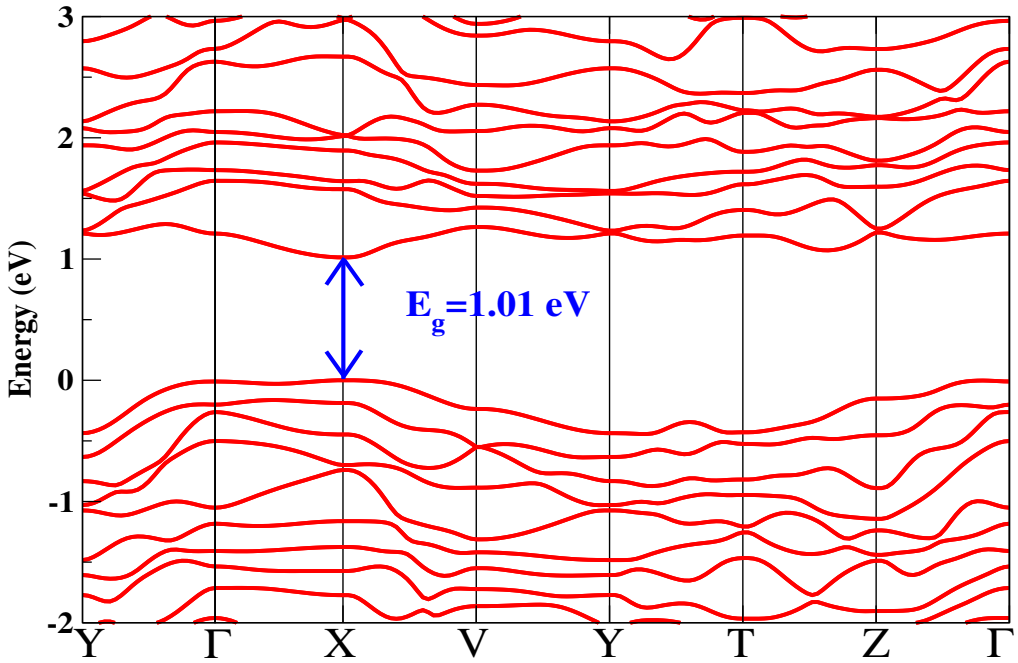

Figure 5.15: Band structure of bulk $ReSe_2$, incorporating spin-orbit coupling

The calculated band structure of monolayer $ReSe_2$ has been shown in Figure 5.16 which finds an indirect gap of 1.10 eV with the valence band maximum lying at a k-point between high-symmetry points Y and Γ. For monolayer ReS_2, the VBM was at a k-point between

Γ and Z, making monolayer ReS_2 indirect bandgap. Earlier density functional theory based calculations had found monolayer $ReSe_2$ to have an indirect gap ranging from 1.15 to of 1.34 eV [46, 47, 49]. Most of these calculations showed an indirect nature of the gap while one set of calculations has found the bandgap to be direct [47]. Incorporation of self-energy corrections in GW method finds the gap to be direct with a value of 2.3 eV [49]. So, as found from our calculations, in going from bulk to monolayer, the bandgap changes by 0.09 eV, which is small. So, similar to ReS_2, $ReSe_2$ shows weak thickness dependence of bandgap. It is worth noting that the change in the bandgap in going from bulk to monolayer is much smaller in $ReSe_2$ than in ReS_2. For ReS_2, it was 0.24 eV. So the layer dependence of bandgap is weaker in $ReSe_2$.

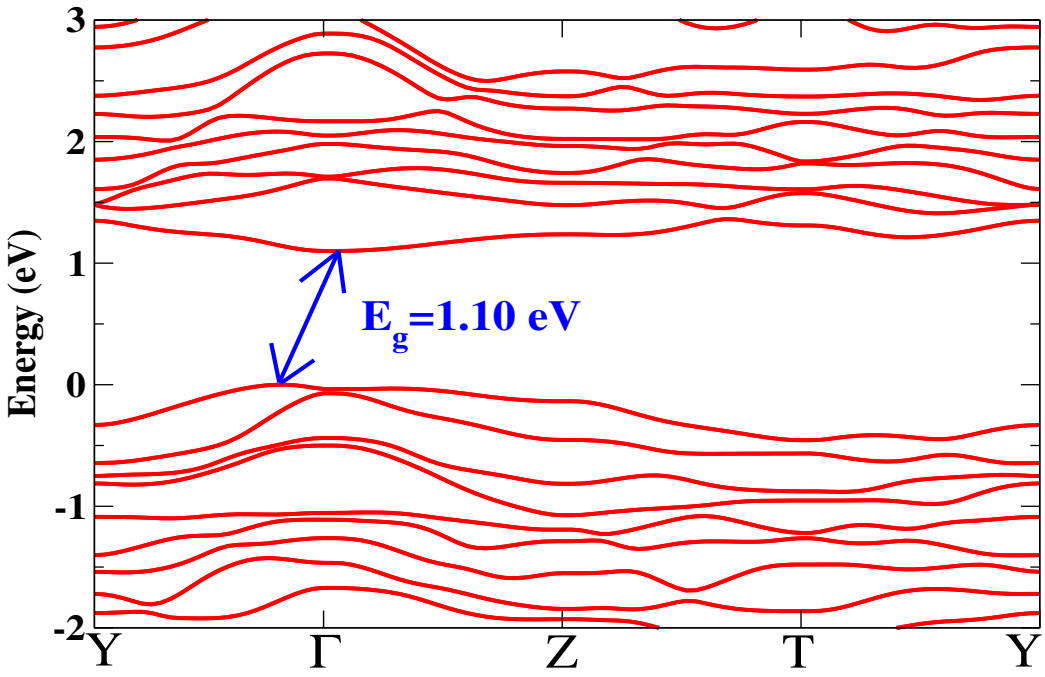

Figure 5.16: Band structure of monolayer $ReSe_2$, incorporating spin-orbit coupling

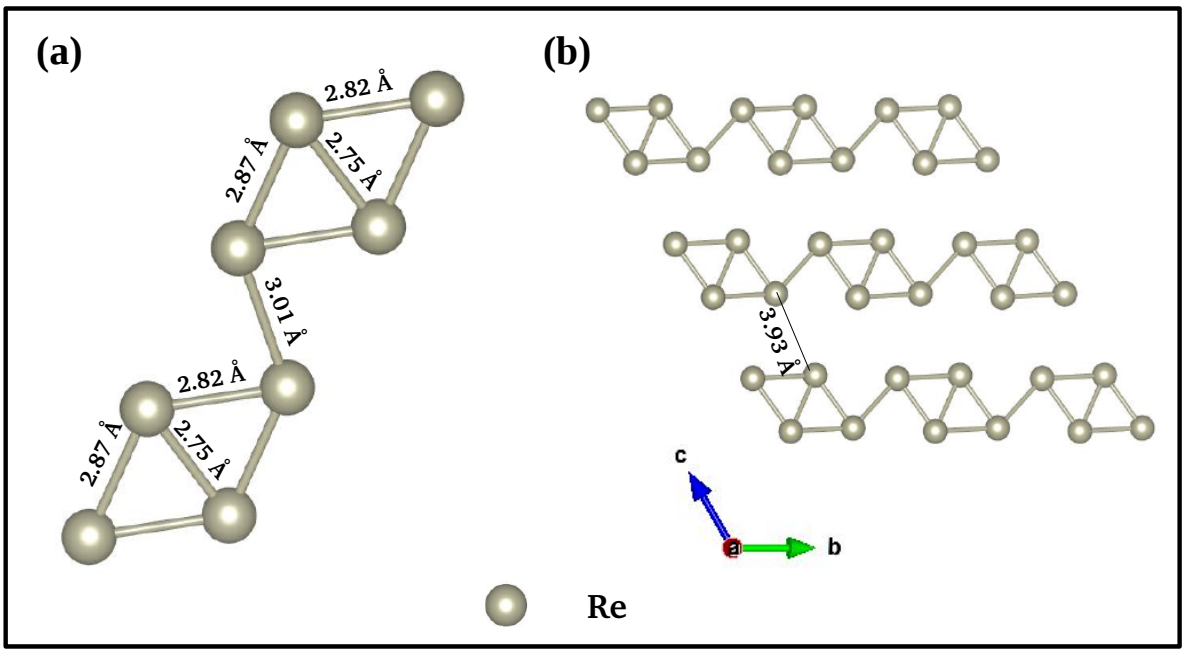

Figure 5.17: (a) Network of Re atoms in a plane in $ReSe_2$. (b) Bondlengths between Re atoms belonging to adjacent Re clusters connected at their corners in $ReSe_2$.

Looking at the structure, we see that similar to ReS_2, each Re plane in $ReSe_2$ consists of diamond chains, i.e. interconnected clusters of Re atoms in shape of parallellograms [Fig. 5.17(b)]. All the Re-Re bondlengths within each cluster are smaller than the bondlength connecting two adjacent clusters [Fig. 5.17(a)]. The intracluster bondlengths vary from 2.75 Å to 2.87 Å. The intercluster bondlength is 3.01 Å. The distance between two neighbouring chains is 3.93 Å.

To study the effect of different structural motifs on the electronic structure, we mapped the *ab-initio* band structure of $ReSe_2$ calculated without spin-orbit interactions [Fig. 5.18] onto a tight-binding model with maximally localized wannier functions as the basis states, similar to the case for ReS_2. We took Re d and Se p states into our basis. We got a good agreement between the *ab-initio* band structure and the tight-binding bands [Fig. 5.19]. We note that the bandgap for bulk $ReSe_2$ without incorporating spin-orbit coupling is 1.13 eV and it turns out to be indirect. The valence band maximum lies between high-symmetry points X and V [Fig. 5.18].

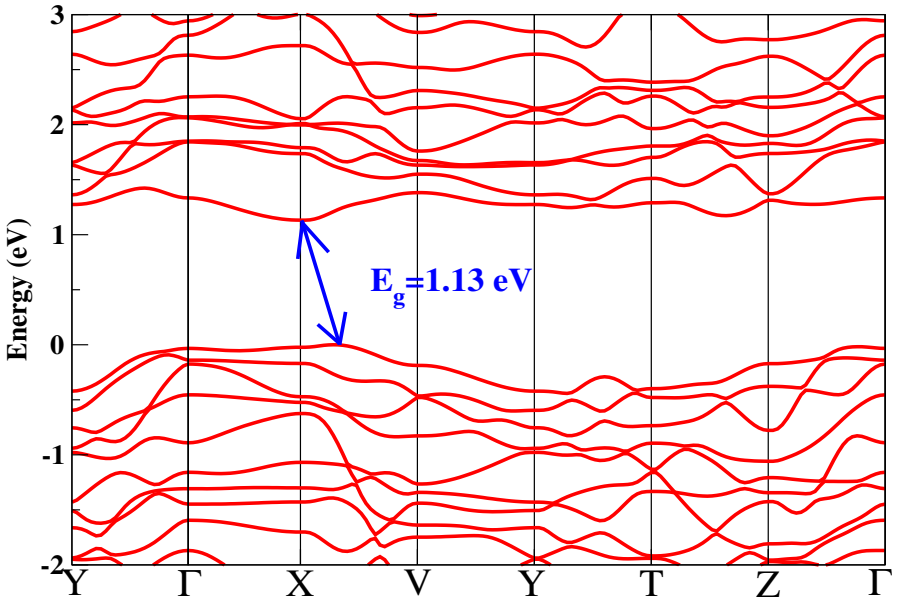

Figure 5.18: Ab-initio band dispersion of bulk $ReSe_2$, without incorporating spin-orbit coupling

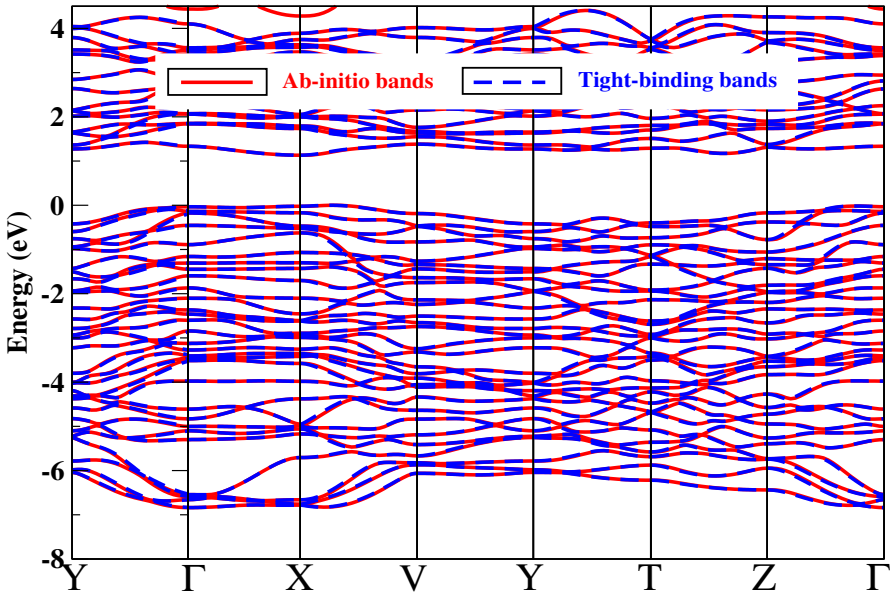

Figure 5.19: Ab-initio band structure of bulk $ReSe_2$, without incorporating spin-orbit coupling, superposed with the band dispersions from the tight-binding model

We follow the same series of steps as were performed for ReS_2. We first switch off all the Re-Re hopping interactions and the resulting band structure shows metallic character [Fig. 5.20]. Next we switch off the interchain coupling and the system continues to be insulating [Fig. 5.21]. The bandgap reduces from 1.13 eV [Fig. 5.18] to 0.97 eV [Fig. 5.21]. So the change in the bandgap due to switching off the interchain interaction is 14

% which reflects weak coupling between chains similar to the case of ReS_2. This can be justified by considering the fact that the distance between chains is 3.93 Å [Fig. 5.17(b)].

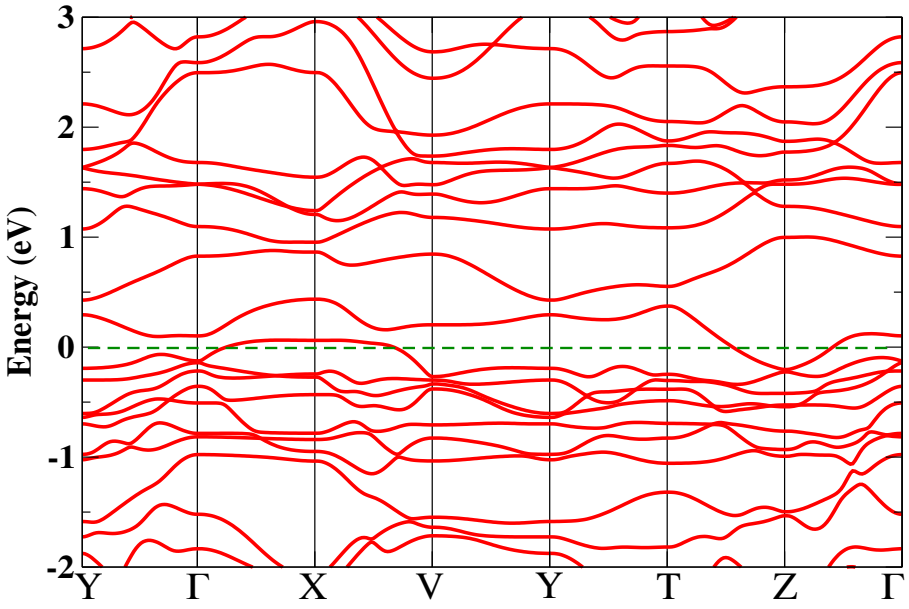

Figure 5.20: Band structure of bulk $ReSe_2$, with all Re-Re hopping interactions switched off in the tight-binding model

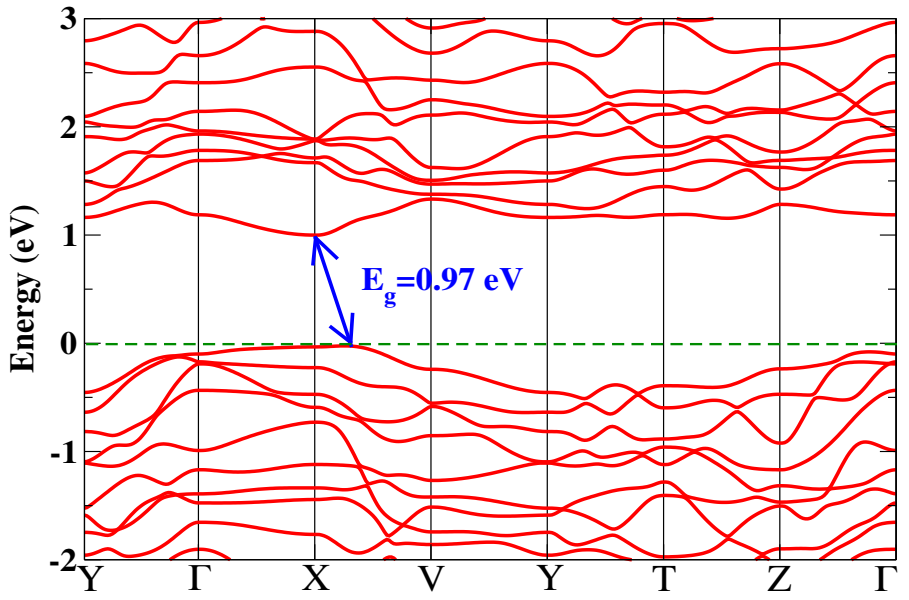

Figure 5.21: Band structure of bulk $ReSe_2$, with the coulping between adjacent Re-chains switched off in the tight-binding model

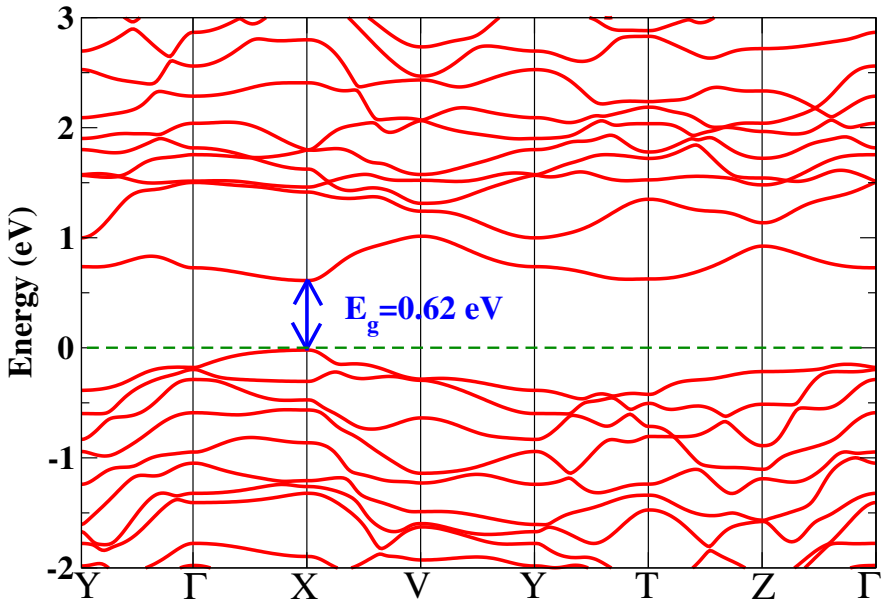

Figure 5.22: Band structure of bulk $ReSe_2$, with the coupling between any two adjacent Re-clusters switched off in addition to switching off the coupling between Re-chains, as obtained from the tight-binding model

In the following step, we switched off the Re-Re coupling between any two adjacent clusters connected at the corners and the resulting band structure still remains insulating with the band gap reduced to 0.62 eV [Fig. 5.22]. This establishes the fact that it is the intracluster interactions that are responsible for the insulating character. So, instead of considering individual Re atoms, we should consider the Re-clusters. Re ions within each cluster interact among themselves and the resulting molecular like orbitals get occupied with electrons to result in the semiconducting ground state for this material.

We then focussed our attention on the other issue which is the weak layer dependence of the bandgap found in $ReSe_2$, which is even weaker than ReS_2. We followed the same approach as we adopted for ReS_2 to investigate the underlying physics behind the weak layer dependence of bandgap in $ReSe_2$. We first enquired whether the interlayer separation can account for the weak layer dependence. A weak layer dependence of bandgap reflects a weak interlayer hopping interaction in $ReSe_2$. A weaker interlayer interaction in $ReSe_2$ would have one expect a larger interlayer spacing in $ReSe_2$. We compared the interlayer spacing in $ReSe_2$ with that in MoS_2 [Fig. 5.23(a) and (b)]. We found that the interlayer spacing is 2.61 Å for $ReSe_2$ [Fig. 5.23(a)] while it is 2.98 Å for MoS_2 [Fig. 5.23(b)]. So, the interlayer separation is indeed smaller in $ReSe_2$ despite the interlayer interaction being weaker. This establishes the fact that, similar to ReS_2, it is not the interlayer spacing that is dictating the interlayer interaction in $ReSe_2$.

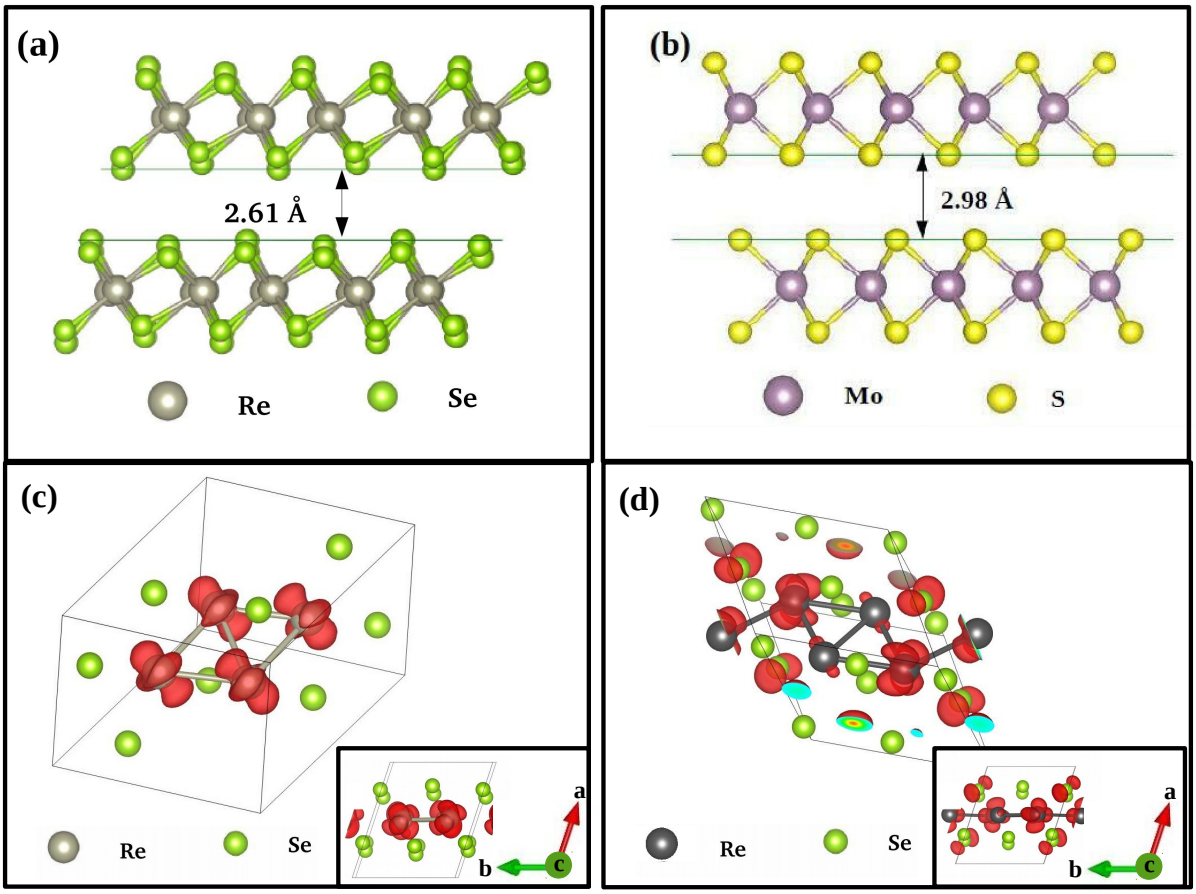

Figure 5.23: Interlayer spacing in (a) $ReSe_2$ and (b) MoS_2. Charge density of (c) valence band maximum and (d) conduction band minimum in $ReSe_2$

The next factor capable of influencing the interlayer hopping interaction is the nature of the orbitals associated with the valence band maximum and the conduction band minimum. We plotted the charge densities corresponding to VBM [Fig. 5.23(c)] and CBM [Fig. 5.23(d)] of $ReSe_2$. We find them to be strongly localized on the Re atoms with Se atoms having small in-plane contribution. So there is very weak overlap of the associated wavefunctions between two adjacent layers. This leads to very weak interlayer hopping interaction. Thus the weak layer dependence of bandgap in $ReSe_2$ is explained.

5.4 Conclusion

In conclusion, we have examined the unusual insulating state associated with a d^3 configuration at the Re site in ReS_2. and $ReSe_2$. We find that this is associated with the 4 Re atoms cluster found in its crystal structure. The presence of metallic bonding between these Re atoms results in the insulating state with VBM and CBM strongly localized in

the Re layer. This leads to the weak interaction between any two layers in ReS_2 and $ReSe_2$, despite the interlayer separation being much smaller than the 2H-MoS_2 which exhibits a strong layer dependence.

Bibliography

[1] Q. H. Wang, K. Kalantar-Zadeh, A. Kis, J. N. Coleman, and M. S. Strano, Nat. Nano. **7**, 699-712 (2012).

[2] S. Balendhran, S. Walia, H. Nili, J. Z. Ou, S. Zhuiykov, R. B. Kaner, S. Sriram, M. Bhaskaran, and K. Kalantar-zadeh, Adv. Funct. Mater. **23**, 3952-3970 (2013).

[3] J. N. Coleman, M. Lotya, A. O'Neill, S. D. Bergin, P. J. King, U. Khan, K. Young, A. Gaucher, S. De, R. J. Smith, I. V. Shvets, S. K. Arora, G. Stanton, H.-Y. Kim, K. Lee, G. T. Kim, G. S. Duesberg, T. Hallam, J. J. Boland, J. J. Wang, J. F. Donegan, J. C. Grunlan, G. Moriarty, A. Shmeliov, R. J. Nicholls, J. M. Perkins, E. M. Grieveson, K. Theuwissen, D. W. McComb, P. D. Nellist, and V. Nicolosi, Science **331**, 568-571 (2011).

[4] Y. Zhang, J. Ye, Y. Matsuhashi, and Y. Iwasa, Nano Lett. **12**, 1136-1140 (2012).

[5] K. S. Novoselov, A. K. Geim, S. V. Morozov, D. Jiang, Y. Zhang,S. V. Dubonos, I. V. Grigorieva, and A. A. Firsov, Science **306**, 666-669 (2004).

[6] K. S. Novoselov, A. K. Geim, S. V. Morozov, D. Jiang, M. I. Katsnelson, I. V. Grigorieva, S. V. Dubonos, and A. A. Firsov, Science **438**, 197-200 (2005).

[7] C. Lee, H. Yan, L. E. Brus, T. F. Heinz, J. Hone, and S. Ryu, ACS Nano **4**, 2695-2700 (2010).

[8] S. Lebègue and O. Eriksson, Phys. Rev. B **79**, 115409-115413 (2009).

[9] G. L. Frey, S. Elani, M. Homyonfer, Y. Feldman, and R. Tenne, Phys. Rev. B **57**, 6666-6671 (1998).

[10] K. K. Kam and B. A. Parkinson, J. Phys. Chem **86**, 463-467 (1982).

[11] X. Qian, J. Liu, L. Fu, and J. Li, Science **346**, 1344-1347 (2014).

[12] B. Pal, A. Singh, S. G., P. Mahale, A. Kumar, S. Thirupathaiah, H. Sezen, M. Amati, L. Gregoratti, U. V. Waghmare, and D. D. Sarma, Phys. Rev. B **96**, 195426 (2017).

[13] E. Canadell, A. LeBeuze, M. A. E. Khalifa, R. Chevrel, and M. H. Whangbo, J. Am. Chem. Soc. **111**, 3778 (1989).

[14] J.-H. Choi and S.-H. Jhi, Journal of Physics: Condensed Matter **30**, 105403 (2018)

[15] D. Pasquier and O. V. Yazyev, Phys. Rev. B **100**, 201103 (2019).

[16] A. Kuc, N. Zibouche, and T. Heine, Phys. Rev. B **83**, 245213 (2011).

[17] W. S. Yun, S. W. Han, S. C. Hong, I. G. Kim, and J. D. Lee, Phys. Rev. B **85**, 033305 (2012).

[18] K. F. Mak, C. Lee, J. Hone, J. Shan, and T. F. Heinz, Phys. Rev. Lett. **105**, 136805 (2010).

[19] W. Jin, P.-C. Yeh, N. Zaki, D. Zhang, J. T. Sadowski, A. Al- Mahboob, A. M. van der Zande, D. A. Chenet, J. I. Dadap, I. P. Herman, P. Sutter, J. Hone, and R. M. Osgood, Phys. Rev. Lett. **111**, 106801 (2013).

[20] L. Zhang and A. Zunger, Nano Lett. **15**, 949-957 (2015).

[21] S. K. Pandey, R. Das, and P. Mahadevan, ACS Omega **5**, 15169 (2020)

[22] S. Tongay, H. Sahin, C. Ko, A. Luce, W. Fan, K. Liu, J. Zhou, Y.-S. Huang, C.-H. Ho, J. Yan, D. F. Ogletree, S. Aloni, J. Ji, S. Li, J. Li, F. M. Peeters, and J. Wu, Nat. Comm. **5**, 3252 (2014).

[23] J. L. Webb, L. S. Hart, D. Wolverson, C. Chen, J. Avila, and M. C. Asensio, Phys. Rev. B **96**, 115205 (2017).

[24] D. Biswas, A. M. Ganose, R. Yano, J. M. Riley, L. Bawden, O. J. Clark, J. Feng, L. Collins-Mcintyre, M. T. Sajjad, W. Meevasana, T. K. Kim, M. Hoesch, J. E. Rault, T. Sasagawa, D. O. Scanlon, and P. D. C. King, Phys. Rev. B **96**, 085205 (2017).

[25] G. Kresse and J. Hafner, Phys. Rev. B **47**, 558-561 (1993).

[26] G. Kresse and J. Hafner, Phys. Rev. B **49**, 14251-14269 (1994).

[27] G. Kresse and J. Furthmüller, Comput. Mat. Sci. **6**, 15-50 (1996).

[28] G. Kresse and J. Furthmüller, Phys. Rev. B **54**, 11169-11186 (1996).

[29] P. E. Blochl, Phys. Rev. B **50**, 17953-17979 (1994).

[30] G. Kresse and D. Joubert, Phys. Rev. B **59**, 1758-1775 (1999).

[31] J. P. Perdew, K. Burke, and M. Ernzerhof, Phys. Rev. Lett. **77**, 3865-3868 (1996).

[32] S. Grimme, Journal of Computational Chemistry **27**, 1787-1799 (2006).

[33] H. H. Murray, S. P. Kelty, R. R. Chianelli, and C. S. Day, Inorg. Chem **33**, 4418-4420 (1994).

[34] A. A. Mostofi, J. R. Yates, Y.-S. Lee, I. Souza, D. Vanderbilt, and N. Marzari, Computer Physics Communications **178**, 685-699 (2008).

[35] C. Franchini, R. Kovacik, M. Marsman, S. Murthy, J. He, C. Ederer, and G. Kresse, J. Phys. Cond. Mat. **24**, 235602 (2012).

[36] S. P. Kelty, A. F. Ruppert, R. R. Chianelli, J. Ren, and M. Whangbo, J. Am. Chem. Soc. **116**, 7857 (1994).

[37] C. H. Ho, Y. S. Huang, K. K. Tiong, and P. C. Liao, Phys. Rev, B **58**, 16130 (1998).

[38] H.-X. Zhong, S. Gao, J.-J. Shi, and L. Yang, Phys. Rev. B **92**, 115438 (2015).

[39] M. Gehlmann, I. Aguilera, G. Bihlmayer, S. Nemsak, P. Nagler, P. Gospodaric, G. Zamborlini, M. Eschbach, V. Feyer, F. Kronast, E. M lynczak, T. Korn, L. Plucinski, C. Schüller, S. Blügel, and C. M. Schneider, Nano Lett. **17**, 5187 (2017).

[40] F. A. Cotton and C. B. Harris, Inorg. Chem. **6**, 5 (1967).

[41] S. K. Pandey, R. Das, and P. Mahadevan, ACS Omega **5**, 15169-15176 (2020).

[42] W. A. Harrison, Electronic Structure and the Properties of Solids: The Physics of the Chemical Bond (Dover, New York, 1967).

[43] P. Li and I. Appelbaum, Phys. Rev. B **92**, 195129 (2015).

[44] J. V. Marzik, R. Kershaw, K. Dwight, A. Wold, Journal of Solid State Chemistry, **51**, 170-175 (1984)

[45] C. H. Ho, P. C. Liao, Y. S. Huang, T. R. Yang, K. K. Tiong, J. Appl. Phys. **81**, 6380 (1997)

[46] D. Wolverson, S. Crampin, A. S. Kazemi, A. Ilie, S. J. Bending, ACS Nano **8**, 11154-11164 (2014)

[47] S. Yang, C. Wang, H. Sahin, H. Chen, Y. Li, S.-S. Li, A. Suslu, F. M. Peeters, Q. Liu, J. Li, S. Tongay, Nano Lett. **15**, 1660-1666 (2015)

[48] P. Eickholt, J. Noky, E. F. Schwier, K. Shimada, K. Miyamoto, T. Okuda, C. Datzer, M. Drüppel, P. Krüger, M. Rohlfing, M. Donath, Phys. Rev. B **97**, 165130 (2018)

[49] H.-X. Zhong, S. Gao, J.-J. Shi, L. Yang, Phys. Rev. B **92**, 115438 (2015)

Chapter 6

Strain Induced Electronic Structure Changes in Monolayer ReS_2

6.1 Introduction

There is broad interest in tuning the electronic and optical properties of semiconductors by application of strain. Among 2D layered semiconductors, monolayer TMDs (MX_2, where M = Mo, W is a transition metal, and X = S, Se is a chalcogen atom) are most suitable for strain engineering owing to their durability to large amount of strain before rupture. In contrast to earlier work on silicon semiconductors [5], GaAs based semiconductors, quantum wells, TMDs transcend in performance because of their band gap which is appropriate for optoelectronic applications and their large strain handling capacity. TMDs can withstand strain higher than 10% [6, 7] and by controlling strain, their electronic and optical properties can be tuned. A direct-to-indirect band gap transition [1, 2] and a semiconducting-to-metal transition [3, 4] have been found in them upon application of uniaxial/biaxial tensile strain.

For MoS_2, bandgap tuning has been achieved using tensile strain [8–11] which even led to a direct to indirect bandgap transition [12–17]. Photoluminescence spectroscopy showed almost linear decrease in the optical bandgap of monolayer of MoS_2 [22] with strain which can be interpreted as a result of reduced orbital overlap. The band gap ultimately becomes an indirect [20] with further increase in strain. Under compressive strain, the direct band gap increases first and then reduces to undergo a direct-to-indirect transition [19, 21]. It is the small energy difference between the direct gap and the indirect gap in MoS_2 which makes it possible for a direct to an indirect gap (at $\sim$ 2% uniaxial strain) transition

and a semiconductor-to-metal transition (at $\sim 10\%$ biaxial strain) to take place at small tensile strain. Blue shift [23] of the optical bandgap occurs in MoS_2 with out-of-plane uniaxial tensile strain. In [18], they have explored the interplay between strain and electronic structure in single layer $MoSe_2$ using Raman and PL spectroscopy, supported by density functional theory based calculations. Here also, the direct bandgap is observed to gradually decrease as the strain is varied from compression to tension, and a direct-to-indirect transition is observed on the compressive side.

In a work [24], based on density functional theory calculations, they found the bandgap to increase with the tensile strain for group IVB TMDs. For group VB TMDs (TaX_2), ferromagnetism is induced or enhanced by the tensile strain, and a direct-to-indirect bandgap transition is induced for group VIB TMDs (CrX_2).

Being incited by the earlier studies of strain effect on the electronic structures of TMDs, we went on to investigate the changes that take place in ReS_2 which is a group VIIB TMD. We find the bandgap to reduce monotonically for both tensile and compressive strain along in-plane lattice vectors. Interestingly, a double hump like feature emerges in the valence band of monolayer of ReS_2 that can be manipulated by strain. There are two interactions at play behind the double hump. They are the Re d - Re d interactions and the Re d - S p interactions. We use strain along in-plane lattice vectors as a parameter and play around with these two interactions to induce a topological transition of the Fermi surface by engineering this double hump.

6.2 Methodology

We started with unstrained structures of monolayer ReS_2. Internal positions were optimized using projected augmented wave (PAW) [25] implementation of density functional theory within the Vienna Ab-initio Simulation Package (VASP) [26, 27]. The exchange-correlation functional was approximated by generalized gradient approximation [28] functional. We made the monolayer structure out of bulk ReS_2 by incorporating 24 Å of vacuum along the out-of-plane direction, which is along lattice vector $\vec{a}$. The in-plane lattice parameters were kept fixed at their experimental values of 6.51 Å and 6.46 Å [29]. We used a k-points mesh of 1 x 8 x 8 for optimization. An energy cutoff of 258.7 eV was used for plane wave basis. We applied uniaxial strain along each of the in-plane lattice vectors and varied them in steps of 1% to generate different structures for our study.

6.3 Results and Discussion

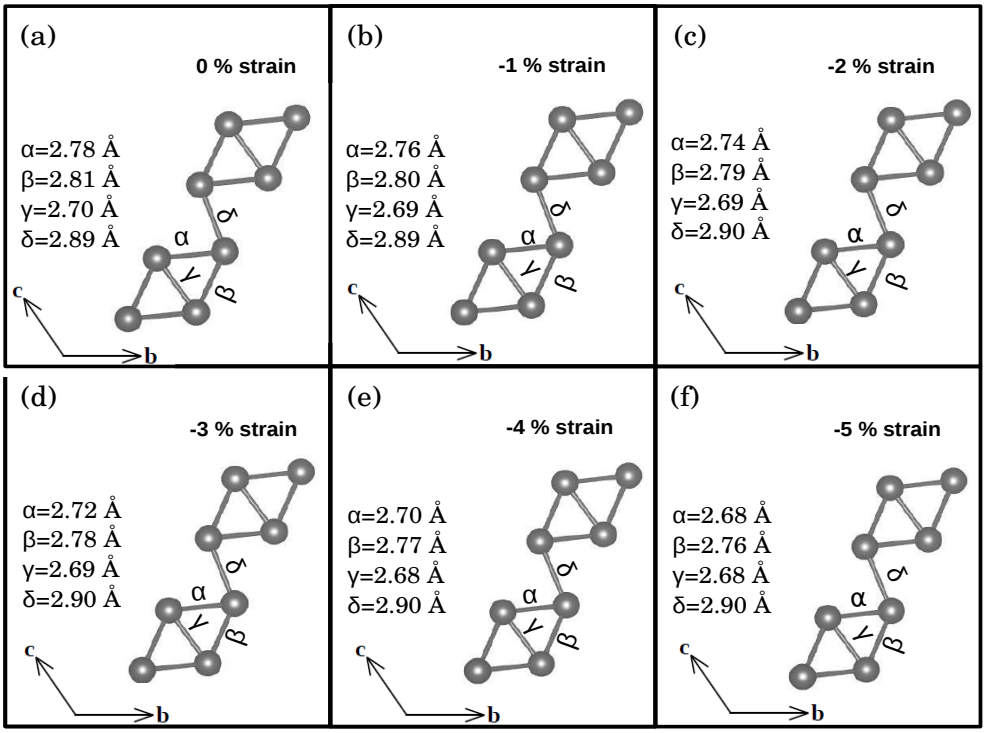

Figure 6.1: Change in the Re-Re bondlengths upon application of compressive strain along lattice vector $\vec{b}$ in increment of 1%. Re-Re bondlengths shown for (a) No strain, (b) 1% compressive strain, (c) 2% compressive strain, (d) 3% compressive strain, (e) 4% compressive strain, (f) 5% compressive strain

We applied uniaxial compressive as well as tensile strain along each of the in-plane lattice vectors and studied the resulting changes in the electronic structure of monolayer ReS_2. First, let us focus on the modifications in electronic structure that emerge after applying strain along lattice vector $\vec{b}$. We began by identifying the changes that take place in the lattice structure and bondlengths. In Figure 6.1, the Re-Re bondlengths have been shown for different compressive strain percentages along lattice vector $\vec{b}$. We find that all the Re-Re bondlengths within each cluster, labelled as α, β and γ, decrease with compression along $\vec{b}$, while the bondlength connecting two adjacent clusters at the corners, labelled by δ, increases. There is considerable change in α from 2.78 Å for 0% strain to 2.68 Å for -5% strain. But change in δ is small, only from 2.89 Å to 2.90 Å. Since the Re-Re interactions are mediated by d orbitals of the Re atoms, a change in the Re-Re bondlengths is equivalent to scaling the d-d interaction strength. Figure 6.2(a) shows the Re-S bondlengths for 0% strain and Figure 6.2(b) shows them for -5% strain. From the figures we find that the Re-S bondlengths also contract with compression with only one

of them rather elongating by 0.01 Å to adjust. Most of the Re-S bondlengths change very little while two of them change considrably with strain. The largest change in Re-S bondlengths is 0.05 Å. Since Re-S interactions are mediated by S p and Re d orbitals, this scales the p-d interaction strength.

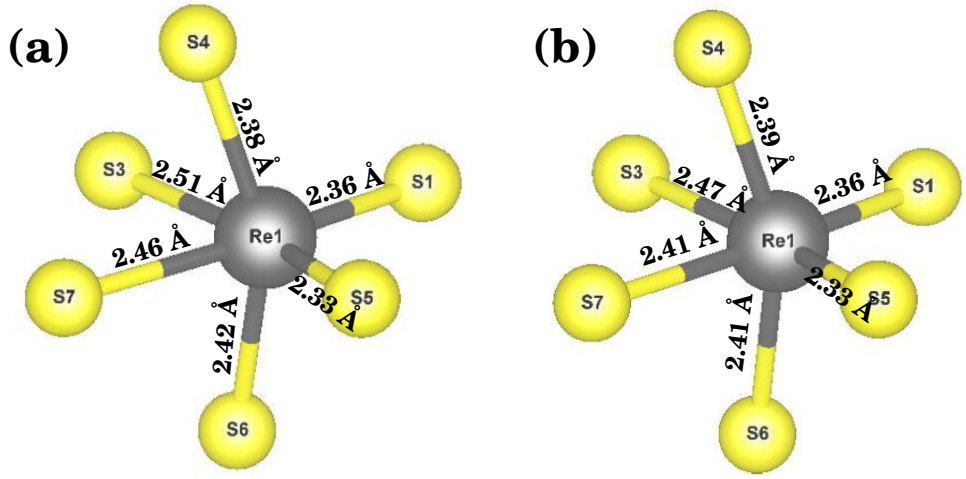

Figure 6.2: Re-S bondlengths for strain along $\vec{b}$: (a) 0% strain, (b) -5% strain

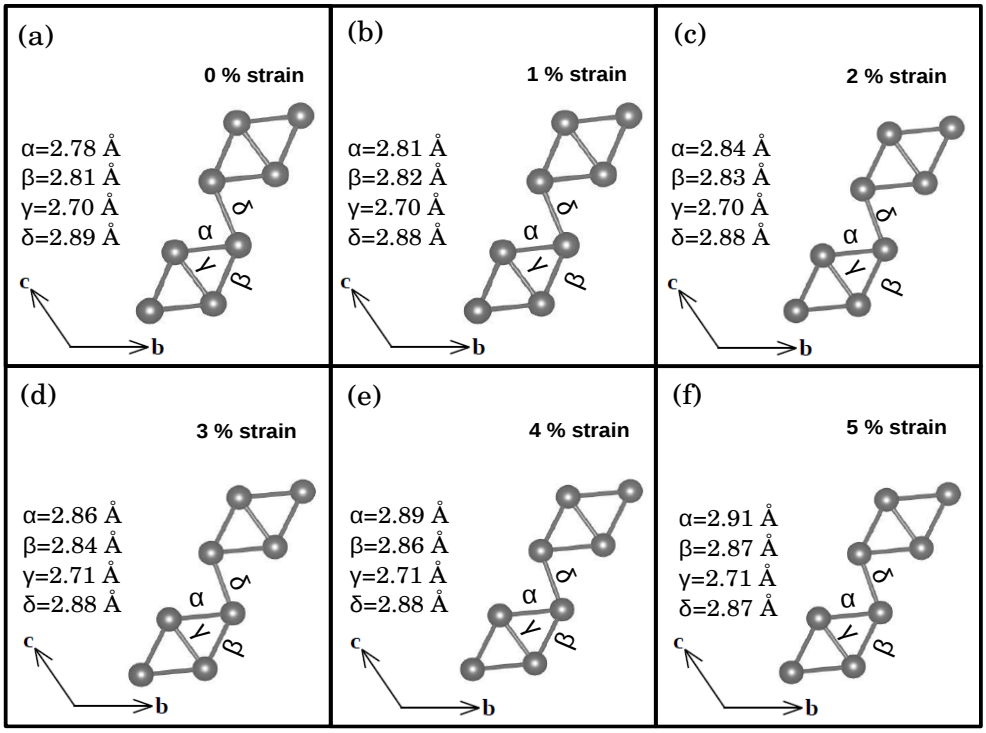

Figure 6.3: Change in the Re-Re bondlengths upon application of tensile strain along lattice vector $\vec{b}$ in increment of 1%. Re-Re bondlengths shown for (a) No strain, (b) 1% tensile strain, (c) 2% tensile strain, (d) 3% tensile strain, (e) 4% tensile strain, (f) 5% tensile strain

Figure 6.3 shows the Re-Re bondlengths for different values of tensile strain along lattice vector $\vec{b}$. We find that all the Re-Re bondlengths within each cluster increase with stretching along $\vec{b}$ while the bondlength connecting two adjacent clusters at the corners, δ, decreases. Here also the change is larger for all the intracluster bondlengths while it is small for the bondlength connecting two clusters.

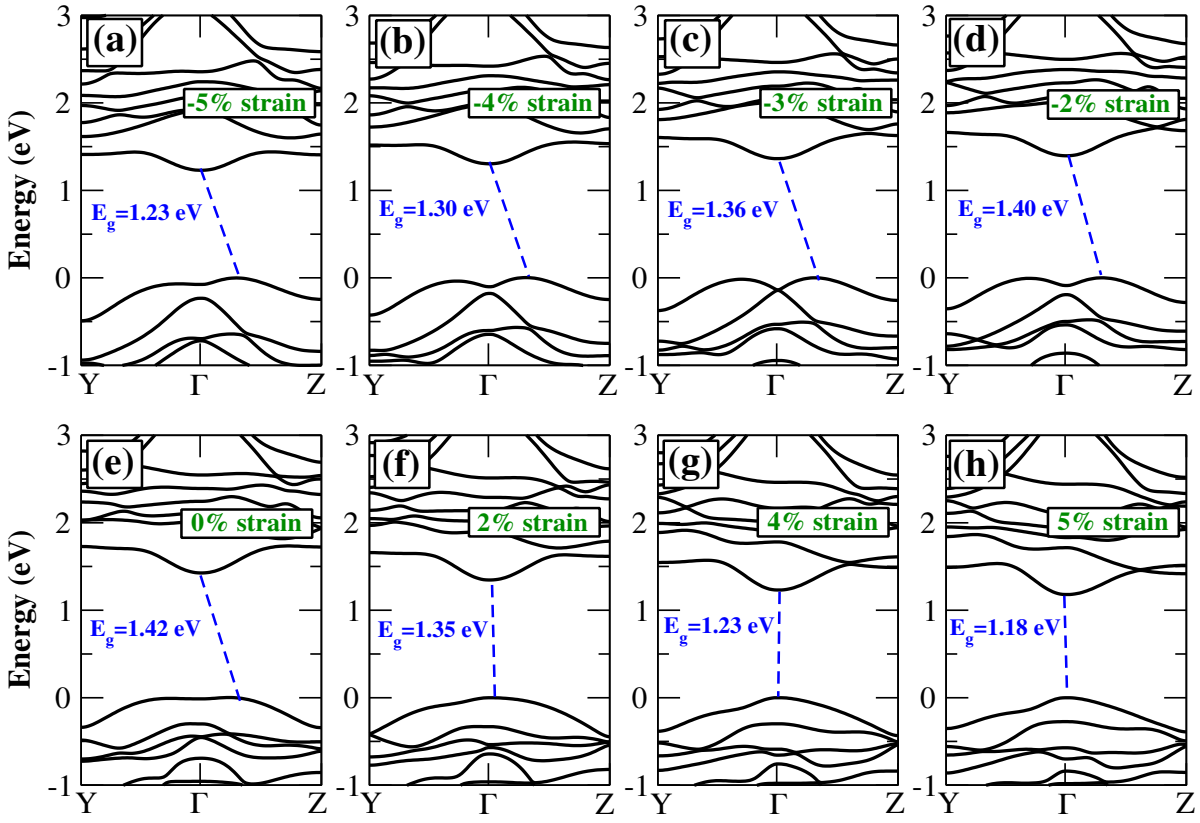

Figure 6.4: Evolution of the bandstructure of monolayer of ReS_2 with strain, both compressive and tensile, along lattice vector $\vec{b}$

We then went on to explore the effects of strain on the bandstructure. The evolution of the monolayer bandstructure with strain along $\vec{b}$ has been shown in Figure 6.4 for all our different choices of compressive as well as tensile strain perecentages. For unstrained case (0%), we see that the material possesses an indirect bandgap of 1.42 eV. The valence band is well separated from the band just below and a double hump like feature is present in the valence band. We find that the bandgap remains indirect upon applying compressive strain and keeps gradually reducing in value with increase in strain perecentage. It drops form its value of 1.42 eV at 0% strain to 1.23 eV for -5% strain. Interestingly, the bandgap turns direct with tensile strain. The value of the bandgap shows similar trend of gradual reduction as it drops form its value of 1.42 eV at 0% strain to 1.18 eV for 5% strain. We see that the double hump like feature in the valence band becomes more prominent

upon moving towards larger value of compressive strain. But the double hump vanishes for tensile strain.

To examine in more detail the factors that contribute to the reduction in bandgap for both compressive and tensile strain, we aligned the bandstructures for all the various strained configurations with respect to the electrostatic core potentials associated with the S atoms. This will help us better compare among the scenario for various structures and trace the shift in valence band energy with strain along $\vec{b}$ [Fig. 6.5], and the same for the conduction band energy [Fig. 6.6].

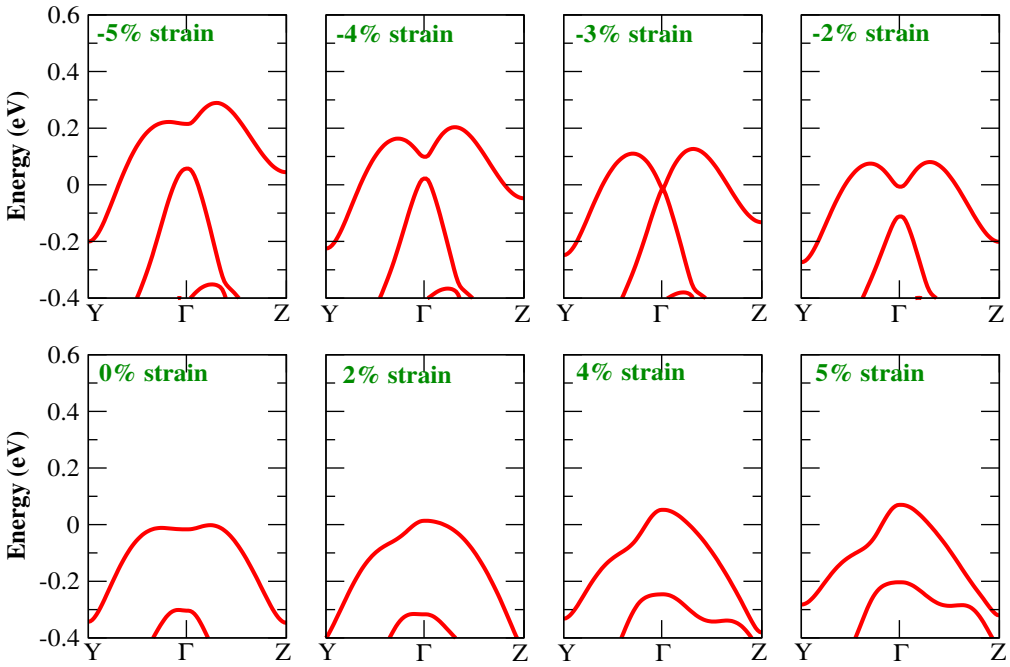

Figure 6.5: Valence band of monolayer of ReS_2 for various strain percentages along lattice vector $\vec{b}$, all aligned with respect to the electrostatic potential of S ions

From Figure 6.5, we find that the valence band maximum shifts upwards in energy with compression. It moves up by 0.28 eV in going from 0% to -5% strain. From Figure 6.6, we also note that the conduction band minimum is pushed upwards with compression where it comes down in energy with tension. The conduction band minimum moves up in energy by 0.1 eV in going from 0% to -5% strain. Since the amount of rising of the valence band maximum is higher than the amount by which the conduction band minimum moves up, this results in a decrease in bandgap upon compression. For tensile strain, again the VBM rises slightly from its value at 0% strain, but the rate is slower. It moves up by 0.07 eV in going from 0% to 5% strain. On the other hand, the conduction band minimum comes down quicker with tension. It moves down by 0.17 eV in going from 0% to 5% strain. Due to the composite effect of both, the bandgap decreases and the decrease in bandgap

is larger for tensile strain. We find that the bandgap is 1.23 eV for 5% compression while it is 1.18 eV for 5% tensile strain.

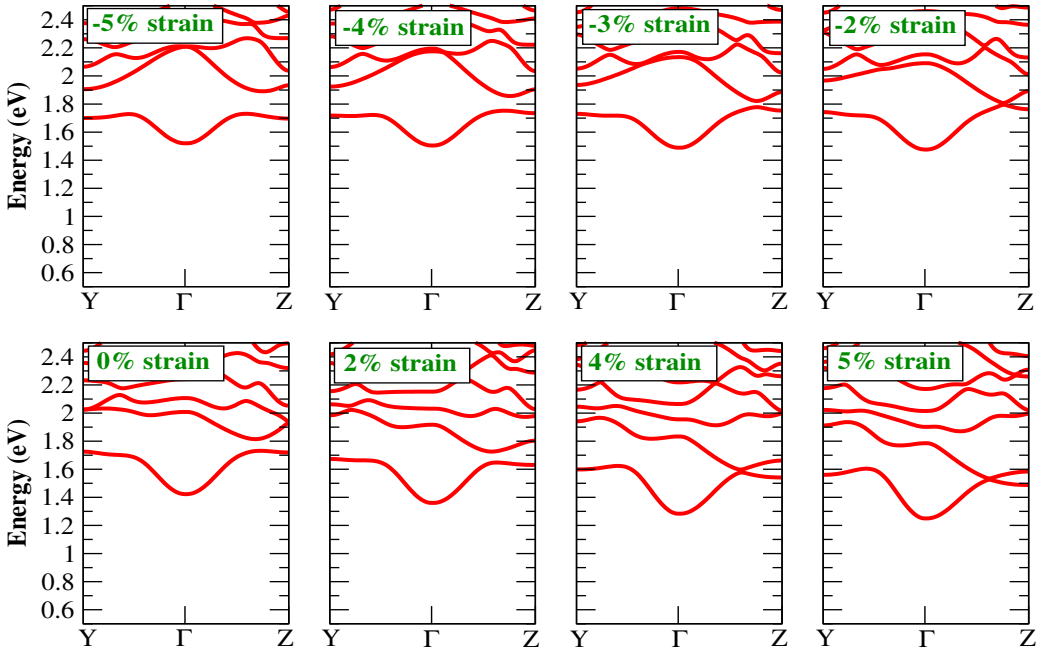

Figure 6.6: Conduction band of monolayer of ReS_2 for various strain percentages along lattice vector $\vec{b}$, all aligned with respect to the electrostatic potential of S ions

Since there are two kinds of fundamental contributors to the shift in the band energy eigenvalues, one is from the onsite energies of the ions and the other is from the hopping interactions between different ions, we wished to estimate their relative weight. We first enquired about the onsite energies. We mapped the ab-inito bandstructure onto a tight-binding model for few of the strained structures using the VASP to WANNIER90 interface, and from our tight-binding calculations, extracted out the onsite energies of the ions. We performed the calculations for 0%, -4% and 4% strain cases. The results have been tabulated in Figure 6.7. We have aligned the energy values with respect to the core potential at Re ion. We additionally subtracted a reference energy of 46.43 eV to reduce the figures. We find that the onsite energies change very little with strain. Hence, we can conclude that the change in the electronic structure with strain is primarily due to the variation in the hopping interaction strengths between ions associated with the change in bondlengths.

MONOLAYER									
	0 % strain			-4 % strain along b			4 % strain along b		
Core potential (E_C) =	-50.88 eV			-50.70 eV			-50.98 eV		
	Energies (E_n) in eV	(E_n- E_C) in eV	(E_n- E_C- E_{ref}) in eV	Energies (E_n) in eV	(E_n- E_C) in eV	(E_n- E_C- E_{ref}) in eV	Energies (E_n) in eV	(E_n- E_C) in eV	(E_n- E_C- E_{ref}) in eV
Re1 d	-4.38	46.50	0.07	-4.27	46.44	0.01	-4.45	46.53	0.1
	-4.29	46.59	0.16	-4.20	46.50	0.07	-4.37	46.61	0.18
	-4.21	46.68	0.25	-4.07	46.63	0.20	-4.30	46.69	0.26
	-2.76	48.13	1.70	-2.55	48.15	1.68	-2.94	46.05	1.61
	-2.71	48.17	1.74	-2.51	48.19	1.76	-2.85	48.13	1.70
Re2 d	-4.39	46.50	0.07	-4.26	46.44	0.01	-4.45	46.53	0.1
	-4.29	46.60	0.17	-4.20	46.50	0.07	-4.37	46.61	0.18
	-4.20	46.68	0.25	-4.07	46.63	0.20	-4.30	46.69	0.26
	-2.75	48.13	1.70	-2.55	48.15	1.68	-2.94	48.04	1.61
	-2.72	48.17	1.74	-2.51	48.19	1.76	-2.85	48.13	1.70
Re3 d	-4.38	46.50	0.07	-4.27	46.43	0.00	-4.50	46.49	0.06
	-4.32	46.57	0.14	-4.22	46.48	0.05	-4.34	46.64	0.21
	-4.31	46.58	0.15	-4.20	46.50	0.07	-4.33	46.65	0.22
	-2.76	48.12	1.69	-2.61	48.10	1.67	-2.87	48.11	1.68
	-2.70	48.18	1.75	-2.52	48.18	1.75	-2.83	48.15	1.72
Re4 d	-4.38	46.50	0.07	-4.27	46.43 ≡E_{ref}	0.00	-4.50	46.49	0.06
	-4.32	46.57	0.14	-4.22	46.48	0.05	-4.34	46.64	0.21
	-4.31	46.58	0.15	-4.20	46.50	0.07	-4.33	46.65	0.22
	-2.76	48.12	1.69	-2.61	48.10	1.67	-2.8720	46.11	1.68
	-2.70	48.18	1.75	-2.52	48.18	1.75	-2.8346	48.15	1.72
S1 p	-6.23	44.66	-1.77	-6.11	44.59	-1.84	-6.29	44.69	-1.74
	-5.54	45.35	-1.08	-5.30	45.40	-1.03	-5.74	45.25	-1.18
	-5.39	45.50	-0.93	-5.18	45.52	-0.91	-5.52	45.46	-0.97

Figure 6.7

We have already noted, from Figure 6.4, that the valence band is well isolated from the band immediately below for 0% strain and shows a double hump like feature with middle point of the humps lying at Γ. But upon increasing compressive strain, the two bands seem to gradually move closer to each other. The double hump becomes more pronounced and the valence band shows a tendency to yield a more prominent dip at Γ for compression and the band just below rises in energy and gradually approaches the valence band (-2%). The two bands ultimately touch together at Γ for -3% strain. We find them again separated from each other at -4% strain and they continue moving away from each other with increasing compression. We speculate that associated with this band crossing of the valence band and the band immediately below at Γ between -2% and -4% strain values, a topological transition has taken place involving an inversion of orbital characters between the two bands.

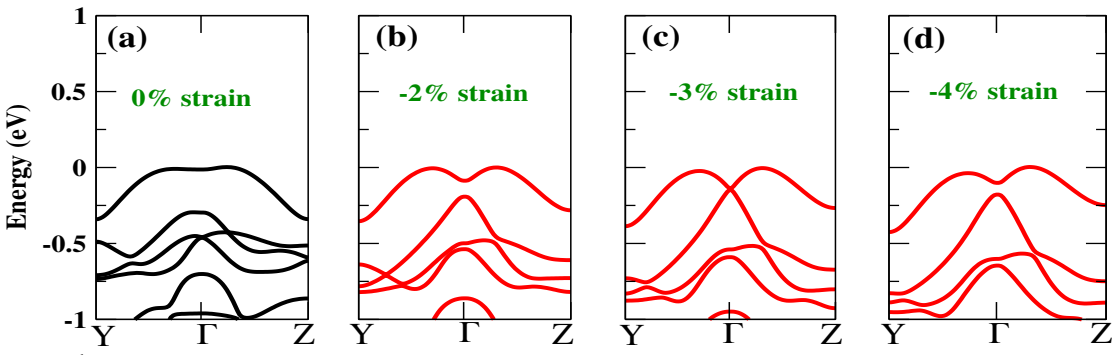

Figure 6.8: Evolution of the valence states in the bandstructure of monolayer of ReS_2 with compressive strain along lattice vector $\vec{b}$

The phenomenon of band crossing has been highlighted in Figure 6.8. In Figure 6.8(b), we see that for -2% strain, the double hump becomes more pronounced and the valence band at Γ comes down in energy. The band just below valence band comes up as if to touch the valence band at Γ. For -3% strain [Figure 6.8(c)], the two bands touch each other at Γ. We see they are again separate from each other at -4% strain in Figure 6.8(d). So, between -2% and -4% strain, there might have taken place an interchange of characters between the valence band and the band below.

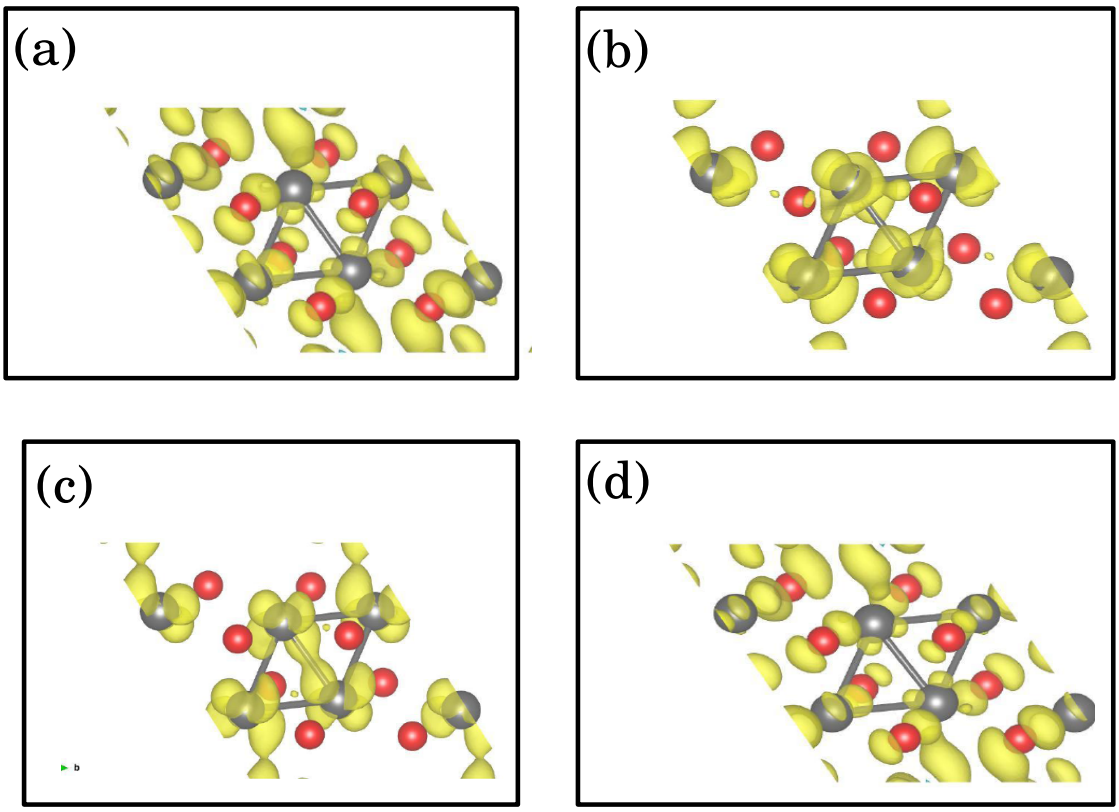

Figure 6.9: Charge densities at Γ for (a) band immediately below the valence band for -2% strain, (b) valence band for -2% strain, (c) band immediately below the valence band for -4% strain, (b) valence band for -4% strain

To confirm any possible inversion of orbital character between the two band at Γ, we plotted the charge densities for the valence band and the band immediately below the valence band at Γ in Figure 6.9. We see that orbital characters of the two bands at Γ got interchanged between the -2% and -4% strain. For -2% strain, the valence band at Γ seems to be primarily contributed by Re d orbitals with negligible contribution from S p states [Fig. 6.9(b)]. The band just below the valence band is seen to have appreciable contribution from S p orbitals [Fig. 6.9(a)]. For -4% strain, the scenario is just the opposite where the orbitals characters seem to have got interchanged between the two bands at Γ [Fig. 6.9(c) and (d)].

To lend further support to the orbital interchange, we plotted the orbital projected band dispersion that will more explicitly show each orbital contribution to the two bands involved. We plotted them for -2% [Fig. 6.10] and -4% [Fig. 6.11] strain. We see that for 2% compressive strain [Fig. 6.10], the valence band at Γ is primarily contributed by Re d_{xy} and Re d_{yz} orbitals. The band immediately below the valence band is chiefly contributed by S p_y and S p_z orbitals.

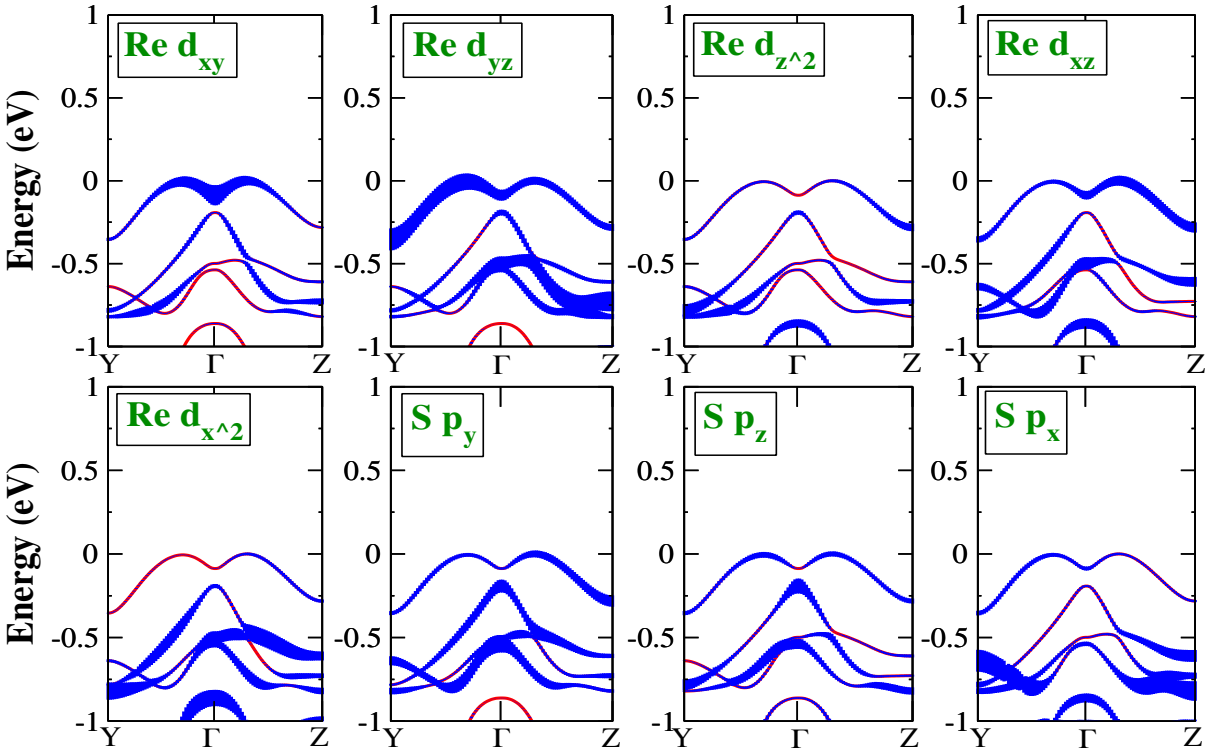

Figure 6.10: Orbital projected bandstructures for monolayer ReS_2 with 2% compressive strain along lattice vector $\vec{b}$

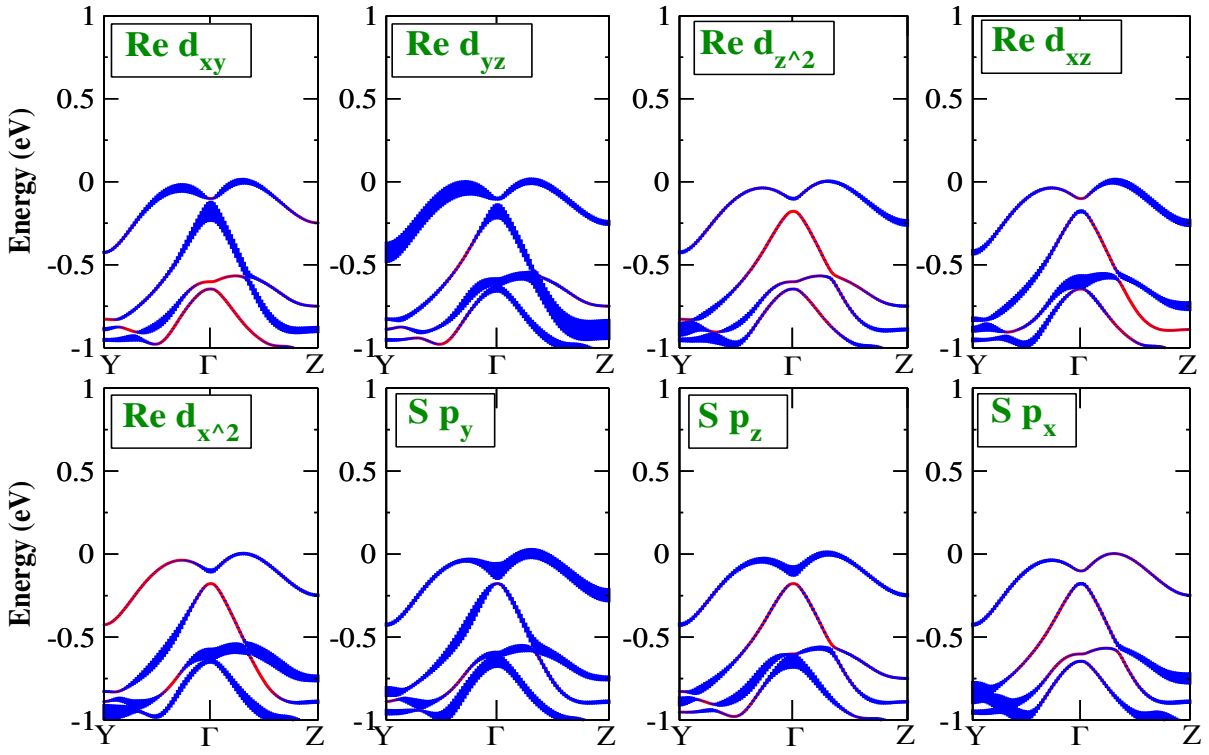

Figure 6.11: Orbital projected bandstructures for monolayer ReS_2 with 4% compressive strain along lattice vector $\vec{b}$

For 4% compressive strain, the picture is inverted [Fig. 6.11]. Here the the valence band at Γ is majorly contributed by S p_y and S p_z orbitals. The band immediately below the valence band is mainly contributed by Re d_{xy} and Re d_{yz} orbitals. Combining with the charge density results, we can proclaim with confidence that there took place an inversion of orbital characters between the valence band and the band immediately below the valence band associated with the band crossing at Γ. This establishes a topological transition to have taken place involving the two bands.

The emergence of the double hump in the valence band in Figure 6.4(a),(b),(c),(d) and (e), for the compressive strain along $\vec{b}$, provides us with an opportunity to trigger a transition involving the Fermi surface, also called Lifshitz transition in the system via carrier doping. Doping the system with holes will bring the Fermi level down and make it cross the valence band. Due to the double hump, hole pockets will appear in the reciprocal space. By controlling the doping, we can conveniently shift the Fermi level along the energy axis to manipulate such hole pockets and thereby realize a topological phase transition of the Fermi surface.

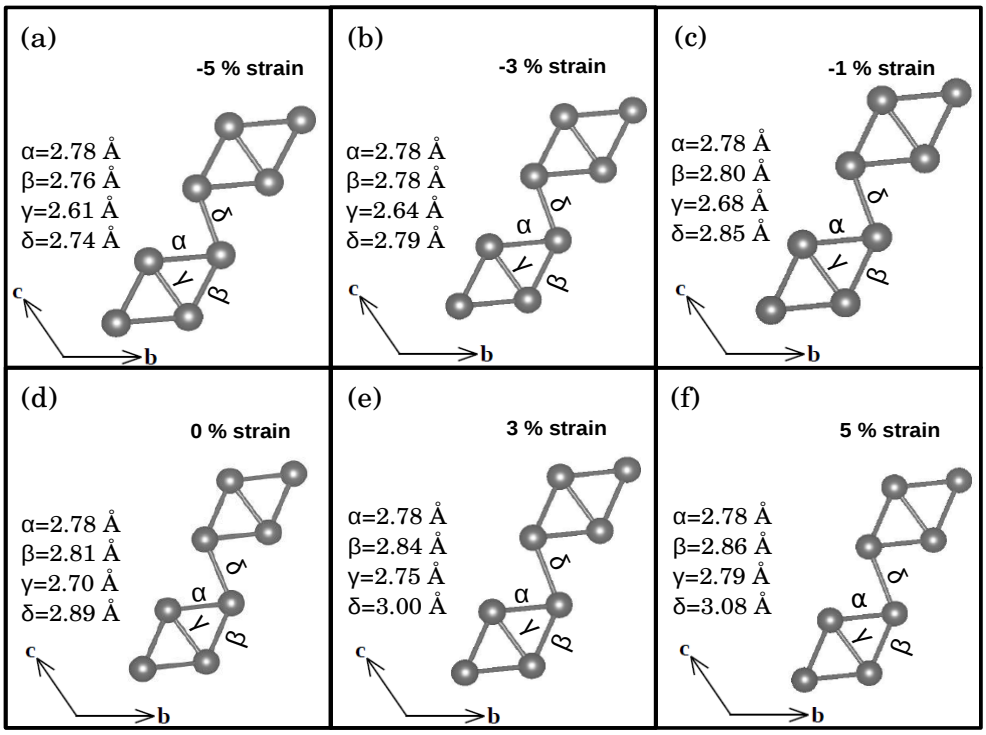

Figure 6.12: Change in the Re-Re bondlengths upon application of compressive as well as tensile strain along lattice vector $\vec{c}$. Re-Re bondlengths shown for (a) 5% compressive strain, (b) 3% compressive strain, (c) 1% compressive strain, (d) 0% strain, (e) 3% tensile strain, (f) 5% tensile strain

Now let us focus on the situation consequent upon applying strain along lattice vector $\vec{c}$. The resulting Re-networks have been shown in Figure 6.12 for different strain percentages, both compressive and tensile. We find that α remains invariant with strain, while β changes little. The greatest impact is on γ and the intercluster bondlength δ. Between -5% to 5% strain, δ changes from 2.74 Å to 3.08 Å. But all the bonds have similar trend, either contracting on compression or elongating on tension. The Re-S coordination has been shown for 0% and -5% strain along $\vec{c}$ in Figure 6.13. Re-S bondlengths appear to change only slightly with strain.

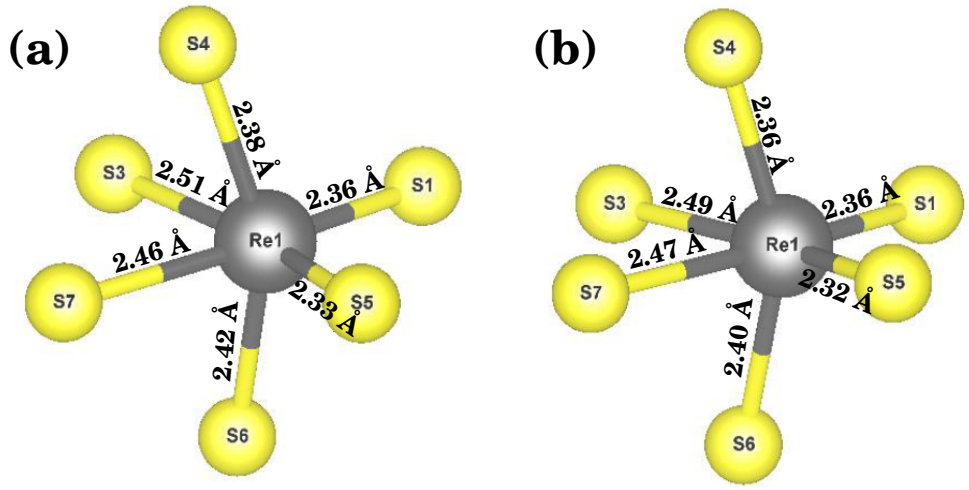

Figure 6.13: Re-S bondlengths for strain along $\vec{c}$: (a) 0% strain, (b) -5% strain

In Figure 6.14, the evolution of the monolayer bandstructure with strain along lattice vector $\vec{c}$ has been shown. Here also, the bandgap reduces from its value at 0% strain for both compressive as well as tensile strain. It drops from 1.42 eV at 0% strain to 1.39 eV for -5% strain and to 1.25 eV for 5% strain. The double hump like feature in the valence band is not so pronounced and it vanishes for large compressive strain. Note that for strain along $\vec{b}$, in contrast, the double hump would rather become more prominent upon application of compressive strain. Another point to note here is the change in the shape of the valence band is monotonic with tensile as well as compressive strain. The reduction in the bandgap with either kind of strain is also smaller as compared to the case of strain along $\vec{b}$ [Fig. 6.4].

Similar to the case of strain along $\vec{b}$, we align the valence bands and the conduction bands with respect to the electrostatic potential at S ion. We see that the valence band maximum moves down monotonically as we go from the compressive to the tensile strain regime [Fig. 6.15]. The valence band maximum moves down by 0.23 eV in going from -5% to 0% strain.

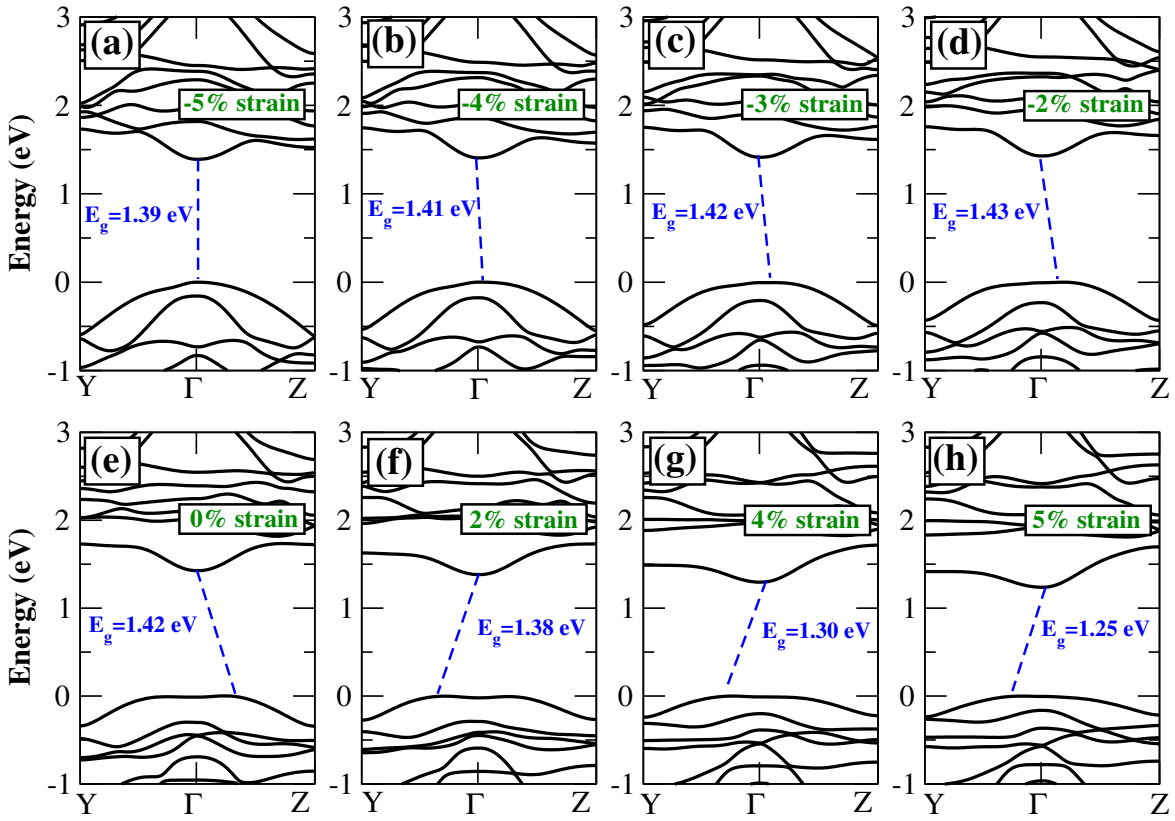

Figure 6.14: Evolution of the bandstructure of monolayer of ReS_2 with strain, both compressive and tensile, along lattice vector $\vec{c}$

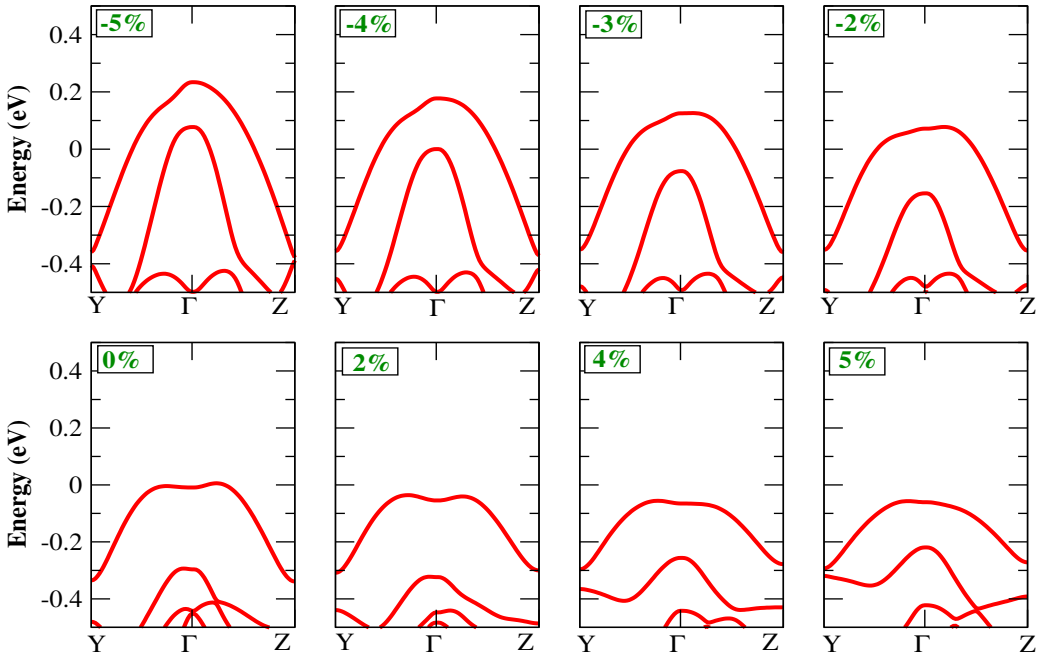

Figure 6.15: Valence band of monolayer of ReS_2 for various strain percentages along lattice vector $\vec{c}$, all aligned with respect to the electrostatic potential of S ions

The conduction band minimum moves down monotonically while going from compressive to tensile strain [Fig. 6.16]. It comes down by 0.19 eV in going from -5% to 0% strain. Hence it is the monotonic rise in the valence band maximum with increasing compression that is contributing to the reduction in bandgap for compressive strain. The valence band maximum comes down by 0.07 eV in going from 0% to 5% strain. The conduction band minimum comes down by 0.25 eV in going from 0% to 5% strain. Hence it is the gradual lowering of the conduction band minimum that is responsible for the reduction in the bandgap for tensile strain.

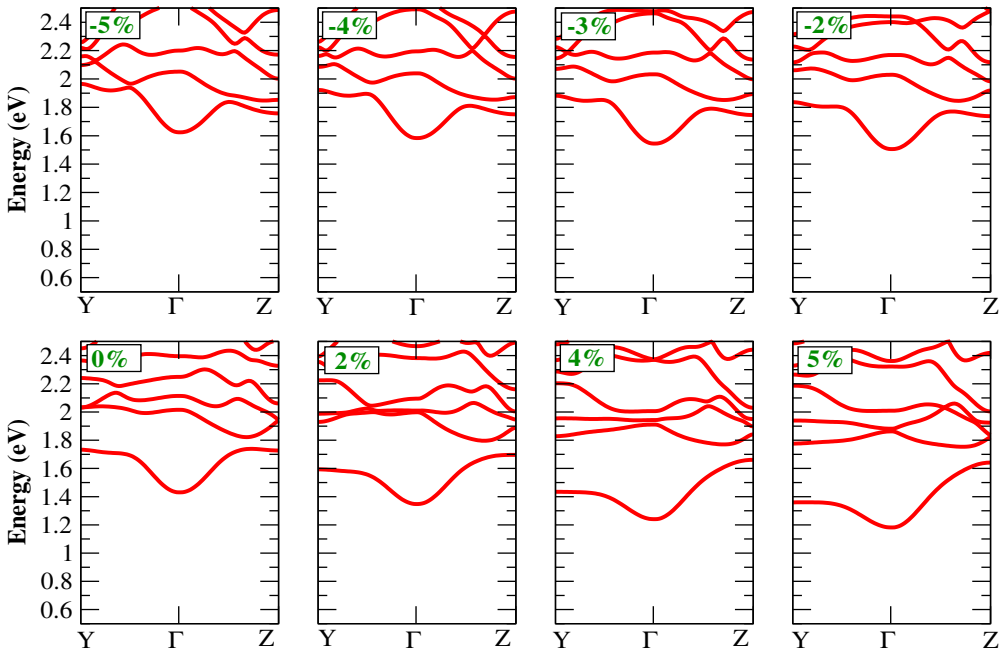

Figure 6.16: Conduction band of monolayer of ReS_2 for various strain percentages along lattice vector $\vec{c}$, all aligned with respect to the electrostatic potential of S ions

6.4 Conclusion

We decided to study the effect of strain on the electronic structure of ReS_2. We chose ReS_2 for our study, because it shows interesting features owing to the various structural motifs that are found in them, like the Re clusters and the one-dimensional chains that interact weakly among themselves. Since by means of strain we can manipulate the various structural motifs, we went on to investigate the changes that take place upon applying compressive as well as tensile strain along the in-plane lattice vectors $\vec{b}$ and $\vec{c}$. We observe different behaviour of the electronic sructure in response to strain along $\vec{b}$ and $\vec{c}$. We found a topological transition to be occurring for the compressive starin along $\vec{b}$.

Bibliography

[1] L. Wang, A. Kutana, and B. I. Yakobson, Ann. Phys. **526**, L7 (2014).

[2] J. Feng, X. Qian, C.-W. Huang, and J. Li, Nat. Photon. **6**, 866 (2012).

[3] E. Scalise, M. Houssa, G. Pourtois, V. Afanas'ev, and A. Stesmans, Nano Res. **5**, 43 (2012).

[4] M. Ghorbani-Asl, S. Borini, A. Kuc, and T. Heine, Phys. Rev. B **87**, 235434 (2013).

[5] J. Bardeen and W. Shockley, Phys. Rev. **80**, 72 (1950).

[6] S. Bertolazzi, J. Brivio, and A. Kis, ACS Nano **5**, 9703 (2011).

[7] A. Castellanos-Gomez, M. Poot, G. A. Steele, H. S. J. van der Zant, N. Agrait, and G. Rubio-Bollinger, Adv. Mater. **24**, 772 (2012).

[8] H. J. Conley, B. Wang, J. I. Ziegler, R. F. Haglund, S. T. Pantelides, and K. I. Bolotin, Nano Lett. **13**, 3626 (2013)

[9] Y. Y. Hui, X. Liu, W. Jie, N. Y. Chan, J. Hao, Y.-T. Hsu, L.-J. Li, W. Guo, and S. P. Lau, ACS Nano **7**, 7126 (2013).

[10] A. Castellanos-Gomez, R. Roldan, E. Cappelluti, M. Buscema, F. Guinea, H. S. J. van der Zant, and G. A. Steele, Nano Lett. **13**, 5361 (2013).

[11] C. R. Zhu, G. Wang, B. L. Liu, X. Marie, X. F. Qiao, X. Zhang,X. X. Wu, H. Fan, P. H. Tan, T. Amand, and B. Urbaszek, Phys. Rev. B **88**, 121301 (2013).

[12] P. Lu, X. Wu, W. Guo, X. C. Zeng, Phys. Chem. Chem. Phys. **14**, 13035-40 (2012)

[13] H. Pan, Y.-W Zhang, J. Phys. Chem. C **116**, 11752-11757 (2012)

[14] Q. Yue, J. Kang, Z. Shao, X. Zhang, S. Chang, G. Wang, S. Qin, J. Li, . Phys. Lett. A **376**, 1166-1170 (2012)

[15] T. Li, Phys. Rev. B **85**, 235407 (2012)

[16] E. Scalise, M. Houssa, G. Pourtois, V. Afanas'ev, A. Stesmans, Nano Res. **5**, 43-48 (2012)

[17] H. Shi, H. Pan, Y.-W. Zhang, B. I. Yakobson, Phys. Rev. B **87**, 155304 (2013)

[18] X. Cheng, L. Jiang, Y. Li, H. Zhang, C. Hu, S. Xie, M. Liu, Z. Qi, Applied Surface Science **521**, 146398 (2020)

[19] [16] A.P. Nayak, T. Pandey, D. Voiry, J. Liu, S.T. Moran, A. Sharma, C. Tan, C.H. Chen, L.J. Li, M. Chhowalla, J.F. Lin, A.K. Singh, D. Akinwande, Nano Lett. **15**, 346-353 (2015)

[20] [22] H.J. Conley, B. Wang, J.I. Ziegler, R.F. Haglund, S.T. Pantelides, K.I. Bolotin, Nano Lett. **13**, 3626-3630 (2013)

[21] [23] E. Scalise, M. Houssa, G. Pourtois, V.V. Afanas'ev, A. Stesmans, Nano Res. **5**, 43-48 (2012)

[22] H. J. Conley, B. Wang, J. I. Ziegler, R. F. Haglund, S. T. Pantelides, and K. I. Bolotin, Nano Lett. **13**, 3626-3630 (2013)

[23] [24] L. Yang, X.D. Cui, J.Y. Zhang, K. Wang, M. Shen, S.S. Zeng, S.A. Dayeh, L. Feng, B. Xiang, Sci. Rep. - UK **4** 5649 (2014)

[24] H. Guo, N. Lu, L. Wang, X. Wu, and X. C. Zeng, J. Phys. Chem. C **118**, 7242-7249 (2014)

[25] P. E. Blöchl, Phys. Rev. B **50**, 17953 (1994); G. Kresse, D. Joubert **59**, 1758 (1999)

[26] G. Kresse, J. Hafner Phys. Rev. B **47**, 558 (1993); G. Kresse, J. Hafner **49**, 14251 (1994); G. Kresse, J. Furthmüller **54**, 11169 (1996)

[27] G. Kresseud, J. Furthmüller, Comput. Mater. Sci. **6**, 15 (1996)

[28] J. P. Perdew, K. Burke, M. Ernzerhof, Phys. Rev. Lett. **77**, 3865 (1996)

[29] H. H. Murray, S. P. Kelty, R. R. Chianelli, C. S. Day, Inorg. Chem. **33**, 4418 (1994)

Chapter 7

Summary of the Thesis Work and Future Plans

In the first project (Chapter 3), we have examined the type-I to type-II transition occurring in GaAs/AlAs heterostructure with varying the thickness of GaAs region. We investigated whether the transition occurs abruptly or gradually. We found it to occur abruptly between 10 and 9 GaAs layers, but the onset of the transition begins much before the actual transition. This has to be experimentally investigated.

In the second project (Chapter 4), we have studied the microscopic origin for differing ground states in ZrX_2 and HfX_2. We have found that it is the metal-chalcogen bond length and hence the hopping parameters that dominates over the charge transfer energy and becomes responsible for the transition. We can also study the effect of pressure and strain to tune these transitions. Experiment can explore the topological transition that we have observed in these systems.

In the third project (Chapter 5), we have probed the physics behind ReS2 being semiconducting despite having an odd number of electrons in outermost d shell. We also probed the origin of weak interlayer interaction in ReS_2. We found the formation of Re clusters to be responsible for opening up a bandgap in ReS2 thereby making it semiconducting. The weak interlayer interaction is attributable to localization of charge densities in the Re plane.

In the fourth project (Chapter 6), we have studied the changes in the electronic structure of monolayer of ReS_2. We have identified a Lifshitz transition under application of strain that can be studied experimentally.